Mean Stress Effects in Temporal and Spectral Fatigue Analysis

Loading & Response and Resistance Contributions

M. Witvoet

TU Delft

DAMEN NAVAL

Mean Stress Effects in Temporal and Spectral Fatigue Analysis

Loading & Response and Resistance Contributions

by

M. Witvoet

to obtain the degree of Master of Science in
Marine Technology at the Delft University of Technology,
to be defended publicly on Tuesday April 26, 2022 at 15:00.

April 14, 2022

Master's Thesis
Document number: MT.21/22.028.M.
Student number: 4464559
Project duration: February 8, 2021 - April 26, 2022
Specialisation: Ship and Offshore Structures

Thesis committee:
Dr. ir. J. H. den Besten — TU Delft, chair
Ir. G. Bufalari — TU Delft
Dr. ir. X. Jiang — TU Delft
Ir. A. L. García-Valenzuela — Damen Naval

Published by: TU Delft, Mechanical, Maritime and Materials Engineering (3mE), Mekelweg 2, 2628 CD Delft, The Netherlands
Electronic version: http://repository.tudelft.nl/

Cover photo: A Sigma frigate turning at high speed during sea trials. Changes in the ship's hydrodynamic profile influence mean stress effects and subsequently fatigue damage (Damen Naval, 2021).

TU Delft DAMEN NAVAL

Preface

Dear reader,

Before you lies my master thesis on *Mean Stress Effect in Temporal and Spectral Fatigue Analysis*. I have written this thesis as a conclusion of the master Marine Technology at Delft University of Technology. During my work, I have received guidance and supervision from Henk den Besten and Gabriele Bufalari (Ship Hydromechanics and Structures, TU Delft) and Alejandro Luna García-Valenzuela (Structural Analysis, Damen Naval).

To them, I would like to express my sincere gratitude. Henk, your thorough and critical scientific attitude has thought me to never stop asking questions, to others or myself. This is something that I am sure will stick with me for the rest of my career. Gabriele, thank you for your guidance during the numerous smaller meetings in which we discussed the difficulties and solutions to the problems I encountered. It helped me remain focused throughout the final stretch of the research.

Alejandro, you introduced me at Damen Naval with great enthusiasm and showed me the ropes regarding structural analysis within a large company. Next to the academic challenges, we faced operational difficulties as well. Thanks to your expertise and great help we were able to overcome most of them and learn a great deal along the way. *Muchísimas gracias!*
To Sandrine, Joep and Izak, thank you for overseeing the project and helping me out where needed. Furthermore, I want to thank Georgios Haniotis and Garry Vandeberg from Infinite Simulation Systems for helping me a lot with the time domain simulations and automation within *Ansys Workbench*.

Last but not least, I want to thank my dear family, friends and girlfriend. Graduating during a pandemic has not been easy, but you pulled me through it. To my mother, father and sister, thank you for having me back at home in Vlissingen when I was working at the office. The weekly travelling was well worth it also thanks to you. To my roommates and study friends, thank you for your support in the form of advice, encouraging words or just a *bakkie* at the *Froudehok*.

To you all, *Bedankt!*

Martijn Witvoet
Delft, April 2022

Summary

Fatigue lifetime has proven to be a leading design parameter for naval vessels [1]. In the field of fatigue analysis and design of welded joints, two overall methods are distinguished: the temporal and spectral approach. In the temporal approach, stress time signals are obtained for a structural detail on which a fatigue assessment concept (like the effective notch stress concept), cycle counting and damage accumulation calculations are carried out. These operations can take up considerable time to set up and perform as simulations are performed at detailed time steps for long durations. The spectral approach on the other hand does not produce stress time signals as it uses a transfer function which linearly translates wave height to stress response. The fatigue lifetime is then calculated using empirical models [2]. This results in a rather fast and effective approach, and therefore typically preferred by the industry.

In the spectral approach, mean stress effects are typically not incorporated due to the highly compressive thermal residual stresses. Recent studies however showed they can have a substantial increasing contribution to the damage [3].

From a loading perspective, spectral calculations typically linearise the hydrodynamic Froude-Krylov force around the mean waterline. The nonlinear (NL) components can be evaluated in the time domain through a direct integration at every time step. Local nonlinear effects can form a large contribution to the fatigue damage [4]. Also, the global hull girder bending moment is expected to change when including nonlinear hydrodynamic behaviour.

A broad literature study presented in this thesis has identified the nonlinear Froude-Krylov (NLFK) and slamming force as the largest contributors to the nonlinear hydrodynamic force for numerous ship types [5]. Their influence on the mean stress response has not been covered in detail. Also, little attention has been paid to incorporating the mean stress effect in the spectral approach because of the lack of mean stress data. A spectral mean stress model was proposed by Niesłony and Böhm [6], but only applied to the older mean stress correction methods and the method was also not verified.

A gap in scientific knowledge was therefore identified and a research roadmap was formulated. The research goal was to provide a first step in the direction of uncovering nonlinear hydrodynamic force contributions to the structural response by focusing on the influence of the NLFK force on the mean stress effect. The findings were to be implemented into a novel spectral approach, offering a quick way to accurately incorporate mean stress while operating in the frequency domain.

Time domain hydrodynamic and structural models were constructed for a pontoon vessel, carrying out constant and variable amplitude simulations. From a fatigue damage perspective, a load case of head seas was chosen. For constant amplitude, nonlinear contributions to the global hull girder bending-induced mean stress turned out to be the largest at the outer fibres, but quite small when compared to the NL-affected stress amplitude. When focusing on local effects around the waterline, no significant NL/L differences were observed. This was attributed to the coarseness of the mesh of the model and the influence of neighbouring geometry.

For the variable amplitude case, simulations of 3 hours were to be performed. Due to a combination of software, hardware and time limitations, only one wave case was evaluated; a JONSWAP spectrum with a significant wave height of 5 metres and peak period of 7.5 seconds. Reviewing the rainflow data showed that a quasi-constant mean stress can be adopted. The resulting value turned out to be in line with the still water bending moment, which could

then be used as input for the spectral mean stress approach [6]. The Walker mean stress correction has been implemented into the novel spectral method to provide higher accuracy for welded joints in the MCF and HCF region. It was found that, for a node set at midship, the novel spectral approach offers a mean reduction in conservatism of 21% as opposed to conventional spectral methods. A mean difference of 16% remained when comparing to the VA time domain mean stress model.

The presented work has provided insight in nonlinear loading & response contributions for a pontoon vessel in both constant, as well as variable amplitude waves. For the ship, linear and nonlinear differences were found to be quite small. This enabled the use of the still water bending moment as an efficient input for the spectral mean stress model.

Future research should focus on the application of the model to naval vessels, as it is believed that nonlinear behaviour will be substantially larger than for the pontoon vessel. Also wide-band correction, effective notch stress concept and nonlinear damage accumulation are links in the total fatigue 'chain' that need to be added in order to arrive at a spectral fatigue model with highly accurate lifetime estimates.

Contents

List of Figures

List of Tables

Nomenclature

Roman Symbols

A	Added mass matrix
B	Damping matrix
C	Stiffness matrix
D	Structural damping matrix
E_t	Integrated spectral energy
F_d	Diffraction force
F_r	Radiation force
F_{FK}	Froude-Krylov force
H	Wave height
$H_{\Delta\sigma}(\omega)$	Linear wave amplitude/stress range transfer function
H_{rms}	Root mean square wave height
K	Structural stiffness matrix
k	Wave number
m_i	Spectral moment, $i = 0, 1, 2, 3, ...$
$S_{\Delta\sigma}(\omega)$	Stress range power density spectrum
$S_\zeta(\omega)$	Wave amplitude power density spectrum

Greek Symbols

δ	Bandwidth parameter
$\eta(t)$	Wave elevation
γ	Peak Enhancement Factor (JONSWAP Spectrum), Walker's Loading & Response Ratio Coefficient
ν_0	Mean zero up-crossing
ν_p	Occurrence of local maxima
ω	Wave frequency
Φ_0	Undisturbed (Froude-Krylov) velocity potential
Φ_7	Diffraction velocity potential
$\Phi_{1..6}$	Radiation velocity potentials
σ_m	Mean stress
σ_{uts}	Ultimate Tensile Stress
θ	Wave heading angle
ε	Wave phase angle

ζ_a	Wave amplitude

Initialisms

CA	Constant Amplitude
COF	Center of Flotation
COG	Center of Gravity
DK	Dirlik Method
FEM	Finite Element Method
FFT	Fast Fourier Transform
FSS	Full Scale Specimen
GRFL	Generalised Random Fatigue Limit
GZ	Gao-Zheng Method
IFFT	Inverse Fast Fourier Transform
IWE	Intermittent Wetting Effect
JONSWAP	Joint North Sea Wave Observation Project
L	Linear
LSS	Large Scale Specimen
MOE	Multi Object Export
NL	Nonlinear
NLFK	Nonlinear Froude-Krylov
NS	Normal Stress
NSX	Normal Stress in X-direction (Global)
NSZ	Normal Stress in Z-direction (Local)
PDF	Probability Density Function
RAO	Response Amplitude Operator
RFC	Rainflow Counting
SFA	Spectral Fatigue Analysis
SQ	Sub-question
SSS	Small Scale Specimen
SWBM	Still Water Bending Moment
TB	Tovo-Benasciutti Method
VA	Variable Amplitude

Chapter 1

Introduction

Fatigue lifetime has proven to be a leading design parameter for slender ships [1]. For the naval vessels designed and built by Damen Naval, fatigue design is therefore a prevalent topic. Lifetime estimates of welded joints, the most sensitive locations in maritime structures, are obtained using calculations in either the time domain (temporal) or frequency domain (spectral). In the temporal approach, stress time signals are obtained for a structural detail on which a fatigue assessment concept (e.g. Hot Spot Structural, Effective Notch Stress Concept, etc.), cycle counting and damage accumulation calculations are then performed. These operations can take up considerable time to set up and perform. The spectral approach on the other hand does not produce stress time signals as it makes use of precalculated operators which linearly translate wave spectra to stress response spectra. An assumed Rayleigh distribution is then used to obtain the fatigue damage. This typically leads to a conservative fatigue damage estimate [7].

Fatigue damage is induced by stress cycles, which are typically defined by their range and mean value, parameters that are not obtained in the spectral approach. The mean stress effect is therefore not directly incorporated in the spectral approach. With respect to the mean stress effect, fatigue assessment concepts as available in codes, guidelines and standards typically do not explicitly account for it. Fatigue resistance curves are typically based on, or translated to $r_{lr} = 0.5$ conditions. Should the considered structural detail be exposed to $r_{lr} < 0.5$ cycles, the lifetime estimate will be conservative. Nonetheless, the mean stress effect in welded joints is typically neglected since the welding-induced quasi-constant mean residual stress is highly tensile. Recent studies regarding generalised fatigue assessment concepts have however shown that the impact of including the mean stress effect can be significant [3].

From loading perspective, calculations in the spectral approach linearise the hydrodynamic Froude-Krylov force around the mean waterline. In the temporal approach, the nonlinear Froude-Krylov (NLFK) force components are obtained through the integration of the actual wave elevation directly at the hull. As structural details around the waterline are considered to be quite fatigue sensitive, including this effect can have a high impact on fatigue assessment accuracy [8]. At the same time, the global hull girder loading is expected to change as well. Fatigue capacity of welds at other locations in the vessel is therefore expected to also change.

As performing the temporal approach demands high computational time, the need for a 'best of both worlds' approach, in which temporal accuracy and spectral efficiency are incorporated, becomes evident. This thesis first aims to review state-of-the-art methods regarding several fatigue analysis 'links' in its total 'chain'. In more detail, recent efforts to formulate novel approaches regarding temporal and spectral fatigue analysis are explored and a missing link is identified. Following, taking advantage of the required calculation time for the spectral approach and considering the consequences of mean waterline linearisations, as well as the importance of mean stress from fatigue resistance perspective, the proposal is to improve the spectral loading & response calculation procedure for nonlinear loading and mean stress effects.

1.1 Motivation

Fatigue-induced damage is a well-known phenomenon in marine structures. As far back as the Second World War, brittle fracture was observed in US naval vessels like the Liberty freighters and T2-tankers [9]. With the introduction of welding, new fatigue concerns arose. Stress concentrations at the weld notches along with the reduced material strength in the weld heat-affected zone provoked the need for accurate fatigue design choices. In the 1960s and '70s, supertankers were heavily affected by fatigue damage. Thousands of cracks were observed after only a few years of service.

Nowadays, numerous improvements with regards to fatigue design have been made. Engineers are able to design safe marine structures by predicting the fatigue lifetime with accurate methods. However, uncertainties are still present in the different stages of fatigue analysis (operational profile, fatigue damage criterion, damage accumulation, etc.) [10]. Conservative estimates are therefore typically preferred and safety factors are widely incorporated [11]. A better understanding of the underlying mechanics and improving the accuracy of the predictions is of great importance.

With worldwide geopolitical tensions rising, as well as the increasing threat of natural disasters due to climate change, the operational profile of naval vessels become wider and more uncertain [12]. For the design and production of new ships for the Dutch and German Navy, Damen Naval experiences increasing requirements regarding capabilities and endurance [13, 14]. The new MKS-180 frigates currently in design for instance have the requirement to operate for two consecutive years without the need for extensive maintenance work [14]. With regards to fatigue design, this poses a real challenge. Less conservative structures are pursued, reducing the structural weight and material costs, but sufficient safety and strength must still be ensured. For Damen Naval, this means that conventional methodologies need to be improved with more high-tech calculation procedures. The complexity of future analyses will only keep rising due to the increasing industry requirements.

1.1.1 Importance

In general, gaining a better understanding on the mechanics and underlying relations regarding fatigue fracture in marine structures will benefit societal, industrial and scientific purposes. From a society point of view, better fatigue design will ensure seaworthy vessels, providing safe transit and work conditions for passengers and crew. Due to fatigue lifetime being a prevalent topic in a wide variety of engineering fields, scientific findings can be shared to benefit them as well (civil infrastructure, automotive, aviation, etc.).

The industry also benefits from fatigue research since more accurate fatigue analysis methods result in less conservative structure design, meaning less required material and corresponding costs. Also, accurate fatigue damage estimates enable predictive maintenance along with a 'digital twin approach' [15]. This benefits ship operators to a large extent.

In the scientific field, the aim should always be to uncover underlying mechanics and question the 'why' of a given problem. With respect to fatigue analysis, there still remain a lot of missing links to uncover. A 'total fatigue life' model is pursued and the incorporation of accurate and generalised stress criteria is a large topic in that respect [16, 3]. With the introduction of the effective notch and total stress concept, one generalised fatigue resistance curve has been formulated, applicable to all welded notches [17]. Yet still, uncertainties in other fields, for instance loading & response, leave challenges for the future of fatigue analysis [10].

1.2 Problem Statement

Following the knowledge gap analysis presented in this thesis, the problem statement can be divided into two parts:

1. The mean stress effect is not accurately incorporated into the spectral approach.
2. Nonlinear contributions (Froude-Krylov, slamming) to the mean stress effect are overlooked.

1.3 Research Question

Following the knowledge gap and the problem statement (section 4.1), the following research question is stated (section 4.2):

> How can the nonlinear Froude-Krylov loading & response-affected mean stress as well as the fatigue resistance consequences be incorporated in a spectral fatigue analysis?

Sub-questions

Subdividing the main research question into three parts (loading & response, fatigue damage, spectral improvement), three sub-questions are stated (section 4.2.1):

1. How does the NLFK force affect the mean stress response?
2. What are the consequences of nonlinear mean stress response contributions for the fatigue damage?
3. Can state-of-the-art WB correction, spectral MSE, stress assessment concept, and (nonlinear) damage accumulation methods be combined to produce a novel spectral approach with improved accuracy?

1.4 Research Scope

This research focuses on linear and nonlinear loading contributions to the (mean stress) response and, subsequently the fatigue damage. During the literature review, the nonlinear Froude-Krylov and slamming force were identified as the main contributors. For this thesis, the focus lies on the nonlinear Froude-Krylov force only.

The possibilities to investigate the nonlinear effects are limited by the capabilities of the available tools. The software of *Ansys Workbench* is used within this thesis to perform the hydrodynamic and structural simulations. Ways to model nonlinearities in constant amplitude, as well as variable amplitude waves are limited. Section 5.5 elaborates on this. Within the available tools, it is made sure that linear and nonlinear contributions are modelled as good as possible.

Furthermore, this research covers one ship type; a pontoon model provided by Damen Naval (section 5.1). Due to confidentiality reasons, as well as the availability of comparable fatigue data sets, this vessel was adopted. A standard steel material is applied (table B.1). No other material types are reviewed.

Finally, while multiple constant amplitude runs have been carried out, only one variable amplitude case was performed. This was due to some severe limitations posed by the software of *Ansys Workbench*, as well as inadequate hardware capability. Full automation of the time domain hydrodynamic and structural simulations and fatigue post-processing was not reached due to this. Numerous manual steps had to be performed, and the available storage capacity became an issue when running longer time traces. Section 5.2.1 elaborates further on this.

1.5 Research Goal

A first step in the direction of investigating nonlinear hydrodynamic force contributions to the structural response by focusing on the relation of the NLFK force with the mean stress is proposed. The goal here is to gain knowledge on the interaction of these two links in the fatigue analysis chain. As a result, a better understanding of the interaction between said loading and response effects will be reached and thereby knowledge will be added to the general approach of fatigue analysis. Results are to be obtained through time domain simulations, and the findings will be plugged into a novel spectral fatigue analysis including state-of-the-art *WB correction*, *spectral MSE*, *stress assessment* and *(nonlinear) damage accumulation* methods. The novel approach will aim to yield more accurate results than former ones while maintaining time efficiency as compared to the temporal approach.

1.6 Report Outline

This thesis presents a thorough literature study and subsequently a modelling and assessment approach to uncover incorporating nonlinear-induced mean stress effects in temporal and, especially, spectral fatigue analysis.

Part I showcases the literature review which was performed before the practical research. Numerous fields in loading & response (chapter 2) and fatigue resistance (chapter 3) are discussed. Concluding, a scientific gap analysis is performed, and the research road map is set up based on the main research question and three sub-questions (chapter 4).

Part II consists of two chapters. First, chapter 5 shows how the temporal approach is set up and verified. The ship model and time domain modelling choices are elaborated and checked for convergence. This provides the answer to the first sub-question. Second, chapter 6 showcases the construction of the novel spectral approach based on the findings of the previous chapter and formulates the results with respect to state-of-the-art methods. It concludes by answering the second and third sub-questions.

Finally, part III evaluates the work. Conclusions are drawn regarding the research questions (chapter 7), and recommendations for future work are formulated (chapter 8). These are summarised in a road map for further research steps to improve upon the presented model (chapter 9).

I

Literature Review

Chapter 2

Loading & Response

This chapter will discuss the literature overview regarding loading and response analysis for marine applications. Section 2.1.1 covers the stochastic modelling of waves for the short- and long-term. Then, the two main approaches in fatigue analysis are distinguished: the temporal and spectral approach. They will be explained in section 2.2 and 2.3 as further subjects fall within the framework of these methods. The approach with regards to fatigue damage calculation for both methods is briefly discussed. In chapter 3, the proceedings regarding fatigue will be further explained. Furthermore, section 2.4 discusses nonlinear contributions in hydrodynamic loading. Finally, section 2.5 showcases state-of-the-art statistical methodology to incorporate these contributions in the spectral approach.

2.1 Wave Statistics

For seagoing vessels, hydrodynamic forces due to waves are the most prevalent loading sources. Because at sea waves behave highly stochastic, statistical methods are often used to describe them. A wave frequency spectrum can be formed by plotting the wave energy against the frequency. This way, the total energy contained in the spectrum can be obtained by integrating the spectrum curve, as stated in equation 2.1. Wave spectra are used not only to describe a wave field in a compact way, but mostly to characterise all possible observations that could have been made under the conditions of the actual observation [18].

$$E_t = \int_0^\infty E(f)df \tag{2.1}$$

The root mean square, mean and significant wave height (H_{rms}, $\bar{H}$ and H_s) are used to describe the statistical properties of the wave spectrum [18].

$$H_{rms}^2 = \int_0^\infty p_R(H)H^2dH = \frac{8}{g\rho}\bar{E} \tag{2.2}$$

Typically in wave modelling, a distinction is made between short-term statistics and long-term statistics. The short term ranges from minutes to several hours, whereas the long term considers periods of dozens of years or more [18]. With this distinction in time frames, different assumptions are applied.

2.1.1 Short-Term

An important assumption when considering short-term wave statistics is that the waves behave stationary, meaning the statistical properties are not affected by a shift in the time origin [2]. When modelling waves, in principle, the wave contribution to the water elevation, or wave elevation, $\eta(t)$ at a certain location (x, y) is considered to be a superposition of n amount of regular wave components as shown in equation 2.3 [19]. Here, a_j is the wave amplitude, ω_j is the radial frequency and ε_j is the random phase of wave component j. These parameters are

all random variables and by using them, the statistical distribution of wave heights was derived by Longuet-Higgins [20]. Using Euler's formula and goniometric identities, equation 2.3 is rewritten in the same line to show the equation in sinusoidal form [21].

$$\eta(t) = Re\left[\sum_{j=1}^{n} a_j e^{i(\omega_j t + \varepsilon_j)}\right] = \sum_{j=1}^{n} a_j \left[cos(\omega_j t)cos(\varepsilon_j) - sin(\omega_j t)sin(\varepsilon_j)\right] \tag{2.3}$$

Because of the stationary nature of the wave elevation, it is assumed to be Normal-distributed (Gaussian). The amplitudes and phases of the regular wave components a_j and ε_j (eq. 2.3) are therefore also assumed to be Gaussian [22].

A second assumption is that the radial frequencies ω_j are grouped within a narrow band around a central frequency ω such that $|\omega_j - \omega_j'|/\omega << 1$ for each wave component j and j'. This is called the *narrow band assumption*. DNV described the degree of bandwidth using the bandwidth parameter δ (eq. 2.4). Here, α incorporates spectral moments m_i as shown in equation 2.5 [23]. The zeroth and higher spectral moments are used to calculate different spectral properties like the standard deviation, skewness and kurtosis, as well as the mean zero up-crossing frequency rate ν_0 and the local maxima statistics ν_p, which are both shown in equation 2.7.

$$\delta = \sqrt{1 - \tilde{\alpha}_1^2} \tag{2.4}$$

$$\widetilde{\alpha}_i = \frac{m_i}{\sqrt{m_0 m_{2i}}},\ i = 1, 2, 3 \ldots \tag{2.5}$$

$$m_i = \int_0^\infty \omega^j S(\omega) d\omega,\ i = 0, 1, 2 \ldots \tag{2.6}$$

$$\nu_0 = \frac{1}{2\pi}\sqrt{\frac{m_2}{m_0}}, \quad \nu_p = \frac{1}{2\pi}\sqrt{\frac{m_4}{m_2}} \tag{2.7}$$

Typically, values of $\delta < 0.1$ are considered to mark a narrow-banded spectrum [24]. The Rayleigh probability density function (PDF) is shown in equation 2.9, utilising the root mean square wave height H_{rms} (eq. 2.8). Observations have shown that this describes narrow-banded spectra, as well as slightly broader spectra quite well [18].

$$H_{rms}^2 = \int_0^\infty p_R(H) H^2 dH = \frac{8}{g\rho}\bar{E} \tag{2.8}$$

$$p_R(H) = \frac{2H}{H_{rms}^2} exp\left(-\left(\frac{H}{H_{rms}}\right)^2\right) \tag{2.9}$$

2.1.2 Long-Term

For the short-term statistics of waves, it was shown that for a *stationary* , *narrow-banded* process, the wave elevation is Gaussian distributed and the wave peak statistics are Rayleigh-distributed. For a long-term process (12+ years), stationary conditions are not met and therefore these assumptions do no longer hold. The long-term is therefore modelled as a large number of stationary short-term sea states, each with their own probability of occurrence. This information is summarised in a wave scatter diagram. This data set provides, for a given period of

time (∼20 years), information on the probability of occurrence of certain wave spectra which are characterised by a significant wave height H_s and wave period T_e.

Because of the instationary nature of the long-term, extreme-value theory is typically applied [18]. For this theory to be applicable, an important requirement is that there is statistical independence between the considered values (for instance wave height). This can only be ensured for a wave elevation time trace when the sampling time is large enough. By applying this theory, the long-term extreme wave height distributions, often interesting for offshore structural design, can be described by the two-parameter Weibull distribution [18]. This distribution has proven to provide good results for modelling long-term extreme wave heights.

2.2 Temporal Approach

In the temporal approach, simulations are carried out in the time domain. During the hydrodynamic analysis, a wave field is applied in real time to the ship structure. Because of this, the method is able to cover the 'full picture'; time-varying linear and nonlinear forces are incorporated in a direct way [25]. The origin of the nonlinear force contributions will be the focus of section 2.4.

In order to perform hydrodynamic analysis in the time domain, appropriate modelling choices should be made. Mohammadi conducted spectral and temporal fatigue analysis for an offshore jacket structure [7]. In the research, the following parameters are of great importance to time domain simulations:

- Time step Δt.
- Number of wave frequencies n_f.
- Number of time signal realisations.
- Simulation time T_{sim}, dependent on repetition of spectral statistics.

The time step should be small enough to accommodate the discretisation of even relatively small waves into acceptable intervals [26]. For instance, a wave with $T_p = 2$ s should be discretised in at least ten steps, so $\Delta t = 0.2$ s. As for the number of frequencies which are included in the formation of the wave field, a sufficient number of frequency components should be included in order to capture even small variations in the water elevation [7].

With regards to the wave component phase shift ε_i, a Normal distribution is assumed [27]. Each wave component has a phase angle which was selected from the distribution. Running a model multiple times with different random phase angle realisations will help representing the statistical properties of the wave spectrum [28]. This can however result in excessive computation time. Mohammadi assumes a narrow-banded wave spectrum, which ensures a repetition of the wave field within a specific time frame [7]. When this is the case, all wave statistics are assumed to be included in the time signal. The required number of time signal realisations with different phase angles is directly related to the simulation time. Kvittem states that three simulations with different phase realisations and a simulation time of one hour will have the same statistical content as one three-hour simulation with one phase realisation [28]. Mohammadi chose for the latter, while Kvittem performed multiple three-hour simulations with ten phase realisations to be able to see convergence in the structural response results [7, 28].

It will be clear that for wider spectra, more statistical content is present. With the narrow-band assumption, there will be less content and therefore simulation time can be shortened. However, it is of importance to make sure that the statistics of a certain time signal realisation

are complete. Using a Fourier transform to obtain the wave spectrum of the time signal realisation is a good way to confirm similarity with the original spectrum.

The general procedure of the temporal approach will now be discussed. A visualisation of the procedure is given in figure 2.1. A relevant wave spectrum $S_{\zeta,i}$, which is taken from the wave scatter diagram, is used to create a time signal of the wave field elevation $\eta(t)$. This can be done by means of an inverse Fourier transform where the regular wave components from the spectrum are used to form the wave elevation. Having obtained a realistic wave field, it is applied to the structure in order to obtain its hydrodynamic response; the centre of gravity (COG) accelerations and pressures on the hull panels. This information can then be transported to a finite element model (FEM) of the structure. By applying the pressures to this model, stress time signals are obtained for every node, which are to be corrected with a fatigue assessment concept (section 3.3). These are exported for post-processing; the fatigue analysis part. Here, rainflow counting is performed on the signal of a node of interest, obtaining the stress ranges, mean stress and number of cycles. The total fatigue damage D_t can then be determined according to linear damage accumulation [8].

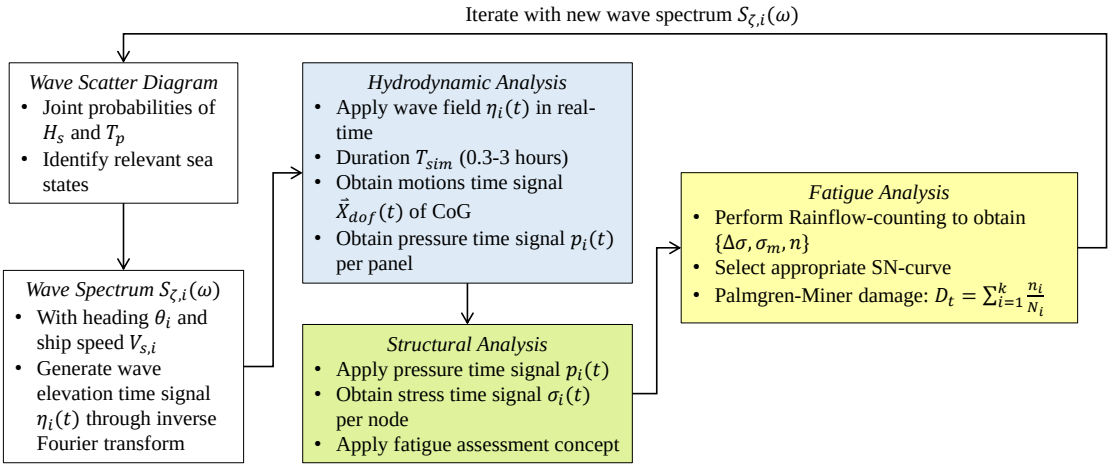

Figure 2.1: A Typical TFA Workflow.

2.3 Spectral Approach

Spectral fatigue analysis (SFA) is an efficient fatigue assessment method which is used to determine the fatigue lifetime of a structure design, reducing time consumption with respect to the temporal approach [1]. With this method, in essence, the ship is modelled as a linear operator between wave-induced loading and structural response [2]. Like stated before, by using the superposition principle, a sea state can be described in a single wave spectrum which describes how energy is divided over the frequencies of the different wave components [19]. For Gaussian, narrow-banded waves the wave amplitudes follow a Rayleigh distribution [19]. Because of the assumption that there is a linear relation between the wave amplitudes and structural response, the latter will therefore also be Rayleigh-distributed.

From the wave scatter diagram, wave spectra are obtained which each have their own probability of occurrence. Each wave spectrum is characterised by the significant wave height H_s and period T_p. From a fatigue perspective, it is known that wave spectra will in the end contribute differently to the fatigue damage, depending on their probability of occurrence. For instance, mild sea states will contribute a lot because of their high probability of occurrence. On the other hand, extreme sea states occur less often but inflict high damage in the low-cycle fatigue range [8]. In order to in the end obtain the total fatigue damage estimation, each short-term

sea state $S_{\zeta,i}$ in the wave scatter diagram is weighted by its coefficient of contribution to fatigue damage [29]. Using these coefficients, a long-term estimation of the total damage can be made.

For a given sea state $S_{\zeta,i}$, the wave field can be described as the summation of an infinite amount of regular, harmonic wave components [18]. These components all have an amplitude $\zeta_a = 1$ m and an individual wave frequency ω_j. They are captured in a wave spectrum which plots the spectral energy density against the wave frequency. In the spectral approach, the wave spectrum of the corresponding sea state is discretised into a number of j regular wave components with frequency ω_j which will be applied to the ship separately during the hydrodynamic analysis. For now, the procedure of SFA will be explained for a single wave spectrum $S_{\zeta,i}$, keeping in mind that it should be repeated to obtain the short-term fatigue damage for every relevant sea state. Note that information of the wave phase angle ε_j, unlike in the temporal approach, is not directly incorporated because the wave spectrum only includes wave height information. The phase is therefore taken as a Gaussian random variable, like discussed in section 2.1.

A visualisation of the process of the discretisation of the wave spectrum is given in figure 2.2. In the figure, the wave field is depicted as an infinite amount of wave components, leading to a continuous wave spectrum. In the spectral approach, this spectrum is discretised in N_ω wave components. Including more wave components will in the end represent the wave field better, but it will also mean a higher computation time. The resulting regular wave is plotted over the ships x-coordinate instead of time because in the spectral approach, a 'snapshot' of each wave will be applied to the ship model, explaining the $\eta(x)$-relation in the figure. The equation of η_j depicted in the figure has its time dependency removed by assessing the wave elevation at $t = 0$. The wave number k_j and phase ε_j are included as shown. Although $\omega_j t$ is zero, ω_j is still incorporated in k_j by the dispersion relation (eq. 2.10) [18]. The spatial coordinate x indicates that the regular wave component is applied along the ship length at one time instant.
The schematic of figure 2.2 leaves the heading of the waves out-of-scope; the problem is reduced to 2D. To incorporate this, a spectrum would have to be formed for multiple wave headings θ. Again, every discretised wave component of these spectra would have to be applied to the ship separately in order to obtain the response spectrum.

$$\omega = \sqrt{gk}, \quad \text{for deep water} \tag{2.10}$$

For hydrodynamic analysis in the spectral approach, a regular wave component with unit wave amplitude ($\zeta_a = 1$ m) and frequency ω_j derived from the wave spectrum is applied to the ship's 3D-model at one moment in time. The software then computes the pressure on the hull by assessing the undisturbed and diffraction potential at each panel [19]. Because every discretised regular wave component is addressed in this manner, a pressure RAO spectrum can be made per panel of the hull, along with a motions RAO spectrum for every degree of freedom. This information is required for the structural response analysis.

In the structural response analysis part the load case (pressure and accelerations RAOs) will be applied to the ship's FEM model. The stress level at every node will be determined using the pressure spectrum which was obtained during the hydrodynamic analysis. The linear transfer function $H_{\Delta\sigma}$ is then formed per node. It links the wave spectrum (with unit wave height) to the response spectrum, according to equation 2.11 [2]. Resulting from this equation is the stress range response spectrum per node $S_{\Delta\sigma}(\omega)$. This is the output of the structural response part and it will be used in the fatigue analysis part.

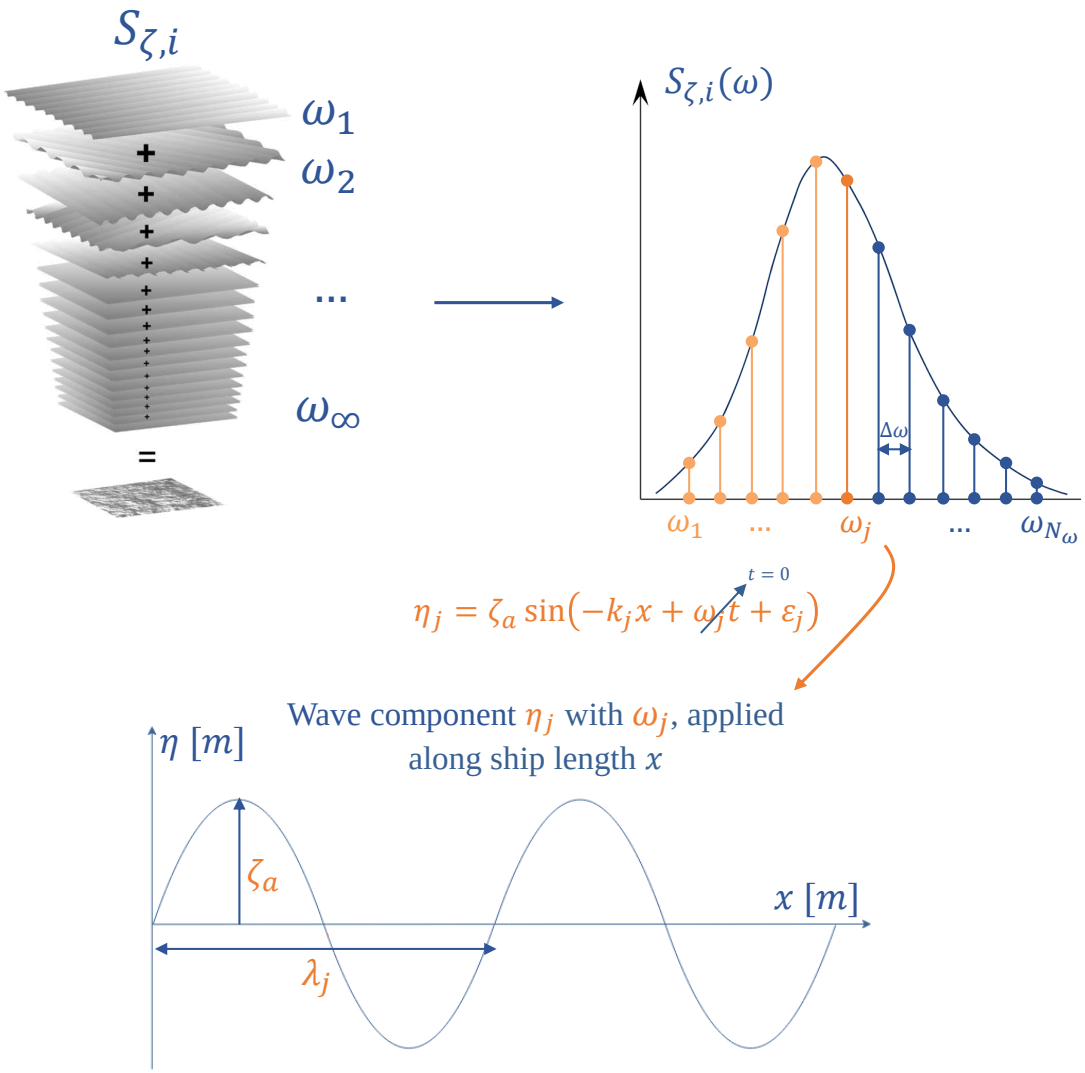

Figure 2.2: Visualisation of wave spectrum discretisation [18, 30]

$$S_{\Delta\sigma,i}(\omega) = |H_{\Delta\sigma}(\omega)|^2 \cdot S_{\zeta,i}(\omega) \tag{2.11}$$

In the fatigue analysis part, the fatigue damage for a given lifetime will be determined. This is done by making use of spectral moments m_0 and m_2 and SN-curves which apply to the structural detail. In more detail, first, spectral moments m_0 and m_2 are obtained from the response spectrum $S_{\Delta\sigma}$. They are then used to determine the mean zero up-crossing frequency of the stress cycles (eq. 2.13). This is done by first calculating the mean zero up-crossing period through equation 2.12 [8]. A FAT-class will have to be defined for every node in order to obtain the SN-curve slope m and intercept $\log(C)$. This can be done by, for instance, using class regulations [11].

The fatigue damage for a lifetime of T_{life} can now be determined by means of equation 2.14 [8]. This equation addresses a single-slope SN-curve.
DNV-GL states a more extensive fatigue damage equation which incorporates the bi-linear SN-curve (eq. 2.15) [11]. Note that in this equation i relates to wave spectrum $S_{\zeta,i}$ and j denotes the heading. For simplicity, further considerations have the heading θ and ship speed V_s incorporated under the 'wave case' of spectrum $S_{\zeta,i}$.

The bi-linear curve accounts for the difference in fatigue damage mechanism between medium and high cycle fatigue [8].

It is clear that different approaches and formulas can be used to determine the fatigue damage. The damage can be set to a certain parameter η. When $\eta = 1$, the fatigue lifetime is reached. Equation 2.14 or 2.15 can therefore be utilised to determine the lifetime of a structural detail. This lifetime can also be taken as input, after which the required FAT-class to reach this lifetime can be determined.

$$T_0 \approx 2\pi\sqrt{\frac{m_0}{m_2}} \tag{2.12}$$

$$f_0 = 1/T_0 \tag{2.13}$$

$$D = \frac{f_0 \cdot T_{life}}{C} \cdot (8m_0)^{\frac{m}{2}} \cdot \Gamma\left(1 + \frac{m}{2}\right) \tag{2.14}$$

$$D_{DNV} = N_D \sum_{i=1,j=1}^{S_\zeta,\theta_j} r_{ij} \left(\frac{\left(2\sqrt{2m_{0ij}}\right)^m}{K_2} \Gamma\left(1 + \frac{m}{2}; \frac{\Delta\sigma_q}{2\sqrt{2m_{0ij}}}\right)^2 + \frac{\left(2\sqrt{2m_{0ij}}\right)^{m+\Delta m\,\prime}}{K_3} \Gamma\left(1 + \frac{m+\Delta m}{2}; \frac{\Delta\sigma_q}{2\sqrt{2m_{0ij}}}\right)^2 \right) \leq \eta \tag{2.15}$$

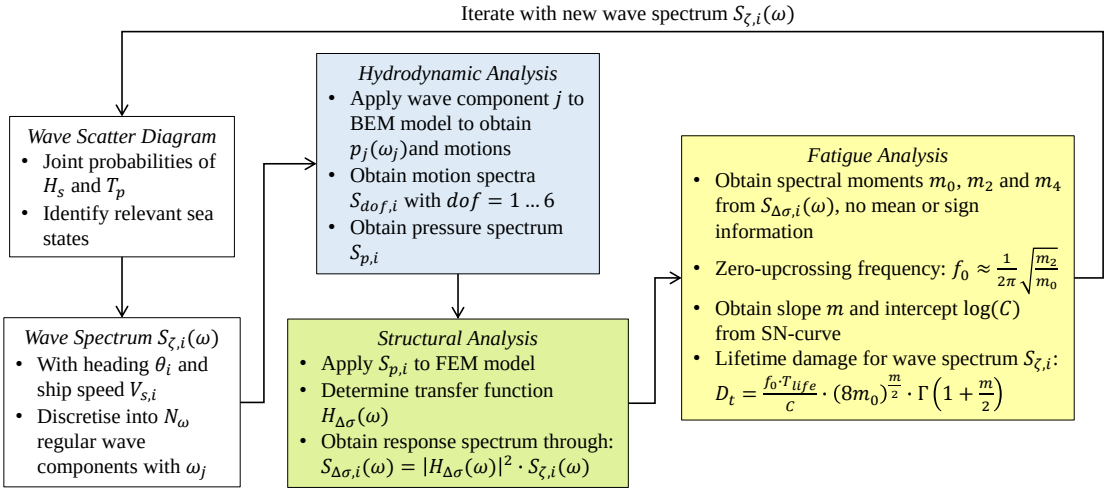

Figure 2.3: A typical SFA workflow.

The spectral fatigue analysis approach is known to be more accurate than prescriptive methods due to the direct calculation of wave loads on the ship's hull [2]. However, because the method operates in the frequency domain, the regular wave components are all applied at only one time instant; a quasi-static approach.

Reflecting on section 2.4.2, nonlinear loading components which were identified are therefore not incorporated in the spectral approach; time-varying components are zero. For cases where nonlinear loading is lower, for instance at calm sea states, this simplification suffices [31]. However, when nonlinearity increases, the presented spectral approach is not able to incorporate these effects. Furthermore, phase information is obtained from a Gaussian distribution. While in the temporal approach the simulation time guaranteed the inclusion of sufficient phase statistics, for the spectral approach this is not the case because of its quasi-static nature. Finally, mean stress is not incorporated at all since no rainflow counting can be performed from the stress response spectrum. The assumptions typically cause the fatigue damage calculated through the spectral approach to be conservative (overestimated) [7].

2.4 Nonlinear Contributions

Having established the way waves are typically modelled, this section will cover the effect these waves can have on a structure. A distinction is made between *loading and response*. Due to the varying water elevation, the ship hull is 'loaded' by a certain pressure. The structure then 'responds' by deforming and building up stresses. In modelling practice, the structure loading can be determined by computational fluid dynamics (CFD) software which incorporates methods like the boundary element method (BEM) [21]. For the response, the finite element method (FEM) is typically applied to obtain the stress in the structure due to the loading.

This section will focus on the mechanics of loading and response in order to set the essential framework for fatigue analysis. The focus lies on the *time domain* and it will be shown how nonlinear components contribute to the wave force over time. Furthermore, the origin of nonlinear wave loading will be discussed. Nonlinear structural response is left out-of-scope, as the steel material is assumed to behave linear-elastically. Phenomena like elasto-plasticity, which contribute to nonlinear structural response, are not considered in this thesis.

2.4.1 Equations of Motion

To set the framework, the equation of motion for the structure is an important starting point. For the case of a free-floating ship, the general expression is given in equation 2.16 [19]. Here, M and A denote the structural and added mass, B denotes the damping and C denotes the restoring term. $\ddot{x}$, $\dot{x}$ and x denote the acceleration, velocity and distance in degree of freedom X. The summation of the added mass, damping and restoring terms is known as the radiation force F_r. Together with the structural mass force ($F_M = M\ddot{X}(t)$) it equals the sum of the Froude-Krylov force F_{FK} and the diffraction force F_d. These forces are determined in boundary element software like *Ansys AQWA* by calculating the radiation ($\Phi_{1..6}$) and diffraction (Φ_7) velocity potentials at the panels of the 3D model [21]. The process of using velocity potentials to obtain the hydrodynamic forces will be discussed in section 2.4.2.

$$M\ddot{X}(t) + \underbrace{A\ddot{X}(t) + B\dot{X}(t) + CX(t)}_{F_r(t);\ \Phi_{1..6}} = \underbrace{F_{FK}(t)}_{\Phi_0} + \underbrace{F_d(t)}_{\Phi_7} \tag{2.16}$$

The expressions for the displacement, velocity and acceleration for a harmonic motion are provided in equation 2.17, 2.18 and 2.19. The time dependence becomes clear from these equations. In these equations, ω is the wave frequency, t is the time, X is the distance and ε is the phase angle. By calculating the radiation potential, the hydrodynamic coefficients of the equation of motion can be determined [21].

$$X(t) = X_a sin(\omega t - \varepsilon) \tag{2.17}$$

$$\dot{X}(t) = X_a \omega cos(\omega t - \varepsilon) \tag{2.18}$$

$$\ddot{X}(t) = -X_a \omega^2 sin(\omega t - \varepsilon) \tag{2.19}$$

The above equations apply to harmonic motions. Should the ship be subjected to an irregular wave field, the equation of motion will have to be modified [32]. This is because the added mass A and the hydrodynamic damping in C are frequency-dependent. The radiation force will then be determined by means of rewriting equation 2.16 to a convolution integral form

(eq. 2.20). Here, m is the structural mass matrix, A_∞ is the fluid added mass matrix at infinite frequency, c is the damping matrix including linear radiation damping effects, K is the total stiffness matrix, and R is the velocity impulse function matrix. This modification is used to provide a more rigorous approach to the radiation force calculation in the time domain. It enhances the capability of handling nonlinear hydrodynamic response of the ship structure [32].

$$\{m + A_\infty\}\,\ddot{X}(t) + c\dot{X}(t) + KX(t) + \int_0^t R(t-\tau)\dot{X}(\tau)d\tau = F_R(t) \tag{2.20}$$

Using the demonstrated framework, for an irregular wave field modelled in the time domain, it is possible to include the nonlinear hydrodynamic response of the structure because the different potentials are evaluated at each panel in a direct, instantaneous way. For the spectral approach, a quasi-static way of modelling is used. Because this approach is less direct, it is not possible to include nonlinearities as accurately as the temporal approach.

2.4.2 Hydrodynamic Loading

The previous section discussed the equations of motion which lie at the basis of hydrodynamic loading and structural response. This section will explain the process of obtaining hydrodynamic forces through the use of velocity potentials along with theory regarding nonlinear hydrodynamic loading. Nonlinear components are inherent to hydrodynamic loading since the interaction of waves with a structure can be highly chaotic. Even for regular waves, higher-order force components can be distinguished [33]. This section will show how these components are obtained.

Velocity Potential

A velocity potential of a fluid flow is a mathematical expression which has the property of providing the velocity of a fluid in a point in the direction of which it is derived [19]. Equation 2.21 depicts a fluid velocity potential for deep water [21]. As one can see, it incorporates the wave frequency ω, number k, amplitude ζ_a and heading θ. Deriving the potential in x-, y- or z-direction provides the velocity in that direction, as is shown in equation 2.22.

$$\Phi(x, y, z, t) = \frac{\zeta_a g}{\omega} \cdot e^{kz} \cdot \sin(kx\cos\theta + ky\sin\theta - \omega t) \tag{2.21}$$

$$u = \frac{\partial \Phi}{\partial x},\ v = \frac{\partial \Phi}{\partial y},\ w = \frac{\partial \Phi}{\partial z} \tag{2.22}$$

The undisturbed velocity potential Φ_0 is used to determine the Froude-Krylov force F_{FK}. For the case of an incoming wave with heading $\theta = 0$, at the surface ($x = 0$) of an infinitely deep wall, the undisturbed potential becomes the expression given in equation 2.23 [21].

$$\Phi_0(z, x, t)|_{\theta=0,\ x=0} = \frac{\zeta_a g}{\omega} \cdot e^{kz} \cdot \cos(\omega t) \tag{2.23}$$

Assuming full reflection of the incoming wave (eq. 2.24), n marking the direction normal to the wall's surface), the diffracted velocity potential describes a wave which propagates in the opposite direction of the undisturbed wave, as shown in equation 2.25.

$$\frac{\partial \Phi_7}{\partial n} = -\frac{\partial \Phi_0}{\partial n} \tag{2.24}$$

$$\Phi_7 = -\frac{\zeta_a g}{\omega} \cdot e^{kz} \cdot \sin(kx + \omega t) \tag{2.25}$$

The resulting velocity potential describes a standing wave at the wall, as shown in equation 2.26.

$$\Phi_0 + \Phi_7 = -2\frac{\zeta_a g}{\omega} \cdot e^{kz} \sin(\omega t) \cos(kx) \tag{2.26}$$

By describing the different components of a wave system (incoming, reflected), different force components can ultimately be distinguished. Using, for instance, only the undisturbed wave velocity potential Φ_0 will enable one to obtain the undisturbed wave force, or Froude-Krylov force.

Pressure

To obtain the total wave force at a wall, first the velocity potential of equation 2.26 is used to determine the pressure. The pressure formulation is obtained through the Bernoulli equation for unsteady flow [21]. Equation 2.27 shows the expression in which the first, second and third term mark the first-order, second-order and hydrostatic contribution respectively.

$$p = \underbrace{-\rho\frac{\partial \Phi}{\partial t}}_{1^{st}\text{ order}} \underbrace{-\frac{1}{2}\rho\left(u^2 + v^2 + w^2\right)}_{2^{nd}\text{ order}} \underbrace{-\rho g z}_{\text{Hydrostatic}} \tag{2.27}$$

Total Wave Force

The total force on the wall can be obtained by multiplying the pressure with the normal vector and integrating over the surface (eq. 2.28). Filling in the pressure formulation, assuming uniform behaviour along the y-coordinate and adressing $x = 0$, results in equation 2.29. This equation can be split up into a term that integrates from infinite water depth ($z = -\infty$) to the mean waterline ($z = 0$) and a term that integrates the instantaneous wave elevation ($z = 0$ to $z = \zeta(t)$), as is shown in equation 2.30. In this equation, the six different terms that together make up for the total wave force can clearly be seen. Naaijen and Wellens provide a detailed derivation of each of these components, in the end averaging the force over one wave period to obtain the mean wave drift force [21]. In this derivation, each component has a certain order ranging from zeroth to third with respect to the wave elevation over time; $\zeta(t)$. The order for each *integrated* component is indicated in equation 2.30 as well. One can see that the total force on the wall consists of a single zeroth-order term which does not contribute to the dynamic solution, one first-order term, three second-order terms and one third-order term. As the contribution of the integration from 0 to $\zeta(t)$ is considered to be small, the third-order term containing $\zeta(t)^3$ is neglected [21]. The second-order terms are also small with respect to the lower-order ones, but can still have an impact of the overall solution when included.

With the different force components now separated, it is possible to see the significance they have in the total wave force. Should one desire to obtain undisturbed (Froude-Krylov) or diffraction contributions to the nonlinear wave force, this can be done by simply plugging in Φ_0 or Φ_7 into equation 2.30.

$$\bar{F} = -\iint_{\mathcal{S}} (p \cdot \bar{n}) dS \tag{2.28}$$

$$F_t = \int_{-\infty}^{\zeta(t)} \rho \left(gz + \frac{\partial \Phi}{\partial t} + \frac{1}{2} \frac{\partial \Phi}{\partial z}^2 \right) dz \tag{2.29}$$

$$F_t = \int_{-\infty}^{0} \rho \Big(\underbrace{gz}_{0^{th}} + \underbrace{\frac{\partial \Phi}{\partial t}}_{1^{st}} + \underbrace{\frac{1}{2} \frac{\partial \Phi}{\partial z}^2}_{2^{nd}} \Big) dz + \int_{0}^{\zeta(t)} \rho \Big(\underbrace{gz}_{2^{nd}} + \underbrace{\frac{\partial \Phi}{\partial t}}_{2^{nd}} + \underbrace{\frac{1}{2} \frac{\partial \Phi}{\partial z}^2}_{3^{rd}} \Big) dz \tag{2.30}$$

2.4.3 Intermittent Wetting Effect

The previous section showed how the nonlinear force components are integrated into the total wave force on a structure. When zooming in to the waterline, additional nonlinear effects show up. An important one is the intermittent wetting effect (IWE). This effect occurs at locations which are intermittently wet and dry. A nonlinear pressure force is at hand, and the stress response becomes nonlinear as well. Hansen studied fatigue damage in side shells and considered the global hull girder bending moment and local wave pressure loads at the mean waterline [34]. It was stated that more than 40% of the fatigue cracks are located in the ship side shell at connections of longitudinals to transverse web frames. The work of Hansen confirmed this.

Figure 2.4 shows pressure time traces for locations inside (P1) and outside (P2) the intermittent wetting-affected area [4]. One can clearly see the 'cut-off' valleys of the P1 signal. This is a sign of intermittent wetting as the peaks occur when the location becomes submerged. Bigot investigated the influence of the IWE on the side shell for several different calculation models [4]. A nonlinear time domain method was used as reference case, and it was concluded that the IWE plays a large role in the nonlinear wave loading at the waterline. Due to this nonlinear loading, linear methods like the spectral approach lack in detail, especially around the waterline.

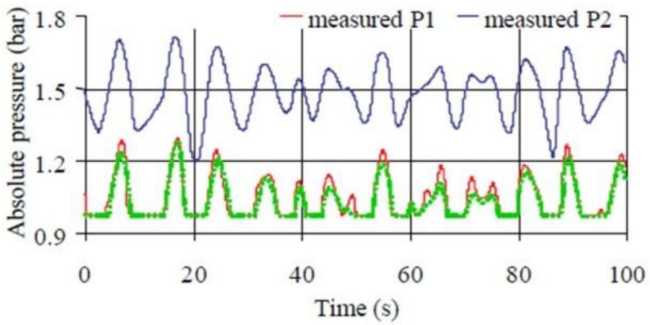

Figure 2.4: Pressure time traces for locations in the IWE area (P1) and outside it (P2).

2.4.4 Dominant Components

In literature, the cause of discrepancy between spectral and temporal fatigue analysis results is mostly attributed to the inclusion of nonlinear hydrodynamic loading in the temporal approach [5, 27]. In the PhD thesis of Wang on (2001) *'Probabilistic Analysis of Nonlinear Wave-induced Loads on Ships'*, the sources which contribute to nonlinearity in the hydrodynamic loading along with the consequences for the short-term statistics of the wave-induced vertical bending moment are investigated for different ship hull types. With respect to the previous section where nonlinear force components were distinguished for a regular wave on a wall, this research takes a more global approach by assessing ship hulls in realistic wave spectra.

Wang finds that nonlinear wave force components cause deviations in the wave load statistics from the Gaussian model (wave elevation distribution) and Rayleigh model (peaks/wave amplitude distribution). The hydrodynamic loading spectrum is then considered to be non-Gaussian and it is found that the three-parameter Weibull distribution is adequate for describing the maxima wave bending moment statistics, which is in line with the findings of Mohammadi [7]. Overall, being able to properly describe the maxima statistics is important in the case of high-nonlinear sea states. This is because the extremes have the highest impact on nonlinear loading [5].

In order to investigate the origin of the shift from the Rayleigh to Weibull distribution, Wang distinguishes four main nonlinear force components, as shown in equation 2.31. Here, $F_{1k,n}(t)$ denotes the slamming force with k being the bending mode shape number. $k = 1$ and $k = 2$ denote the first (rigid) modes, whereafter higher mode numbers represent the flexible bending modes. This way, the nonlinear force components are distinguished for every mode shape. $F_{2k,n}(t)$ reflects the hydrodynamic forces due to the nonlinear modifications of the two dimensional added mass and $F_{3k,n}(t)$ marks its derivation to x. Together they make up for the nonlinear effects in the fluid added mass, damping and diffraction force. $F_{4k,n}(t)$ is the nonlinear modification of the Froude-Krylov force and the hydrostatic restoring force.

$$F_{k,n}(t) = \underbrace{F_{1k,n}(t)}_{\text{Slamming}} + \underbrace{F_{2k,n}(t) + F_{3k,n}(t)}_{\substack{\text{Added mass,}\\ \text{damping,}\\ \text{diffraction}}} + \underbrace{F_{4k,n}(t)}_{\substack{\text{Froude-Krylov,}\\ \text{restoring}}}, \quad k = 1, 2, .., m \tag{2.31}$$

The nonlinear force components from equation 2.31 are addressed by Wang in order to find their relative importance for the total nonlinear wave load [5]. The Weibull shape parameters fitted to the time histories of the bending moments caused by the different nonlinear components ($M_{1..4}$) are examined. Also, the 'full' bending moment M which contains all the nonlinear components is considered.

It is found that for a merchant ship the slamming force, the nonlinear Froude-Krylov force, and the nonlinear hydrostatic force are dominant in the wave load calculation. While nonlinear effects in the added mass often get left out, Wang has found that including also this nonlinear force component results in more adequate estimations [5].

Wang compares the nonlinear component results with the linearly estimated hogging and sagging moments, which is shown in table 2.1 and 2.2, respectively. These tables show the Weibull parameter c, the peak hogging/sagging moment from the time signal and the ratio with the linearly estimated maximum moment. The Weibull parameter c depicts how much the distribution deviates from the Rayleigh distribution ($c = 2$) which is assumed in linear theory.

From tables 2.1 and 2.2, a couple of things become clear. First, it is observed that the moment induced by the slamming force (M_1) results in a great deviation from the Rayleigh model. Also, the slamming force hardly affects the hogging moment, as its c-value lies within the range of 2 there. Second, the nonlinear added mass induced moment M_2 has a small contribution for hogging as well as sagging. This also holds for the term of M_3 which is associated with the longitudinal derivative of the added mass. Third, the nonlinearity in the Froude-Krylov and hydrostatic force induced moment (M_4) has significant nonlinear impact on the sagging and hogging maxima statistics. The sagging extreme is double the linear extreme while the hogging extreme is only 69% of the linear extreme value.

A final note is that when all nonlinearities are included (M), the total effect on the wave load

statistics is not a simple summation of the effect of each nonlinearity since the four nonlinear effects also interact with one another. It can be concluded that among all the sources of nonlinearity the slamming force F_1 and the nonlinear Froude-Krylov and restoring force F_4 are dominant in affecting the sagging peak statistics. For the hogging peak statistics, F_4 is also dominant along with the added mass term F_2. The following sections will go more in-depth on the important sources of nonlinear loading: the hull shape, slamming, and the nonlinear Froude-Krylov force.

Table 2.1: Weibull shape parameter c and extreme value of the **hogging** moment peaks $M_{e,sag}$ for five bending moment time histories $M_{1..4}$ and M [5]. Linear extreme hogging moment $M_{e,linear} = 7.77E8$ Nm.

	c	$M_{e,\text{ hog}}$ (Nm)	$M_{e,hog}/M_{e,\text{ linear}}$
M_1	1.92	$7.86 * 10^8$	1.01
M_2	1.42	$12.0 * 10^8$	1.54
M_3	1.93	$7.78 * 10^8$	1.00
M_4	2.53	$5.40 * 10^8$	0.69
M	2.28	$6.71 * 10^8$	0.86

Table 2.2: Weibull shape parameter c and extreme value of the **sagging** moment peaks $M_{e,sag}$ for five bending moment time histories $M_{1..4}$ and M [5]. Linear extreme sagging moment $M_{e,linear} = 7.77E8$ Nm.

	c	$M_{e,sag}$(Nm)	$M_{e,sag}/M_{e,linear}$
M_1	1.11	$15.1 * 10^8$	1.94
M_2	3.04	$4.30 * 10^8$	0.55
M_3	1.75	$8.93 * 10^8$	1.15
M_4	1.63	$16.0 * 10^8$	2.06
M	1.26	$16.1 * 10^8$	2.07

Hull Shape

Overall, it can be noticed that the nonlinear sagging moment deviates further from the linear case than the hogging moment. This is not directly explained by Wang, but an indication is given when considering the hull shape influence to nonlinear loading.

It is stated by Wang that the results from tables 2.2 and 2.1 are only valid for the specific hull shape of the considered ship as the hull shape has a big influence on the magnitude of nonlinearity in the seakeeping. The more nonlinear the hull shape (large bow flare, small block coefficient), the more the slamming, nonlinear Froude-Krylov and nonlinear hydrostatic forces come into play. In the final chapter, the effect of bow flare on the wave load statistics is therefore addressed in order to see how the statistics change.

It was concluded that a larger bow flare leads to a larger sagging moment at mid ship, which is mostly due to larger slamming effects. The wave bending moment peak Weibull distribution moves to the left (skewness > 0) and becomes more narrow (kurtosis > 3) as the bow flare increases.

Reflecting on tables 2.2 and 2.1, the difference in hogging and sagging moment nonlinear deviation can be explained by the influence of the hull shape. Nonlinear loading plays a larger role where the hull shape is also nonlinear (aft and bow). With slamming and nonlinear Froude-Krylov being large contributors, the upward forces result in large nonlinear sagging moments. In a hogging condition, the water integration at the midship plays a vital role. Since the hull shape is far more linear here, nonlinear deviation in the hogging moment is smaller.

Slamming Force

From the nonlinear force components identified by Wang, the slamming force turned out to be one of the most important ones. Accurately modelling the slamming force is therefore of interest when addressing nonlinear hull shapes in extreme waves.

In the PhD thesis of Tuitman on *'Hydro-Elastic Response of Ship Structures to Slamming Induced Whipping'*, the modelling of slamming-induced whipping is discussed in great detail. Whipping is the phenomenon where a transient slamming loading leads to transient structural vibrations [8]. Tuitman points out that these vibrations can contribute to fatigue damage by a large extent. Therefore, the adequate modelling of slamming at extreme sea states is of great importance. Tools to calculate slamming loads are scarce, and therefore, a practical method to calculate the global and local response of the ship structure due to seakeeping loading including slamming loading has been developed [27]. In this method, the slamming calculation is incorporated into a hydroelastic time domain analysis. This is done by initiating a wedge water entry simulation whenever the relative velocity of the bow to the water surface exceeds a certain threshold. The slamming force is then calculated in a direct, accurate way. It goes without saying that the implementation of this additional simulation inside the time domain analysis yields higher computational demand.

Tuitman shows that the influence of incorporating hydro-elasticity is evident, as including flexible modes results in lower slamming forces [27]. The direct approach in which the slamming calculation was incorporated is compared with a method in which the slamming loads were calculated after the seakeeping analysis. It turned out that the latter resulted in higher slamming loads, indicating the effectiveness of directly incorporating the slamming into the seakeeping analysis.

In the second part of the PhD of Tuitman, verification studies are performed using multiple ship types [27]. A comparison is made between the spectral and temporal approach for two large container vessels. For mild sea conditions, the results of the hydrodynamic response of the two methods were close to each other. For more severe sea states, the difference increased. This indicates the aforementioned discrepancy between the two approaches because of the inclusion of nonlinear hydrodynamic loading. For the two container vessels, it was found that the inclusion of the slamming induced whipping led to a mean fatigue lifetime decrease of 40%.

Nonlinear Froude-Krylov Force

Next to the slamming force, the nonlinear Froude-Krylov force is found to contribute substantially to the total nonlinear force [5]. Section 2.4.2 discussed the origin of the nonlinear Froude-Krylov force, stating that the component can be uncovered by plugging the undisturbed wave velocity potential Φ_0 into pressure equation 2.27.

Recalling equation 2.30, the difference between the linear and nonlinear Froude-Krylov components become clear. The first term includes the first-order $\frac{\partial \Psi}{\partial t}$-term, which is integrated over the mean wetted surface ($-\infty$ to 0). To obtain the nonlinear Froude-Krylov force, the second term comes into play where the higher-order terms are integrated over the instantaneous wetted surface. The research of [35] adopts the same definition of the linear and nonlinear Froude-Krylov force as well. In this research, the value of including nonlinear force components in the model of a heaving wave energy converter is discussed, focusing on nine different modelling options which include the nonlinear component. For the case of the wave energy converter device, a linear model was found to be adequate at wave periods away from heave resonance. However, at resonance, the modelling of nonlinear forces becomes important, especially since a wave energy converter should be able to operate well at large heave motions. The importance of including the nonlinear Froude-Krylov force at resonance was also confirmed by the research of Jang, in which the nonlinear behaviour of an Arctic spar

structure was observed under multiple regular and irregular wave conditions [36].

2.4.5 Mean Components

Section 2.4.2 concluded with the formulation of the total force of a single wave component on a vertical wall. The *mean wave drift force* ($\bar{F}$) is a mean component within this total force that is obtained when averaging over time, for instance one wave period. For the given case, the mean wave drift force amounts to the formulation in equation 2.32.

The derivation provided by Naaijen and Wellens [21] showcases that the mean wave drift force is dependent solely on the second-order terms of the total force F_t (eq. 2.30). It therefore shares a square relation with the wave amplitude ζ_a.

From the perspective of the temporal versus spectral approach, it becomes clear that the temporal approach is capable of including the mean wave drift force, thus improving on capturing mean (stress) effects.

$$\bar{F} = -\frac{1}{2}\rho g \zeta_a^2 \tag{2.32}$$

2.5 Statistical Representations

This section will discuss what researchers have found to be the main cause of the difference between the spectral and temporal approach and which efforts are made to improve the spectral approach.

2.5.1 Narrow Band Assumption

In the paper of Mohammadi on efficient time domain analysis and its comparison to frequency domain results for an offshore jacket, the aim is to quantify the gain in accuracy and reliability with the use of the temporal approach as opposed to the spectral approach [7]. Upon comparison, it is found that the response spectra obtained through both methods were quite the same. However, large differences in fatigue damage were observed. Mohammadi concludes that this is caused by the narrow band assumption resulting in Rayleigh-distributed stress ranges for the spectral approach. Gao et al. goes into further detail as to why different results are encountered [24]. Due to the inclusion of nonlinearities, the aforementioned spectrum becomes wide-banded. Slamming-induced whipping effects typically cause a bimodal spectrum; a high-frequency response peak is identified. Methods to correct for these phenomena are discussed in section 2.5.3.

The temporal method uses a direct approach in which rainflow counting is applied to the stress time signal. In the paper of Mohammadi, a Weibull distribution turned out to be the best fit for the resulting stress range histogram, as opposed to the Rayleigh PDF of the spectral approach [7]. This causes an even larger difference in the resulting fatigue damage due to its third-order relation with the stress range [8]. In the end, no analytical support is available for the Weibull-distributed stress range spectrum, but it is widely accepted since it has often proven to provide a good fit [5].

The narrow band assumption holds for cases where nonlinear loading and response is low, e.g. linear waves and linear structural response. Recalling section 2.4.4, ships with higher block coefficients were considered as being 'linear' hull shapes. For these ships in mild seas, nonlinear loading is expected to be low and the narrow band assumption holds. For that case, the stress range spectrum can be formed by a Rayleigh distribution.

2.5.2 Non-Gaussianity

In the spectral approach, when the response spectrum of a structure is Gaussian and narrow-banded, the stress range distribution is assumed to be Rayleigh-distributed. Mohammadi showed that this assumption leads to conservative fatigue damage estimates and Gao et al. states that, for the time domain analysis, the inclusion of nonlinearities in the hydrodynamic seakeeping can lead to a wide-banded or bimodal spectrum [7, 24]. These phenomena will be discussed in section 2.5.3. The spectrum will also become non-Gaussian, meaning there is a certain deviation from the symmetrical Normal distribution. The spectrum can shift horizontally (skewness) and become more steep or flat (kurtosis).

In practice, such a deviation can be attributed to, for instance, highly-nonlinear hydrodynamic loading due to the nonlinear Froude-Krylov force. Wang specified that ships with nonlinear hull shapes, mostly a low block coefficient and large bow flare, are more susceptible to these kinds of loads since the pressure distribution increases nonlinearly [5]. Naval ships in particular are subjected to nonlinear loading since they typically meet this profile [1].

To account for non-Gaussianity, Wang proposes the Hermite model as a solution. Gao et al. confirms that this model has been used for decades and it is the first choice for handling non-Gaussian problems. The Hermite model transforms a Gaussian process $U(t)$ into a non-Gaussian one $X(t)$ by using a transformation $g()$ (eq. 2.33). This transformation takes the form of a monotonic polynomial which uses the first four statistical moments; the mean μ, variance σ^2, skewness γ_1 and kurtosis γ_2.

$$X(t) = g(U(t)) \tag{2.33}$$

The advantage of the Hermite model is that the transformation from the Gaussian process $U(t)$ to the non-Gaussian one $X(t)$ can reduce nonlinear analysis to a simple representation of well-established results for linear Gaussian processes [5]. This model can be used with spectral fatigue analysis in order to obtain nonlinear seakeeping behaviour. Extensive time domain simulations are then no longer necessary. Some drawbacks are that this model assumes a narrowband spectrum and is no longer valid for wide band spectra due to strong nonlinear loading. The next section will therefore discuss the inclusion of the wideband spectrum into the spectral approach in more detail.

2.5.3 Wide Band and Bimodal Corrections

Having established a solution to account for non-Gaussianity, the second problem which arises due to the inclusion of nonlinearities will now be discussed. As stated earlier, nonlinearities in the seakeeping behaviour can alter the narrow band response spectrum to a wide-banded or bimodal one. For instance, when a ship encounters heavy slamming, resulting whipping effects might lead to high-frequency vibrations in the response in addition to the lower-frequency response of the wave impact [27]. The response spectrum will then have two peaks and is therefore bimodal. Hydro-elastic analysis is typically required to uncover the whipping response. Furthermore, due to other nonlinear effects, the spectral peak might also become wide-banded, meaning more frequencies have a significant contribution. Gao et al. makes use of the bandwidth parameter (eq. 2.4, section 2.1.1) to distinguish between narrow band and wide band spectra [24].

In order to accurately represent the stress range distribution for nonlinear cases, the bimodality and wide-bandedness have to be taken into account. In the past, numerous efforts have been made to implement these effects in the spectral approach. Gao et al. provides a clear overview of the research done in this field and proposes a novel method to improve the spectral approach accuracy further [24]. They aim to compare the two prominent methods of Dirlik (DK) [37] and Tovo and Benasciutti (TB) [38] with their own method (GZ) in order

to show the performance of the methods for wide-banded, bimodal processes. In the paper, several case studies considering ideal and practical bimodal spectra applicable to ocean structure engineering are performed. The accuracy of the underlying Gaussian fatigue damage and the corresponding correction factor for each spectral method (DK, TB, GZ) is addressed. This comparison is of interest to this study and will be discussed in this section, but the main methodology of the three spectral methods will be considered first.

Dirlik

The Dirlik method (DK) has been widely used for many engineering situations [24]. At the time, Dirlik provided a thorough review and extension on fatigue analysis methods [37]. Here, the focus lied on cycle counting and fatigue life prediction methods. With regards to wide-banded spectra, a data-fitted equation for the stress range PDF and fatigue damage was developed.

A representative stress spectrum $G(\omega)$ was used as starting point. A stress time series was generated 20 times in an attempt to capture all the statistical parameters of the spectrum. Every time series was discretised into 108 peaks. This way, there would be roughly 5 data points between successive peaks and troughs. This resolution was considered sufficiently fine to generate a smooth stress time series for rainflow counting purposes.

Dirlik formulates the stress amplitude PDF after a fitting analysis on the stress data following from rainflow counting of the time signal [37]. Equation 2.34 provides the expression for the PDF. Here, σ_U is used to normalise the expression in order to compare it to the other methods discussed by Gao et al. [24]. Furthermore, $z = r/\sigma_U$ denotes the normalised stress amplitude. The expressions for the mean frequency x_m and parameters H_1, H_2, H_3, h and V are gathered in equation 2.35.

$$f_{DK}(r) = \frac{1}{\sigma_U}\left[\frac{H_1}{V}e^{-z/V} + \frac{H_2 z}{h^2}e^{-z^2/2h^2} + H_3 z e^{-z^2/2}\right] \tag{2.34}$$

$$\begin{gathered} x_m = \frac{\lambda_1}{\lambda_0}\sqrt{\frac{\lambda_2}{\lambda_4}}, \quad H_1 = \frac{2\left(x_m - \tilde{\alpha}_2^2\right)}{1+\tilde{\alpha}_2^2}, \quad h = \frac{\tilde{\alpha}_2 - x_m - H_1^2}{1-\tilde{\alpha}_2 - H_1 + H_1^2} \\ H_2 = \frac{1-\tilde{\alpha}_2 - H_1 + H_1^2}{1-h}, \quad H_3 = 1 - H_1 - H_2, \quad V = \frac{1.25(\tilde{\alpha}_2 - H_3 - H_2 h)}{H_1} \end{gathered} \tag{2.35}$$

By using the PDF of equation 2.34, Dirlik is able to formulate the fatigue damage per unit time, as shown in equation 2.36. Here, ν_p is calculated according to equation 2.7, C is obtained from the SN-curve intercept $\log(C)$, σ_U is the reference stress and $\Gamma()$ denotes a Gamma function. This equation proved to be accurate for many Gaussian situations. However, Gao et al. states that recent studies have shown that accurate fatigue estimation for materials with FAT-class parameter $m > 5$ (high-cycle fatigue region) require time series that contain at least one million stress cycles with 32 data points in each cycle to yield accurate results [24]. Also, non-Gaussian cases are left out-of-scope. Gao et al. therefore aims to combine the wide band correction methods with the Hermite model in order to include both effects caused by the inclusion of nonlinearities.

$$\bar{D}_{DK} = \frac{2^m \upsilon_p}{C}\sigma_U^m\left[H_1 V^m \Gamma(1+m) + 2^{m/2}\Gamma(1+m/2)\left(H_2|h|^m + H_3\right)\right] \tag{2.36}$$

Tovo-Benasciutti

As previously mentioned in the method of Dirlik, using distribution curves fitted to rainflow data is a common approach. Benasciutti and Tovo state that a theoretical framework is not available for wide band Gaussian processes [39]. This is due to the complexity of the approach to extracting cycles are from a time signal. Due to this, the relation between the stress spectrum

and the resulting rainflow cycle distribution is impossible to express in a simple formula. Also, the true set of spectral parameters to be included in this relation is still under discussion.

Benasciutti and Tovo proved that in any stationary Gaussian process, while assuming linear damage accumulation, the fatigue damage determined by rainflow counting is always bounded by two damage calculation approaches, namely the range-mean (RM) counted damage and the level-crossing (LC) counted damage (eq. 2.37) [38] .

$$\bar{D}_{RM} \leq \bar{D}_{RFC} \leq \bar{D}_{LC} \tag{2.37}$$

$\bar{D}_{LC}$ and $\bar{D}_{RM}$ are expressed in equations 2.38 and 2.39, respectively. These equations use the same parameters (ν_p, C, σ_U, etc.) as discussed in earlier sections.

$$\bar{D}_{LC} = \frac{\nu_p}{C}\tilde{\alpha}_2 \left(2\sqrt{2}\sigma_U\right)^m \Gamma\left(1+\frac{m}{2}\right) = \bar{D}_{NB} \tag{2.38}$$

$$\bar{D}_{RM} = \frac{\nu_p}{C} \left(2\sqrt{2}\sigma_U\tilde{\alpha}_2\right)^m \Gamma\left(1+\frac{m}{2}\right) = \tilde{\alpha}_2^{m-1}\bar{D}_{NB} \tag{2.39}$$

Benasciutti and Tovo used equation 2.37 to apply a wide band correction and expressed the wide band fatigue damage $\bar{D}_{TB}$ in terms of the narrow band fatigue damage $\bar{D}_{NB}$ [38]. Their resulting damage formula is given in equation 2.40, showing how the narrow band damage is corrected in terms of the level-crossing- and range-mean-calculated fatigue damage. Here, b_{TB} is the correction factor obtained after calibrating with 286 time domain simulations using five different power spectra. These numerical experiments to determine b_{TB} involved two fatigue resistance cases, namely $m = 3$ and $m = 5$, applicable to mid- and high-cycle fatigue, respectively.

$$\bar{D}_{TB} = b_{TB}\bar{D}_{LC} + (1-b_{TB})\,\bar{D}_{RM} = \left[b_{TB} + (1-b_{TB})\,\tilde{\alpha}_2^{m-1}\right]\bar{D}_{NB} \tag{2.40}$$

$$b_{TB} = \frac{(\tilde{\alpha}_1-\tilde{\alpha}_2)\left[1.112\,(1+\tilde{\alpha}_1\tilde{\alpha}_2-(\tilde{\alpha}_1+\tilde{\alpha}_2))\,e^{2.11\tilde{\alpha}_2}+(\tilde{\alpha}_1-\tilde{\alpha}_2)\right]}{(\tilde{\alpha}_2-1)^2} \tag{2.41}$$

Benasciutti and Tovo then propose to combine this wide band correction with a correction for non-Gaussian power spectra in terms of skewness and kurtosis coefficients [38]. Their efforts regarding this, along with those of others, will be discussed in section 2.5.4.

Gao-Zheng Method

The methods of Dirlik and Tovo-Benasciutti are able to account for general wide band processes [37, 38]. This also includes bimodal spectra, of which the origin was accounted to phenomena like slamming-induced whipping (section 2.4.2). Gao and Zheng proposed a method to account for the interaction between low-frequency (LF) and high-frequency (HF) peaks in the bimodal spectrum [31]. To illustrate this, a typical rectangular bimodal spectrum is adopted which has also been used in prior studies (figure 2.5a). In order to describe the interaction between the two peaks, some parameters are defined. Equation 2.42 and 2.43 denote the mid-frequency ratio and the power ratio. These equations respectively incorporate the frequency and the power density of both peaks in order to capture the bimodal character of the spectrum. Equation 2.42 depicts the mid-frequency ratio where $\omega_{HF,\,\mathrm{mid}}$ and $\omega_{LF,\,\mathrm{mid}}$ are the frequency at the middle of either the high-frequency (HF) or low-frequency (LF) peak. The ratio of the surfaces beneath both peaks, the power ratio β, is given in equation 2.43. It

is is calculated with $G(\omega)$ being the spectral density function. Figure 2.5a indicates some of the aforementioned parameters and figure 2.5b depicts the discretisation of both bands into bins. This discretisation is performed to enable numerical evaluation of equation 2.43.

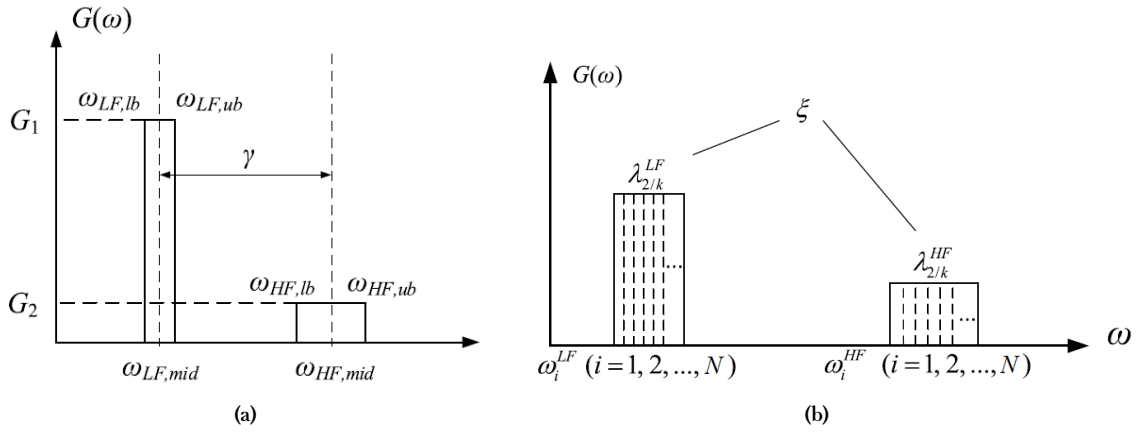

Figure 2.5: A typical rectangular bimodal spectrum with its parameters (a) and a discretisation of the LF and HF bands (b) [24]

$$\gamma = \omega_{HF,\,\mathrm{mid}} \,/\, \omega_{LF,\,\mathrm{mid}} \tag{2.42}$$

$$\beta = \int_{\omega_{HF,lb}}^{\omega_{HF,ub}} G(\omega)d\omega \,/\, \int_{\omega_{LF,lb}}^{\omega_{LF,ub}} G(\omega)d\omega \tag{2.43}$$

Gao and Zheng formulate the total fatigue damage as shown in equation 2.44 [31]. One can see that its first two terms are similar to the spectral damage of equation 2.14. However, the third term in the equation includes three terms which correspond to the damage contribution of both peak bands ($\lambda_{2/m}^{LF}$ and $\lambda_{2/m}^{HF}$) and the interaction between both peaks ($\lambda_{2/m}^{LF\&HF}$). These terms are dependent on the peak characteristics and are given in equation 2.45 and 2.46. To formulate these equations, both peak bands are divided into N amount of smaller bands with a width of $\Delta\omega$. For every individual frequency ω_i in either the LF or HF band, each parameter is calculated.

The interaction between the peaks is given by $\lambda_{2/m}^{LF\&HF}$ and it includes the terms of $\lambda_{2/m}^{LF}$ and $\lambda_{2/m}^{HF}$ in a square root times an empirical factor ξ. This factor is a function of γ, β, and k and is determined by Gao and Zheng through a nonlinear optimisation technique combined with a comprehensive data set generated by a large number of Monte Carlo simulations [31].

$$\bar{D}_{\mathrm{total}} = \frac{(2\sqrt{2})^m}{2\pi C} \cdot \Gamma\left(1+\frac{m}{2}\right) \cdot \left(\lambda_{2/m}^{LF} + \lambda_{2/m}^{HF} + \lambda_{2/m}^{LF\&HF}\right)^{m/2} \tag{2.44}$$

$$\lambda_{2/m}^{LF} = \sum_{i=1}^{N} \left(\omega_i^{LF}\right)^{2/m} G\left(\omega_i^{LF}\right) \Delta\omega^{LF}, \quad \lambda_{2/m}^{HF} = \sum_{i=1}^{N} \left(\omega_i^{HF}\right)^{2/m} G\left(\omega_i^{HF}\right) \Delta\omega^{HF} \tag{2.45}$$

$$\lambda_{2/m}^{LF\&HF} = \sum_{i=1}^{N} \xi \sqrt{\left[\left(\omega_i^{LF}\right)^{2/m} G\left(\omega_i^{LF}\right) \Delta\omega^{LF}\right] \cdot \left[\left(\omega_i^{HF}\right)^{2/m} G\left(\omega_i^{HF}\right) \Delta\omega^{HF}\right]} \tag{2.46}$$

Comparison

The three aforementioned correction methods have been used extensively over the years and have proved their adequacy. Gao et al. examines these methods and discusses their properties and drawbacks [24]. This section will summarise the findings and provide an overview on the performance of each method.

Table 2.3 provides a first overview of the properties of the three considered methods. It states the spectra that the methods account for, the stress range PDF that they produce and the assumption on the asymmetry of the distribution. TB combines the symmetry approach of LC with the asymmetry approach of RM. Furthermore, GZ assumes its bimodal spectra to be symmetric around their respective band centre lines.

Table 2.3: Overview of the properties of the three methods [24].

Method	Spectra included	PDF	Assumption of asymmetry
DK	WB	Amplitude PDF	Symmetry
TB	WB, NG	Peak-trough JPDF	"LC's symmetry" + "RM's asymmetry"
GZ	WB, BM	Peak-trough JPDF	Symmetric LF and HF bands

In their paper on non-Gaussian bimodal processes, Gao et al. aim to quantify the error in spectral methods like the one from Benasciutti and Tovo caused by the empirical correction factors that are proposed [24, 38]. Figure 2.6 shows the difference in stress range distribution for the Dirlik [37], Tovo-Benasciutti [38] and Rayleigh distribution compared to the time domain method, which is deemed as the most accurate. These distributions are transformed from an underlying bimodal Gaussian process with peaks δ_{LF} and δ_{HF} and parameters α_3 and α_4 (figure 2.6). $g(r)/r$ indicates the non-dimensionalised applied Hermite transformation which increases as the rainflow amplitude r ($= \Delta\sigma/2$) increases.

One can see that for this example case, the DK method is fairly close to the accurate time domain reference results at $r > 1.5$. For smaller rainflow amplitudes, DK shows less similar results. Recalling the methodology of DK, this distribution was fitted on stress range data. The peculiar dip towards $r = 0$ has not been explained by Dirlik [37]. TB is also able to provide better results than the plotted Rayleigh distribution, but is not fully in line with the temporal results.

Furthermore, Gao et al. summarises the Gaussian WB correction methods in table 2.4 [24]. One can see that, for different material parameters with SN-slope m, GZ is able to provide results within 5% of the TD results. Furthermore, the narrow band Rayleigh assumption has large differences, followed by TB and DK for higher values of m. Overall, the error seems to increase for higher values of m. The reason behind this is not explained by Gao et al. [24].

Method	m=3	m=4	m=5	m=6
Time domain	5.43	22.87	107.83	554.27
NB	6.51	27.69	130.14	664.56
	19.91 %	21.10 %	20.69 %	19.90 %
TB	5.07	19.87	87.81	428.81
	-6.53 %	-13.11 %	-18.57 %	-22.63 %
DK	4.97	20.12	92.19	464.77
	-8.51 %	-12.02 %	-14.51 %	-16.15 %
GZ	5.24	21.89	102.92	529.79
	-3.53 %	-4.28 %	-4.55 %	-4.42 %

Table 2.4: Bimodal Gaussian fatigue damage comparison for an example case for different fatigue resistance slopes m [24].

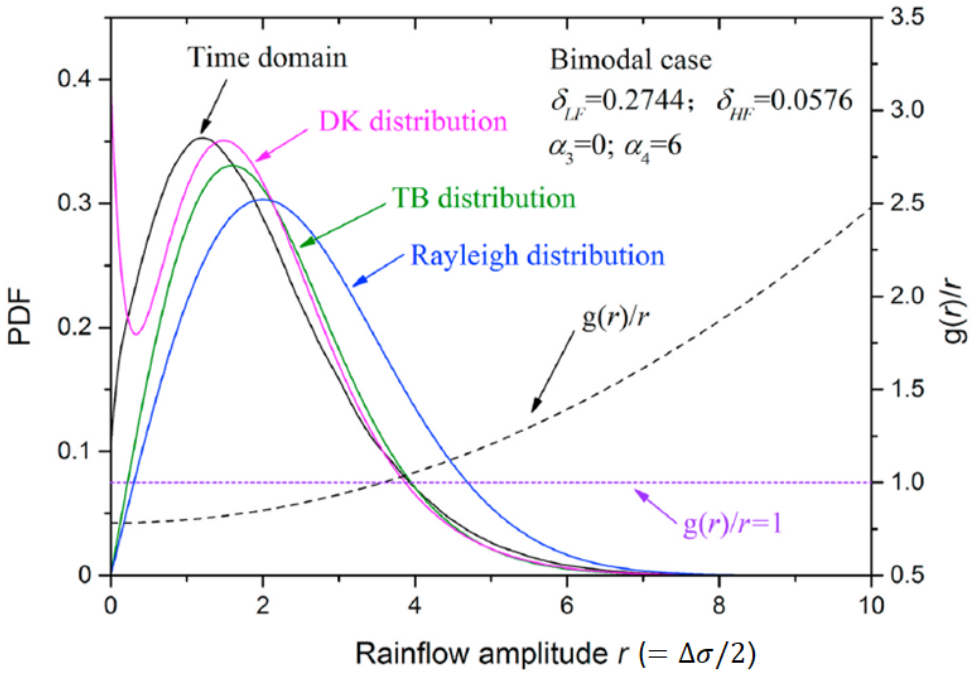

Figure 2.6: Comparison of Rayleigh, Tovo-Benasciutti, Dirlik and time domain stress range PDF's [24]

2.5.4 Combination of Non-Gaussian and Wide Band Corrections

In essence, the Hermite transformation can be used with any spectral method as long as the method could produce a peak-trough joint probability density function (JPDF) of the rainflow stress cycles of the underlying Gaussian process [24]. However, the DK distribution does not provide such a JPDF and the TB distribution can only provide an empirically approximated JPDF (table 2.3). Table 2.5 compares the WB methods in combination with the NG correction with each other. One can see that the GZ with NG correction again provides the smallest error with respect to the time domain results. An important note is that this is likely because a bimodal case is considered, which GZ is especially designed for.

α_3, α_4	Method	m=3	m=4	m=5	m=6
(0,4)	TD	6.73	35.31	222.03	1630.15
	NB&C$_{ng}^{WT}$	18.16 %	18.33 %	17.44 %	16.75 %
	TB&C$_{ng}^{TB}$	-10.15 %	-18.09 %	-23.96 %	-27.72 %
	DK&C$_{ng}^{DK}$	-12.55 %	-15.99 %	-18.06 %	-19.10 %
	GZ&C$_{ng}^{WT}$	-4.93 %	-6.47 %	-7.12 %	-6.93 %

Table 2.5: Bimodal non-Gaussian fatigue damage comparison per unit time for different fatigue resistance slopes m [24].

It is clear that extensive research has been done on how to empirically improve the spectral approach in order to capture nonlinear seakeeping effects. By combined use of the Hermite transformation for NG and various probability models for WB processes (DK, TB, GZ), the fatigue correction factor can be calculated for multiple types of spectra. Result accuracy therefore depends on the estimation of the (WB) Gaussian fatigue damage and the non-Gaussian correction. Gao et al. states that the method which combines these two the best is the novel GZ method [24]. This method in the end was able to produce a maximum error of 8% compared to the time domain results whereas other methods had a maximum error of 15%.

Chapter 3

Fatigue Resistance

3.1 Fundamental Mechanics and Equations

In marine vessels, welded details are identified as being the most fatigue-sensitive locations [8]. Microscopic stress concentrations (mSC's) due to the interaction of grains (orientation, dislocation) are known to cause nucleation of fatigue cracks. Also at macro scale, stress concentrations (MSC's) occur in the form of corrosion pits, manufacturing defects, or voids.
Based on observations, three phases in the total fatigue life are identified: the initiation of a crack, its propagation, and its final fracture [40]. Crack nucleation typically takes place at intrusions and extrusions at the material surface due to cyclic loading-induced slip, but at weld toes initiation is usually detected at undercuts or other imperfections in the welded material. At weld roots, inclusions of air pockets might occur, along with other typical material impurities.
The majority of the fatigue life happens in the first two phases. The distribution of time spent in each phase differs per material, geometry, and loading. For instance, a base (plate) material will have a relatively long initiation period whereas at a welded notch this period is much shorter.

3.1.1 Fatigue Resistance Curves

In the past, numerous experiments have been carried out, subjecting several welded specimens to different loads [8]. Depending on the magnitude of strain a specimen is subject to, the fatigue strength mechanism is based on plasticity or elasticity. At high-strain cycles, plasticity dominates the fatigue mechanism and the specimen is bound to fail after fewer cycles N. For lower amplitudes of strain, elasticity becomes the governing factor and higher numbers of cycles are attained.
Due to this change in mechanics, multiple fatigue ranges are identified: low- and high-cycle fatigue (LCF and HCF). For more clarity, [8] proposes to add mid-cycle fatigue (MCF) as well. There is no clear consensus on the transition of these ranges, but typically the transition from LCF to MCF is assumed at $N = 10^4$ cycles and MCF to HCF happens at $N \approx 10^7$ cycles.

The loading versus the amount of fatigue lifetime cycles is most commonly displayed in a Wöhler, or fatigue resistance curve [8]. Figure 3.1 displays a typical fatigue resistance curve in which S marks the adopted fatigue damage criterion. This could be the strain range e as mentioned before, energy W or stress range S. Typically, the stress range is used. The stress criterion depends heavily on the adopted stress assessment concept, which will be covered in section 3.3.
During specimen testing, the stress criterion is the independent parameter, although it is represented on the vertical axis in the SN-curve. The number of cycles is the result of the specimen test and is therefore the dependent variable.

Applying the same loading to a series of specimen with a constant stress range S, the fatigue lifetime will turn out different for every test. This is due to the random nature of mSC's and

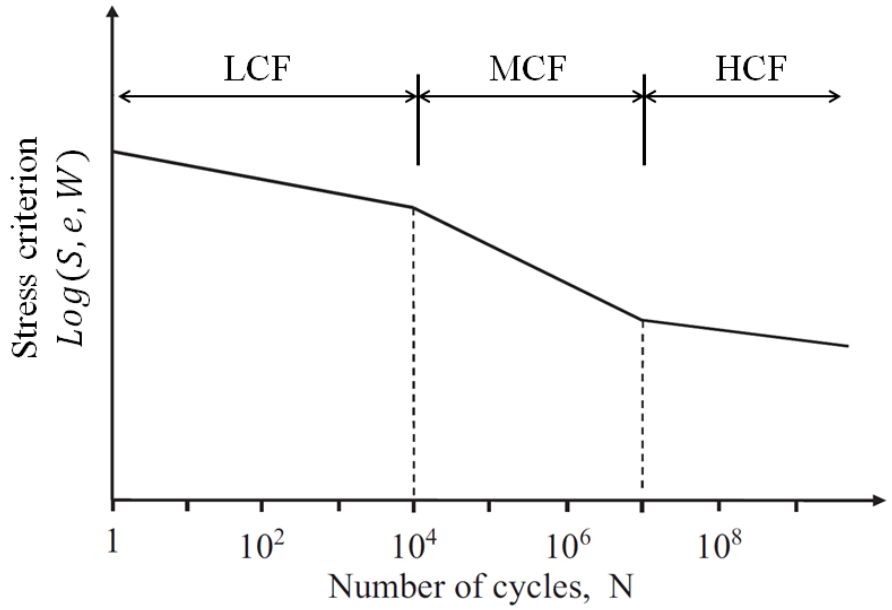

Figure 3.1: Typical fatigue resistance curve representation [40].

MSC's in each specimen. A certain scatter is therefore inherent. Sufficient data are required to form a reliable SN-curve for a structural detail. When tests have been performed over a wide range of stress range levels, regression analysis can be used to draw the SN-curves for LCF, MCF, and HCF [8]. At HCF, the amount of cycles is limited due test time considerations. Tests are stopped before failure, resulting in right-censored data.

Using regression analysis, the most likely SN-curve parameter constants are established. Equation 3.1 formulates how these constants are applied in the single-slope formulation. They are the fatigue strength parameter C (also called the intercept) and slope parameter m; the *Basquin* parameters. Typical values of the fatigue strength are within 12 to 13 and the slope is around 3 for a single-slope model in the MCF region. As $\log(C)$ is strength-dependent, adopting a specimen of different strength can shift the curve to the left (weaker) or right (stronger). The slope m depends on the dominant damage mechanism (crack initiation or growth), and will be different for various materials, as well as fatigue life phases (LCF, MCF, HCF). This is because of the aforementioned phenomenon of plasticity dominating the LCF region and elasticity dominating the MCF and HCF regions. In more detail, the LCF region is dictated by growth, while in the HCF region initiation controls the fatigue lifetime [8]. Also, in the LCF range, elasto-plasticity plays a key role, while for the HCF region elasticity dominates. Due to this, the slope m is decreased in the LCF region and increased in the MCF region. Note that in figure 3.1, this shows by a *steeper* curve in LCF and *flatter* in HCF; a counter-intuitive feature stemming from the SN-curve formulation of equation 3.1. So while the same single-slope formulation can be used for the different regions, the slope m changes because of the change in damage mechanism.

$$\begin{aligned} \log(N) &= \log(C) - m\log(S) \\ N &= CS^{-m} \end{aligned} \tag{3.1}$$

3.1.2 Rainflow Counting

The procedure of obtaining fatigue resistance curves through specimen testing has been explained. To construct a typical single-slope SN-curve, a test is carried out at constant amplitude (CA) stress on a small scale specimen (SSS). In practice however, due to ocean waves

being a superposition of multiple regular wave components, a seagoing vessel will be subjected to variable amplitude (VA) loading. To be able to calculate VA fatigue damage, CA SN-curves can nevertheless still be used.

To analyse a given VA stress time signal (figure 3.2a), the temporal or spectral approach can be used [8]. Both are so-called cycle-by-cycle methods in which cycle information is obtained from the signal. The temporal and spectral approach are further discussed in section 2.2 and 2.3, respectively.

The most common method to obtain cycle information from a signal is rainflow counting [8]. The goal of this approach is to obtain stress ranges and the amount of times they occur in the signal. The methodology will now be explained in more detail.

To obtain cycle information from a (stress) time signal, the VA signal is first discretised into its peaks and valleys (figure 3.2b). Stress reversals can now be observed. Fatigue damage occurs over a cyclic load which introduces a hysteresis loop [8]. These loops show up in the stress-strain curve when the material is cyclically loaded. A visualisation is provided in figure 3.2c, where the discretised signal has been turned -90°. One can imagine rain water flowing down this pagoda roof-like signal. In general, a cycle is counted when:

- A valley of greater magnitude is encountered.
- A rain drop merges with a flow started at an earlier peak.
- The end of a peak-valley sequence is reached.

Looking at the hysteresis graph in 3.2c, when going from peak 0 to valley 1, one can see the corresponding path the stress-strain relation takes. As the signal travels from point 2 to 3 and past the level of 2 again (point 2'), a closed hysteresis loop is formed. This would be registered as a whole cycle, whereas 0-1 would be a half cycle. A coding example of the rainflow algorithm is provided in Appendix A. Here, the number (n_i) of whole and half stress cycles ($\Delta\sigma_i$) is obtained, along with the mean values of these cycles ($\sigma_{m,i}$).

3.1.3 Damage Accumulation

Having identified each cycle and its corresponding stress range $\Delta\sigma$, the fatigue damage can be determined using Palmgren-Miner's hypothesis [8]. In the conventional method, linear damage accumulation is assumed.

The counted stress ranges are accommodated into bins of a certain range to form a stress range histogram. It is assumed that every bin contributes to the total fatigue damage according to its damage ratio, as is shown in equation 3.2. Here, n_i is the amount of times stress range $\Delta\sigma_i$ has occurred. N_i is the amount of cycles until failure, obtained from a CA fatigue resistance curve for the specific structural detail. When designing a structure, the damage over the structure's lifetime should be kept under a certain design threshold η. When damage $D = 1$, failure of the material will occur. To apply a safety margin, η is typically set at a value lower than 1 [8].

$$D = \sum_{i=1}^{k} \frac{n_i}{N_i} \leq \eta, \quad 0 < \eta \leq 1 \tag{3.2}$$

With this procedure, some information of the original time signal is lost. For instance, the sequence effect is not included as the preceding stress cycles have no influence on the damage ratio of a later stress cycle. Another example is the shape of the cycle (saw-tooth, sinusoidal, etc.). This information is lost since the signal is discretised into its peaks and valleys (figure 3.2).

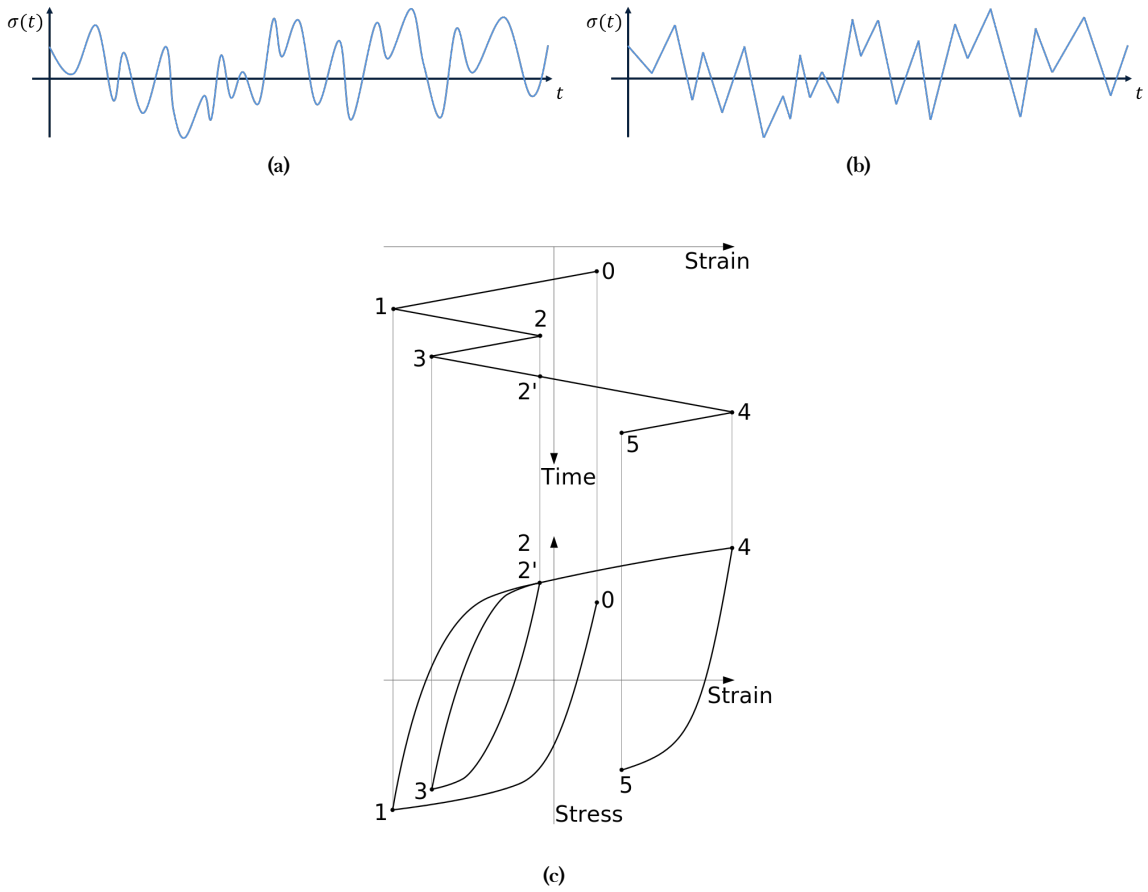

Figure 3.2: A VA stress time signal (a), its transformation to a peak-valley sequence (b) and the link to stress-strain hysteresis loops (c) [41].

3.2 Mean Stress Effects

In a VA stress response time signal, a dynamic and mean component can be distinguished, according to equation 3.3. In this case, σ_m is the *global* mean; the mean value over the whole time signal. With rainflow counting, mean components for every stress cycle were also identified.

$$\sigma(t) = \sigma_d(t) + \sigma_m \tag{3.3}$$

Summarising the mean stress components and their origin [8]:

1. Residual mean stress: a thermal stress due to welding-induced deformation.
2. Global mean stress: a static mechanical load due to ship weight, cargo storage, structural detail weight, etc.
3. Local mean stress: the mean value of an individual stress cycle.

It is of interest to include the mean stress effect in the fatigue assessment because it can either positively or negatively influence the fatigue lifetime. For the mean stress sources listed above, thermal residual and mechanical components are distinguished [8]. For instance, when a weld is subjected to a compressive residual stress, its fatigue lifetime will increase due to the weakened influence of tensional loads. Also, the structural weight of the ship, or some smaller structural details, will induce a static (tensile) stress component. Finally, when exposed to wave

loading, every stress cycle will have a mean stress component around which the stress range oscillates. This mean stress level matters since fatigue damage of the same stress range $\Delta\sigma$ will be higher when its mean stress level is higher. The mean stress effect due to dynamic loading will be the main focus of this section.

First, some nomenclature surrounding the mean stress effect will be indicated. Figure 3.3 illustrates different situations in which the maximum and minimum stress, σ_{max} and σ_{min}, have different values. As a convention, positive stress values denote tensile stress and negative values denote compressive stress. To capture the relation between the maximum and minimum stress, the mechanical load ratio r_{lr} is introduced [8]. This is the ratio of the minimum and maximum stress as depicted in equation 3.4. As can be seen in the figure, the minimum stress can be positive (3.3a), zero (3.3b), non-zero (3.3c) and equally opposite to the maximum stress (3.3d). These yield different values of r_{lr} in the domain $\{-\infty < r_{lr} \leq 1\}$. The symmetry case of $r_{lr} = -1$ marks a fully-reversed stress range.

$$r_{lr} = \frac{\sigma_{min}}{\sigma_{max}}, \ \{-\infty < r_{lr} \leq 1\} \tag{3.4}$$

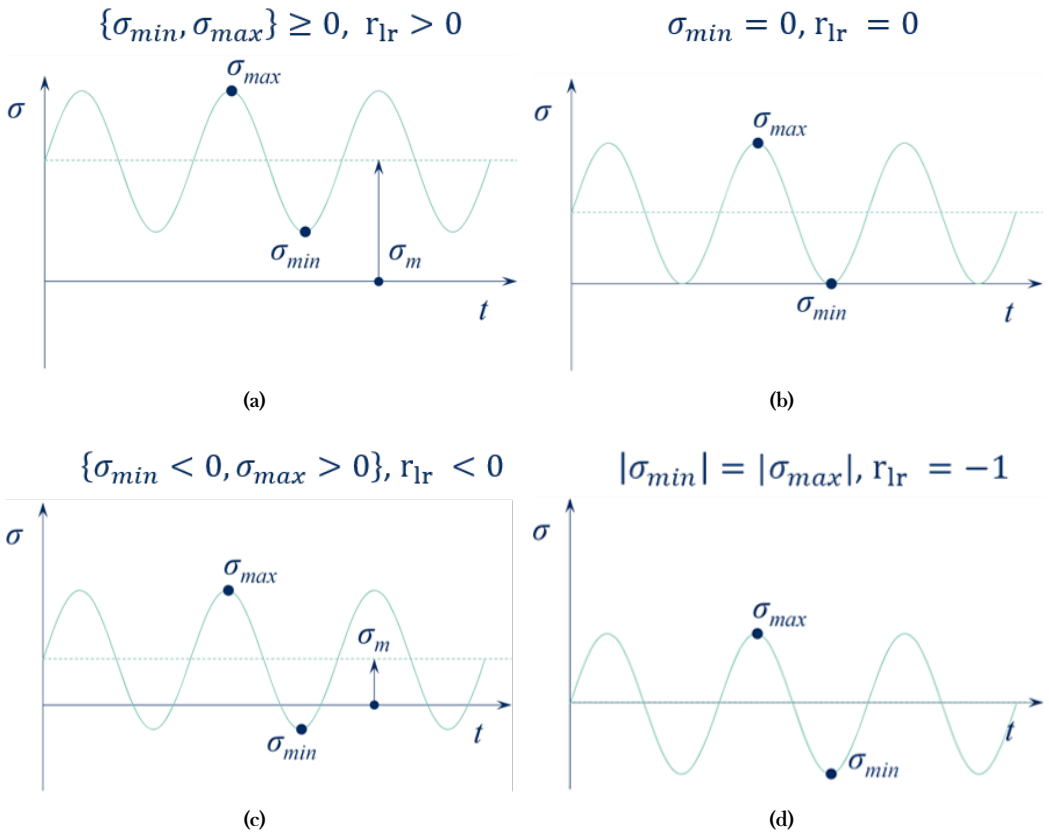

Figure 3.3: Visualisation of different values of r_{lr} [8]. **(d)** marks the fully-reversed case.

When applying different loading cases from figure 3.3 to a structural detail, test results show that the fatigue strength parameter $\log(C)$, also called the intercept, is affected. The slope of the SN-curve does not change since no material parameters are changed, but increasing r_{lr} will lead to a lower value of $\log(C)$, causing a lower fatigue lifetime for a constant loading S. In other words, when the stress cycle revolves around a higher (tensile) mean value, the fatigue life decreases. On the other hand, a compressive mean stress makes the stress cycle less damaging [42]. In the past, numerous models have been developed to describe this mean stress effect.

3.2.1 Mean Stress Correction Models

For engineering and design practices, DNV prescribes a simple formulation to account for mean stress in welded joints (eq. 3.5). In addition to the mean stress correction factor f_{mean}, other factors to apply to a stress range are stated, including plate thickness, material and post-weld treatment. Graphically, equation 3.5 is related to $\sigma_m/\Delta\sigma$ as shown in figure 3.4. One can see that for higher tensional (positive) mean stress levels, the effective stress range is not increased. Only a stress range reduction is applied for lower mean stress levels.

$$f_{\text{mean}} = \begin{cases} \min\left[1.0; (0.9 + 0.2\frac{\sigma_{\text{mean}}}{2\cdot\Delta\sigma})\right] & \text{for } (\sigma_{\text{mean}} \geq 0) \\ \max\left[0.7; (0.9 + 0.4\frac{\sigma_{\text{mean}}}{2\cdot\Delta\sigma})\right] & \text{for } (\sigma_{\text{mean}} < 0) \end{cases} \tag{3.5}$$

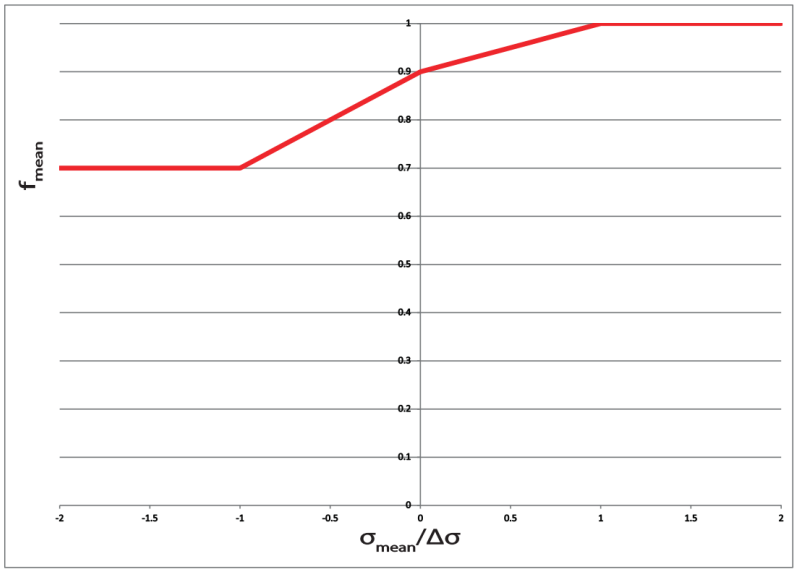

Figure 3.4: The stress range reduction factor for welded details [11].

In the scientific field, mean stress corrections are performed in more detail than proposed by DNV. A mean stress model translates a cycles' stress range with a given mean stress to a fully reversed (effective) stress range. An SN-curve established at $r_{lr} = -1$ can then be used to obtain the damage of the cycles. This way, only one SN-curve has to be used instead of a large number of SN-curves for every stress range with its own value of r_{lr}. The premise on which these methods are built is that the maximum stress should not exceed the ultimate strength. This means that as the mean stress increases in the tensile region, the stress range has to decrease [8]. It can therefore be stated that the fatigue strength $\log(C)$ depends on the ratio of mean stress and ultimate strength (eq. 3.6). Due to the exponential nature of the SN-curve, this relation is assumed to be nonlinear as well. Fatigue tests have also suggested this relation [8]. Once again, it is of interest to relate the $r_{lr} \neq -1$ SN-curves to the $r_{lr} = -1$ SN-curve. The aforementioned nonlinear relation is depicted in equation 3.6. Here, $C_{r=-1}$ denotes the fatigue strength for the $r_{lr} = -1$ case and α is a parameter which has to be defined in order to link the $r_{lr} = -1$ and $r_{lr} \neq -1$ case in a proper fashion.

$$C = f\left(\frac{\sigma_m}{\sigma_u}\right) = C_{r_{lr=-1}} \cdot \exp\left(-\alpha\frac{\sigma_m}{\sigma_u}\right) \tag{3.6}$$

For a single-slope $r_{lr} = -1$ SN-curve in the MCF region, the general formulation is given in equation 3.7. The ratio of S and S_{rlr} is used in order to obtain a formulation for the effective stress, provided in equation 3.8 [8].

$$S = C \cdot N^{-\frac{1}{m}}, \quad S_{r_{lr=-1}} = C_{r_{lr=-1}} \cdot N_{r_{lr=-1}}^{-\frac{1}{m}} \tag{3.7}$$

$$\frac{S}{S_{r_{lr=-1}}} = \exp\left\{-\alpha\left(\frac{\sigma_m}{\sigma_u}\right)\right\} \tag{3.8}$$

In fatigue resistance curves, S is defined in the form of a stress range. To focus on the relation of the mean stress and the stress range, empirical models express the relation of equation 3.8 in terms of the effective stress (eq. 3.9). This is the stress range at $r_{lr} = -1$ which causes the same fatigue damage as the actual stress range $\Delta\sigma$. By using this method, all the stress ranges at different mean stresses are related to the SN-curve of $S_{r_{lr=-1}}$.

$$\frac{\Delta\sigma}{\Delta\sigma_{eff}} \approx 1 - \alpha\left(\frac{\sigma_m}{\sigma_u}\right) \rightarrow \Delta\sigma_{eff} = \frac{\Delta\sigma}{1 - \alpha\frac{\sigma_m}{\sigma_u}} \tag{3.9}$$

Over the years, empirical models have been developed to describe the influence of mean stress to the fatigue resistance. Different values have been proposed for α, each having a different applicability with respect to the LCF, MCF or HCF range [8].

Den Besten mentions the Gerber (eq. 3.10), Goodman (eq. 3.11), Soderberg (eq. 3.12), and Kwofie (eq. 3.16) methods [16, 43, 44]. The Gerber method takes $\alpha = \sigma_m/\sigma_u$, causing a quadratic term in equation 3.9, disabling the distinction between tensile and compressive cycles [45, 8]. Goodman does account for this by using $\alpha = 1$. Both have proven to be quite valid from a universal engineering point of view. Goodman for instance provides good results for small mean stress and stress ranges (HCF region) [8], but in other regions they both have conservative results. Soderberg modified Goodman to include the material yield strength instead of the ultimate strength ($\sigma_u = \sigma_y$), but is also quite conservative and therefore hardly used [8]. The Morrow equation takes $\alpha = 1$ and substitutes the fatigue fracture strength coefficient $\sigma_{f'}$ for the ultimate strength σ_u (eq. 3.13) [46]. For high-strength steels where the fracture strength approaches the ultimate strength, this method is known to be quite adequate [42]. However, like said before, this method requires stress range data in order to determine $\sigma_{f'}$.

Furthermore, the Smith Watson Topper (SWT) method provides good results with a simple expression (eq. 3.14). The Walker method continues to build on SWT, and includes a fitting parameter γ which indicates the material's sensitivity to mean stress [47, 42]. This parameter is also called the loading and response ratio coefficient. Kwofie adopts $\alpha = 2$ in order to form its mean stress expression, but this equation has been validated with a small data set of 10 different materials [44, 45]. Exponential models like Kwofie [44] and Walker [47] are especially applicable to welded joints in the MCF and HCF region where the stress range is small and the mechanical and thermal residual mean stress is high.

Gaya da Silva stated that the Morrow, SWT and Walker method are the most frequently used mean stress corrections [42]. Walker formulates a relationship of the stress range with the maximum stress which introduces γ (eq. 3.15). The lower γ, the higher the mean stress sensitivity becomes. For metals, the value of γ ranges from 0.3 to 0.8 (eq. 3.15). For steel, a value of 0.7 is common [8]. Experimental data are require to calibrate the material parameter γ, which can be a drawback for this method. Qin et al. has found that for a generalised fatigue data set $\gamma = 0.92$ is the most likely estimate (MLE) for a generalised welded joint [3]. The introduction of γ has given the Walker method a versatility that is unmatched by the earlier correction methods [48].

$$\text{Gerber, 1874:} \quad \Delta\sigma_{eff} = \frac{\Delta\sigma}{1 - \left(\frac{\sigma_m}{\sigma_{uts}}\right)^2} \tag{3.10}$$

$$\text{Goodman, 1899:} \quad \Delta\sigma_{eff} = \frac{\Delta\sigma}{1 - \frac{\sigma_m}{\sigma_{uts}}} \tag{3.11}$$

$$\text{Soderberg, 1930:} \quad \Delta\sigma_{eff} = \frac{\Delta\sigma}{1 - \frac{\sigma_m}{\sigma_Y}} \tag{3.12}$$

$$\text{Morrow, 1964:} \quad \Delta\sigma_{eff} = \frac{\Delta\sigma}{1 - \frac{\sigma_m}{\sigma_{f'}}} \tag{3.13}$$

$$\text{SWT, 1970:} \quad \Delta\sigma_{eff} = \frac{\Delta\sigma}{(1 - r_{lr})^{0.5}} \tag{3.14}$$

$$\text{Walker, 1970:} \quad \Delta\sigma_{eff} = \Delta\sigma^{\gamma}\sigma_{max}^{(1-\gamma)} = \frac{\Delta\sigma}{(1 - r_{lr})^{1-\gamma}}, \quad \gamma \in [0.3, 0.8] \tag{3.15}$$

$$\text{Kwofie, 2001:} \quad \Delta\sigma_{eff} = \frac{\Delta\sigma}{1 - 2\frac{\sigma_m}{\sigma_{uts}}} \tag{3.16}$$

Figure 3.5 summarises the discussed methods and plots their values of the mean stress, normalised by the material's ultimate strength (σ_m/σ_u), against the actual stress range, normalised by the effective stress range ($\Delta\sigma/\Delta\sigma_{eff}$) [8]. The dotted lines indicate the values of the mechanical load ratio r_{lr}. The figure shows quite clearly how the different methods relate to each other. One can see that for small values of σ_m/σ_u the different methods are close to 1. When σ_m/σ_u increases, the methods yield different results.

The older method of Gerber yields values of $\Delta\sigma/\Delta\sigma_{eff}$ closer to 1 in the $\{0 < \sigma_m/\sigma_u < 0.5\}$ range, which corresponds to the LCF region; the region where the Gerber method was designed for [8]. In other words, Gerber estimates the effective stress range to be close to the actual stress range for higher mean stress values. This indicates the aforementioned conservatism; Gerber yields a higher effective stress range at higher mean stress levels, causing a higher fatigue damage in the end. At $\sigma_m/\sigma_u > 0.5$, the Gerber curve drops quickly. This falls within the MCF and HCF region, where the stress ranges are smaller due to the mean stress being high. Since Gerber provides a formulation for general engineering practices, effects occurring in the notch-affected region are not taken into account.

The method of Gerber is mostly applied in the LCF region where elasto-plasticity in the (weld) notch becomes significant at increasing σ_m/σ_u. Exponential methods like SWT, Walker and Kwofie are often used for MCF/HCF welded joint cases. At these ranges, the stress range is relatively small and the mean stress is quite high due to the mechanical and thermal residual components. The exponential models take this into account.
Focusing on Walker, the formulation of equation 3.15 generates the exponential relation as seen in figure 3.5. At high levels of σ_m/σ_u, the curve reaches an asymptote by which higher values of $\Delta\sigma/\Delta\sigma_{eff}$ than methods like Soderberg, Goodman and Gerber are attained. Its results are less conservative than SWT and Morrow over the whole domain, and in the HCF region it is more conservative than the Gerber method. It is believed that [47] is able to provide the most accurate relation in the case of welded notches since the material's sensitivity to the mean stress is included in the equation.

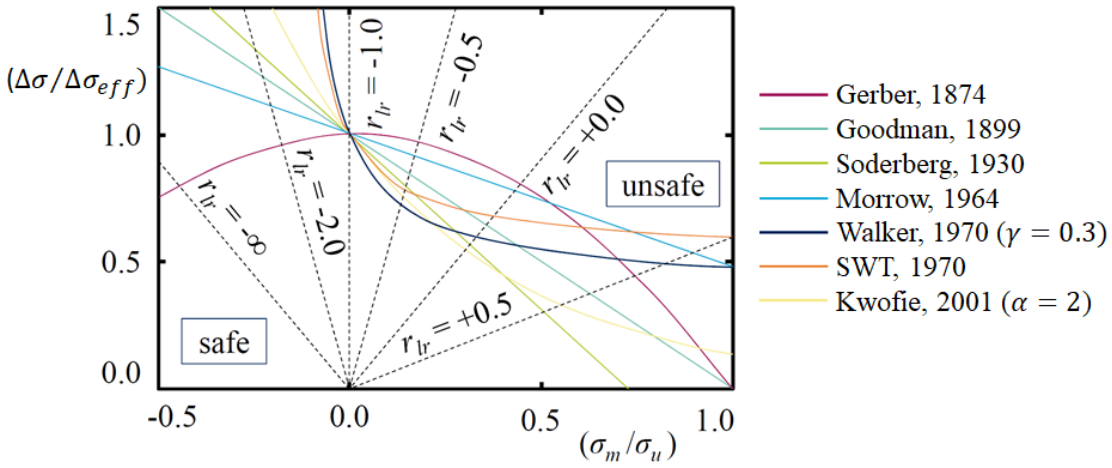

Figure 3.5: Overview of different MSE methods [8]

Papuga et al. re-evaluates a lot of MSE methods, including the aforementioned ones, with regards to their performance [45]. An important foundation for this study is the research of Dowling in which an extensive validation set of experimental, strain-controlled, results was presented [48]. These results were likely to be affected by initial overload cycles and therefore Papuga et al. creates a new data set which contains results of smooth, unnotched, axially loaded specimens [45]. A comparison is made between the resulting fatigue strength data of these specimens subjected to a loading at $r_{lr} = -1$ with the estimates of the different MSE methods for the same load case. The fatigue index error ΔFI indicates how much the MSE methods' effective stress amplitude ($\sigma_{a,eff}$) deviates from the experimental data ($\sigma_{a,exp}$) (eq. 3.17).

$$\Delta FI = \frac{\sigma_{a,eff} - \sigma_{a,exp}}{\sigma_{a,exp}} \tag{3.17}$$

Upon comparison, Papuga et al. draws a couple of conclusions [45]. First, the SWT method yields similar results for the Walker method for aluminium alloys due to material parameter γ similarity. Furthermore, the Walker method proved to yield the lowest values of ΔFI (within 5%) and therefore provides the closest estimations to the experimental results. Dowling has proposed to include the dependency on the material's tensile strength in the Walker parameter γ [48]. Papuga finds that this inclusion is reasonable, although the dependency is quite weak [45].

It can be concluded that the Walker method yields accurate results due to its ability to incorporate the base material's sensitivity to mean stress in the loading & response ratio coefficient γ. Calibrating this parameter, however, requires non-zero mean stress data of the material. When this is not available, equations based on existing fitting values can be used to make estimates for steels [48]. For welded joints, Qin et al. concluded that the material parameter should be set at 0.92 to incorporate thermal residual stress as well as welding imperfections [3].

3.2.2 Variable Amplitude Loading & Response Conditions

Up until now the mean stress effect for the case of constant amplitude (CA) was discussed. For a structural detail subjected to realistic wave loads, the stress time signal will have variable amplitude (VA). Rainflow counting is used to obtain the stress ranges occurring in the signal. This is then related to the appropriate SN-curve in order to then determine the fatigue damage. An important note is that SN-curves typically contain data for constant amplitude

loading. When variable amplitude loading is the case, there are two approaches to relate CA and VA stresses [8]. First, the fatigue damage parameter can be estimated using CA and representative, small scale specimen, VA test data. An appropriate SN-curve can then be fitted to this data and a $\log(C)$ shift will occur. Second, it is also possible to estimate the equivalent SN-curve parameters. Should the VA SN-data fit within the CA scatter band, then full fatigue damage ($\eta = 1$) is assumed. This second method therefore omits the calculation of fatigue damage through linear accumulation. The first method is used most commonly [8].

To account for the mean stress of individual cycles in a stress time signal, the algorithm that is used should include the mean stress information of each one. Obtaining this information is quite straight forward and was also discussed in section 3.1. When the time signal is discretised into peaks, the mean value can be obtained through equation 3.18. Here, σ_{i-1} and σ_{i-2} denote the two previous peaks in the signal. These are summed and divided by 2, providing the mean stress of that particular cycle.

For every stress cycle, three parameters are thus obtained: the mechanical load ratio r_{rl}, the stress range $\Delta\sigma$ and whether the specific cycle is a full or a half one. This data can elegantly be visualised in a 3D rainflow matrix. An example is given in figure 3.6, where 3.6a depicts an example stress time signal and 3.6b shows the corresponding 3D rainflow matrix.

$$\sigma_{m,i-1} = \frac{\sigma_{i-1} + \sigma_{i-2}}{2} \tag{3.18}$$

After obtaining the mean stress information, each cycle can be transformed to its equivalent stress range. In the previous section it was determined that the Walker correction method is a preferable approach to do this [47]. By using this algorithm, the mean stress value of every stress cycle can be incorporated in the variable amplitude fatigue assessment. Class regulations prescribe a mean stress reduction factor for every stress range [11]. This factor varies from 0.7 for $\sigma_m < 0$ up to 1.0 for $\sigma_m \leq 0$ for welded joints. For some engineering purposes this approach suffices, however, the use of a detailed mean stress correction is omitted.

3.2.3 Spectral Approach

When performing fatigue analysis in the frequency domain, information on the mean values of every stress range is not readily available as opposed to the temporal approach. In literature, this problem has had only occasional coverage. Kihl 1999 derived a formula to find the expected number of cycles until crack initiation for the case of random, narrow band loading with a nonzero mean stress value [49]. This formula is shown in equation 3.19 and it includes the global mean stress σ_m, tensile strength σ_t, SN-curve slope m, fatigue strength parameter C, and RMS stress of narrow band loading spectrum σ_x. The term between brackets accounts for the mean stress value as it modifies the cycle number by means of the Goodman correction. In line with results from test specimens [49], this equation increases the fatigue life for compressive mean stress and decreases it for tensile mean stress.

$$N_{cal} = \left(1 - \frac{\sigma_m}{\sigma_{uts}}\right)^m \frac{2^{-\frac{m}{C}} \sigma_x^{-m} C}{\Gamma\left(1 + \frac{m}{2}\right)} \tag{3.19}$$

Łagoda et al. performed uniaxial random load fatigue tests with different mean values [50]. It was found that in the case of 'symmetric' stress time signals with zero global mean, the local mean values of the individual stress cycles do not strongly influence the calculated fatigue life. Hence, no correction for the local mean values was needed. For 'asymmetric' time signals, two methods to account for the global and local mean values were proposed, aside from the method of not taking them into account at all. The first method transforms the stress ranges to equivalent ones with zero mean using a mean stress correction (Goodman,

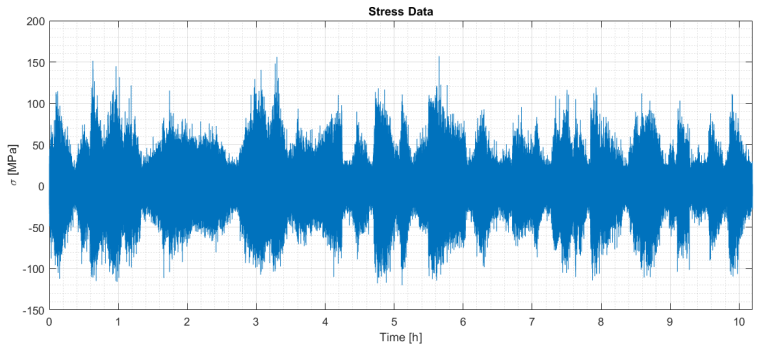

(a) Stress time signal over 10 hours.

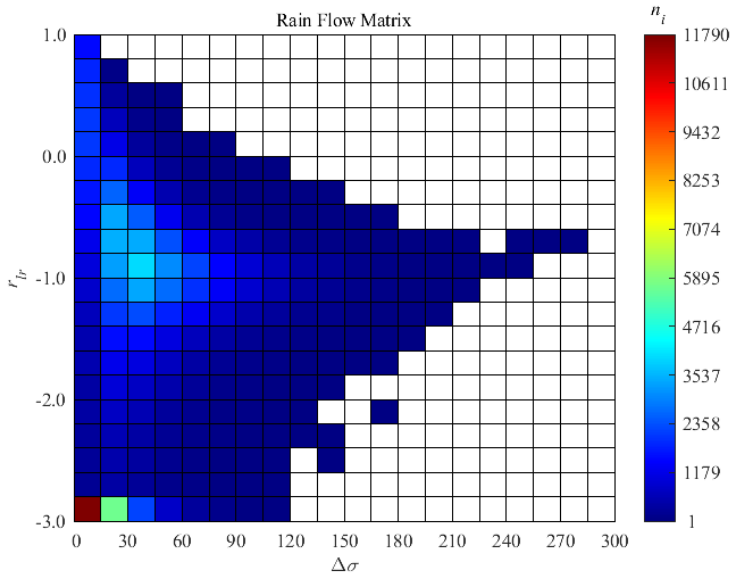

(b) Rainflow matrix containing load ratio r_{lr}, stress range $\Delta\sigma$ and amount of cycles n_i.

Figure 3.6: An example stress time signal and its corresponding 3D rainflow matrix [8].

Gerber, SWT, etc.). The second method transforms instantaneous values of the stress signal. The global mean is removed from the signal, leaving the time-varying part. This signal is then transformed to a symmetric zero-mean time signal with equivalent stress ranges. It is found that both approaches yield similar results, independent of the chosen mean stress correction. This indicates that when one desires to include the mean stress effect, it suffices to convert every stress cycle to an equivalent zero-mean cycle by using a suitable mean stress correction; removing the global mean is not necessary. 10HNAP steel was used for testing, and it was found that the Goodman equation was adequate for covering the mean stress effect. The research of Łagoda et al. is recommended for more details on these methods [50].

Niesłony and Böhm [6] have proposed a methodology in which the mean stress effect is incorporated in the spectral approach, building on the research of Kihl and Sarkani [49] and Łagoda et al. [50]. The aim is to construct a fatigue life formulation which includes the mean stress methodology for variable amplitude and wide band processes.

First, the transfer function shown in equation 3.20 is used to calculate the effective stress distribution from the original stress distribution. In this equation, $K(\sigma_m)$ denotes a factor based on a chosen MSE method (eq. 3.21). This factor is used to translate the stress range spectrum $S_{\Delta\sigma}(\omega)$ to the effective stress range spectrum $S_{\Delta\sigma_{eff}}(\omega)$. This way, the mean stress effect is taken into account in a linear way. This approach is also adopted in the work of Gao

et al. to account for the mean stress in the frequency domain [51]. This research focused on a method to predict multiaxial fatigue life.

$$S_{\sigma_{eff}}(\omega) = K(\sigma_m)^2 S_\sigma(\omega) \tag{3.20}$$

$$K(\sigma_m) = \frac{1}{1 - \alpha\frac{\sigma_m}{\sigma_u}}, \quad \alpha = \{\alpha_{Goodman},\ \alpha_{Walker},\ \alpha_{SWT},\ ...\} \tag{3.21}$$

Niesłony and Böhm then propose to proceed with the corrected stress spectrum and use the stress range probability distribution proposed by Dirlik to account for wide-bandedness (eq. 2.34) [6, 37]. Section 2.5.3 covers this method, along with other wide band methods, in more detail. Along with Palmgren-Miner's damage accumulation rule, the fatigue lifetime in terms of cycles is estimated as shown in equation 3.22. Here, N_{Ns} denotes the fatigue lifetime as calculated by Niesłony and Böhm, $f_{DK}(S_{\sigma_{eff}})$ is the probability density function of the Dirlik method as shown in section 2.5.3. $S_{\sigma_{eff}}$ is used to calculate several parameters that are needed for this PDF. $N(S_{\sigma_{eff}})$ is the single-slope Basquin-type fatigue life formulation (section 3.1, equation 3.1) which now uses $S_{\sigma_{eff}}$ as input as well.

$$N_{Ns} = \left(\int_0^\infty \frac{f_{DK}(S_{\sigma_{eff}})}{N(S_{\sigma_{eff}})} d\sigma_{eff} \right)^{-1} \tag{3.22}$$

In short, Niesłony and Böhm provide a way to include the mean stress effect in the spectral approach by using a linear transfer function to transform the stress range distribution into an effective stress range distribution. A mean stress correction is plugged in the transfer function in order to account for the mean stress levels in the cycles. To summarise, the following methodology is proposed [6]:

1. Convert the stress time signal into a power spectrum $S_\sigma(\omega)$ and determine the global mean σ_m.
2. Calculate $K(\sigma_m)$ according to a mean stress correction appropriate for the material's mean stress sensitivity.
3. Calculate the transformed effective stress power spectrum $S_{\sigma_{eff}}(\omega)$ according to equation 3.20.
4. Apply Dirlik's stress range PDF (eq. 2.34) and Palmgren-Miner's damage accumulation to obtain the fatigue lifetime (eq. 3.22).

In the research of Niesłony and Böhm, it is concluded that the proposed method is capable of including the mean stress effect for wide band processes. Although it is stated that the resulting power spectral density function is similar to the one obtained straight from a time domain simulation, verification of the proposed model is yet to be done. Furthermore, unlike the two methods covered by Łagoda et al. [50], Niesłony and Böhm [6] in the end do not account for the (local) stress cycle mean values, as only the global mean is covered. In the work of Gao et al. [51], the global mean is also used as input for the mean stress correction. Incorporating the local mean values is important when dealing with an asymmetric time signal [50].

Another problem that arises is when only the stress spectrum $S_\sigma(\omega)$ is known. As it is not possible to directly obtain individual stress ranges and their mean values from this spectrum, one could argue that the hybrid method should be applied to obtain this information. By converting the spectrum into a time signal through an inverse Fourier transform, the individual stress ranges and their mean values can then be obtained through rainflow counting.

However, the global mean remains zero, while in reality a compressive or tensional mean value could be at hand. Obtaining mean stress information while operating solely within the static calculations of frequency domain therefore remains a challenge.

3.3 Stress-Based Assessment Concepts

When a welded joint is considered for fatigue analysis, an appropriate stress criterion should be adopted. In general, the stress criterion translates the nodal stresses determined through FEM or strain gauge measurements to representative stresses at the weld notch of the hot spot structural detail [8]. For SSS experimental results, the strain data measured at a distance from the weld notch also needs to be translated to the notch using a stress criterion.

For welded joints, a distinction is made between welded joint types A, B or C (figure 3.7). Hot spot type A is located at a weld toe of an ending attachment on the plate surface, hot spot B is located at the weld toe of an ending attachment on the plate edge side and hot spot type C is located at the weld toe of an attached plate or of the plate surface. For all hot spot types, typically mode-I (normal stress) and mode-III (shear stress) are governing. The hot spot types have different properties with respect to the way the fatigue crack can propagate and thus different fatigue resistance applies for each type.

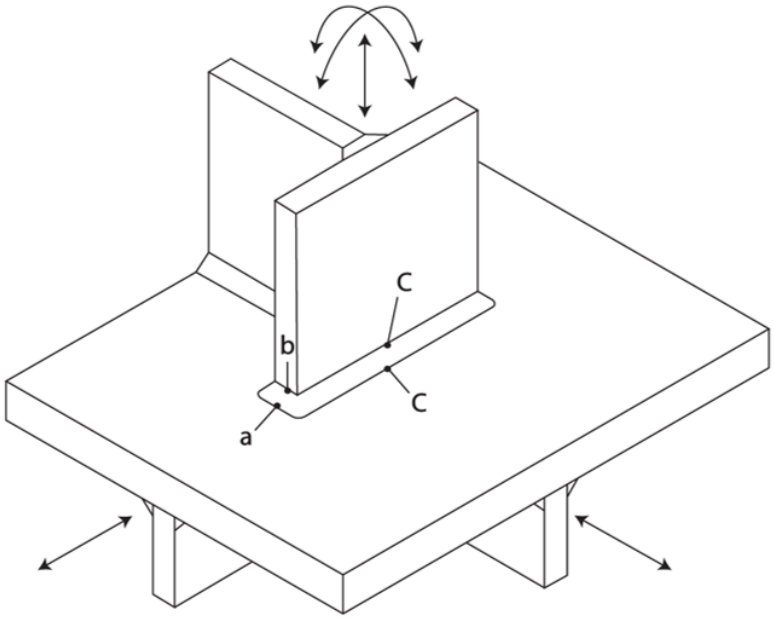

Figure 3.7: Hot spot types A, B and C [11].

A stress criterion will get increasingly accurate when more local information is added. As this will also be more computationally demanding, the selection of a fatigue assessment concept is always a trade-off between the accuracy one wants to achieve and the complexity of the fatigue damage criterion [8].

In general, fatigue stress-based assessment concepts aim at improving fatigue strength reliability and life time confidence [8]. Multiple stages of crack growth should be taken into account, correlating intact and cracked geometry parameters. Furthermore, when incorporating more local information of the structural detail, higher accuracy can be attained (at the cost of higher time demand).

Different assessment concepts have been developed over time. These concepts are characterised by the following parameters:

1. Information level: global or local
2. Geometry: intact or cracked
3. Criterion parameter: stress, strain or energy
4. Process zone: point, line, area or volume

The information level indicates at which scale the concept operates. Whether crack initiation or micro/macro crack growth is dominant determines which geometry criterion should be adopted; either intact or cracked. Furthermore, depending on work hardening, elasto-plasticity and the multi-axiality examinations, a stress, strain or energy parameter can be used [52]. This particular choice depends on the material properties and the nature of the loading. In general, stress-based criteria are applicable to cases of linear-elastic response and are therefore widely used [8].

Finally, depending on the structural detail's geometry, a point, line, area or volume process zone can be adopted.

Over the years, multiple stress assessment concepts have been developed. Den Besten and Qin et al. provide a clear overview of them, indicating the individual properties and applications [52, 3]. It is shown that research is moving towards a complete strength, multi-scale and total life criterion. When generalising over a multitude of specimen scales (SSS, LSS and FSS), the amount of fatigue resistance curves reduces. Increased complexity is however a consequence. Like stated before, a balance should be found between sufficient model accuracy and computational feasibility.

An overview of the stress assessment concepts available is given in figure 3.8. The information level (global, local) and geometry parameter (intact, cracked) are changing from left to right. The criterion parameter (stress, strain, energy) is changing from bottom to top. The lower row depicts typical SN-curves corresponding with the stress criterion. One can see that the amount of curves decreases when moving left to right. This is because as a concept increases in level of detail, a more general SN-curve is obtained [3].

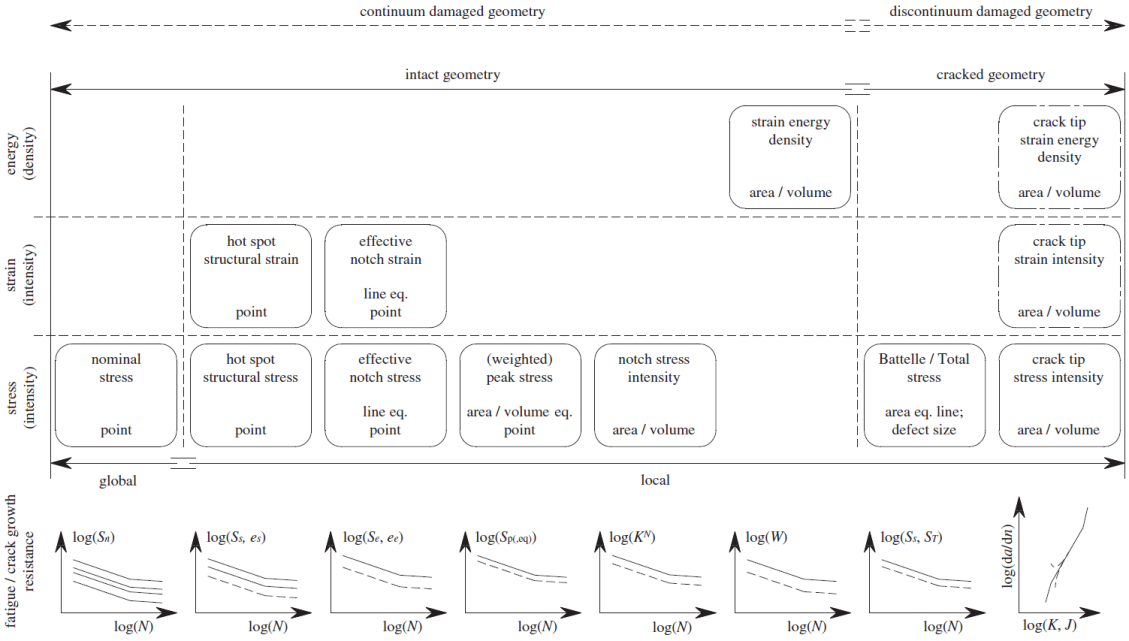

Figure 3.8: Fatigue stress assessments concept overview [52].

The stress assessment concepts that will be discussed in this review are:

1. Nominal stress (NSC)
2. Hot spot structural stress (HSSC)
3. Effective notch stress (ENSC)
4. Total stress (TSC)

These specific concepts are highlighted in this literature review because they are most commonly used and they cover a wide range of included detail; from minor to high complexity (figure 3.8). To give a clear view of their applicability, the pros and cons will also be discussed. This is done according to the work of [52] in which an elaborate review is presented. Qin evaluated the nominal stress, structural hot spot stress and effective notch stress concepts and later provided evaluations regarding the effective notch and total stress concepts [17, 3]. Furthermore, Deul has provided a concise and clear overview of these prevalent concepts [10].

3.3.1 Nominal Stress Concept (NSC)

The nominal stress concept $S_n = \Delta\sigma$ is characterised as a global fatigue damage criterion. It is defined at a distance from a structural detail so that it is not influenced by this detail. Figure 3.9 shows the position of σ_n with respect to the structural detail. One can see the distance that needs to be covered and the extrapolation to the weld toe that becomes inherent to this concept.

When a structural detail can easily be identified in the full scale structure, the nominal stress concept requires little effort as its complexity remains quite low. The complexity present is already incorporated in the corresponding fatigue resistance curves [8]. Since theoretically there are an infinite number of structural details, an infinite number of fatigue resistance curves can exist [52]. The challenge is to incorporate more local information of a structural (welded) detail, so that a general curve can be established, reducing the infinite amount of SN-curves to, ideally, one. For the nominal stress concept, as long as the parameters that determine the fatigue resistance (material, geometry, loading & response, environment, weld failure location, and weld quality) fit the established FAT class, the nominal stress concept can be applied and complexity is relatively low. S_n is defined as a point criterion, meaning size effects due to, for instance, the notch response are not included. Furthermore, it must be noted that in complex FEM-structures, the determination of S_n gets rather complicated as other structural details close by will influence the stress value.

3.3.2 Hot Spot Structural Stress Concept (HSSC)

The hot spot structural stress concept considers a local stress criterion as opposed to the global criterion adopted in the nominal stress concept (figure 3.8). It is a linear elastic intact geometry parameter which assumes that the largest part of the lifetime N is spent in the crack initiation phase. The equilibrium equivalent far field stress is now involved, meaning that the effect of the structure on the stress value is now taken into account. The hot spot stress is therefore defined as the equilibrium equivalent stress at the hot spot location.

The hot spot structural stress concept S_s is able to incorporate more local information based on material, geometry, loading & response and environment contributions [52]. However, looking at figure 3.9, the parameters t_b, t_c, l_w, h_w, a_n and notch radius ρ are still not included. This means that there is theoretically still an infinite number of SN-curves.
This concept considers the extent to which a structural detail is load carrying (LC) or non-load carrying (NLC). This parameter is directly linked to the self-equilibrating stress, so it tells in an elegant way what this stress is at, for instance, the weld toe (figure 3.9). In more detail, to incorporate the weld load carrying level, the average normal stress in the weld throat

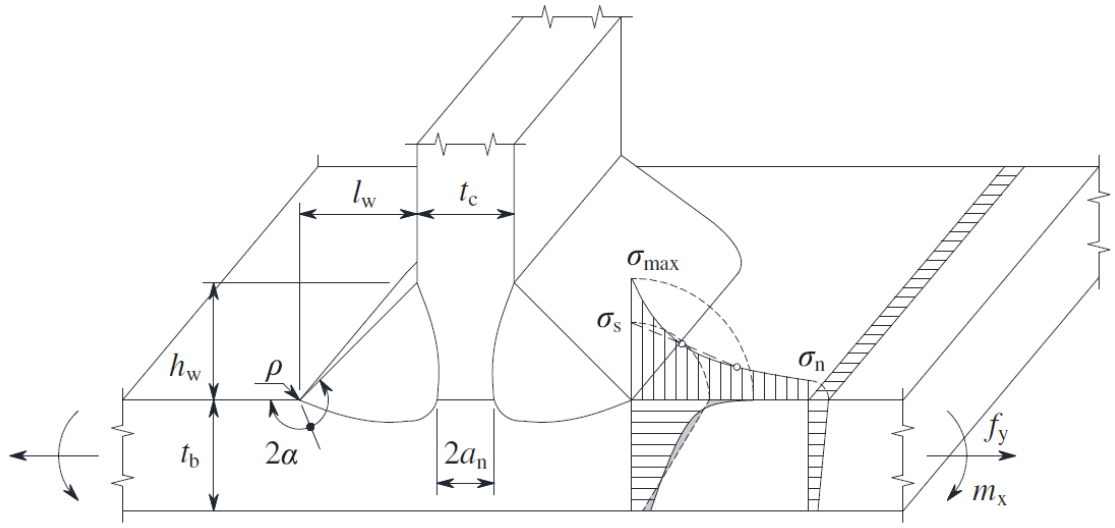

Figure 3.9: Stress distributions induced by a normal force and bending component and parameters indicating weld dimensions [52].

cross-section is used as an adequate measure [52]. Size effects can now be included as the plate thickness t_b and weld dimensions l_w and h_w are accounted for. It must be noted that this stress concept is limited to weld toe induced failures since fatigue damage at the weld root is hard to measure in practice. S_s is obtained by linear surface interpolation of two FE stress values.
Regarding the location of S_s, one must be aware of the self-equilibrating stress which can become involved for different values of t_p as well as for increased weld notch load carrying level [52].

The hot spot structural stress concept is a widely used concept due to its accuracy and accessibility [40].

3.3.3 Effective Notch Stress Concept (ENSC)

Looking at figure 3.9, σ_{max} is defined at the start of the weld toe. When modelled, this notch is infinitely sharp, i.e. the notch radius ρ is zero. However, in practice, due to weld imperfections or other production parameters, the notch radius is not equal to zero. This means that the modelled peak stress σ_{max} is conservative (too high). The effective notch stress concept S_e is obtained by adopting a micro- and meso-structural notch support hypothesis [52]. The idea is to average the notch stress over a material characteristic length. This parameter is defined as ρ^* and it involves the zone 1 and 2 stress gradient; the peak stress is supported by the notch stress gradient. A fictitious ρ_f can be used to artificially enlarge the real radius ρ. ρ_f then includes the micro-structural support length ρ^* (material dependent) and a support factor s which includes the geometry and loading and response contribution [8]. ρ^* is a material characteristic parameter, but the heat-affected zone and weld material effects are not included. An engineering radius ρ_e is therefore adopted.

In short, the effective notch stress concept takes notch elasto-plasticity explicitly into account and uses a material, rather than as-welded joint structure, resistance curve. With the amount of local information included in the effective notch stress concept, the amount of SN-curves has been reduced to one [52]. The effective notch stress concept is able to determine the stress concentration factor quite adequately and due to its increased complexity it is considered to be a sophisticated concept.

3.3.4 Total Stress Concept (TSC)

The total stress concept builds on the effective notch stress concept. The criterion S_T aims to include cracked geometry data and is based on an area equivalent line criterion (figure 3.8) [3].

The criterion incorporates the effective structural stress range $\Delta\sigma_s$ and a scaling parameter based on the plate thickness into account. This way, gradient-induced size effects are included. Since it is a cracked geometry-based criterion, the notch crack growth is incorporated, using an initial crack length as input. This is where TSC differs from ENSC. An assumption is that these defects in the weld have happened during the initiation phase.

The fatigue life is expressed as a function of the crack length development [10]. This zone 2 notch stress gradient parameter is based on the assumption that the majority of the fatigue lifetime is spent in the growth region, while defects in the welds consume the initiation phase [3].

Maximum likelihood regression analysis has proved that this method is in fact an improvement in accuracy with respect to the effective notch stress criterion and the other aforementioned ones.

The main advantage of this novel stress criterion is that one fatigue resistance curve is attained by incorporating sufficient geometry detail. However, more time is typically consumed in performing this concept compared to the aforementioned stress concepts.

3.4 Damage Accumulation

In section 3.1, the common procedure of linear damage accumulation was discussed. As the name suggests, this theory assumes that each stress cycle block contributes linearly, according to its damage ratio obtained through linking the stress ranges obtained through rainflow counting to an SN-curve.

As opposed to this linear assumption, fatigue damage has proven to be highly varying when accounting for its load time history. Sequence effects are a big source of this alteration. Leonetti [53] proposed a fatigue life prediction model under variable amplitude loading by using the 'Six Parameters Random Fatigue Limit Model' (6PRFLM), which was originally produced for CA purposes by the same author [54], and combining it with the damage limit model of Kunz (NLDAM) [55]. The model was applied to Rayleigh-distributed random stress block loading and requires a parameter ζ to be calibrated based on the linear elastic fracture mechanics of the material. Ultimately, the model was able to predict longer fatigue lives than estimated through conservative class code like DNV [11].

Deul [10] performed a thorough literature review focusing on novel damage accumulation methods and identified an improvement of the model NLDAM of Leonetti [53] where, instead of the nominal stress concept, the effective notch stress concept was implemented into the model. A database of random variable amplitude fatigue data was set up to analyse a variety of model combinations (NLDAM, LDAM, ENSC, HSSC).
Using the model combinations to predict fatigue lifetime and comparing it to the experimental data, it was found that the NLDAM&ENSC model formed by Deul [10] was able to reduce conservatism even more. The scatter was largely reduced, but not entirely. A recommendation was therefore to combine NLDAM with the total stress concept TSC in order to reach a total life criterion, including nonlinear damage accumulation.

Chapter 4

Research Plan

The previous chapter provided a thorough overview of the state-of-the-art regarding temporal and spectral fatigue analysis. In fatigue analysis, when starting with a wave field and finishing with an estimated fatigue damage (either spectral or temporal), it has become evident that there are multiple 'links' in the total 'chain' of modelling steps to be made (figure 2.1 and 2.3). In literature, the proper modelling of several of these links has been thoroughly researched. In some work, the entire fatigue analysis chain is modelled, like in the work of Mohammadi where a full time domain model is considered [7]. Proper model design choices have to be made here in order to ultimately make an accurate fatigue damage estimate. Other work focuses on single chain links, for instance the work of Gao et al. in which correction methods for wide-banded, bimodal spectra were investigated [24].

In this chapter, first, a gap in scientific knowledge will be identified; a 'missing link' in the fatigue analysis chain. Following this finding, a research question is formulated along with several sub-questions and hypotheses. Finally, a research plan is set up to answer all sub-questions and ultimately the main research question.

4.1 Knowledge Gap

In the field of loading and response (section 2.4.4), sources of nonlinear loading were observed. From these sources, the slamming and nonlinear Froude-Krylov (NLFK) force contribute significantly to the total nonlinear force [5]. In more detail, the slamming force originates from high impact velocity at the ships bow due to extreme waves. The NLFK force is obtained by integrating the instantaneous wave elevation at the ship hull instead of linearising around the mean waterline.

Typically, in spectral fatigue analysis, the stress range spectrum $S_{\Delta\sigma}(\omega)$ resulting from the wave load is assumed to be linearly related to the wave height spectrum $S_\zeta(\omega)$ [2]. A narrow band stress spectrum $S_\sigma(\omega)$ is assumed, justifying the use of the Rayleigh distribution for the stress range spectrum. However, the inclusion of the aforementioned nonlinear force contributions are bound to alter this narrow band response spectrum. Slamming-induced whipping vibrations for instance can cause a bimodal spectrum and the NLFK force tends to widen the spectrum [27, 5].

Numerous methods have been proposed to account for non-Gaussian, wide-banded/bimodal spectra [24], as was covered in section 2.5.3. With these methods, higher fatigue damage calculation accuracy can be attained compared to the (conservative) Rayleigh distribution (figure 2.6, table 2.3 and 2.4). In general, during the calculation of the damage, only the stress range effects are taken into account as the Rayleigh-distributed stress range spectrum $S_{\Delta\sigma}(\omega)$ is transformed into a non-Gaussian one. The mean value at which each stress range occurs is not considered; no mean stress information becomes available in the derivation of the stress range spectrum.

Including the mean stress in the spectral approach has been the focus of several studies [49, 50, 6]. These are however scarce in comparison to the work that has been done regarding

the non-Gaussian spectrum correction methods, which were summarised quite clearly by Gao et al. [24]. Others have used this research and the proposed method to implement in their fatigue lifetime models [51]. The widely accepted method corrects the stress range spectrum for the mean stress by means of a linear transfer function (eq. 3.20). The input for the correction operator $K(\sigma_m)$ is the global mean stress σ_m. This way, the local mean stress values of the stress cycles are not accounted for. In some cases, taking the local mean values into account is crucial for the result accuracy. However, typically the mean stress effect of individual cycles is ignored [8].

When focusing on the NLFK force, due to the direct integration of the water elevation at the ship hull, mean components in this force are expected [36]. Through loading and response, these mean components will end up in the stress response, causing a NLFK-induced mean stress effect. Niesłony and Böhm took steps towards a direct correction for mean stress in the spectral approach, but this was done by assuming a prescribed stress time signal; the origin of this signal was left out-of-scope [6]. Investigating the influence of the NLFK force on the mean stress response is of interest as it will uncover underlying mechanics in loading & response and fatigue analysis that have not been touched before. When calculating fatigue damage, novel stress assessment concepts like the effective notch stress [3] and damage accumulation concepts like nonlinear damage accumulation [10] can be applied to provide ample detail to the model.

A first step in the direction of investigating nonlinear hydrodynamic force contributions to the structural response by focusing on the relation of the NLFK force with the mean stress is proposed. The goal here is to gain knowledge on the interaction of these two links in the fatigue analysis chain. As a result, a better understanding of the interaction between said loading and response effects will be reached and thereby knowledge will be added to the general approach of fatigue analysis. Results are to be obtained through time domain simulations, and the findings will be plugged into a novel spectral fatigue analysis including state-of-the-art *WB correction*, *spectral MSE*, *stress assessment* and *(nonlinear) damage accumulation* methods. The novel approach will aim to yield more accurate results than former ones while maintaining time efficiency as compared to the temporal approach.

4.2 Research Question

From the identified gap in scientific knowledge, a direction for further research has been established. In this section, a research question is formulated, accompanied by several sub-questions.

The research question that follows from the problem definition is as follows:

How can the nonlinear Froude-Krylov loading & response-affected mean stress as well as the fatigue resistance consequences be incorporated in a spectral fatigue analysis?

The question reflects the goal of finding a direct relation between the NLFK force and the mean stress effect and implementing it in the spectral approach in order to get a more accurate representation and understanding of the underlying mechanics. Multiple steps will have to be taken to answer this question. These are reflected in the following sub-questions.

4.2.1 Sub-questions

The main research question can be subdivided into three parts: loading & response, fatigue damage and spectral approach improvement. Three corresponding sub-questions (SQ) have been formed which lead up to the main research question. They have been stated below along with some side notes which elaborate on the steps to be taken to answer the particular sub-question. Sub-question SQ1 marks the loading & response phase, SQ2 marks fatigue

damage phase, and SQ3 and SQ4 cover the spectral improvement phase.

SQ1. How does the NLFK force affect the mean stress response?

- **a.** How is a nonlinear FK versus linear FK hydrodynamic problem modelled?
- **b.** Which load case is most relevant to capture critical NLFK force effects?
- **c.** Which locations in the ship structure show the largest response due to NLFK effects?

SQ2. What are the consequences of nonlinear mean stress response contributions for the fatigue damage?

SQ3. Can state-of-the-art WB correction, spectral MSE, stress assessment concept, and (nonlinear) damage accumulation methods be combined to produce a novel spectral approach with improved accuracy?

- **a.** Combine Niesłony and Böhm spectral method with Walker mean stress correction [6, 47].
- **b.** Apply NG/WB correction method (TB, GZ).
- **c.** Apply NLDAM in combination with ENSC [10].
- **d.** Verify against time domain result.

4.2.2 Hypotheses

Based on the main research question and the five sub-questions in combination with the findings of the literature review, hypotheses are formed.

H1. NLFK force effects will be most dominant around the waterline of the ship structure.

H2. The NLFK force has an increasing influence on the mean stress response and therefore fatigue damage.

H3. As state-of-the-art NG correction, spectral MSE, stress assessment concept, and (nonlinear) damage accumulation methods individually improve fatigue damage accumulation, combining them will also yield improved results.

It is expected that the link between the NLFK force and the mean stress response will be strong. The NLFK force has proven to be a dominant source of nonlinear force [5] and due to the integration of the instantaneous waterline, mean components in the time signal are expected to occur [21]. This is presumed to translate heavily to the stress signal, causing similar mean stresses per stress cycle as well. By combining state-of-the-art spectrum correction methods, which account for wide-bandedness/non-Gaussianity/bimodality with spectral mean stress effect methods, an improved approach to the spectral loading and response part is pursued. The next step is to apply the effective notch stress concept in combination with nonlinear damage accumulation [10] to include state-of-the-art methodology in the spectral fatigue improvement part.

4.3 Methodology

The methodology of this research is based on the step-by-step plan on answering each sub-question (SQ).

4.3.1 SQ1: Mean Stress Response

Reflecting on the main and sub research questions, the focus on the NLFK force-induced mean stress response is evident. **SQ1** and its bullet points mark the start of the research approach. A seakeeping vessel will be modelled twice: including LFK and NLFK separately (**SQ1a**). For both cases, multiple wave load cases will be generated, aiming to uncover the increase of the NLFK force over increasing wave height and multiple wave angles. This is all done in the time domain to capture detailed nonlinear behaviour.

For the ship structure, it is of interest to find critical locations at which fatigue strength will be governing. As mentioned in hypothesis H1, the NLFK effects are expected to be largest around the waterline, so locations will be checked here and at other off-centre locations around the ship in order to compare (**SQ1c**).
Damen Naval has provided the test case of a pontoon model. Luna García-Valenzuela performed spectral fatigue analysis on this model, identifying critical hot spots and generating a first spectral data set. The pontoon model will be showcased in more detail in section 5.1.

An extensive data set of stress, shear (contained in $\vec{\sigma}(t)$), and displacements ($\vec{d}(t)$) in all directions (x, y, z) will be obtained for the nodes of interest in the time domain. Regarding the wave (load) cases (**SQ1b**), regular waves of varying height will be applied in multiple directions first. Later on, irregular wave spectra will be applied. This way, the increase of nonlinearity should become evident and a clear relation can be found.

As the input of the model will be the wave amplitude ζ_a and the wave heading θ, for wave case i, equation 4.1 denotes the 'function' that is performed. In context, figure 2.1 from section 2.2 forms the basis for the time domain procedure. The function '*LoadingResponse*' will consist of hydrodynamic and structural analysis performed in *Ansys AQWA* and *Mechanical*, respectively. With recent versions, load mapping of hydrodynamic pressure time domain results to structural response calculation has been made a quite straight-forward process [56].

$$\left[\vec{\sigma}(t),\ \vec{d}(t)\right]_i = LoadingResponse(\zeta_{a,i},\ \theta_i), \quad \text{for wave case } i \tag{4.1}$$

By performing the loading and response analysis in Ansys, accurate stress and deformation time domain results have been established. From this data set, the stress in normal direction of a structural detail is of interest in order to obtain hot spot type A, B or C information.

The resulting stress time signal will be used in post-processing to determine the fatigue damage. Rainflow-counting is used to obtain the rainflow histogram which includes cycle counts, stress ranges and mechanical load ratios (figure 3.6b). The histograms from NLFK and LFK can then be compared to gain insight on the NLFK influence on the mean stress response, ultimately answering **SQ1**.

4.3.2 SQ2: Fatigue Damage

Having obtained the 3D rainflow histograms, the fatigue damage can be obtained first by using linear damage accumulation and the nominal stress criterion. An appropriate mean stress correction is expected to be the one of [47]. This however depends on whether mean stress sensitivity data of the material is available, as was concluded in section 3.2. Otherwise, the [43] method proved to be quite adequate as well.

This first 'simple' fatigue damage model will be used to get an initial impression on the consequences of NLFK on the fatigue damage. With the results of the mean stress response and fatigue damage for NLFK, LFK, and for multiple wave cases, a clear relation is expected to show and H2 can be confirmed or discarded. Having completed the first model, improvements with more sophisticated methods like nonlinear damage accumulation in combination with the effective notch stress concept can be applied.

For the stress concept, because nodal time data will have been generated, global normal and local bending stress components can easily be uncovered. Applying the effective notch stress concept will therefore be feasible.

Ultimately, a sophisticated stress time domain and fatigue damage data set including the effective notch stress concept and nonlinear damage accumulation will have been set up.

4.3.3 SQ3: Novel Spectral Approach

When a sophisticated time domain method has been established, the obtained data are to be used to construct a novel spectral approach. This method will in the end be calibrated with the reliable time domain data and provide ample time efficiency inherent to the spectral approach.

From section 2.5.3, it became clear that there are numerous methods to account for non-Gaussianity, bimodality and wide-bandedness. However **SQ2** will yield insight on the influence of NLFK on the response spectrum, it is expected that a non-Gaussian and wide band correction will be needed. The TB method was designed for this case, while the GZ method extended it to bimodal spectra. Since bimodal spectra are inherent to hydro-elastic (whipping) cases, the need for this model is not expected in the scope of this thesis, as the focus lies on the NLFK force. Nevertheless, the literature study has identified several methods from which the appropriate one will be picked when the response spectra are known.

The spectral MSE method proposed by [6] will also be implemented in the model. Although verification of this method has not been carried out, applying it in this research is a good opportunity to gain more insight (**SQ3b**).

Finally, the spectral NLDAM using ENSC as proposed by [10] can be applied to obtain a novel spectral approach which is based on extensive time domain data.

Verification and Validation

To verify the improved spectral method, the time domain data set will be used as benchmark. When the spectral results match the time domain results, including NLDAM and ENSC, the novel approach can be considered to be verified.

Validation of the time domain loading and response results remains a challenge since a full ship structure is modelled as 'specimen' after which the focus is shifted to smaller structural details. Exact data of these structural details is not available as no full scale testing (FSS) has been carried out for the pontoon model. To some extent, validation can however be carried out. For a structural detail in the ship, fatigue test data for a similar specimen can be selected in available databases. Attention should be paid to the applied boundary conditions of this experiment, as it should be similar to the ones applied for the structural detail in the ship.

Upon further identification of adequate verification and validation methods, **SQ3** will be answered. After completing this part, H3 can be checked. Having answered this final subquestion, the main research question can be answered.

4.4 Concluding Remarks

This chapter has presented a detailed scientific gap identification and formulated an approach to answering the research question and its sub-questions. Using this structure, a step-by-step methodology has been formulated. Following these steps, a broad time domain database for the pontoon model will be constructed. The ENSC and an appropriate mean stress criterion will be applied to improve the time domain model and obtain more accurate results.

Using these results as a benchmark, a novel spectral approach will be set up using state-of-the-art methodology. The fatigue damage results can be verified with the time domain data. Validation is a challenge as FSS data are not available for the pontoon. Test data from specimens similar to the structural detail assessed in the pontoon model are therefore the only option.

Finally, having answered all sub-questions, the main research question can be answered. The set goal of incorporating the found NLFK force-induced effects into a spectral approach will then be reached.

II

Modelling

Chapter 5

Temporal Approach

This chapter showcases the methodology surrounding the temporal approach model. The details of the pontoon model are discussed in section 5.1. After that, section 5.2 shows the overall workflow used for the model. Sections 5.3 and 5.4 dive into the modelling of the hydrodynamic and structural model, respectively. Section 5.5 then discusses how the nonlinear and linear cases are modelled for the CA and VA models. The findings of the CA model are shown in section 5.6. The further modelling of the VA model is discussed in section 5.7. Following the comparison of the VA temporal and spectral results in section 5.8, conclusions are drawn in section 5.9.

5.1 Ship Details

Naval vessels were identified as being quite fatigue-sensitive due to their slenderness and broad operational profile [1]. For this project, no naval vessel data or models were available from Damen Naval. This was due to the availability of relevant data and confidentiality of naval ship models. However, a large non-confidential data set was available for the pontoon ship *Tobias*. On this model, an extensive spectral fatigue analysis was performed by Luna García-Valenzuela, identifying critical hot spots and generating a first spectral data set [1]. The pontoon model is depicted in figure 5.1. Two FEM mesh models were made available: 80k and 256k nodes. For computation capacity reasons, the 80k model was chosen, reducing computation time while still preserving detail. Figure 5.1 shows the real-life (5.1a) and meshed (5.1b) ship. Table 5.1 shows the dimensions and other properties of the ship. Here, the origin of the global coordinate system is positioned at the aft. Appendix B.1 showcases additional internal construction details (figure B.1 & B.2), along with details on the different plate thicknesses (figure B.3).

The availability of the structural model and the spectral fatigue data set made for a proper data supply for the temporal model.

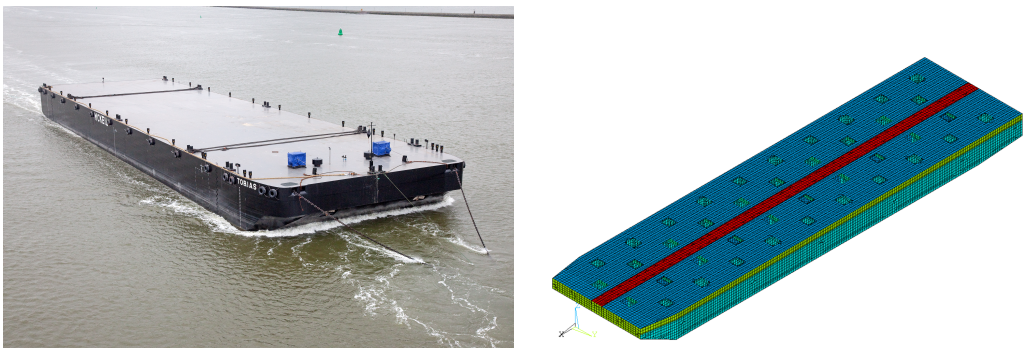

(a) (b)

Figure 5.1: Pontoon 'Tobias' and its FEM mesh [1].

Table 5.1: Properties of the pontoon [1].

Length	85	m	C_b	0.93	-
Breadth	22	m	CoG_{aft}	{43.2, 0, 2.64}	m
Height	5	m	CoB_{aft}	43.1	m
Draft amidships	2.25	m	CoF_{aft}	41.9	m
Displacement	3999	t	Trim	-0.42	°

5.2 Overall Workflow

In the temporal model, hydrodynamic and mechanical simulations are performed using *Ansys AQWA* and *Mechanical*, respectively. These modules are included in *Ansys Workbench* and can exchange information [57]. Figure 5.2 shows the workflow used in the project in order to perform time domain simulations. In every block, the dotted points indicate the properties/settings of the module. The arrow at the bottom indicates the output for the next module. Note that in *Structural Response*, the mass matrix is calculated according to the FEM model. The properties of this matrix have to be inputted to the *Hydrodynamic Diffraction* module before running a simulation. This way, similarity of the mass properties is ensured throughout the model. At the final block of *Structural Response*, the stress time traces are extracted into CSV files. These are then inputted for fatigue post-processing using *Python* (see section 2.2, figure 2.1). For the *Hydrodynamic* and *Structural* modules, a detailed overview of the settings is provided in appendix B.3 and B.4. Section B.4.2 elaborates on the procedure for exporting the results from *Structural Response*.

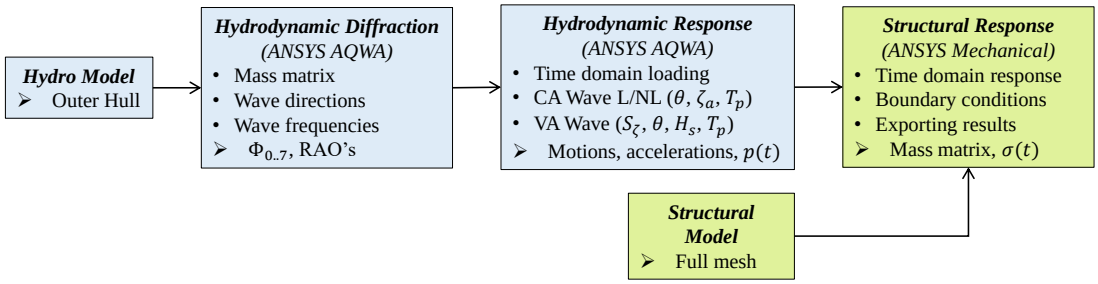

Figure 5.2: Overall *Ansys Workbench* workflow.

5.2.1 Automation

When running multiple wave cases, automating as much actions as possible is important for working efficiently and error-free. Research has been done on how to automate the execution of the three blocks *Hydrodynamic Diffraction*, *Hydrodynamic Response* and *Structural Response* (figure 5.2). In the end, numerous settings had to be entered manually. It was possible to alter values like wave parameters or simulation time by making different design points. However, it was impossible to run the entire workflow (from *Hydrodynamic* to *Structural*) right away. *Structural Response* had to be opened and executed manually.

Efforts to perform automatic runs and obtain the stress time traces with one batch file were aborted because of time considerations for the overall project. As of now, it is not likely that with the used version of *Ansys Workbench* (2020R2), the process can be automated entirely. For obtaining the results, manual steps were still needed, causing longer computation time and a higher risk of errors.

Should full automation be further pursued, then more research into the exact programming of

Ansys Workbench is required. It is expected that some opportunities lie within the manipulation of the project's result files (.RST). Furthermore, the *Scripting* tool within *Mechanical* is quite promising for automation purposes. However, the combination of a general script that steers both the *Hydrodynamic* and *Structural* models remains a goal to be reached. This also applies to the steering of *Ansys'* Application Customization Toolkits (ACT's), which are now used for the hydrodynamic pressure mapping and the exporting of the stress results to .CSV files (Multi Object Export ACT [58]). As of now, the *Scripting* tool is not properly capable of steering these ACT's as well.

Because of these limitations in combination with limited hardware capacity (RAM, storage), it was not possible to solve more than one 3-hour VA load case. The solved VA case will be discussed in section 5.7.
The hydrodynamic and structural models will be further explained in the next sections.

5.3 Hydrodynamic Model

Ansys AQWA utilises a hydrodynamic model of the ship's outer hull. This body is used in *Hydrodynamic Diffraction* to calculate the hydrodynamic potentials Φ_0 (Froude-Krylov), $\Phi_{1..6}$ (radiation) and Φ_7 (diffraction), which were discussed in section 2.4.1 (eq. 2.16). As input, also data on the ship's structural mass are required. This is obtained from the model in *Structural Response*.

In the *Hydrodynamic Response* module, the diffraction data are used to perform time domain seakeeping simulations using a near-field panel method approach [32]. It is ensured that the ship is kept in place and does not yaw by applying sufficient boundary conditions. Constant (CA) or variable amplitude (VA) waves can be applied. For the latter, a JONSWAP or Pierson-Moskowitz spectrum can be defined through their respective parameters [18]. Over the timeframe, hydrodynamic pressures on the hull are recorded. This information is then transferred to the *Structural Response* module.

5.4 Structural Model

In *Ansys Mechanical*, the structural model is imported. The mesh of 80k nodes is used and the origin of the global coordinate system is shifted from the aft to the center of flotation (COF) to provide a more convenient coordinate system. Stress results are not affected by this choice.

5.4.1 Mesh

The imported structural model makes use of surface and line bodies, which correspond to shell and line elements respectively. The surface bodies are used to model the larger plate sections and the line bodies are used for defining the stiffeners. This mainly includes the longitudinal stiffeners on the ship bottom, side, and deck plates (see appendix B.1). Some larger longitudinal stiffeners located around the connection of the longitudinal bulkheads with the deck or the bottom are in fact modelled as surface bodies.

The line body-modelled stiffeners are not meshed like the surface elements, but they do add stiffness as they have a defined cross section. Because of this, with the 80k mesh it is not possible to assess detailed hot spots at, for instance, stiffener web - transverse frame intersection. Furthermore, although the model consists of a large amount of nodes, locally the mesh is quite coarse. At the midship side shell, elements have a mean size of roughly 0.5x0.5 metres. With respect to the local plate thickness, which is around 14 mm (figure B.3), this is a significant difference. This coarseness prevents further detailed analysis at stiffener hot spots. A local mesh refinement would be required for conducting this analysis. The mesh element size would need to be reduced drastically to meet the same order of magnitude as the local plate thickness.

5.4.2 Boundary Conditions

For modelling a free floating structure like the pontoon, adequate boundary conditions need to be chosen in order to obtain a realistic response while also preventing rigid body motion.

For this model, boundary conditions at nodes at the aft and bow are applied. These are in line with practices recommended by DNV and are also applied in the work of Luna García-Valenzuela [23, 1]. The boundary conditions that are applied to these nodes are depicted in figure 5.3. A clarification for the DOF's they restrict is given in table 5.2. Being simply supported, moments are zero at the ends. Looking at table 5.2, the displacement in Z-direction is restricted for most nodes; A, C and D. These conditions prevent the structure from responding with rigid body motion when subjected to waves.

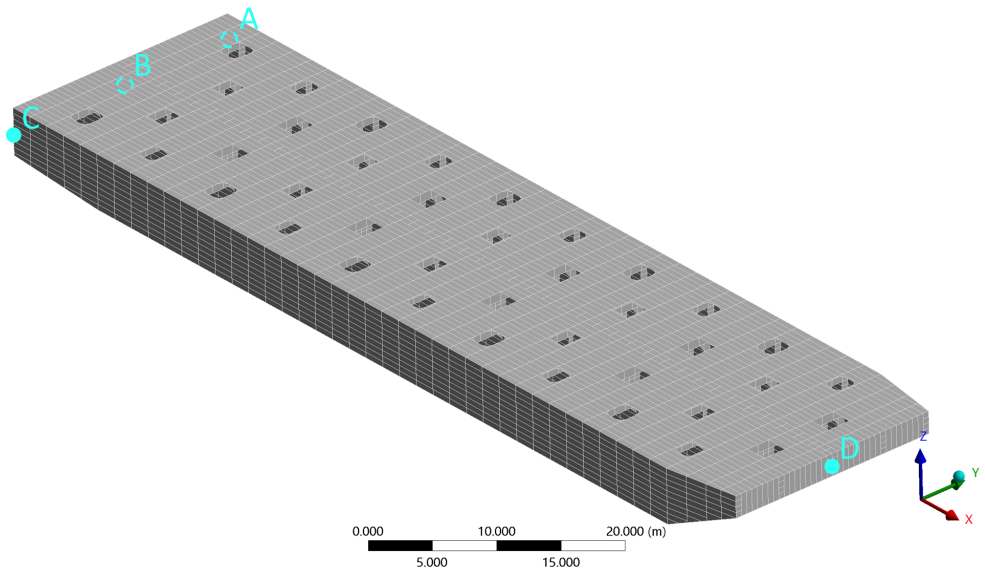

Figure 5.3: Locations of applied boundary conditions.

Table 5.2: Applied simply supported boundary conditions.

ID	Location	x	y	z
A	Aft PS	Free	Free	0
B	Aft MS	0	0	Free
C	Aft SB	Free	Free	0
D	Bow MS	Free	0	0

In reality, a floating structure stays afloat due to the hydrostatic pressure counterbalancing its weight. In the *Hydrodynamic* module, the ship draft is specified and the displacement and buoyant force are calculated. When moving data to the *Structural* module, the same overall balance of buoyant and gravity forces must be satisfied. In reality, the ship is loaded with cargo, or ballast tanks are filled to ensure sufficient draft and stability. The specified draft and displacement of the pontoon (table 5.1) apply to a ballast sailing condition. In order to ensure displacement similarity between the hydrodynamic and structural modules, the extra mass of the ballast is to be modelled as well. In the spectral model of Luna García-Valenzuela [1], this was done by increasing the density of the steel, so that the total structural mass matches that of the displaced mass. Other material parameters like the Young's Modulus, Poisson ratio and tensile and compressive yield strength are kept the same. This way, the stress response in the structure was not affected. The applied material parameters for the structural steel are specified in appendix B.4, table B.1

It is acknowledged that increasing the structural density to match the displaced mass does not promote realism of the model. Efforts were made to model the ballast condition by applying point masses in different compartments. A proper distributed pressure load was not achieved since the point masses affected the structural deformation locally. A simplified approach was therefore chosen, and the structural density was increased to meet the ship's design displacement. This ensured a mass distribution which was more evenly spread, as the alteration applied to every structural element. As this way of modelling is also in line with how the spectral model is set up, to which a comparison is made later on, it is important to keep most of the modelling choices the same. For a more sophisticated time domain model however, the ballast or load conditions should be modelled in a more detailed, evenly distributed way.

When subjected to a wave, the hydrostatic equilibrium still holds. However, pressure changes on the hull disturb the force equilibrium, resulting in accelerations. For a real ship, no simply supported boundary conditions exist; it floats freely. A boundary condition in addition to the aforementioned ones is required to simulate the 'real' boundary condition of the water pressure on the hull. This is where *inertia relief* comes into play, which will be discussed in the next section.

Inertia Relief

In real life, a ship is not constrained at the aforementioned boundary condition locations. As the hydrostatic pressure is in the end what keeps the ship from sinking, when subjected to a wave, using only the boundary conditions of table 5.2 does not cover the real situation. Another boundary condition is needed to simulate the hydrostatic pressure and compensate the reaction forces at the constraints.

In order to simulate the hydrostatic pressure as good as possible and keep the reaction forces low, *inertia relief* is typically used [59, 60]. Inertia relief has been a well-known approach for free-floating systems like aeroplanes, ships or satellites [59]. It balances the external loading with internal loads and accelerations within the structure itself [60]. The sum of forces and moments are calculated and counterbalanced in order to reach a 'static equilibrium'. The vessel can then be modelled as being afloat.

In combination with the boundary conditions, rigid body motion is prevented while also ensuring a realistic boundary condition similar to the hydrostatic pressure.

Reaction Forces

Inertia relief was enabled within *Ansys Mechanical*. The reaction forces were checked after each simulation. It was found that, due to the implementation of inertia relief, the reaction forces at the boundary conditions (table 5.2) were sufficiently small ($\leq 0.005 F_{buoyancy}$).

The applied boundary conditions were checked and approved in cooperation with Haniotis from Infinite Simulation Systems [61].

5.5 Linear and Nonlinear Loading Modelling

In the scope of this research, the influence of nonlinear loading is investigated, focusing on the nonlinear Froude-Krylov force (NLFK). This section provides information on the workflow regarding the modelling of the linear and nonlinear cases. Constant amplitude wave cases are the starting point. Here, linear and nonlinear wave theory is applied in separate cases to emulate the LFK and NLFK effects. Thereafter, the NL/L modelling in the VA case is discussed.

5.5.1 Constant Amplitude

In the CA model, *Airy wave theory* is applied for the linear case and *Stokes 2nd-order wave theory* for the nonlinear case [62, 63]. In 1845, Airy developed linear wave theory for harmonic surface gravity waves [62, 18]. The main assumption is that the regular wave components propagate freely and do not interact with each other. This underlines the random phase/amplitude model of section 2.1. The main requirement is that the considered waves are small with respect to their wavelength and the water depth [18]. Stokes proposed an addition to the linear wave theory of Airy by adding extra harmonic waves to the basic harmonic formulation [63].

The Airy wave theory and the Stokes addition are shown in equations 5.1 and 5.2. The details of the Stokes term ($\varepsilon^2\eta_2(x,t)$) are given in equation 5.3. One can see that the addition of Stokes becomes smaller as the wave depth increases; the $\sinh^3(kd)$ term increases faster than $\cosh(kd)$ as d increases.

$$\eta_{Airy}(x,t) = a\cos(\omega t - kx) = \varepsilon\eta_1(x,t) \tag{5.1}$$

$$\eta_{Stokes}(x,t) = \varepsilon\eta_1(x,t) + \varepsilon^2\eta_2(x,t) \tag{5.2}$$

$$\varepsilon^2\eta_2(x,t) = ka^2\frac{\cosh(kd)}{4\sinh^3(kd)}[2+\cosh(2kd)]\cos[2(\omega t - kx)] \tag{5.3}$$

The choice for using these wave theories to emulate the NL/L FK cases was made because of the limited capabilities of *Ansys AQWA*. No other options were available for isolating linear and nonlinear loading. In the end, both wave theories affect the wave loading differently because of the different input for the calculation of the Froude-Krylov force. The extent to which the nonlinear wave modelling yields differences in the loading is analysed in section 5.6.3.

5.5.2 Variable Amplitude

After the CA NL/L case study, the complexity of the analysis is increased by considering variable-amplitude (irregular) waves. In *Ansys AQWA*, nonlinear wave theory is automatically applied here, as the option of Airy/Stokes wave theory is no longer available. The linear case here will consist of the spectral dataset provided by Luna García-Valenzuela [1]. The linear transfer function (eq. 2.11, section 2.3), which scales the given sea state to a stress response spectrum, causes the spectral approach to yield linear results. In the time domain, nonlinear seakeeping behaviour is incorporated, as was shown in section 2.4, leading to nonlinear results in the response.

5.5.3 Concluding Remarks (SQ1a)

Comparing the linear and nonlinear *CA* cases will in general indicate the influence of the NLFK force on the stress response because of the way the linear and nonlinear waves are modelled. It is acknowledged that the NL/L modelling is not ideal because one would prefer isolating the full NLFK and LFK in two separate cases. This is however not possible within *Ansys AQWA*.

Having observed NL effects for regular waves, the findings can be carried over to the VA cases in which the time domain simulations will include multiple nonlinear loading components (section 2.4.4). By increasing complexity, the goal is to step-by-step see the influence of increasing nonlinearity to the stress response. Concluding, table 5.3 shows the origin of the {CA, VA}, {linear, nonlinear} data sets as discussed in this section. A detailed project overview is provided in appendix B.1. For the CA and VA project setup, section B.2 gives a clear depiction of both.

Table 5.3: Overview of {CA, VA} and {linear, nonlinear} data origin.

Wave type	Linear data	Nonlinear data
CA	Airy wave theory	Stokes 2^{nd}-order wave theory
VA	Spectral data set [1]	Temporal model

Sub-question 1a
How is a nonlinear FK versus linear FK hydrodynamic problem modelled?

The stated overall workflow combines multiple blocks of operations (CFD, FEM, post-processing) in order to uncover NL/L FK effects. The main tools, *Ansys AQWA* and *Mechanical*, are provided by Damen Naval. Along with these tools, literature research helped shape the final model and provide the answer to **SQ1a**:

A NL/L FK force comparison model consists of three main Ansys modules: AQWA Diffraction, AQWA Response and Mechanical. Successively, they determine the ship's hydrodynamic coefficients, seakeeping and structural response for a given wave load case. NL/L modelling is done by altering the applied wave theory in AQWA Response

5.6 Constant Amplitude Loading & Response

This section showcases the comparison of linear and nonlinear wave-induced stress response for constant amplitude (regular) waves. A critical wave case is determined using a transfer function (RAO) analysis after which a suitable time step is determined with a convergence study. Then, the modelling of the linear and nonlinear waves is explained. This leads to the stress response comparison study at the end of the section. With this comparison, this section will conclude by answering sub-questions **SQ1b** and **SQ1c**.

5.6.1 Load Case

Sub-question **SQ1b** considers which load cases are relevant to capture the NLFK force effects. As it is expected that nonlinear effects will be predominant at wave cases which yield a large response, the focus lies on the peak periods of the ship. At these wave periods, the global moment response of the ship is the highest. Given the fact that the global longitudinal bending moment (M_Y or RY) is governing for fatigue damage [1, 7], the RAO of this loading component is of most importance and will be the focus of the further determination of the load case.

Longitudinal Bending Moment RAO

Using the *Diffraction* module of *Ansys AQWA*, the RAO's of all DOF's are determined. They are displayed in appendix C.1. Each RAO is determined for 20 frequencies ranging from 0.1 to 3.8 rad/s. This correlates to wave periods of around 1.6 to 63 s. The wave heading is also iterated, ranging from -180° to +180° with a step size of 22.5°.

Figure 5.4 displays the longitudinal bending moment RAO RY; the governing loading component [1, 7]. RAO's of headings -180° to -22.5° are left out as they are the same as their positive-heading counterparts. One can see that for headings 0.0° and 180°, the longitudinal bending moment response is the largest out of all headings at a wave period of around 8 s. This indicates that for following and head seas, large bending moments are expected at this peak period. Because of the ship's forward speed, head seas is chosen as this will cause additional loads. This leads to the 'critical' case of head seas.

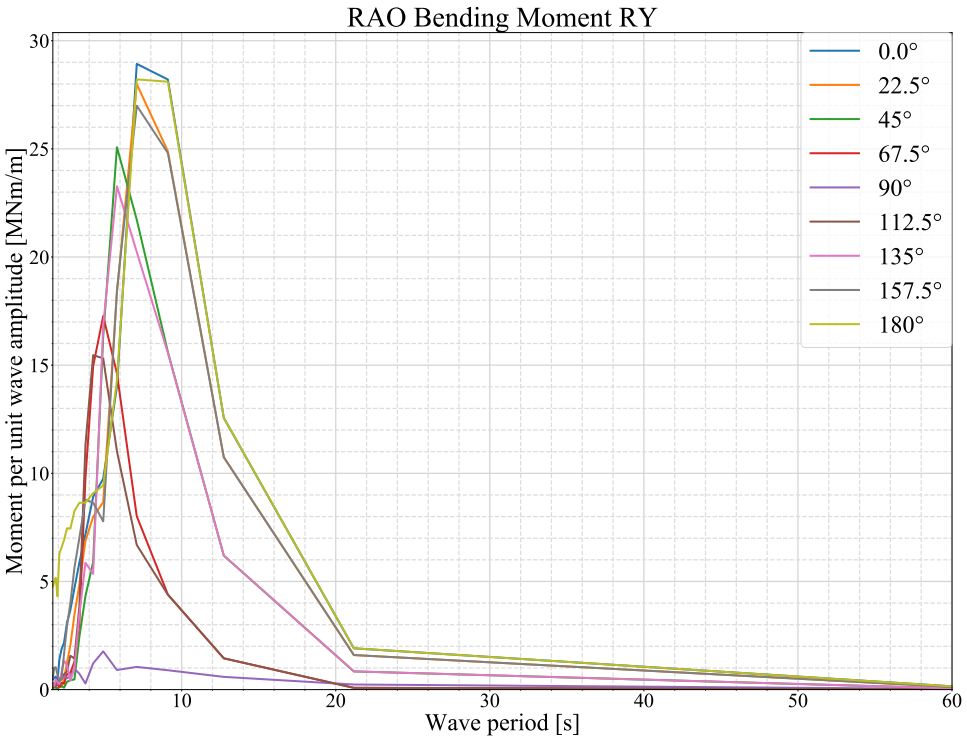

Figure 5.4: Longitudinal bending moment RAO RY for multiple wave headings.

5.6.2 Time Step Convergence

Before performing the time domain simulations, time step size (dt) convergence has to be verified. Because of data storage capacity, an optimum time step needed to be chosen. While a smaller time step ensures ample detail, it also causes more required storage space. A larger time step makes the resulting signal 'coarser' (a term also used for mesh size indication), but reduces the total result file size. This also depends on the length of the simulation.

When applying a wave, a certain time step resolution is required. Typically, a single wavelength is to be divided into five time steps, covering a start, valley, up-crossing, peak and end value [59]. Should the time step be larger, the wave discretisation becomes coarser. To illustrate the effect of a coarser or finer time step, and to confirm convergence for the evaluated case, two waves with a different period are evaluated; T_p = {3, 7.4} s. By means of the dispersion relation (eq. 2.10), these wave cases result in wavelengths of λ = {0.4, 1.0}L_s, respectively. Especially the 1.0L_s case is considered to be critical because the wavelength is equal to the length of the ship and therefore large hogging and sagging moments are expected [1]. These waves have a steepness of H/λ = {4.7e-1, 1.2e-2}, respectively. A shorter wave (T_p = 3 s) is steeper and therefore a shorter time step is required to cover a full wave period.

This is illustrated in figure 5.5. For a node in the midship section, the stress response over two minutes is plotted for both wave cases. The applied time steps are $dt = \{0.1, 0.5, 1\}$ s. For the steep wave (figure 5.5a), one can clearly see the way the coarse time step of 1 s cuts off, or truncates, the peaks of the 'real' wave signal of dt = 0.1 s. Important stress cycle data are therefore lost. For the longer wave which is less steep (figure 5.5b), there is more margin when choosing a larger time step; the peaks get truncated much less.

Damage Comparison

For eight nodes around the midship web frame, time steps of dt = 0.1 until dt = 1.0 s with steps of 0.1 s are evaluated. The dt = 0.7 results were not obtained due to a corruption of the data file. This is however accepted as the remaining data set provides sufficient detail.

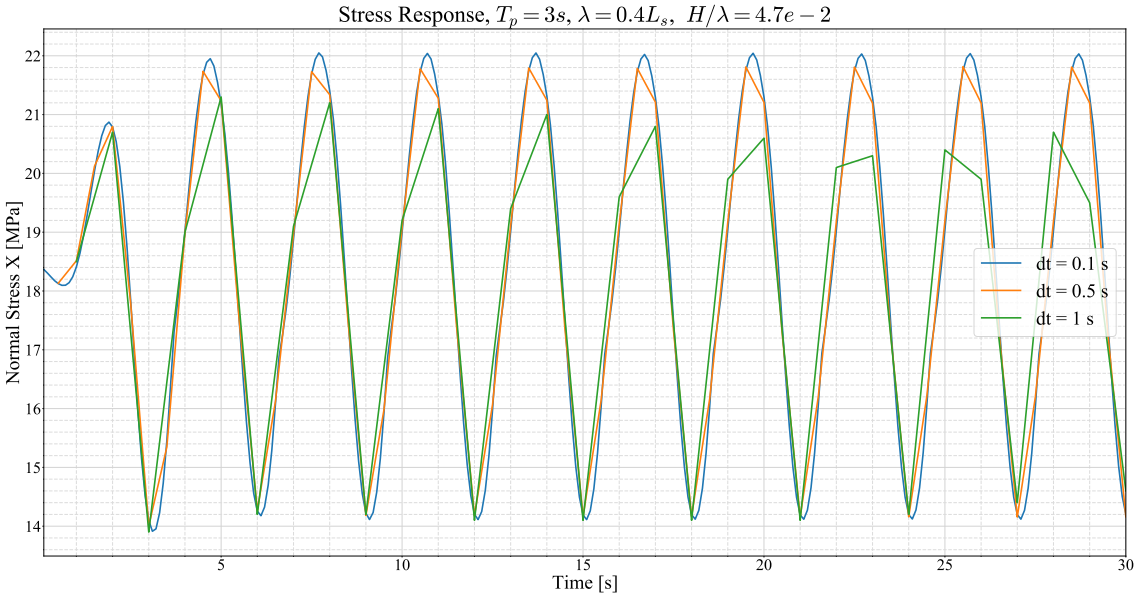

(a)

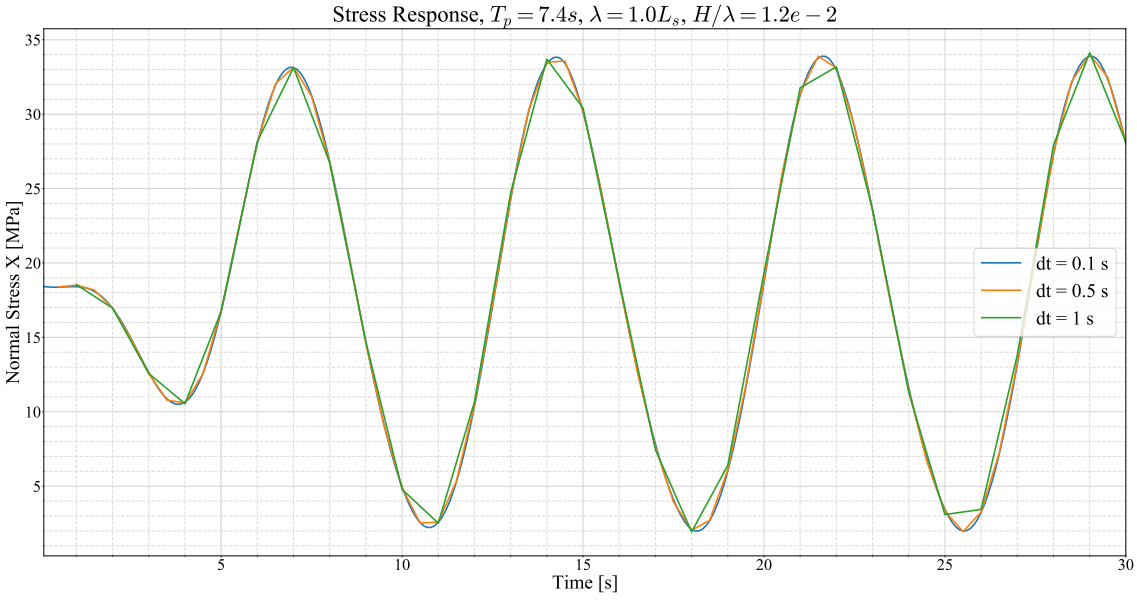

(b)

Figure 5.5: Difference in wave discretisation for T_p = 3 s and 7.4 s, for a midship node.

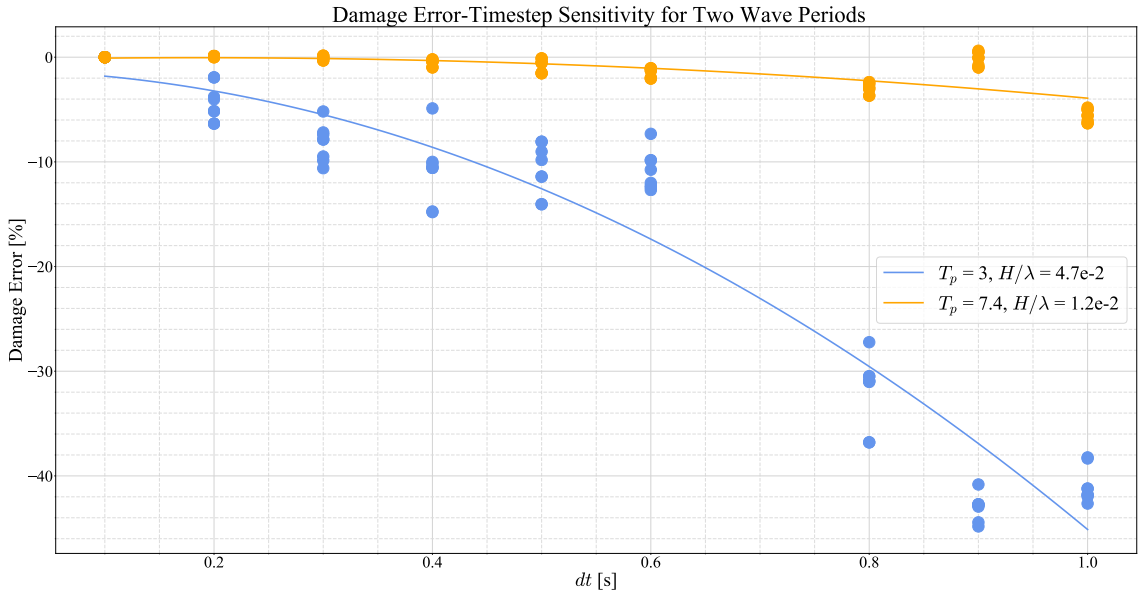

Figure 5.6: Fatigue damage sensitivity to time step size comparison for $T_p = \{3, 7.4\}s$

On the signals, rainflow counting is performed to determine the damage. As peaks are truncated, smaller cycles are obtained which causes a third-order difference in fatigue damage in the end (section 3.1, equation 3.1). Because of this third-order enhancement, a convergence of the damage results ensures even more wave discretization convergence. For the damage calculation, a typical SN-curve of $\log(C) = 12$ and $m = 3$ is used [8]. Palmgren-Miner linear damage accumulation was then used to determine the total damage over the two-minute timeframe (eq. 3.2).

Figure 5.6 shows the damage error comparison for both wave cases. For every considered time step, the percentual damage difference with the dt = 0.1 s case is plotted for the eight considered nodes. With the dt = 0.1 s case as a benchmark, one can see that the percentual damage error increases as the time step increases for both wave cases. In other words, the damage estimate decreases for a coarser time step. This is because the peaks of the real signal are truncated, therefore decreasing the stress range and eventually the damage. A clear difference can be seen when comparing both wave cases. For the steeper wave of T_p = 3 s, the error increases rapidly as the time step increases. Judging from the slope of the second-order polynomial fitted to the data points, there is no convergence for the T_p = 3 s case. For the T_p = 7.4 s case, the slope of the fitted polynomial is quite smaller, and damage errors only start exceeding 2% after $dt = 0.6$ s. As the peak period of the head seas wave case is around 7.5 to 8.5 seconds, the time step that can be adopted has a maximum of dt = 0.5 s.

Concluding Remarks

For the $\{Tp, dt\}$ = {7.4, 0.9} s case, the data points are quite higher than the rest of the wave case set. This can be explained by the random nature of the time step discretisation of the wave signal. Looking at figure 5.5b, it can be seen that some peaks of the signal are truncated when the time step is 0.9 s. Concluding on the time step convergence study, it is shown that for the larger wavelength case of T_p = 7.4 s, a time step of no larger than dt = 0.5 s is to be chosen in order to capture the full scope of the modelled wave. For reference, this is even smaller than the time step Mohammadi recommends, namely $dt = T_p/10 = 0.74$ [7]. The choice for the smaller time step of 0.5 s is made because there is additional uncertainty due to the missing data at dt = 0.7 s.

5.6.3 Linear and Nonlinear Response

Section 5.5 discussed the procedure of modelling of the CA NL/L cases. This section will show the execution of this procedure and its results.

Reflecting on sub-question **SQ3c**, a location which is most sensitive to nonlinear loading is sought after. Additional to this question, it is of interest to uncover whether the NLFK force induces the greatest differences either *globally* or *locally*. For global effects, the longitudinal bending moment-induced normal stress NSX is the greatest contributor as it induces a far field stress on structural details [8]. Local effects can be induced by local water pressure-induced plate bending. Submerged outer shell plating is expected to be affected the most. At the waterline, intermittent wetting effects can occur due to the emerging/submerging of the plate (section 2.4.3). Local stress is characterised by the stress in the direction of the shortest dimension of the plate. Typically this is in vertical Z-direction. Therefore, the NSZ-component is used to investigate local effects.

For the NL/L case, CA waves of increasing wave amplitude ($\zeta_a = \{1, 2, 5\}$ m) are applied for the identified critical load case of $\{T_p, \theta\}$ = {8.1 s, 180°} (head seas). These wave amplitudes are chosen to uncover increasing nonlinear response. It is acknowledged that the higher wave cases are not realistic for the ship's operational profile as they exceed the ship depth of 5 metres drastically. The run time is two minutes in order to capture sufficient wave periods in the response.

To test hypothesis **H1**, a vertical selection of nodes is chosen over the height of the side shell, in between two web frames. This selection is depicted in figure 5.7. The vertical selection is situated 0.9 m in front of the midship web frame (X=0.9m).

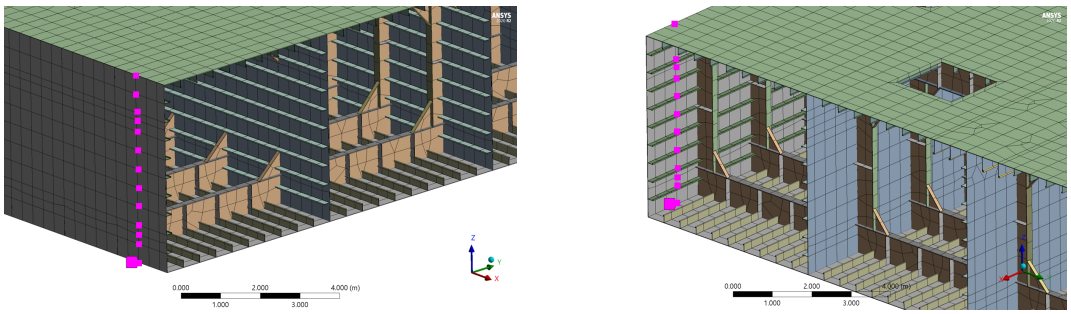

(a) (b)

Figure 5.7: Two views on the first selection nodes (pink) over the ship height D at the side shell.

The normal stress (NS) response of these nodes is recorded over the run time. This is done in global X, Y and Z - direction. Focusing on NSX and NSZ, the global and local response can be uncovered, respectively. For each stress response signal {node, NL/L}, the maximum and minimum value is obtained to calculate the maximum stress range and its mean value. Furthermore, also the variance is calculated, giving more insight in the deviation from the mean.

To compare both the linear and nonlinear case, the results for the nodes on the first node selection are first reviewed. This selection considers a vertical line on the side shell in between two web frames. Afterwards, a larger second selection of nodes on the side shell is reviewed.

Selection 1: Vertical Line on Side Shell

Figure 5.8 depicts the NSX stress range $\Delta\sigma$, mean stress σ_m and variance σ^2 for the linear (triangle) and nonlinear (circle) case for the vertical node selection at $x = 0.9$ m.

Looking at the figure, one can see the increase in stress range for increasing wave amplitude as

expected. Moving away from the neutral axis, which is around 19 cm above the waterline, the stress range increases as the outer fibre is reached. This is in line with the NSX distribution shown in figure C.2 (appendix C.2.1) where the stress response for the second node selection are shown. From figure 5.8, what stands out is that the absolute difference ($\Delta\sigma_{NL} - \Delta\sigma_L$) increases with increasing wave amplitude. This is a first indication of nonlinear loading-induced contributions to the global stress range response.

With regards to mean stress, differences between linear and nonlinear response remain small. A shift in mean stress can however be observed when increasing the wave amplitude. ζ_2 shows a small increment in mean stress with respect to ζ_1; a 'clockwise' shift. ζ_5 has a 'counter-clockwise' shift with respect to the other two wave cases; the mean stress has decreased. Upon review, this is caused by the peaks of the ζ_5 case not increasing significantly with respect to those of the ζ_2 case whereas the trough values decrease drastically. Because of this, the initial positive mean stress as observed in the milder cases reduces. In appendix C.2.2, figure C.5 shows the time traces for the three waves of the top deck node. When looking at the peaks, one can see that these seem to increase less rapidly with respect to the decrease of the troughs. In general, the maximum shift in mean stress from ζ_1 to ζ_5 is around 15 MPa; a small change relative to the stress range.

As the time traces represent the response of the top deck node, the compressive troughs occur when the ship is in sagging condition. It appears that the sagging response is amplified over increasing wave amplitude. This is in line with the results of Wang, where the overall deviation from the linear moment was greater for sagging conditions than for hogging conditions (table 2.1 and 2.2) [5]. Visualising the case, these findings also make sense. When the ship is in sagging condition, incoming waves at the bow amplify the sagging moment as the bow is pointing upward. When in hogging condition, the bow is pointing downward and the incoming waves have less effect on the hogging moment. This explains why, for the given deck node, the peaks increase less fast than the troughs decrease.

As for the variance, a similar behaviour as with the stress range is identified. This makes sense as the variance is defined as the expected squared deviation from the mean, as shown in equation 5.4 [64]. Because of this square relation, as the stress range increases linearly over the wave amplitude, the variance seems to increase nonlinearly; a second-order relation. As for this case a CA wave is applied, calculating the variance in addition to the stress range is not of great value for the overall analysis. For VA cases, the variance can provide solid additional information. For the CA case it is however used to check the second-order relation mentioned above.

$$\sigma^2 = \frac{1}{N}\sum_{i=1}^{N}(x_i - \mu)^2 \tag{5.4}$$

Figure 5.9 depicts the stress range, mean stress and variance for the NSZ component. This component is used to uncover local effects. Looking at the stress range, an increase over the wave amplitude is again observed. This time, however, the largest increase and difference between the NL/L case occurs beneath the waterline. This is caused by the direct effect of the water pressure. Above the waterline, the stress range also increases over the wave amplitude, although much less than the submerged part. For higher waves, the upper parts also submerge for certain periods of time, causing local stresses.

For the mean stress response, the nodes in the $-0.4 < z/D < -0.2$ range show a sudden positive (tension) mean stress as opposed to the surrounding nodes which predominantly have negative mean stress. Upon review, it turns out that the submerged plate is pushed inwards at increasing pressure. This happens at times right after the water column has been piling up.

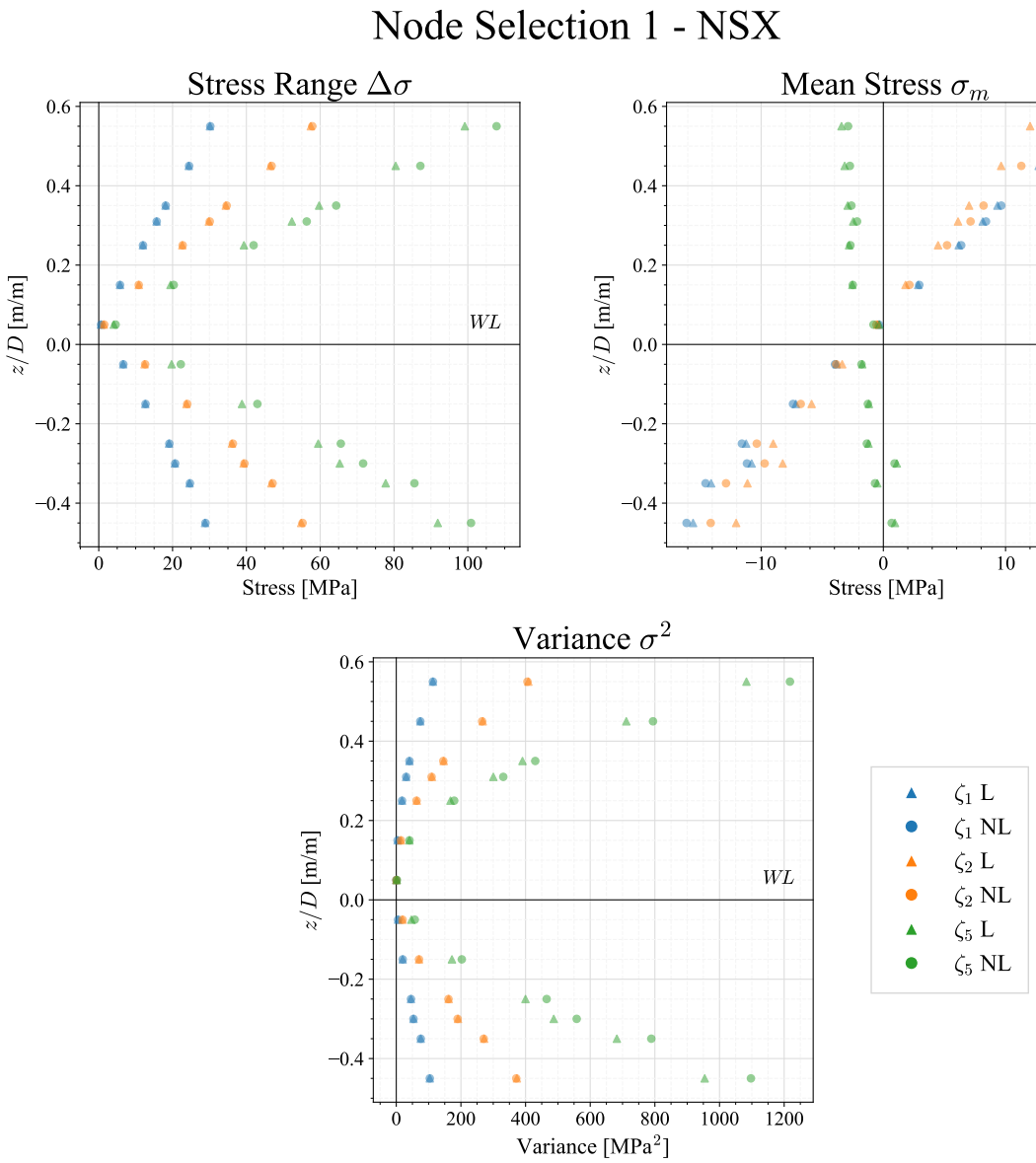

Figure 5.8: Selection 1 NL/L comparison regarding stress range, mean stress and variance for three wave cases in NSX

For this analysis, the inner fibres of the side shell plating are observed. When pressed, these fibres enter a tensional state. Figures C.3 and C.4 (appendix C.2.1) show two views of the NSZ components at two different time instances ($t = \{118.4, 120\}$ s). One can clearly see the buildup of stress in the lower region as a wave peak has passed. The rest of the vertical side shell section shows no stress concentration building up. At the intersection with the transverse frames however, larger stresses occur at the earlier time step.

Finally, the variance once again shows similar behaviour as for the stress range respone; larger values and NL/L differences for increasing wave height underneath the waterline.

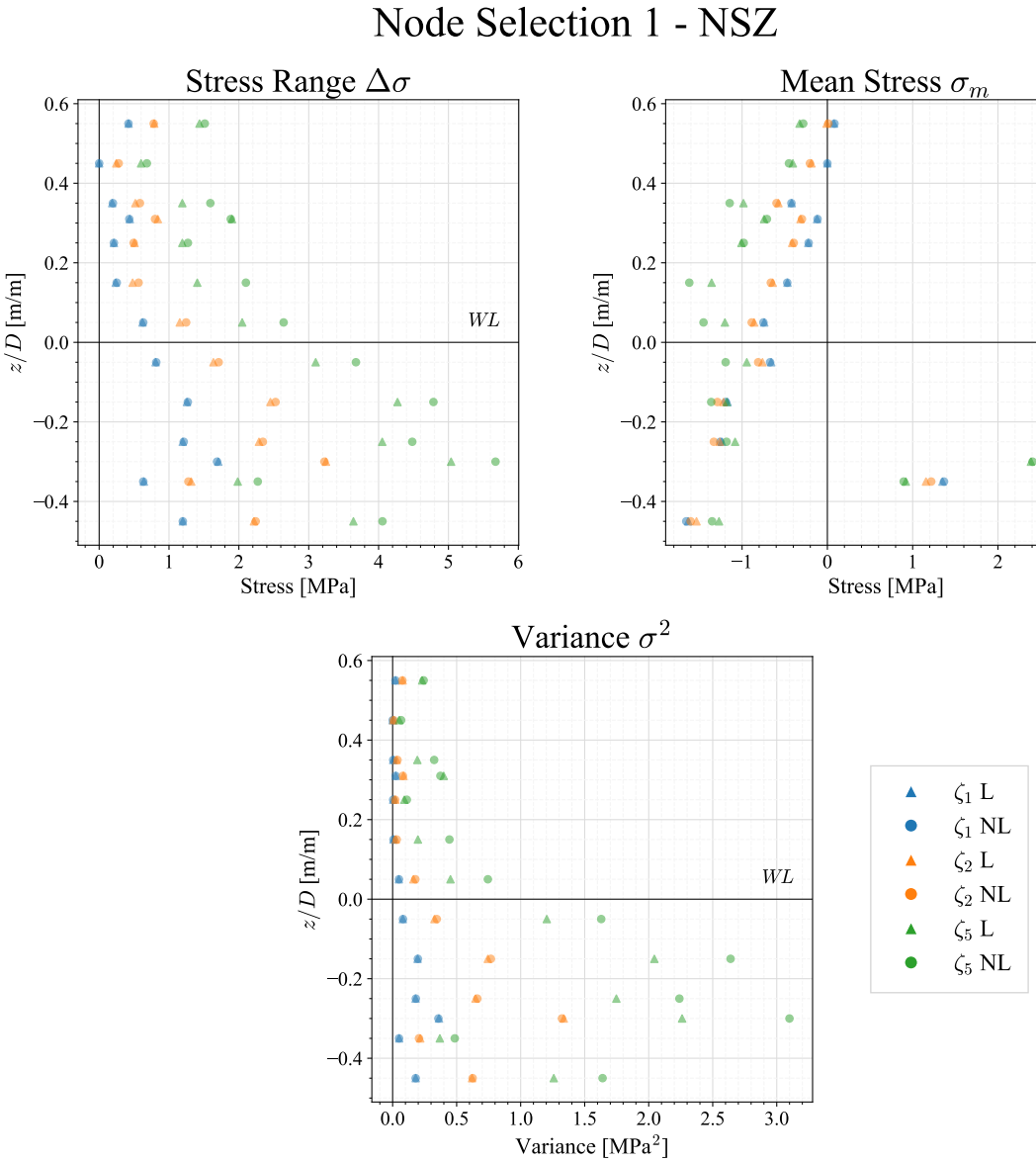

Figure 5.9: Selection 1 NL/L comparison regarding stress range, mean stress and variance for three wave cases in NSZ

Selection 2: Multiple Side Shell Nodes

Having observed the global and local stress response for nodes along a vertical line on the side shell, more nodes were added to gain additional insight. Figure 5.10 shows the selection in more detail. Nodes have been selected along the side shell, on the bottom and deck and some on the transverse frame. This is done to gain a more general insight in how different parts of the side shell behave under NL/L loading.

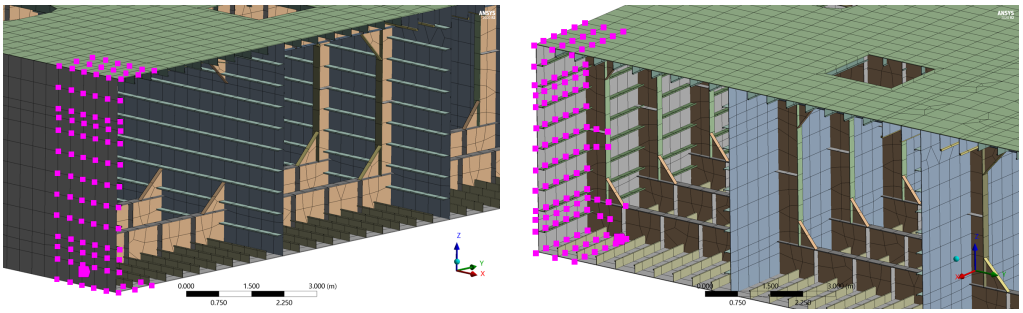

(a) (b)

Figure 5.10: Two views on the second selection of nodes (pink) at the side shell.

For the selected nodes, the same procedure as with the first selection is performed. Only now, to provide a clearer view, the difference between the NL/L case is calculated and plotted as *one data point*. This difference is expressed as an 'absolute' one for the stress range and mean stress (eq. 5.5) and as a 'relative' (percentual) one for the variance (eq. 5.6). This way, a clear increase in NL/L stress response difference is shown.

$$\Delta^{NL,L}_{\{\Delta\sigma,\sigma_m\}} = \{\Delta\sigma,\sigma_m\}_{NL} - \{\Delta\sigma,\sigma_m\}_{L} \tag{5.5}$$

$$\delta^{NL,L}_{\sigma^2} = \left(\sigma^2_{NL}/\sigma^2_{L} - 1\right) * 100\% \tag{5.6}$$

For the global NSX response, the stress range for the full node selection shows the same behaviour as the first selection. The stress range NL/L difference increases with increasing wave amplitude. For the mean stress, an increase occurs from ζ_1 to ζ_2, after which a decrease shows when moving to ζ_5. Also, the scatter increases significantly for the ζ_5 set. This is again an indication of nonlinear global mean stress response.

For both stress range and mean stress, it must be noted that the observed NL/L differences are quite small. The stress range increase for the (unrealistic) extreme case of ζ_5 is around 10 MPa at most. The mean stress shift over increasing wave amplitude is evident, but amounts to around 2 MPa for the most extreme case.

For the variance, a percentual NL/L difference increase does again show for the node selection. Some larger differences show around and beneath the waterline. Upon review, these large 'outliers' were caused by small NL variance values being divided by even smaller L values. This is the reason the range of the variance graph was set from -50 to 50%. Even then, some outliers do show, but the overall increase in NL/L variance difference still shows.

For the local stress component NSZ, the absolute differences for the stress range and mean stress are also quite small. Larger scatters are observed for the mean stress and variance. This is likely due to the influence of other structural details, like the transverse frame. A node which shares the side shell and transverse frame body in general shows a larger NSZ response because of the additional strength the frame offers. When focusing on the stress range and mean stress, the NL/L absolute differences are even smaller than for the NSX case ($\sim$4 MPa and $\sim$1 MPa at most).

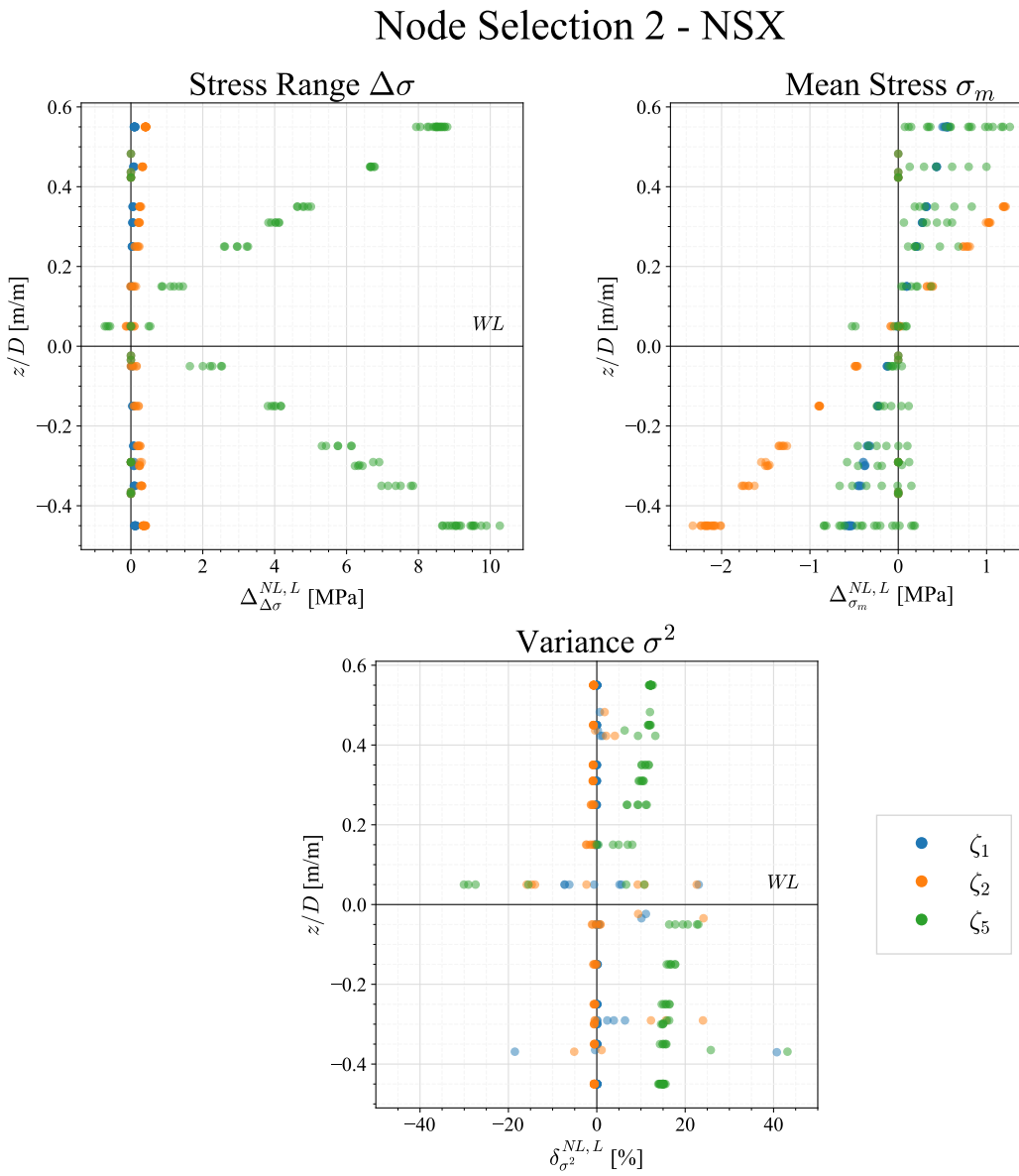

Figure 5.11: Selection 2 NL/L comparison regarding stress range, mean stress and variance for three wave cases in NSX

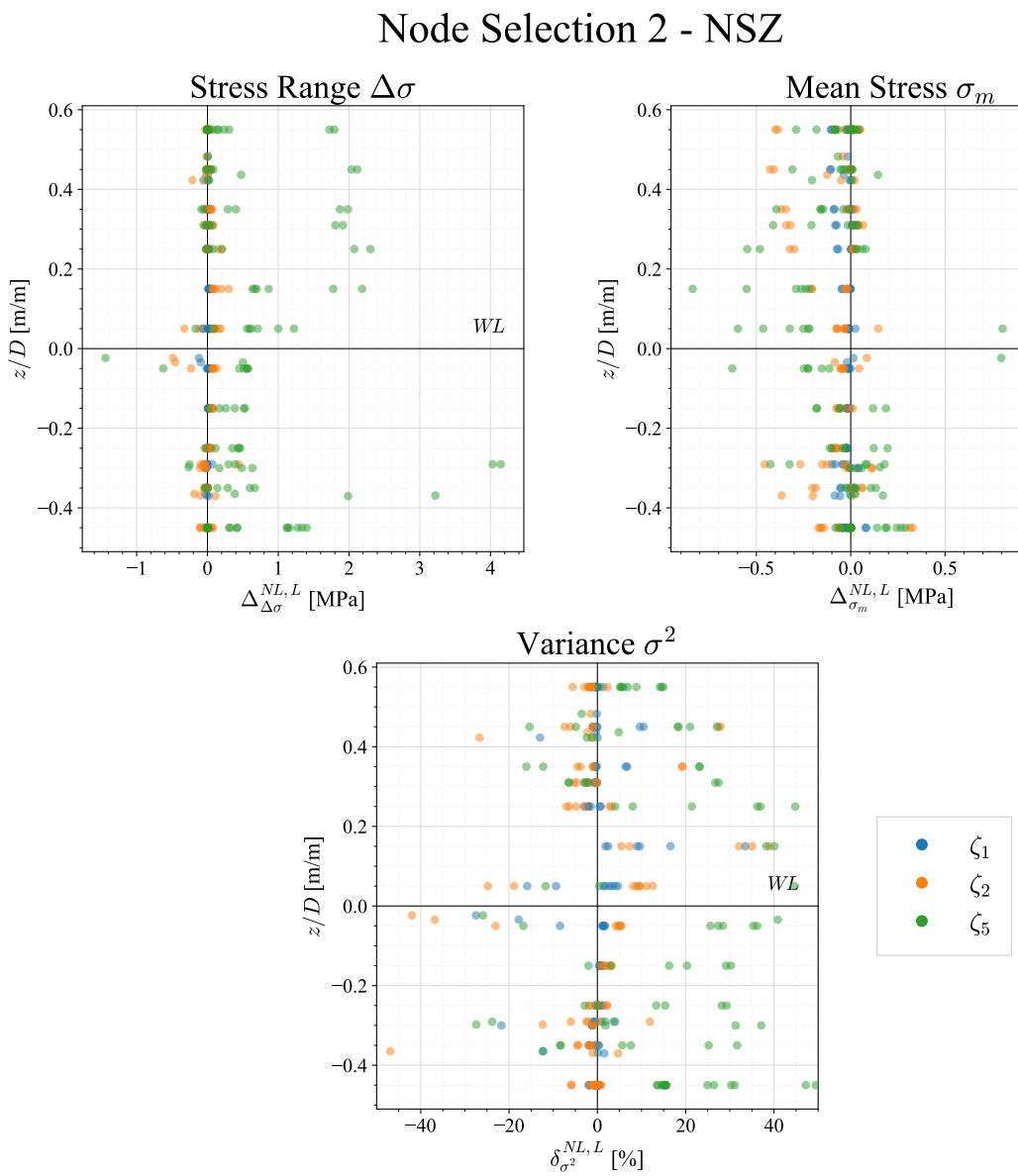

Figure 5.12: Selection 2 NL/L comparison regarding stress range, mean stress and variance for three wave cases in NSZ

5.6.4 Intermittent Wetting Effect

Having investigated the global and local effects of the constant amplitude waves at multiple locations, attention is now paid to intermittent wetting effects (section 2.4.3). As this is a local effect, the normal stress in Z-direction (NSZ) is observed for three locations around the waterline; one metre above, at the waterline and one metre below the waterline. A beam seas CA wave of $H = 3\ m, T_p = 8\ s$ is applied; perpendicular to the ship's side shell. The run time for this simulation is 30 seconds.

The resulting NSZ response is plotted for the three locations, as shown in figure 5.13. One can see that the more a node is emerged from the water, the less stress response it shows. Overall, it can be seen that the high node returns to zero for longer periods of time because it is submerged less. At the peak points, the waterline node returns to zero for shorter periods, and the submerged node does not even reach exactly zero stress.

All nodes are in a compressive state when submerged. This is attributed to the influence of the neighbouring geometry. At lower nodes, tension in normal Z-direction was noticed. This is in line with the stress contour plots in appendix C.2.1, figure C.4.

Beforehand, it was expected that the nonlinear response at the waterline would be significant. From the data presented in this section (5.6.3), it has become clear that local effects are minimal in comparison to the global (NSX) effects. The intermittent wetting effect does show for the assessed case, but not in such an expressed way as literature showed (section 2.4.3) [4]. This is attributed to the effect of neighbouring geometry, softening the effect of being emerged/submerged. Furthermore, the mesh at the waterline is quite coarse (~0.5 by 0.5 m). Nodes on the side shell are only placed on locations where longitudinal stiffeners are attached. This removes the capability of observing local bending effects in between side shell stiffeners. A refinement would be required to observe more detailed intermittent wetting effects.

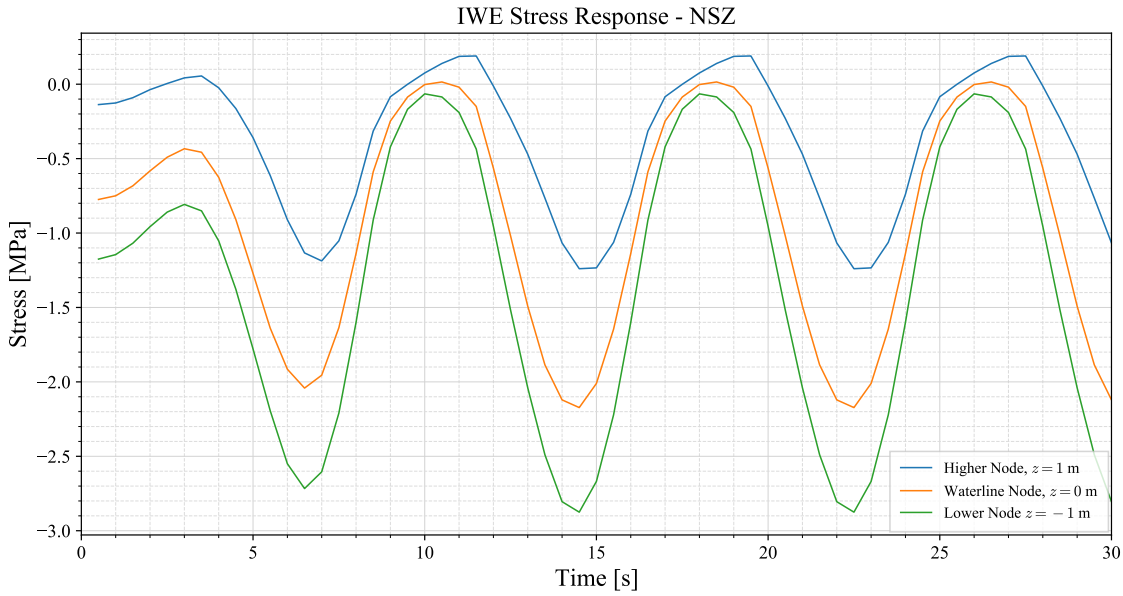

Figure 5.13: Stress response in normal Z-direction for an initially emerged, waterline and initially submerged node ($H = 3\ m, T_p = 8\ s, \theta = 90°$).

5.6.5 Concluding Remarks (SQ1b & SQ1c)

This section started by determining the critical load case, after which the location of the critical response was investigated. These two investigations covered sub-questions **SQ1a** and **SQ1b**.

Sub-question 1b

Which load case is most relevant to capture critical NLFK force effects?

With the determination of the critical load case, the answer to sub-question **SQ1b** is as follows:

> For the pontoon vessel, a head seas condition ($\theta = 180°$) with a period of $T_p \approx 8.1s$ yields the largest longitudinal bending moment (RY) response which is considered to be most critical to fatigue damage.

~

Performing NL/L CA loading and response simulations for a two-minute time frame has revealed that globally, the largest NL/L differences are induced at the outer fibres. At these locations, for the extreme, unrealistic, case of a wave amplitude of 5 metres (ζ_5), the largest NL/L difference amounted to 10 MPa; a negligible value. As for the mean stress, a shift was observed over increasing wave amplitude. Because the peak values of the response signal increased slower than the trough values, the mean stress first increased after which it decreased when increasing the wave amplitude.

The variance was calculated to confirm similarity with the stress range plots. This was true as the variance also showed a second-order course over the height of the side shell.

For a larger selection of nodes, the same behaviour as for the first selection was observed for the global stress response NSX. For the local stress response NSZ, larger scatter occurred which is attributed to the influence of the transverse frames.

It has become evident that, with the modelled NL/L cases, differences in stress response are minimal. Even for extreme wave cases, relatively small differences were observed. Reflecting on section 5.5.1, this small difference is attributed to the way the linear and nonlinear waves are modelled. Bounded by the capabilities of *Ansys AQWA*, the only way to influence the calculation of the Froude-Krylov force was through manipulating the applied wave theory. With the shown results, it has turned out that the differences in response due to these two ways of modelling are quite negligible.

Concluding, the observations have provided new insight in NL effects on structural response. The accurate modelling of the LFK force was not entirely possible due to software restrictions. Instead, linear and nonlinear wave theory was applied to alter the FK force. Small differences were observed. Still, increasing relative difference between NL/L were observed at certain locations, leading to an answer to sub-question **SQ1b**.

Sub-question 1c

Which locations in the ship structure show the largest response due to NLFK effects?

The goal of the constant amplitude test cases was to determine structural locations sensitive to NL loading. The global NSX response turned out to be governing over the local NSZ and intermittent wetting response. Investigating the NL/L response difference over the height of the midship side shell section has led to the following answer of **SQ1c**:

> When considering the global loading component NSX which is found to be most critical to fatigue damage, the top deck and bottom nodes (outer fibres) at midship show the largest NL/L response difference for the critical load case.

5.7 Variable Amplitude Loading & Response

Following the constant amplitude (CA) case study, this section showcases the variable amplitude (VA) analysis. Reflecting on table 5.3, the linear (L) data set is provided by the established spectral model of Damen Naval [1]. In this section, the nonlinear data set is constructed by performing VA time domain simulations for the critical load case of the ship. Although the previous section established that NL/L differences were small in the CA case, the difference in NL/L input for the VA study can provide new insights.

This section will explain the methodology used to obtain stress time traces from a VA load case. Since statistical content is applied in the model in the form of wave elevation, it is of great importance to ensure convergence with respect to the simulation length. The next sections will showcase how convergence is reached for the generated time traces. The main tool to check convergence is the fast fourier transform (FFT), of which the applied methodology will be explained first. Afterwards, the convergence of the wave elevation and stress response is demonstrated. Finally, the methodology regarding mean stress correction is shown and verified. Section 5.8 will discuss the results of the VA analysis compared to the results of the spectral model of Luna García-Valenzuela [1].

5.7.1 Fourier Transforms

A wave elevation time signal can be transformed into a spectrum by means of the *fast Fourier transform* (FFT). As discussed in section 2.1, an irregular (VA) wave field can be represented by a large sum of regular (CA) wave components. By performing a Fourier transform, these components are gathered in a Power Spectral Density graph (PSD).

As discussed briefly in section 3.2.3, the hybrid method can be used to shift from spectral to temporal fatigue analysis. This is done by using the *inverse fast Fourier transform* (IFFT). Bufalari performed time domain analyses and used both FFT and IFFT [59]. Equation 5.7 shows the way a wave can be built up using a given wave spectrum $S(\omega)$.

$$h(t) = \lim_{n\to\infty} \lim_{\delta\omega\to 0} \sum_{i=1}^{n} \sqrt{2S\left(\omega_i\right)\delta\omega}\cos\left(-\omega_i t + \theta_i\right) \tag{5.7}$$

In the numerical realm, the continuous equation 5.7 becomes discrete. The code for both FFT and IFFT operations has been provided for this thesis [59]. *Python*-coded FFT and IFFT functions are defined as shown in equation 5.8 and 5.9, respectively [65]. Here, $y[k]$ marks the fourier-transformed array of $x[n]$. Using these functions, some more operations are required to obtain the spectrum from the time trace and vice versa.

$$y[k] = \sum_{n=0}^{N-1} e^{-2\pi j \frac{kn}{N}} x[n], \quad \text{(FFT)} \tag{5.8}$$

$$x[n] = \frac{1}{N} \sum_{k=0}^{N-1} e^{2\pi j \frac{kn}{N}} y[k], \quad \text{(IFFT)} \tag{5.9}$$

Spectral Leakage and Hamming Variable

When performing FFT, the time trace data must be pre-processed first. The main reason for this is spectral leakage [66]. Spectral leakage occurs when an 'unfinished' wave is passed to the FFT; a wave which has a non-integer period. The FFT then tends to overestimate the amount of frequencies present in the signal. For instance, a CA wave might be represented by way more frequency components than the one that is actually there. This phenomenon is

caused by the FFT assuming that the input signal is 'complete'; it covers an integer amount of periods. When the signal has a non-integer amount of periods, something which is almost inherent to a VA signal, it must be verified that the signal is cut on the right timing. Because VA signals are considered, this is a hard task. Windowing functions offer a solution in this case.

The windowing function used in this model is that of Hamming [67]. Equation 5.10 shows the formulation for this windowing function. Here, n is the Hamming variable which is to lie within 0 and $M-1$, with M being the amount of data points of the considered signal.

In the end the Hamming function smoothens the spectrum signal obtained from the time trace [68]. It needs to be chosen wisely, lower values tend to give a more rough signal. The Hamming function (eq. 5.10) provides a so-called 'apodization'; a smoothing at the foot. Discontinuities at the lower and higher values of the spectrum are smoothed.

$$w(n) = 0.54 - 0.46\cos\left(\frac{2\pi n}{M-1}\right), \quad 0 \leq n \leq M-1 \tag{5.10}$$

Figure 5.14 shows the influence the Hamming variable has on the realisation of the spectrum of a wave elevation signal of 3 hours. Despite the smoothing, at the tails, distortions can be observed. These small peaks have been identified as numerical errors and do not represent any real wave elevation content. When increasing Ham, the distortions decrease. However, the peak also decreases, providing an overall worse fit to the original loading spectrum. Additional smoothing was applied at the tails to provide a good overall fit of the spectrum.

The used code is displayed in appendix C.3.1, showing the FFT and IFFT code. The Hamming variable n was set to 200 to provide a good fit without too much tail distortion.

Using the Fourier transform, a time signal can effectively be converted into a spectrum. This way, multiple time traces could for instance be compared based on their statistical properties. In the current work, the temporal results (NL) will be converted into spectra in order to compare them to the spectral results (L).

5.7.2 Simulation Time Convergence

When performing a variable amplitude (VA) loading and response analysis, a realisation of a wave spectrum is applied in the time domain. The duration of this realisation is indicated by the simulation time. As stated by Mohammadi, the simulation time should be sufficiently long as to accommodate all statistical contents of the applied spectrum [7]. Should a realisation be too short, then the resulting response spectra are not representing the entire process. As discussed in section 2.2, Mohammadi assumes a narrow-banded wave spectrum, which ensures a repetition of the wave field within a specific time frame.

For the current temporal model, the response is expected to be wide-banded due to the inclusion of nonlinear loading. Repetition of the statistical content is therefore at stake. It is therefore of interest to investigate how long the simulation time should be. When realising multiple runs with the right simulation time, the produced response spectra should be the same.

The simulation time adopted by Mohammadi is 3 hours, as recommended by ABS [7, 69]. To test the impact the simulation time has on a spectrum, this section will investigate the difference between *theoretical* and *measured* wave elevation spectra. When these two spectra are aligned, it is assumed that the stress response spectrum is also converged. With regards to data storage capacity, multiple runs of shorter simulation time can be carried out and pasted together. For the case of a semi-submersible wind turbine, Kvittem found that simulations of 1 hour captured sufficient fatigue effects [28].

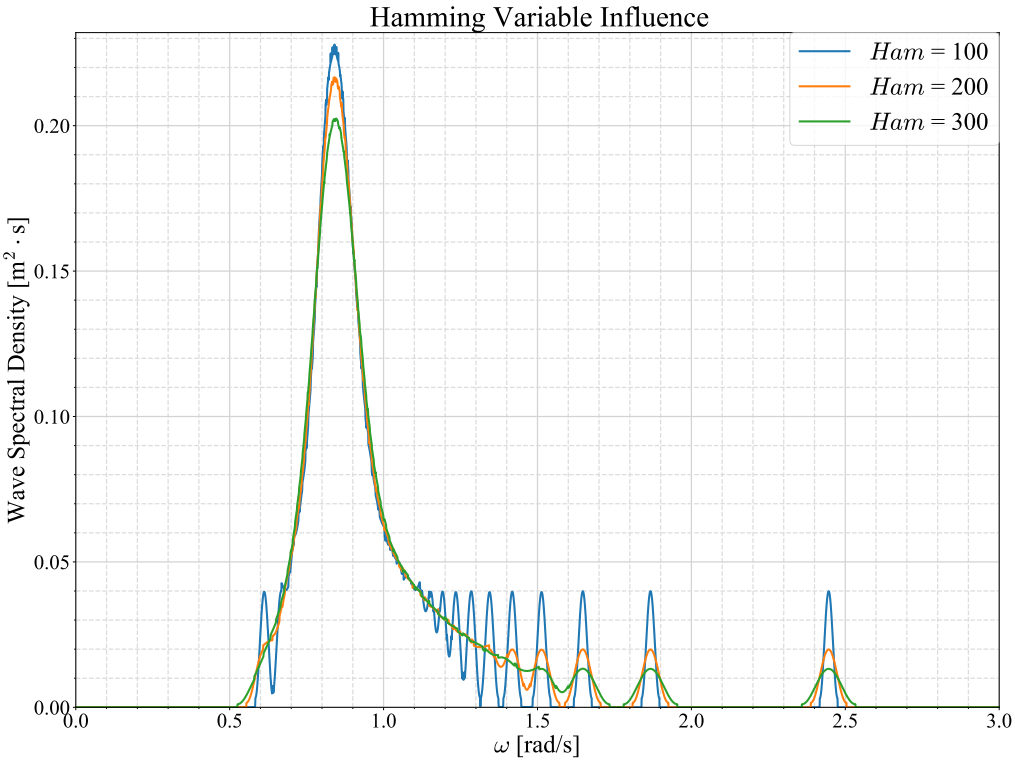

Figure 5.14: Influence of Hamming variable on resulting spectrum.

As the adopted 3/1-hour durations of Mohammadi and Kvittem are quite different, a simulation time convergence study is carried out in this section.

Wave Elevation Convergence

A first step in uncovering simulation time convergence is by reviewing the statistical content of the wave elevation and comparing it to the theoretical wave spectrum which is applied. From the original JONSWAP spectrum, a wave realisation of 3 hours is made. From the resulting time trace, portions of 10 minutes are taken: $T_{sim} = \{10, 20, ...180\}$ min. The wave elevation is measured at $\{X, Y\} = \{0, -11\}$ m, at starboard midship. The time traces of this wave elevation are converted back into spectra. The resulting comparison is made in figure 5.15. One can clearly see that, for increasing T_{sim}, a better fit with the original wave elevation spectrum is attained. For T_{sim} = 3 h, the reproduced spectrum has almost reached the original spectrum's peak.

Judging from this simulation time review, a 3-hour simulation provides a good fit to the original spectrum.

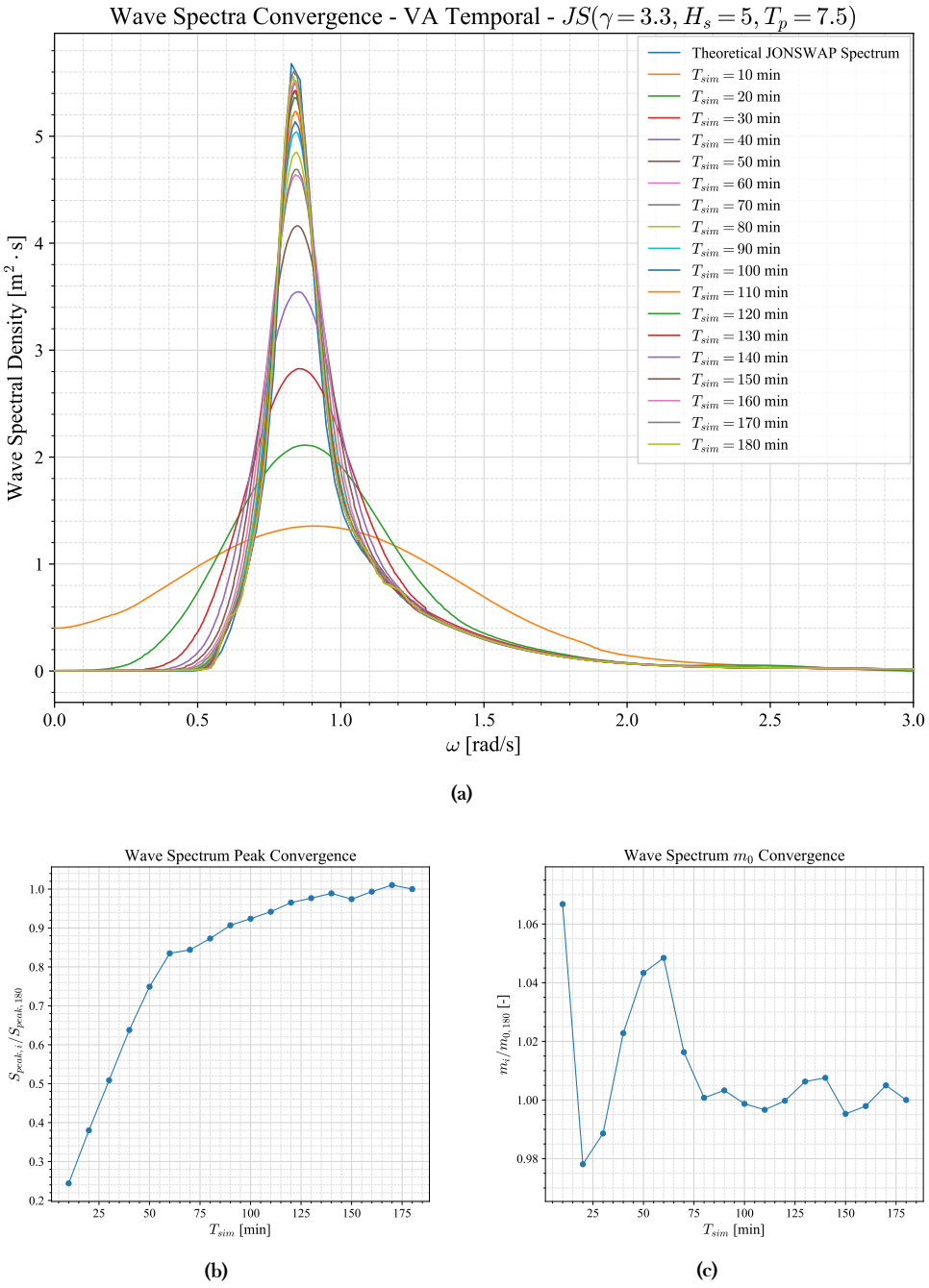

Figure 5.15: Wave elevation spectra convergence over increasing T_{sim}.

Joining Stress Time Traces

Because of the model's capacity restrictions induced by the available hardware (section 5.2.1), 10.5-minute runs are carried out separately and the resulting traces are joined in the post-processing part. For each stress time trace, the initiation period of 30 seconds is removed in order to obtain the pure response in a developed sea.

The remaining 10-minute time traces are joined using a smoothing approach. In this approach, the first time trace is cut at the final mean crossing. The next time trace is then cut at its first mean crossing with the same signal direction (ascending/descending). This way, it is ensured that all stress time traces are smoothly joined and no coarse frequency content is introduced. This approach is in line with the time domain simulations performed by Tuitman [27]. It should be noted that, due to the cutting of the runs, some data is lost. On the 3-hour

data set, this was around 1.4 minutes; a minor loss.

Stress Response Convergence

The wave elevation convergence study indicates that after two hours, the wave spectrum starts to converge. Only the spectrum peak value increases slightly when T_{sim} is increased to 3 hours. For the stress response spectra, obtained from the stress time traces, a similar convergence study is carried out. For the wave case of JS ($H_s = 5$ m, $T_p = 7.5$ s, $\gamma = 3.3$), a total of 3 hours of simulation time is obtained. This is with removed initiation periods (30 seconds).

Figure 5.16a depicts the stress spectra obtained from 10 to 180 minutes for the raw VA stress signal. The first thing that stands out is the high peak close to ω=0 rad/s. Because the raw signal is passed into the FFT, the global mean value of the signal is represented in the spectrum as a frequency component approaching zero.
Figures 5.16b and 5.16c indicate the values of the peaks and variance m_0 for increasing T_{sim}, respectively. For the peak value, this increases linearly over increasing simulation time. This is because the peak corresponding to the mean stress component keeps increasing. This increase is expected to be caused by the mean component having a zero-value for its amplitude, something which the FFT model can't handle computationally-wise (section 5.7.1). The result is a linearly increasing zero-frequency peak.

For the variance m_0 (figure 5.16c), large fluctuations occur in the lower T_{sim} regions due to the increasing kurtosis (steepness) of the spectrum. After 70 minutes, the $m_{0,i}/m_{0,180}$ value shows a clear decrease towards 1.00. Differences are well below 2% after 80 minutes and the spectrum variance is converged at 180 minutes.

Because of the singular behaviour for the raw data spectrum, the same convergence study is carried out for the signal with removed global mean. Figure 5.17 shows the convergence graphs for this case. The peaks in figure 5.17a are converging to the same value ($\sim$1050 MPa^2/s) as for the raw data. Looking at the convergence of these peaks in more detail, figure 5.17b shows a gradual course at which the peak values fall within 5% of the final value after 140 minutes. For the variance (figure 5.17c), a faster convergence is observed as results are within 5% after 70 minutes. Differences are well within 2% at the final steps of T_{sim}. It can therefore be concluded that the removed mean stress response has converged with a sufficiently long simulation time of 3 hours.

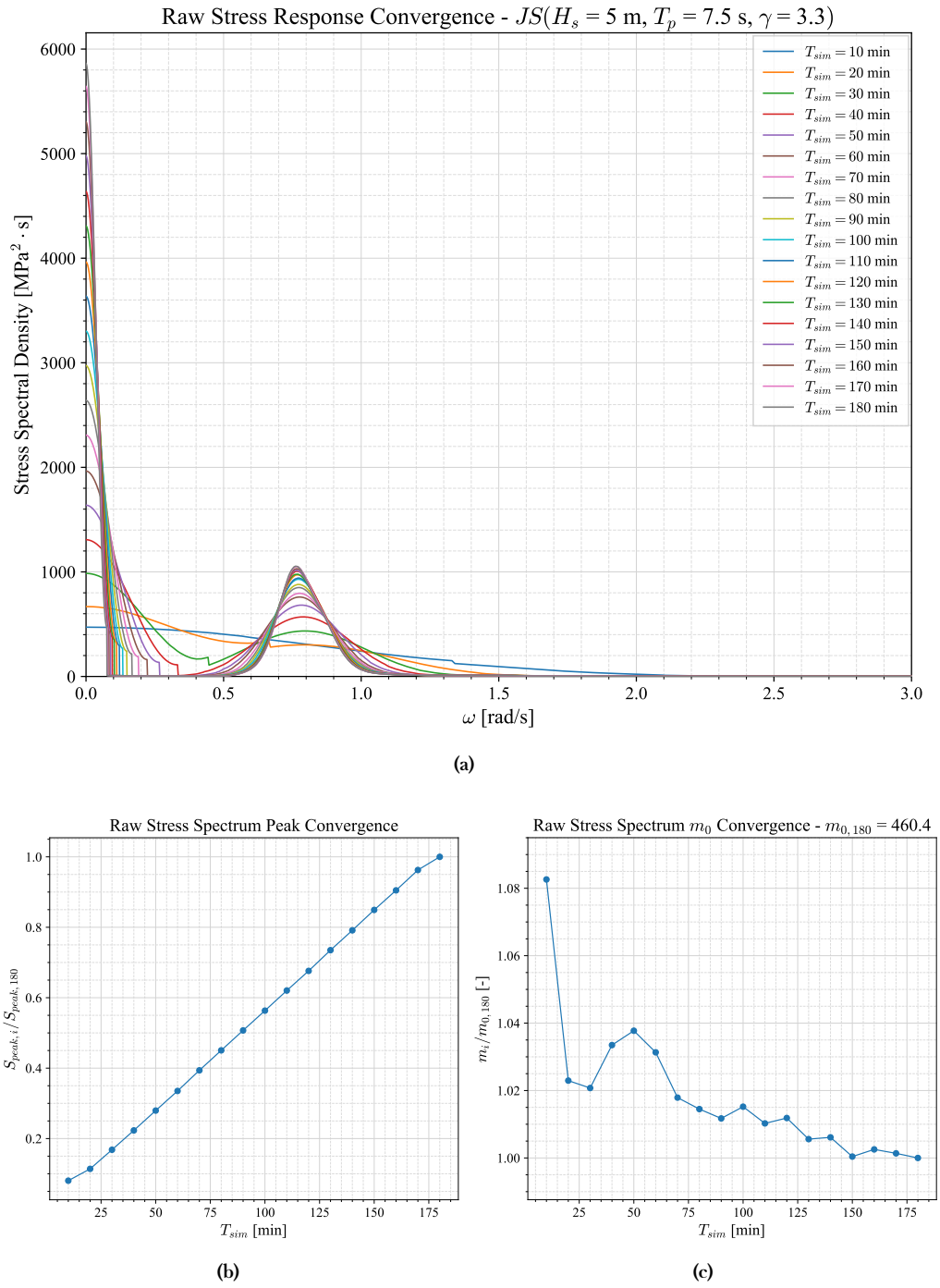

Figure 5.16: Raw stress response spectra convergence over increasing T_{sim}.

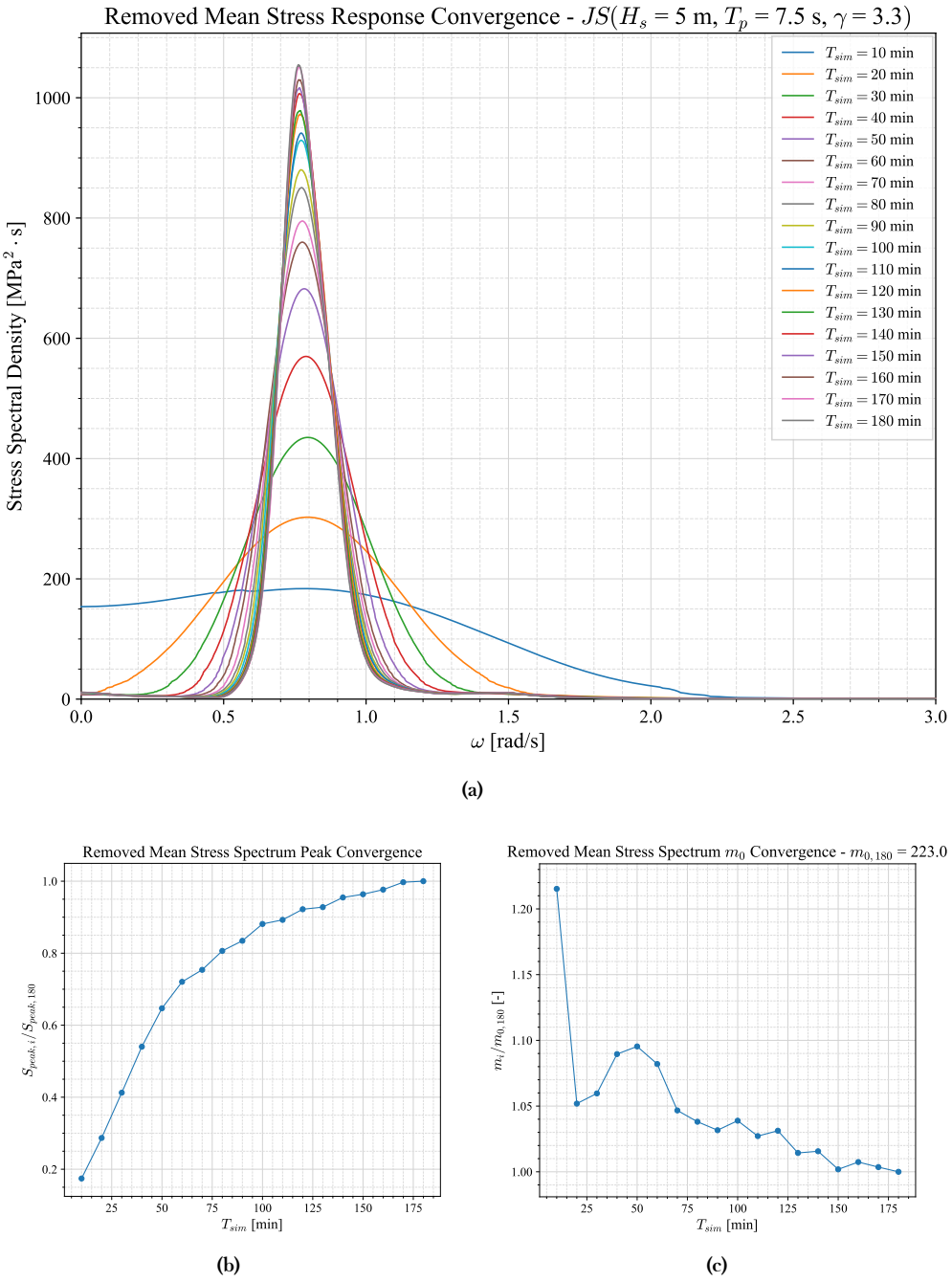

Figure 5.17: Removed mean stress response spectra convergence over increasing T_{sim}.

5.7.3 Rainflow Counting

Having ensured convergence for the generated time traces, these data are transferred to the post-processing model. This model is formulated in a *Python* code in which, among others, rainflow counting and a mean stress effect correction is carried out.

With regards to rainflow counting, the algorithm formulated in *Standard Practices for Cycle Counting in Fatigue Analysis* [70] has been used. The algorithm is provided within the 'Rainflow' environment available in *Python*. In addition, Niesłony and Böhm utilised the same practice for their rainflow model [71]. From the rainflow counting algorithm, every counted cycle has a corresponding range $\Delta\sigma$, mean σ_m, starting point and end point.

5.7.4 Mean Stress Effect

From a generated stress time trace, a global mean stress $\sigma_{m,global}$ can be obtained by simply taking the mean value of the entire time trace. In later sections, different mean stress contributions are evaluated. An important one is the still water bending moment (SWBM).

Loading and Response Ratio

In section 3.2, equation 3.4 provided the formulation for the loading and response ratio r_{lr}. This formulation is rewritten in equation 5.11. With the range and mean stress of every cycle, $r_{lr,i}$ can be determined.

$$r_{lr} = \frac{\sigma_{min}}{\sigma_{max}} = \frac{\sigma_m - \Delta\sigma/2}{\sigma_m + \Delta\sigma/2} \tag{5.11}$$

Walker Correction

With r_{lr} calculated for every cycle, the Walker correction can be applied using equation 5.12 discussed in section 3.2. For steel, the mean stress material sensitivity factor γ is typically kept at 0.7 [8]. Qin showed that, for the generalised random fatigue limit (GRFL) model, this factor yields the best fit to the large welded joints fatigue test data set when set to 0.92 [3]. This indicates that the stress range contributes around 90% to the effective stress value whereas ∼10% is contributed by the mean stress, which covers the welding-induced residual stress as well as the mechanical loading and response component. Along with this adoption, fully compressive cycles are given an r_{lr} value of -3 in order to avoid r_{lr} values higher than 1 and imaginary values from equation 5.11.

$$\Delta\sigma_{eff} = \Delta\sigma^{\gamma}\sigma_{max}^{(1-\gamma)} = \frac{\Delta\sigma}{(1-r_{lr})^{1-\gamma}}, \quad \gamma \in [0.3, 0.8] \tag{5.12}$$

Using this equation, and the modifications regarding (fully) compressive cycles, the course of the loading and response ratio is displayed in figure 5.18. One can see that before $\sigma_m/\Delta\sigma = 0.25$, r_{lr} is kept at -3, emulating the minus-infinity condition of r_{lr} that applies to compressive cases. At $\sigma_m/\Delta\sigma = 0$, the mean stress is zero and thus the cycle is fully reversed; r_{lr}=-1. At r_{lr}=0.5, r_{lr}=0, indicating the case where σ_{min} is exactly zero. For increasing positive values of $\sigma_m/\Delta\sigma$, r_{lr} approaches 1 asymptotically. Values higher or equal than 1 are not possible because that would mean that $\sigma_{min} = \sigma_{max}$, causing a division by zero in the Walker equation (eq. 5.12). Values higher than 1, which indicate fully compressive cases, would cause imaginary results in the Walker equation. To avoid this, cases of $r_{lr} > 1$ are given a value of -3.

Fatigue Damage

In the literature review, section 3.1.1 discussed the application of SN-curves to determine the damage of a certain stress time trace. The approach for this model is done the same way while having included the mean stress effect in the former step.

For every cycle n_i at a particular stress range level, the corresponding number of cycles to fatigue failure N_i is calculated using the SN-curve formulation (eq. 3.1). A general SN-curve of $\log(C) = 12$ and $m = 3$ is used for this model. The stress ranges have been corrected for their respective mean stress to the fully reversed ($r_{lr} = -1$) case of the SN-curve. The total damage of the time trace can then be calculated using linear damage accumulation (eq. 3.2).

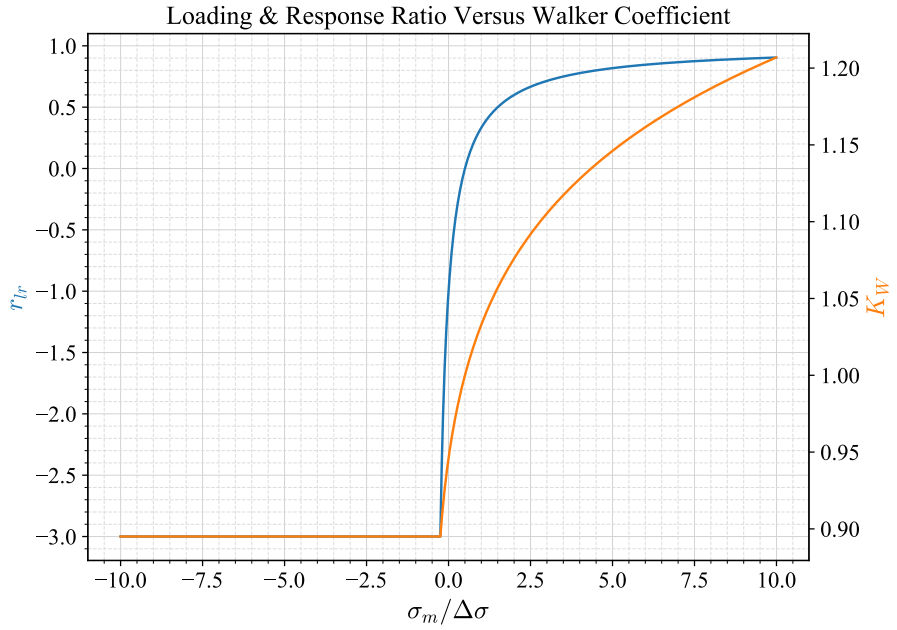

Figure 5.18: r_{lr} and Walker coefficient K_W ($\gamma = 0.92$) (eq. 3.21) over $\sigma_m/\Delta\sigma$.

5.8 Temporal versus Spectral Loading & Response

With the set goal for the simulation time, VA simulations have been carried out in the hydrodynamic and structural model discussed in this chapter. This is done for the case of $\{H_s, T_p, \theta, V_s\} = \{5\ m, 7.5\ s, 180°,\ 3\ kn\}$. The peak period differs slightly from the period applied in the CA analysis. This is because from the spectral results, data on only certain peak periods is available. The period of 7.5 s comes closest to the ship's peak period of 8.1 s and is close to the case where the wavelength equals the ship length ($\lambda = L_s$); a critical case as well [1].

The results shown in this section belong to a top-deck node (figure 5.19). This node was chosen because of the top deck being largely NL/L sensitive, as was shown in the CA study of section 5.6). In the next chapter, analyses for nodes at different heights will be carried out as well.

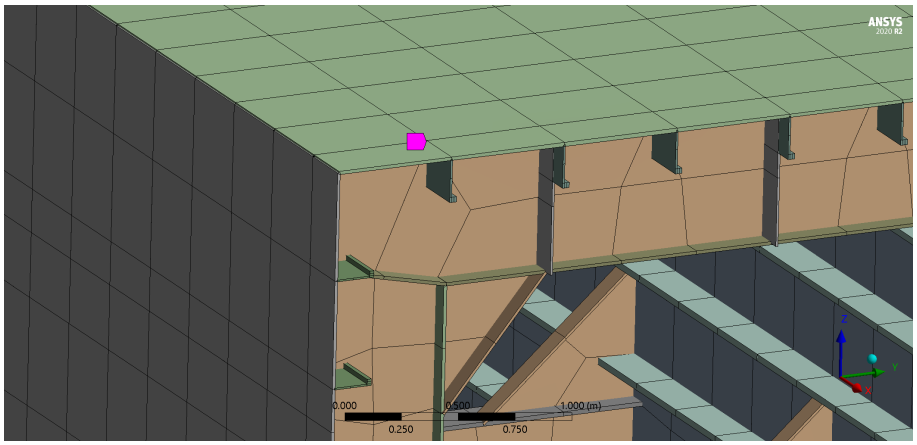

Figure 5.19: Top deck node at midship used for analysis.

5.8.1 Spectral Approach Data Set

The model of Luna García-Valenzuela has provided the stress response spectra data [1]. The pressure distribution of a wave with frequency ω_i and wave height H = 1 m is applied to the ship with one of its peaks at midship. For this static case, the stress response of every node is saved. This procedure is then iterated for increasing frequencies. The stress response RAO $H_\sigma(\omega)$ is then formed by plotting the response at every wave frequency.

Figure 5.20 shows the spectral RAO for the selected node and load case. One can see the peak at which stress response is the highest. At higher frequencies (>1.2 rad/s), other peaks can be observed. When visualising that at every frequency a regular wave is applied statically, this wave will decrease in wavelength over increasing frequency (eq. 2.10). At around 1.25, 1.475 and 1.7 rad/s, wavelengths are met that the buoyant force creates a higher hogging moment than the waves with frequencies close to them. Overall, these peaks are quite small when comparing them to the large peak at around $\omega = 0.85$ rad/s.

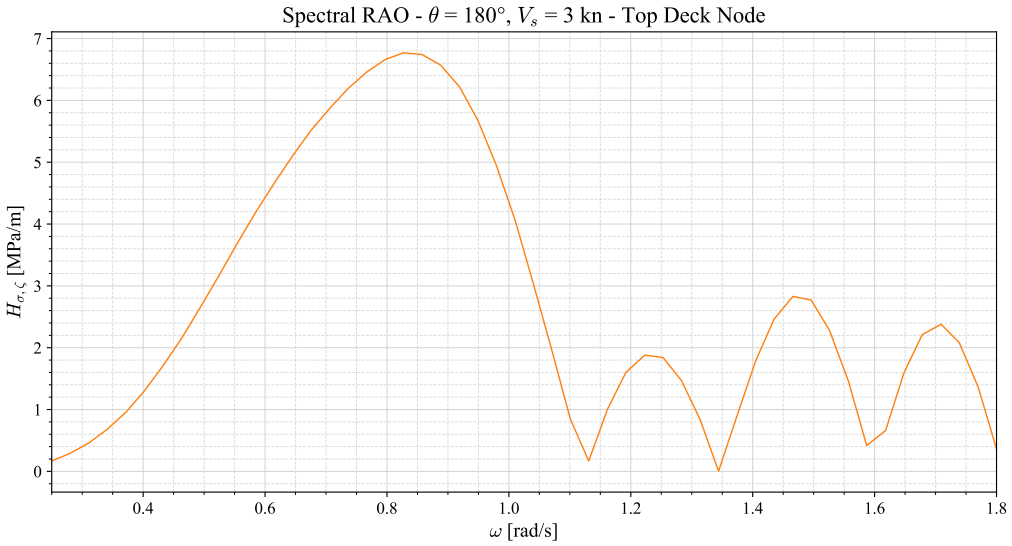

Figure 5.20: Spectral NSX RAO example for top deck node, head seas waves with V_s=3 kn.

5.8.2 Pseudo-time Domain Approach

Because the main focus of this research is on nonlinear-induced effects caused by shifting to the time domain, a pseudo-time approach was performed in order to provide an intermediate step to show gradual changes when shifting from the frequency domain to the time domain. In this approach, complexity is added by simulating in the time domain, but the same approach as the spectral method is maintained. In more detail, waves of increasing frequency are once again added one by one, but now for a time period of 30 seconds. After it was made sure that the response is stationary over time, the amplitude of the signal is taken as data point for the pseudo-time RAO. Repeating this for every assessed wave frequency provides the RAO data points.

As was shown in section 5.6, the nonlinear response increases as the wave height increases. To emphasise this phenomenon, the pseudo-time approach is performed for waves of 1 and 5 metres wave height. For 22 frequencies, the H1 case is carried out. For the H5 case, frequencies above 1.5 rad/s were not able to be calculated as the waves became too steep. The peak frequency was however contained well within the available frequency range.

Figure 5.21 shows the comparison of the two pseudo-time RAO's and the spectral RAO. Overall, the RAO's are close to each other. The maximum difference occurs between the $H1$ and $H5$ case; around 1 MPa/m. For $H1$, the peak response is higher than the spectral approach, whereas the $H5$ case lies close to it. It therefore appears that, over increasing wave height, the *relative* response becomes lower. It is expected that this is due to the increase in nonlinear hydrodynamic effects (section 2.4, equation 2.27). For a clearer picture, additional wave cases within the $H1$ and $H5$ range and higher than $H5$ should be simulated.

In general, it was expected that the $H1$ case would lie closer to the spectral RAO. Right now, the $H5$ RAO lies the closest to it. It is expected that due to the coarse frequency steps, the $H1$ RAO is not as detailed as it should be. Because it is amplified by $H_s = 5^2$, errors get amplified by this factor. This results in the $H1$ being higher than the spectral and $H5$ RAO's, while it was expected that they would lie closer together.

Compared to the spectral RAO, both pseudo-time RAO's are wider, indicating additional frequency content especially at higher frequencies ($\omega = 1.00$ to 1.25 rad/s). This wide-band effect is attributed to nonlinear behaviour in the hydrodynamic loading because of the shift from spectral to time domain. This is in line with the literature findings of section 2.5.3.

It can be concluded that introducing the time domain component by applying the pseudo-time approach has indicated that small differences occur in the resulting RAO's. These differences occur because of introduced nonlinear hydrodynamic behaviour, but they are relatively small. Overall, it can be said that the RAO's are well in line with each other, given the coarseness of frequency steps on which they are based. This coarseness is an important point of criticism. Although the RAO's give a good insight in the relation between the pseudo-time and spectral approach, additional frequencies should be added to gain a more detailed and accurate view.

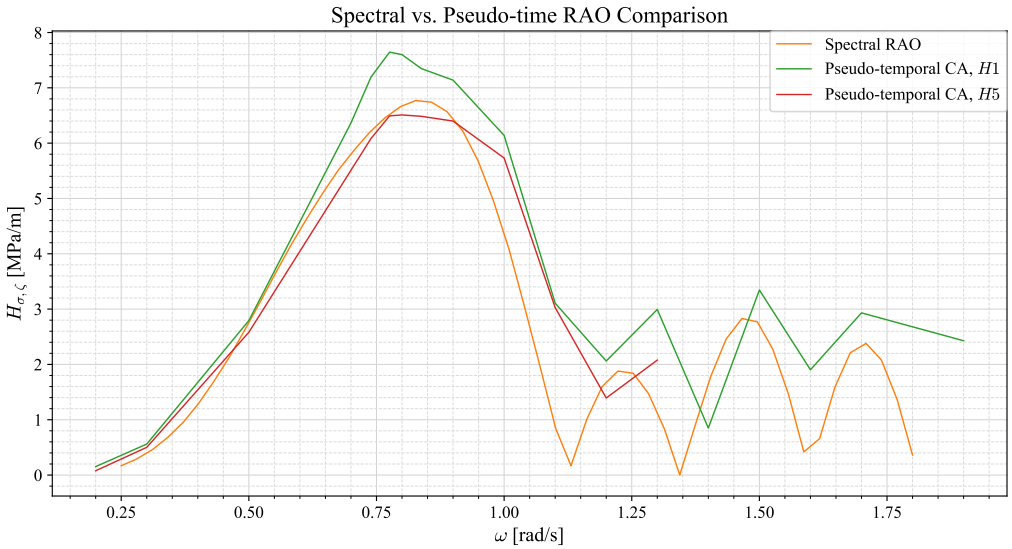

Figure 5.21: Spectral versus pseudo-time NSX RAO comparison for top deck node and head seas waves at V_s=3 kn.

5.8.3 Stress Response Comparison

The next step of introducing detail in the model is shifting from the pseudo-time (CA) to the full temporal model (VA). The model described in section 5.7 was performed for the load case of $\{H_s, T_p, \theta, V_s\} = \{5\text{ m}, 7.5\text{ s}, 180°,\ 3\text{ kn}\}$, resulting in a data set for the nodes of selection 2 (section 5.6.3) for a total of 3 hours.

The full 3-hour stress time trace with smoothly joined 10-minute runs and removed global mean is shown in figure 5.22. Looking at the data, large peaks of around 40 MPa occasionally do occur. Furthermore, peaks of around 20 and 30 MPa occur more frequently. Smaller peaks, while harder to observe, are also present.

For the final comparison, the stress time trace is converted into a spectrum using the FFT methodology of section 5.7.1.

For the pseudo-time and spectral RAO's, equation 5.13 is applied. As the main assumption is that stress response scales linearly with wave height, squaring the RAO and multiplying by a sea state of choice provides the stress response spectrum $S_\sigma(\omega)$, as discussed in more detail in section 2.2.

$$S_\sigma(\omega) = |H_\sigma(\omega)|^2 \cdot S_\zeta(\omega) \tag{5.13}$$

Figure 5.23 displays the comparison of the temporal VA, the spectral and both pseudo-time stress response spectra. One thing that immediately stands out is the substantial difference between the VA temporal and the other spectra. Not only the total amount of energy (m_0) is much higher (~4 times) for the temporal VA spectrum, the peak frequency also differs slightly; around 0.75 rad/s for the VA spectrum and 0.85 rad/s for the other spectra. This indicates a slight difference in stress peak response occurring when shifting from static and pseudo-time CA simulations to a full VA case. The spectra of pseudo-time and frequency domain approach are actually in line. It would however benefit the analysis if they were less coarse. For the spectral result, data is missing around 0.85 rad/s, which is around the peak frequency. A refinement in frequencies that are assessed is therefore required.

For both the temporal and spectral approach, the applied methodologies were thoroughly checked. The convergence studies of the wave elevation and stress response have already in-

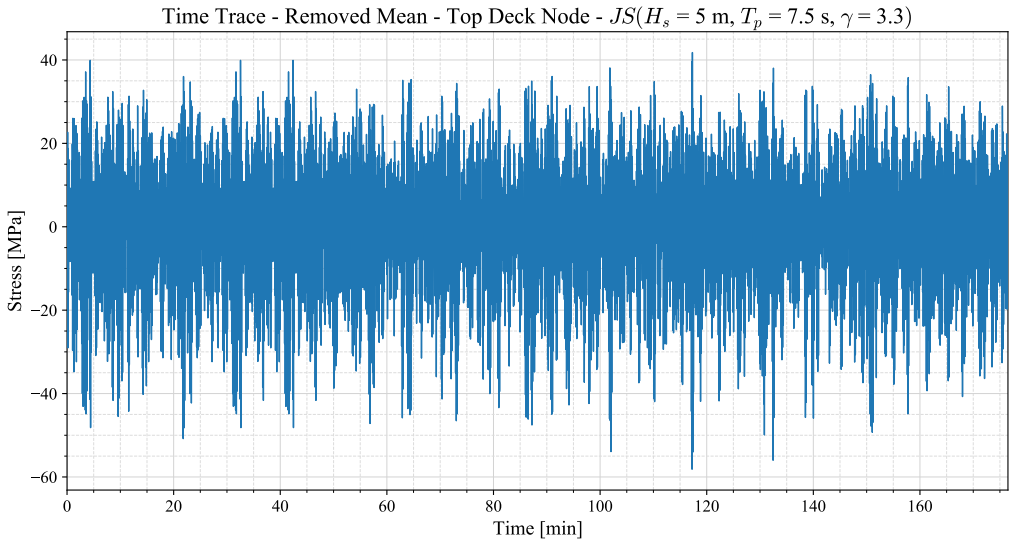

Figure 5.22: Temporal VA stress time trace for a JONSWAP ($H_s = 5$ m, $T_p = 7.5$ s, $\gamma = 3.3$).

dicated that the Fourier code should be sound. Furthermore, the pseudo-time approach delivers RAO's that are in line with the spectral approach; indicating that huge differences occur when shifting from a CA to VA analysis. In the end, a difference is expected between both temporal and spectral spectra; literature continuously points out that the temporal approach should be less conservative [7]. The *Hydrodynamic Response* module is therefore expected to contain the error. As *Ansys AQWA* has only implemented forward speed simulations a couple of years back, there is a suspicion that the error lies within the modelling of the speed. Numerous checks have been carried out, simulating different speed cases (zero speed, forward speed in *Diffraction*, forward speed in *Response*). These checks did also not solve the problem. Due to the black box nature of *Ansys AQWA*, the cause of the error was not found in the end. A check that remains to be made is what happens when adding multiple regular wave components to the pseudo-time case. This would provide extra detail on how the results change when complexity is increased. Sadly, this option is not available within *Ansys AQWA*.

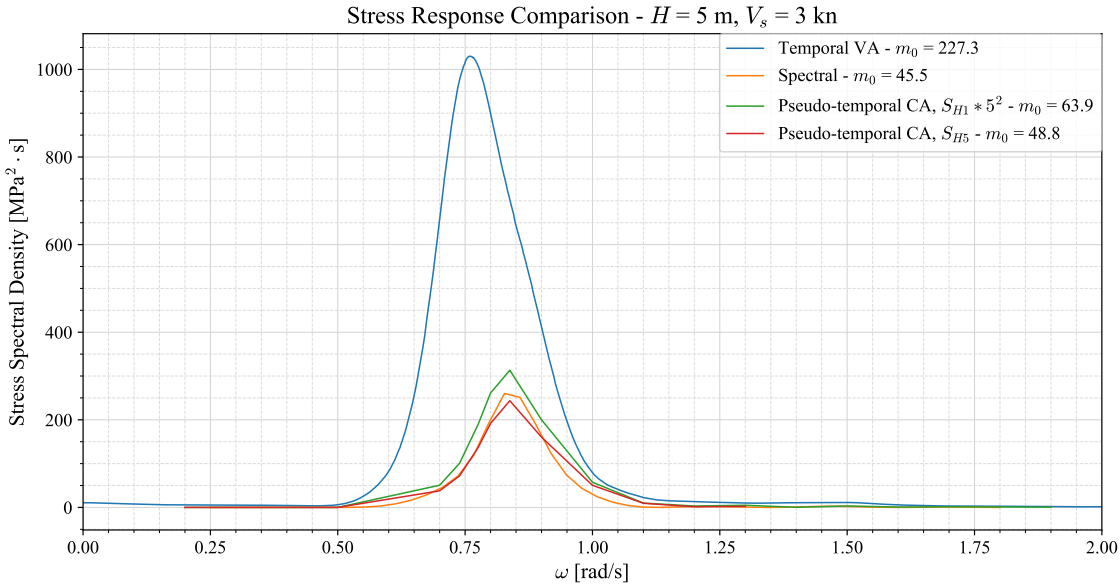

Figure 5.23: Comparison of VA temporal (removed mean), pseudo-time ($H = \{1, 5\}$ m) and spectral stress response for the deck node.

5.9 Concluding Remarks

In this chapter, the hydrodynamic and structural model have been constructed in order to perform CA and VA analyses. The CA analysis served to observe FK force-induced NL/L effects in the mean stress response and answer sub-questions **SQ1a**, **SQ1b** and **SQ1c**. In the VA analysis, numerous verification studies have been carried out. A pseudo-time CA analysis was added for increased insight on the effect of shifting to the time domain. The resulting VA temporal stress response spectrum has been compared to the spectral and pseudo-time spectra, revealing large differences between the VA and other spectra. This difference was judged to be too large not to expect an error. The cause of this error has been narrowed down to the *Hydrodynamic Response* model, as numerous checks were performed. Sadly, the error has not been fixed, leaving a discrepancy between the VA temporal and the CA pseudo-time and spectral results.

5.9.1 Sub-Question 1

Sub-questions **SQ1a**, **SQ1b** and **SQ1c** have been answered during the modelling and CA analysis; indicating the steps required to answer **SQ1** (section 5.6). These steps covered the construction of the NL/L temporal model, the selection of the most relevant load case and the critical locations at which NL/L effects are the largest. The selected load case is that of a head seas condition with a period of 8.09 seconds to match the longitudinal bending moment natural frequency. Regarding the critical locations, it was found that, in the current model, local effects are minimal. Intermittent wetting effects do not show, even when analysing the response at the side shell waterline for a beam seas condition. Reviewing the global hull girder bending moment, the normal stress in X-direction showed the largest contribution to NL/L effects at the outer fibres of the midship section. The NL/L difference in mean stress first increases over increasing wave amplitude ($\zeta = 1$ m to 2 m), after which it decreases ($\zeta = 2$ m to 5 m).

Sub-question 1 states:

How does the NLFK force affect the mean stress response?

The NL/L CA analysis has led to the answer to this sub-question:

> The global hull girder bending component induces the largest NL/L difference for the mean stress. This occurs at the outer fibres, where for the load case of head seas, NL/L mean stress differences rised over increasing wave height. The maximum NL-induced mean stress response was however small in comparison to the global mean stress and the stress ranges.

With this conclusion, **H1** is *rejected*. The expectation was that local effects would be substantial in the constructed model. As the largest differences occur at the outer fibres, this hypothesis no longer holds.

5.9.2 Model Limitations

Within the framework *Ansys Workbench*, the detailed modelling of linear and nonlinear cases was limited. Section 5.5 has elaborated on this and showed how the selection of 'Airy waves' provided the linear case, while the 'Stokes 2nd-order waves' characterised the nonlinear case. This was not ideal, as the research focused on the differences in NL/L Froude-Krylov-induced mean stress effects. The full LFK and NLFK were not isolated, but the selected methods were the best modelling choices available within *Ansys AQWA*.

Furthermore, as discussed in section 5.2.1, several setbacks were encountered with regards to automation. It was not possible to fully automate the time domain simulation and result

exporting process. Due to hardware limitations, it was a cumbersome task to obtain converged stress time traces. Because of this, only one variable amplitude wave case of 3 hours was solved.

5.9.3 Spectra Discrepancy

Upon comparing the VA temporal stress response with the pseudo-time and spectral results, a large difference was observed. With the pseudo-time and spectral response spectra being in line, an error is expected to occur when shifting from a regular to an irregular wave analysis within the *Hydrodynamic* and *Hydrodynamic Response* modules. As the wave elevation has shown to converge towards the input JONSWAP spectrum, the error has been narrowed down to the *Mechanical* module. As this module operates much like a black box, the error has not been fixed as of now.

Chapter 6

Novel Spectral Approach

The previous chapter showed the methodology regarding the temporal approach. This chapter will discuss the implementation of the temporal findings into the novel spectral approach. From the temporal approach, rainflow analysis is performed in order to obtain detailed stress range, mean stress and cycle frequency data. This data will then be used to uncover relations which can then be used as input in the spectral approach.

In more detail and recalling the scope of **SQ3**, the Walker mean stress model will be combined with the spectral mean stress model of Niesłony and Böhm. For this model, the mean stress and stress range are the input parameters. The time domain results will be used to uncover a reliable representation for these two variables in the frequency domain.

Finally, a comparison between numerous established (MSE) methods will be made in order to show the gain in accuracy provided by the constructed novel spectral approach.

6.1 Temporal Approach Findings

For the 3-hour time trace of the deck node (figure 5.19), rainflow counting is applied according to the methodology as shown in section 5.7.3. For every cycle, a range, mean, starting point and end point is identified.

6.1.1 Rainflow Cycle Frequency

Since no mean stress information is available when performing the spectral approach, the time trace is used to review trends regarding mean stress against stress range and frequency. With regards to frequency, information on the frequency of every cycle is obtained by using its corresponding start and end step. Multiplying the amount of steps with the time step of 0.5 s gives the period of the cycle. Dividing the period and multiplying by 2π provides the frequency of the cycle in rad/s. This procedure is depicted in equation 6.1.

$$\omega_i = \frac{2\pi}{(i_{end} - i_{start}) \cdot dt} \tag{6.1}$$

Looking at equation 6.1, one can notice that there is a minimum observable frequency when $i_{end} - i_{start} = 1$; $2\pi/0.5 = 12.57$ rad/s. When the period is covered in 2 steps, the frequency becomes 6.28 rad/s, etc. Figure 6.1 depicts the observable frequencies for the rainflow data due to the chosen time step. The upper period (T) is marked by the longest cycle occurring in the assessed time trace. Due to the chosen time step and the frequency formula given in equation 6.1, the scale of present frequencies is logarithmic. When reviewing the response spectra from section 5.8, the domain of interest lies within 0 to 3 rad/s. Looking at figure 6.1, sufficient frequency content can be represented in this range.

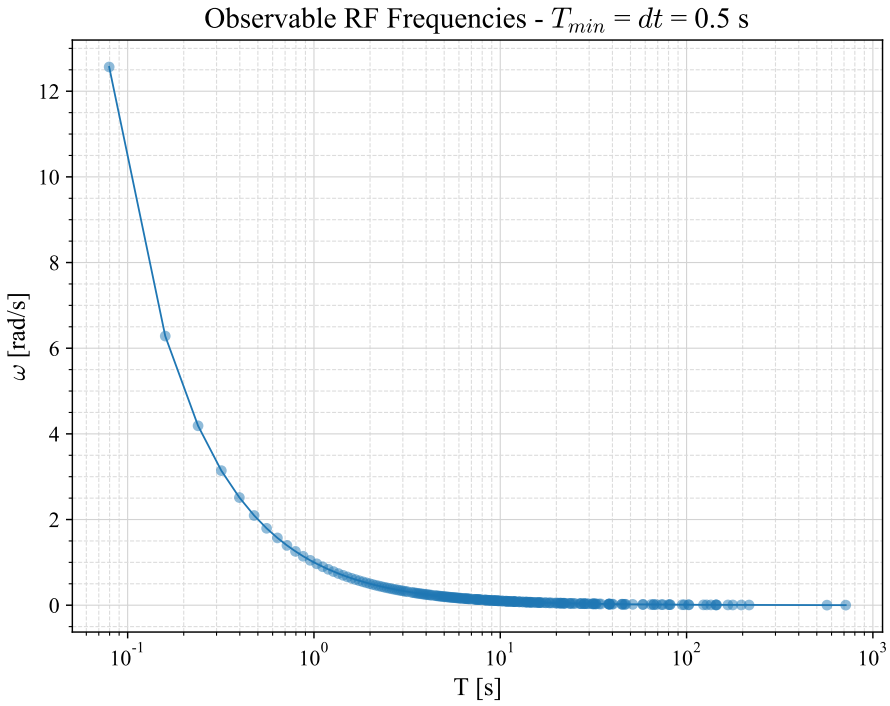

Figure 6.1: Observed rainflow frequencies with time step dt = 0.5 s.

6.1.2 Rainflow Data Visualisation

With the established framework for obtaining $\{\Delta\sigma, \sigma_m, \omega\}$, the data are plotted in a scatter diagram format for the 3-hour time trace of the deck node. Figure 6.2 showcases the data in three ways, shifting the axis on which a variable is plotted. Note that the third axis is indicated by colour. The colourbar has a logarithmic scale when it displays the frequency.

In figure 6.2a, the range and mean are plotted on the x- and y-axis, while the frequency is indicated by the (logarithmic) colour scale. One can see the variation in observed stress ranges from close to zero up to 100 MPa. In the mid-stress range segment (10 to 60 MPa), the mean value of σ_m is quasi-constant. At the higher stress range region the mean stress of the cycles drops. At the lower region, around stress ranges close to zero, a large mean stress scatter appears. This is attributed to small fluctuations in the stress response signal occurring on the larger 'waves'. These can happen either on wave troughs or peaks, causing the large mean stress scatter. Because these ranges are quite small, their damage contribution is negligibly small as well.

Figure 6.2b shows another representation of the data with different axes; frequency and stress range on the x- and y-axis and the mean stress depicted in colour. An overall decreasing stress range is noticed when the frequency increases. This makes sense as higher peaks are less likely to occur and thus large stress ranges take longer to be completed. At frequency range ω = 0.6 to 1.0 rad/s, an apparent 'gap' in stress range content shows. Stress ranges do not rise above 40 MPa, but after ω = 1.0 rad/s, there is a large peak. Recalling section 5.6.1, the natural frequency of the longitudinal bending moment of the ship was identified to be ω_n = 0.78 rad/s (figure 5.4). This falls within the identified gap from ω = 0.6 to 1.0 rad/s.

The final figure, 6.2c, one last shift of axes has been done, showing the frequency and mean stress on the x- and y-axis and the stress range in colour. For increasing frequency, the scatter in the mean stress increases, but the stress range decreases. This also has become clear from figure 6.2a. Around ω = 0.6 to 1.0 rad/s, once again a smaller range in data points can be seen.

From the figures, the following conclusions can be drawn:

- Regarding the overall values of the mean stress, these vary from close to zero to around 25 MPa; a quite small range compared to the stress ranges which can go up to 100 MPa. This will make the accompanied mean stress effect less prevalent and therefore, the quasi-constant *global* mean assumption for the σ_m data set is adopted.
- Over increasing frequency, the stress range drops significantly while the mean stress increases only slightly.
- From ω = 0.6 to 1.0 rad/s, fewer data points occur which have smaller $\Delta\sigma$ and σ_m values than adjacent frequencies. Within this frequency range, the natural frequency for the longitudinal bending moment of the ship is situated; ω_n = 0.78 rad/s.

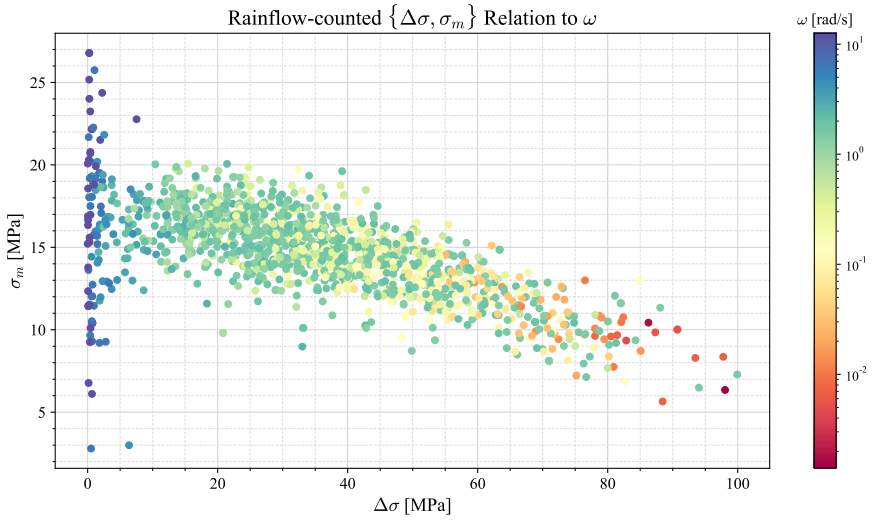

(a)

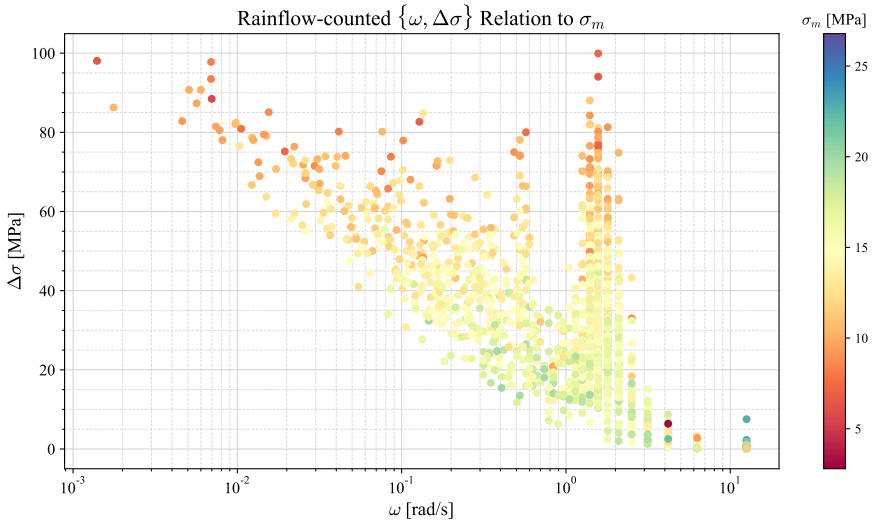

(b)

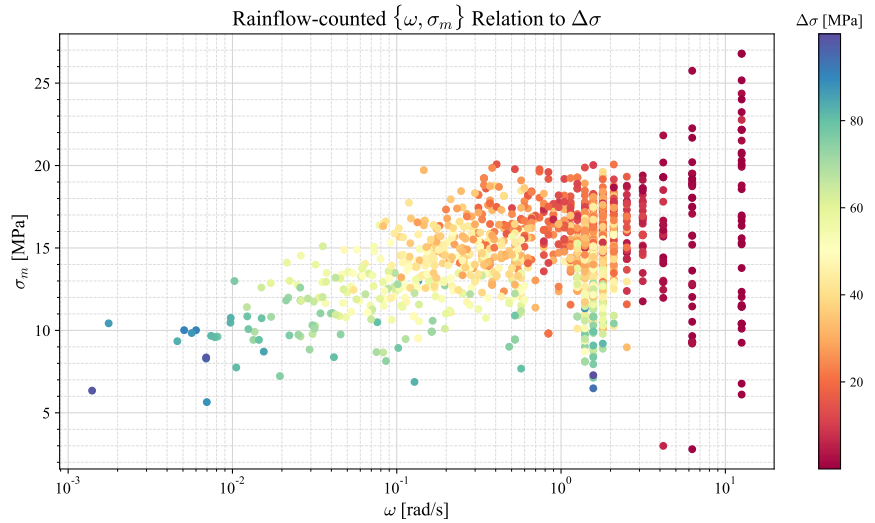

(c)

Figure 6.2: Rainflow-counted $\{\Delta\sigma, \sigma_m, \omega\}$ data with in the third axis ω **(a)**, σ_m **(b)** and $\Delta\sigma$ **(c)** for the top node.

6.1.3 Loading and Response Ratio

With the shown data, the loading and response ratio was calculated and plotted to observe its frequency dependency. Figure 6.3 shows the r_{lr} of each cycle against its frequency. As the frequency increases, r_{lr} increases as well. This happens over a asymptotic course, with large scatter around ω = 0.6 and 1.1 rad/s; roughly the same locations as the data concentration peaks of the earlier figures (6.2b and 6.2c). At $\omega \approx 1.1$ rad/s, a large cluster of data are centred with large scatter in r_{lr}.
The next section will analyse the influence of ω and r_{lr} on the fatigue damage D.

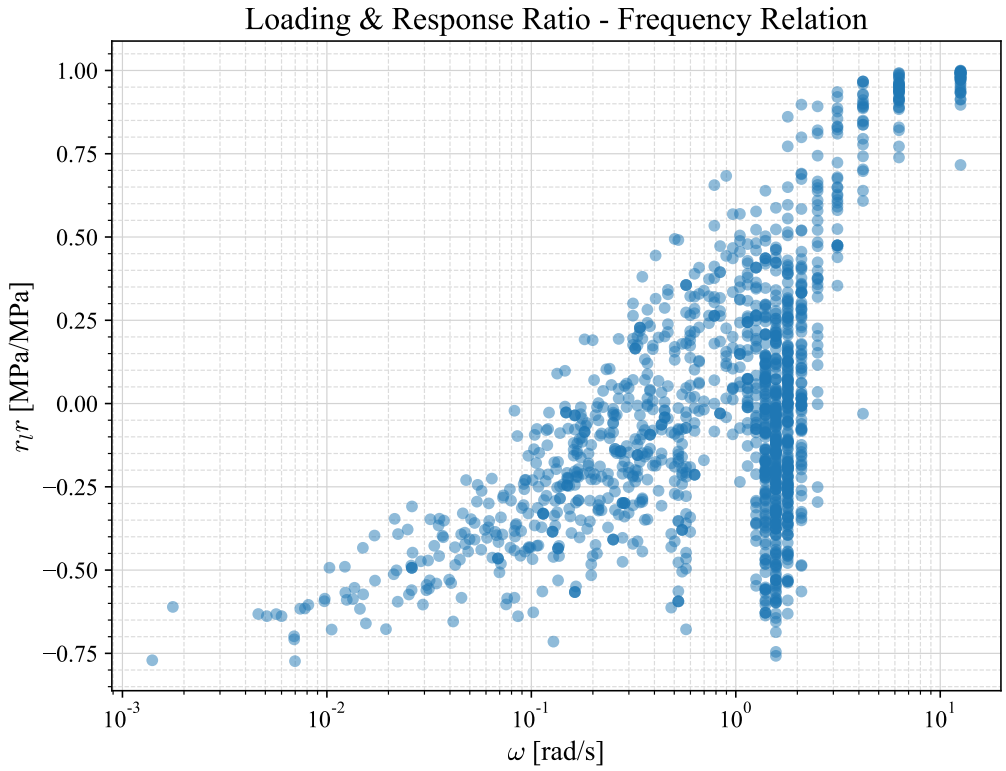

Figure 6.3: Loading and response ratio against frequency for every cycle - top deck node.

6.1.4 Frequency Influence on Damage

The r_{lr} over ω data has shown a large scatter at most frequency levels. Physically, this means that at a certain frequency level, the mean stress and stress range of certain cycles at that level vary significantly. In other words, cycles with the same frequency can occur at way different mean stress levels and have significantly different ranges.

For further illustration, the inflicted fatigue damage of each cycle is included into the data visualisation. Figure 6.5 shows three different axis views of the $\{\omega, r_{lr}, D\}$ data set. In these plots, the damage of each cycle is calculated through a standard $r_{lr} = -1$ SN-curve ($m = 3$, $\log(C) = 12$, section 3.1.1). Each damage is divided by the maximum damage done by a cycle (D_i/D_{max}); a damage ratio. Figure 6.5a is similar to figure 6.3, only now it has the damage ratio plotted on the third axis. Note that the scale of the damage ratio colour bar is made logarithmic to show a more clear distinction in colour. This logarithmic scale is only applied when the damage ratio is on the colour bar axis. Looking at the figure, one can see once again the large scatter or r_{lr} over frequency, but also a large scatter in damage ratio values for the same frequency.

In between $\omega = 1$ and 3 rad/s, a large data cluster is observed. Figure 6.3 shows the density more clearly; the highly-concentrated data points form a dark blue area. Focusing on this

cluster, it can be seen that almost the full range of r_{lr} is represented in the damage. Especially the higher damage ranges are present at lower values of r_{lr}. The contribution of this cluster to the total damage over the time trace has been investigated. It was found that, of the total damage, 46% is caused by cycles within $\omega = [1, 3]$ rad/s. At lower frequencies ($\omega < 1$ rad/s) 54% of the damage is done. Above $\omega = 3$ rad/s, no real damage is dealt; only 0.02%. These percentages are also shown in figure 6.5a.

Shifting the axes to the representation shown in figure 6.5b, damage has declined significantly after ω= 3 rad/s. At lower frequencies, the scatter in damage is quite large again. A final shift to r_{lr} and the damage ratio on the x- and y-axis (figure 6.5c) gives a much more correlated data set. One can see the damage decreasing as r_{lr} increases from -0.75 up to 1.0. Although the global mean is positive (tension), stress amplitudes larger than the mean occur, causing partially compressive cycles. This is the reason for cycles with negative r_{lr} values.

The frequency content of the rainflow data does not show a strong connection to the loading and response ratio (incorporating $\sigma_m$and $\Delta\sigma$) and the inflicted fatigue damage. The loading and response ratio however does show a strong connection to the damage. At the lower levels of r_{lr}, higher damage values are observed for the given time trace.

A final visualisation is given in figure 6.4, where the original $\Delta\sigma$ and σ_m values are plotted along with the Walker-corrected damage D. Here, a clear relation between the damage and the stress range shows. As the stress range increases, the damage increases as well. This is in line with the logarithmic relation coming from using the SN-curve, which was also depicted in figure 6.5c.

It can be concluded that the damage is dominated mainly by the stress range. In addition to this variable, no clear frequency-dependency with any of the rainflow variables $\{\sigma_m, \Delta\sigma, r_{lr}, D\}$ was found. Regarding the mean stress, it was observed that over the rainflow data a quasi-constant mean stress value can be drawn. This is a first indication of the applicability of a single, global mean stress value as input for the novel spectral approach.

The next section will explore this applicability for other locations in node selection 2. After that, it will be further investigated how a proper mean stress value can be obtained when operating solely in the frequency domain.

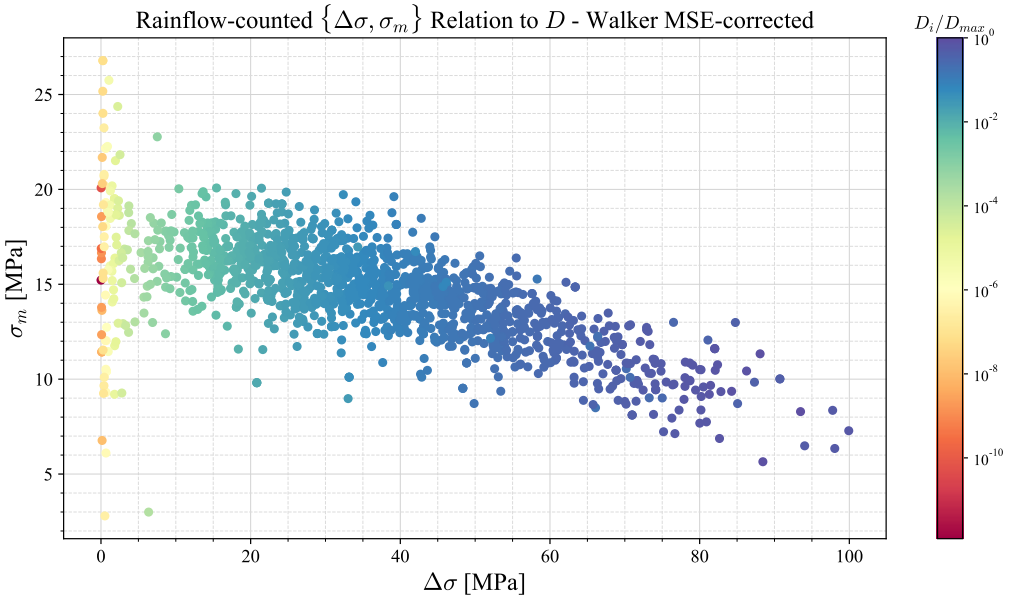

Figure 6.4: Rainflow-counted $\{\Delta\sigma,\sigma_m, D\}$ data. The damage is corrected for the mean stress using Walker.

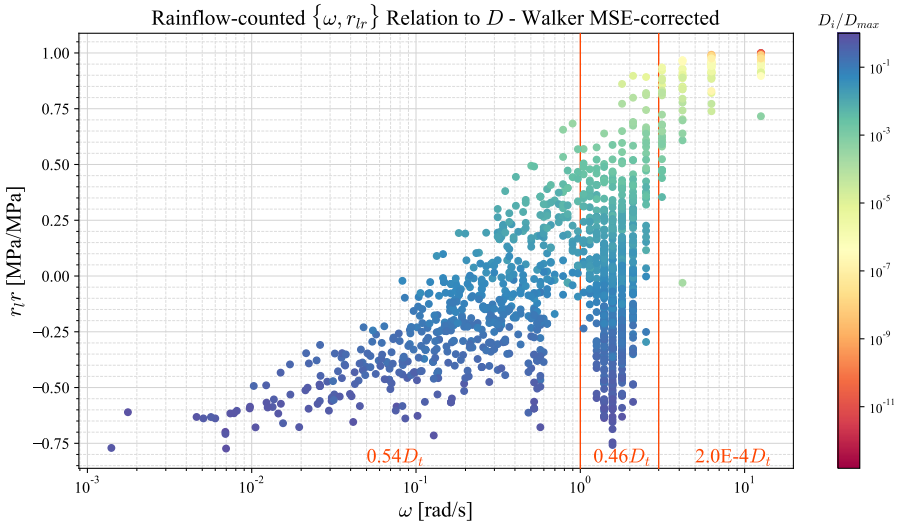

(a)

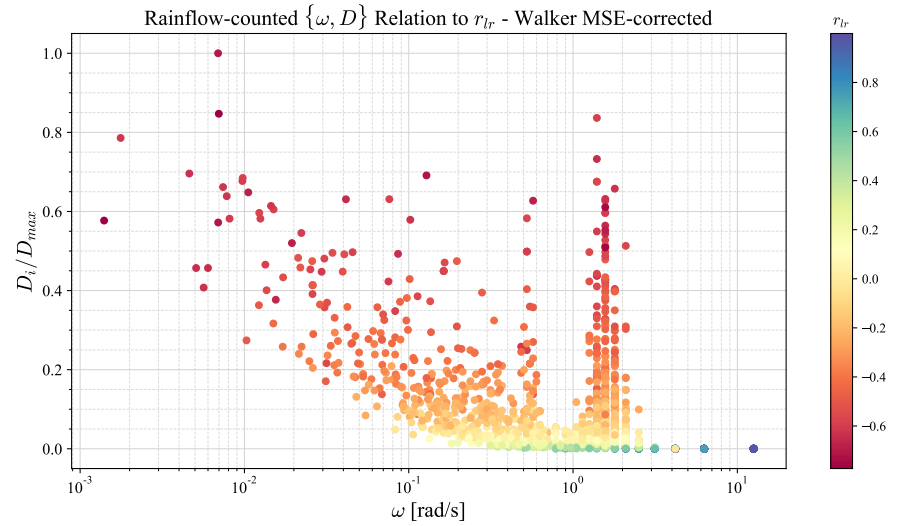

(b)

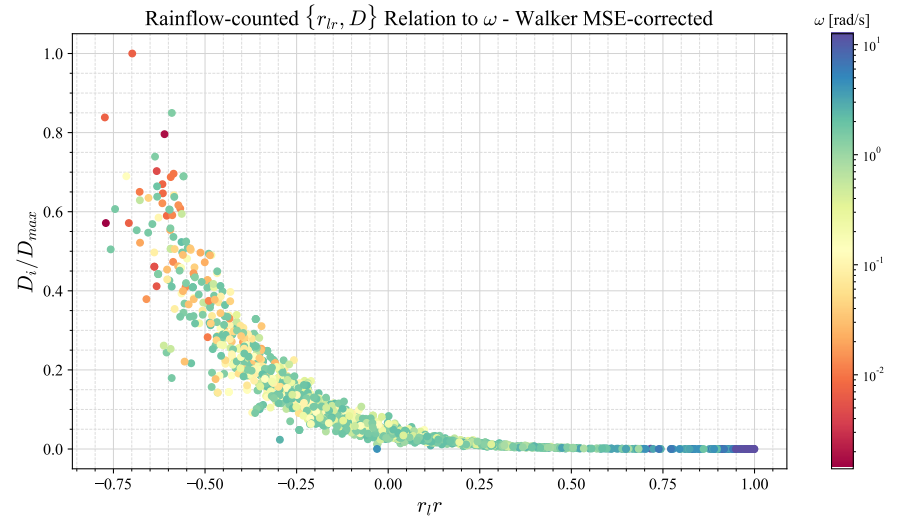

(c)

Figure 6.5: Rainflow-counted $\{\omega, r_{lr}, D\}$ data with in the third axis D_i/D_{max} **(a)**, r_{lr} **(b)** and ω **(c)** for the top node. The damage is corrected for the mean stress using Walker. Figure **(a)** includes the total damage distribution, focusing on the cluster at $\omega = [1, 3]$ rad/s.

6.1.5 Full Node Set

The previous analysis covered the rainflow data of the midship top node (figure 5.19). The main findings were that the mean stress is quasi-constant over all cycles while the frequency content does not show a strong relation to it. Also, 54% of the damage was done at frequencies lower than 1 rad/s; cycles with high stress ranges. Above 1 rad/s, a data cluster appeared with a wide range r_{lr} values. This cluster contributed 46% to the total damage.

With these conclusions, it is important to investigate how nodes at other locations respond and whether their rainflow data are in line with the expectations that were set in the previous section. In this section, first, a midship waterline and bottom node are added to the analysis. The nodes are shown in figure 6.6 along with the top node for reference. The damage analysis performed for the top deck node is now conducted for these other nodes. Second, the full node set set will be evaluated with regards to the quasi-constant mean stress observations in order to verify its applicability.

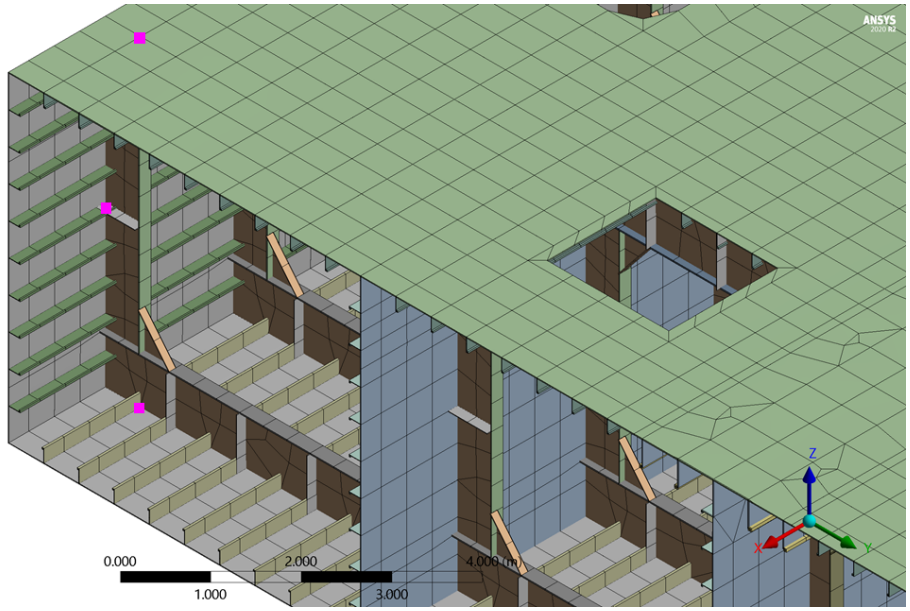

Figure 6.6: Locations of the top deck, waterline and bottom nodes.

Comparison Waterline and Bottom Node

Following the $\{\omega, r_{lr}, D\}$ analysis performed on the top deck node, the same procedure is carried out for the waterline and bottom node (figure 6.6). In appendix C.5, figures C.6 and C.7 show the results for the waterline and bottom node, respectively.

As fully compressive cycles are prevalent at both of these locations, r_{lr} values of -3 occur quite often. At the waterline, the data cluster seen at the top node around $\omega = [1, 3]$ rad/s is less expressed. 31% of the damage is done within this range, whereas 60% of the total damage occurs at the lower frequency range. Overall, the most cycles have a quite small damage compared to the larger outliers. This can be attributed to the fact that the waterline is close to the neutral axis. Stress ranges become so small that numerical errors can induce large differences between the damage of two cycles.

For the bottom node, a similar amount of damage is located within the $\omega = [1, 3]$ rad/s cluster as for the top deck node: 45%. At the lower frequency region, this is 55% and above 3 rad/s, no real damage is done. This similarity is expected due to the 'mirrored' behaviour in comparison to the top deck node.

Table 6.1 compares the total damage for the three node locations. Due to the overall hogging condition and the distinction between compressive and tensional cycles, the top deck node

suffers the most damage. At the waterline, damage due to the global hull girder bending moment is negligible. The bottom node endures 74% of the top deck damage.

Table 6.1: Damage comparison for top deck, waterline and bottom nodes.

Location	Total Damage	D/D_{Top}
Top deck	1.19E-04	1.00
Waterline	8.99E-10	7.55E-06
Bottom	8.79E-05	0.738

Quasi-constant Mean

Appendix C.4 contains the rainflow plots for $\{\Delta\sigma, \sigma_m, \omega\}$ for the waterline and bottom node. For the waterline node, the magnitude of the $\{\Delta\sigma, \sigma_m\}$ response is much smaller than that of the top node. This is because the global NSX stress component is addressed. Because the waterline lies close to the neutral axis, this component remains quite small. Nonetheless, a quasi-constant mean value can be seen in figure C.6a. For the stress range over frequency (figure C.6b), one can see a similar course as for the top node (figure 6.2b). Only now, the spread in $\Delta\sigma$ is much more compressed; there is a lower scatter in stress range. This is because the waterline node experiences much less stress due to its location close to the neutral axis. So not only has $\Delta\sigma$ decreased drastically, the values show a more coherent course over increasing frequency. Still, observing a clear relation, in this case for $\Delta\sigma(\omega)$, is infeasible due to the large spread for different locations. The same observations apply to the mean stress over frequency plot (figure C.6c); a similar shape as for the top node but with much smaller values.

For the bottom node the three rainflow plots show a 'mirrored' version of the top node (figure C.7). Because of the global hogging condition, the top is in tension and the bottom is in compression. This is reflected in the top deck and bottom node rainflow figures and it is the cause of the 'mirrored' data. Looking at figure C.7a, the mean stress lies beneath zero (compression) and increases over increasing $\Delta\sigma$. Like for the top node, the mean stress moves towards zero, but from the opposite direction. For the stress range over frequency (figure C.7b), the same shape of the scatter is observed as with the top node (figure 6.2b). The maximum values are slightly smaller than those of the top node, something which can be explained by the fact that the bottom node is submerged while the top node is out in the air. The mean stress over frequency plot (figure C.7c) shows again a resemblance with the top node, only flipped upside down. This is again caused by the difference in mean stress due to the hogging condition.

The data gaps around $\omega = 1$ rad/s do again show, especially for the bottom node. For the waterline node, these gaps are less expressed, but can however be observed.

It can be concluded that the findings for the two other locations, the waterline and the bottom, are in line with those for the top node. The quasi-constant mean assumption holds for the waterline, where $\{\Delta\sigma, \sigma_m\}$ values are quite small. Also the bottom node showed expected behaviour as the data was 'mirrored' with respect to the top node.

Loading & Response Ratio

For the two nodes, the loading and response ratio has been plotted in figure 6.7. As opposed to the $\{r_{lr}, \omega\}$ plot of the top node (figure 6.3), these two scatter plots show a much less coherent course over increasing frequency. For the waterline node (figure 6.7a), increasing scatter shows. At $r_{lr} = -3$, the data are truncated, due to the imposed rule regarding compressive cycles (section 5.7.4).

For the bottom node (figure 6.7b), a lot more cycles have $r_{lr} = -3$ due to their fully compressive nature. This makes sense as the ship's bottom is in compression most of the time.

The maximum r_{lr} values are around -1.25; much lower than for the waterline node, which approached $r_{lr} = 1$. This can be explained again by the compressive nature at the bottom location.

The loading & response ratio for the waterline and bottom node show significant scatter, just like for the top node. Both data sets are capped at $r_{lr} = -3$ because of the model's definition for compressive cycles.
The analysis of these two additional nodes gives extra certainty that in fact, no useful $\{\Delta\sigma, \sigma_m, r_{lr}\}$ relation with the frequency can be obtained.

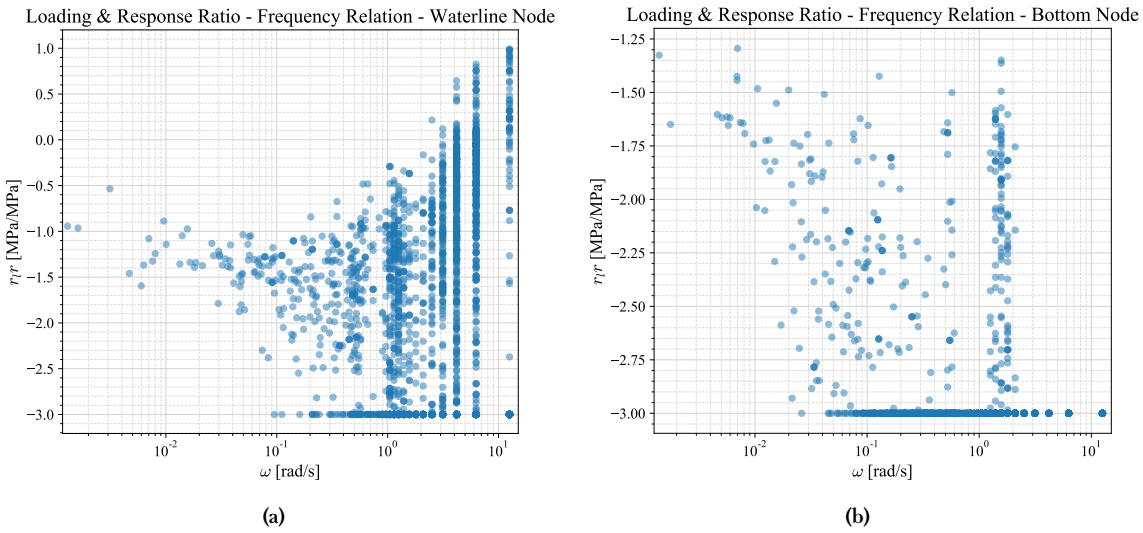

(a) (b)

Figure 6.7: Loading and response ratio against frequency for the waterline **(a)** and bottom node **(b)**.

6.1.6 Global Mean Stress

The previous section indicated that for three nodes at the top, waterline and bottom of the midship, the rainflow data are in line with the expectations.
As the mean stress component for the three locations showed a quasi-constant course, this is a strong lead to a general σ_m input for the spectral approach. However, it must be further ensured that this assumption holds. Therefore, the full node set of **selection 2** will be evaluated in this section.

In more detail, the validity of the quasi-constant mean stress assumption must be tested for the full node selection. Because there are 116 nodes in the node set, performing an analysis similar to the previous section for every node is not possible within a reasonable time frame. Therefore, for every node, a check is done to judge the fit of the quasi-constant mean value.

Based on the fact that the damage of a cycle is largely dependent on its stress range [8], the variance of the mean data is compared to that of the stress range data. This gives a clear indication on the respective scatter. Figure 6.8 displays the $Var(\sigma_m)/Var(\Delta\sigma)$ values of the rainflow data set for every node in the selection. This data is plotted against each node's respective nondimensional z-coordinate. Looking at the figure, one can see that the majority of the data points have a mean stress variance within 2.5% of the stress range data. The mean for the whole scatter lies at 3.5%. This indicates that the scatter in the mean stress data is quite small relative to that of the stress range. As the stress range contributes the most to the damage (∼90% [3]), the mean percentage of 3.5% is accepted.

Mostly around the waterline there are some outliers, which are caused by small values being amplified in both the mean stress and the stress range. The division of both their variances

then results in larger differences, however the particular stress response is too small to have a real impact on the damage in the end.

From this check, it can be concluded that the quasi-constant assumption holds throughout the majority of the nodes. Outliers around the waterline are caused by numerical error within the significantly small mean stress and stress range values. Therefore, they are negligible when it comes to fatigue damage.

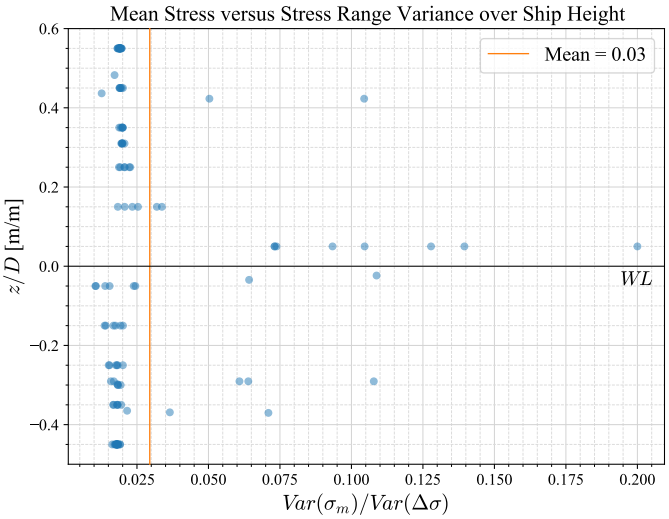

Figure 6.8: Variance ratio of rainflow data σ_m and $\Delta\sigma$ for node selection 2, over the nondimensional ship height.

Still Water Bending Moment

As it was shown in the previous section that the mean stress behaves quasi-constant for the majority of the selected nodes, the focus now lies on finding a simplified, but effective, mean stress input value for the spectral approach.

The still water bending moment (SWBM) is the moment a ship experiences when lying in still water. Based on the ship's structure and loading condition (ballast, full cargo, etc.), the SWBM will vary over the ship's lifetime. For a given loading condition, the SWBM induces a mean stress in the structure. This mean stress component can also be detected in dynamic stress signals. In the design phase, when the structural model is available, the still water bending moment can easily be calculated by simulating the ship in a still water condition. Practically, this is done by applying a significantly long wave ($\lambda >> L_s$) and obtaining the load at a certain time step. When this load is mapped to the structural response module (section 5.2, figure 5.2), a constant stress for every node is obtained. This is marked as the *SWBM-induced mean stress*; $\sigma_{m,SWBM}$.

As the above procedure takes a fairly short time and is simple to perform, using $\sigma_{m,SWBM}$ thus makes for a perfect mean stress input for the spectral mean stress model. This section will further justify the choice for the SWBM rather than using the mean of a lengthy time signal or the local mean values from rainflow data.

The SWBM-induced mean stress $\sigma_{m,SWBM}$ is recorded for the pontoon. To see how the adoption of $\sigma_{m,SWBM}$ relates to the actual mean data, two comparisons are performed. First, $\sigma_{m,SWBM}$ is compared to the global mean of the stress time trace itself (σ_m). Second, $\sigma_{m,SWBM}$ is compared to the mean value of the rainflow data $\sigma_{m,RF}$, which is calculated as follows:

$$\sigma_{m,RF} = \frac{\sum_{i=1}^{N_{cycles}} \sigma_{m,i}}{N_{cycles}} \tag{6.2}$$

These comparisons are done for all selected nodes and figure 6.9 shows the results. Figure 6.9a shows the comparison with the global mean. One can see that most data points have values of $\sigma_{m,SWBM}/\sigma_m \approx 1.1$. The mean of the data set lies below that due to outliers: $\sigma_{m,SWBM}/\sigma_m = 1.07$. This means that overall, the adoption of the SWBM leads to a slightly higher mean stress. Comparing $\sigma_{m,SWBM}$ to the rainflow mean, as shown in figure 6.9b, one can see that a similar trend occurs. Here, the mean difference is slightly higher; $\sigma_{m,SWBM}/\sigma_m = 1.12$.

It can be concluded that the adoption of $\sigma_{m,SWBM}$ leads to a conservative global mean stress of around 7 to 12%, judging from the analysis performed on the selected midship nodes. This conservatism is accepted in order to continue the formation of the spectral mean stress model.

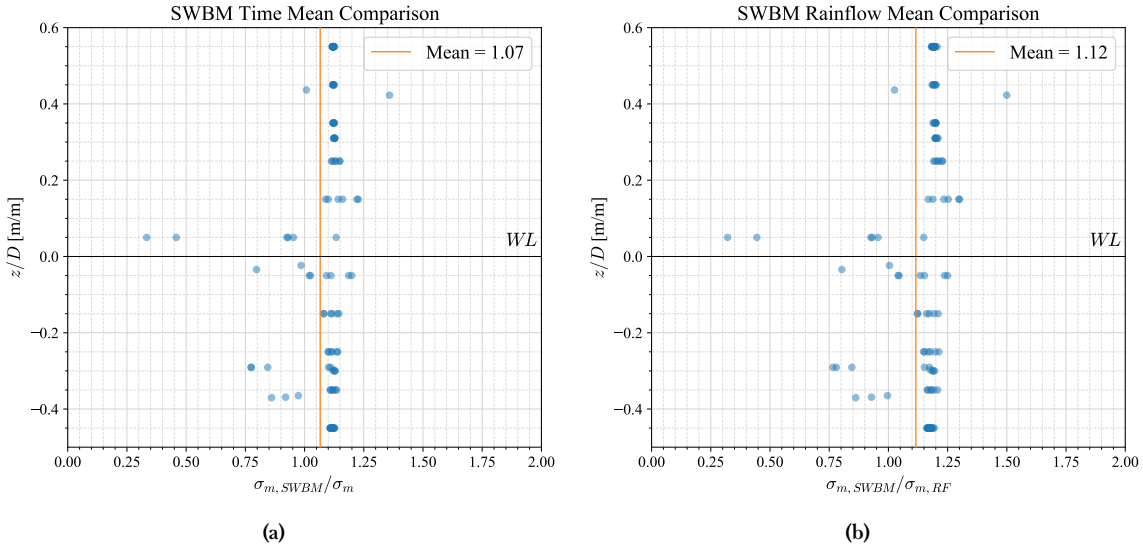

(a) (b)

Figure 6.9: Comparison of SWBM-induced mean stress versus the time trace mean **(a)** and rainflow mean **(b)** for node selection 2, over the nondimensional ship height.

Global versus Local Mean Stress

The previous section showed that the adoption of the SWBM-induced mean stress is around 7% conservative with respect to the global time trace mean. As this was accepted, the next step is to verify whether the adoption of a global mean over addressing the local mean of each cycle is also acceptable. This is important since only the global mean will be applied in the novel spectral approach.

Niesłony formulated two mean stress approaches in the time domain [6]:

1. Transforming a stress signal based on its *global* mean stress.
2. Transforming every individual cycle by its *local* mean stress.

Łagoda stated that for both approaches, using rainflow counting, the same damage is obtained [50]. This statement is reviewed in this section for the node set data to ensure the validity of the global mean stress adoption. This is also done for the Walker correction to see whether the global approach also applies there, as it has not been done before.

For the full node set, the fatigue damage is calculated based on aforementioned methods *1* and *2*. The resulting damage for the global approach (*1*) is divided by the local approach (*2*) to

indicate their respective difference. This procedure is performed using both the Gerber and Goodman model (eq. 3.10, 3.11) as was proposed in Niesłony's work [6]. It has been stated that these mean stress corrections do not take into account weld geometry, thermal residual stress, or the sensitivity of the material to mean stress [3, 47]. This makes them inadequate for assessing fatigue damage of welded joints in the MCF and HCF region [16, 3].

Using Walker's model with loading & response ratio coefficient $\gamma = 0.92$, welding quality-induced deficits as well as residual stress have been incorporated [3]. This coefficient indicates that the effective stress range is dominated by the original stress range ($\sim$90%), while the mean stress contributes around 10%. In literature, the Walker correction has been deemed as the most adequate mean stress method for welded joints due to its versatility (section 3.2.1).

While for the Gerber and Goodman corrections only a mean stress value is required as input, for the Walker correction also stress range data is required. It is not possible to formulate a single 'global' stress range. Therefore, for the local versus global analysis of Walker, the global mean stress is applied to every individual cycle, taking into account its stress range $\Delta\sigma_i$. This way, the global mean stress is incorporated, but local cycles are still evaluated.

Figure 6.10 shows the results for the procedure. The damage ratio for every node is plotted against its z-coordinate. For the Gerber method (6.10a), one can see the nonlinear course of the damage ratio over the ship height. This is due to the quadratic term in its equation (3.10). Overall, the damage ratios are quite small, with a maximum of around 0.15% for the outer fibres. For the Goodman method (6.10b), a linear course over the ship height is observed. Also here differences increase towards the outer fibres, only at a larger percentage; $\pm$2%, with a maximum of +2.5%. This increased difference with respect to the Gerber method indicates that the method is more sensitive to the choice of the global method over the local method. The course of both mean stress corrections over the ship height is in line with the findings of section 5.6.3, where nonlinear effects were increased at the outer fibres.

For the Walker method, much larger differences are observed. At the top deck ($z/D_{ship} = 0.55$), the damage difference of the global over the local approach is 8%. Moving down, this difference stays roughly the same, until the waterline is reached. There, differences increase rapidly up to around 37%.

To understand where this large increase in global/local difference comes from, for both the global and local method, the calculated Walker coefficients K_W for every cycle are reviewed. This is done for the top deck, waterline and bottom node (figure 6.6). The K_W value was compared to the mean stress, stress range and their ratio for every cycle. As this provided quite extensive data, the plots of this analysis are placed in appendix C.6.

Figure C.10, depicts the data for the top deck node. One can see that the local (blue) and global (orange) methods are quite well in line. This explains the relatively small differences above the waterline in figure 6.10c. It is clear that the global mean stress at this location is in line with the majority of the local mean stresses, meaning most cycles are centred around the global mean.

For the waterline node (figure C.11), large differences in K_W become clear. As for the global method, the global mean is implemented according to equation 5.11 and 5.12, a clear connection to this equation shows when comparing to the mean stress and stress range (figures C.11a and C.11b). For the local method, this connection is less strong, as the scatter is quite large. Figure C.11c displayed huge values of $\sigma_m/\Delta\sigma$. This is because of the σ_m and $\Delta\sigma$ values being so small around the waterline that they are limited by computer precision. Already small mean stress levels can have significantly smaller stress ranges, and vice versa, causing large $\sigma_m/\Delta\sigma$ values. It is because of this that figure C.11c was capped at [-5, 5]. It has become clear that for the waterline, due to numerical errors, large differences occur.

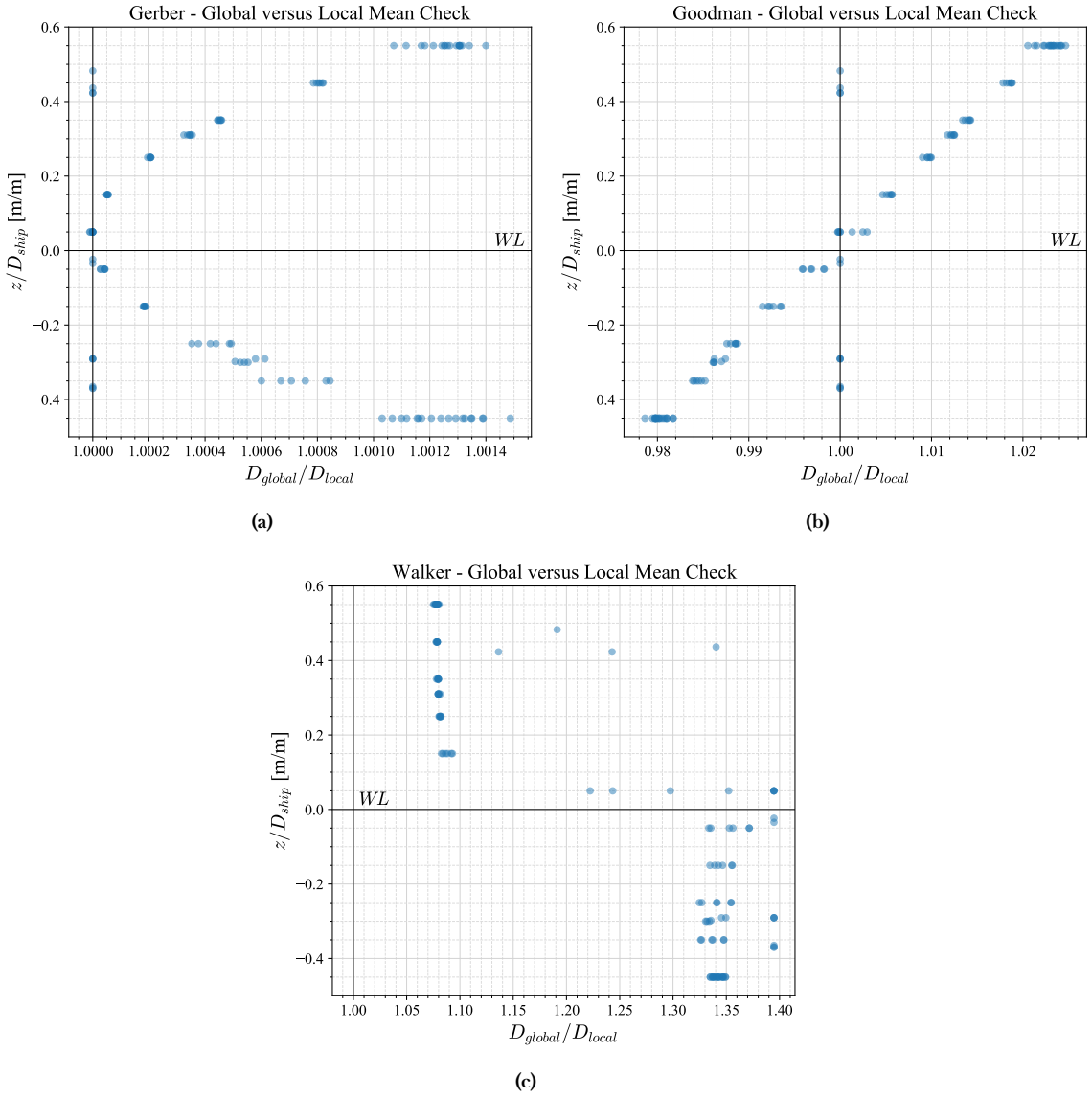

Figure 6.10: Global versus local mean stress correction comparison for Gerber **(a)**, Goodman **(b)** and Walker **(c)** corrections.

For the bottom node (figure C.12), the global data shows a strong connection with the stress range (C.12b), while it is less prevalent with the mean stress (C.12a). This confirms the stress range as governing the Walker mean stress effect over the actual mean stress [3]. The local data shows a clear difference with the global set, only for the ratio $\sigma_m/\Delta\sigma$ they are more in line.

Furthermore, the lower limit of r_{lr}at -3 shows clearly in the graphs as well, as at lower values of σ_m and $\Delta\sigma$ K_W becomes constant. Figure C.12c was also capped because of unrealistic outliers due to numerical error.

Concluding, the difference between the global and local methods of Gerber and Goodman are acceptably small, especially for the Gerber method. For the Goodman method, the largest difference was observed to 2.5% at a top deck node. This percentage is still quite small compared to the aforementioned influence of the stress range over the mean stress. For the Walker method, it has become clear that at lower levels of the ship height, below the waterline, differences in local and global approach become quite large. With the ship having an overall

hogging condition, the mean values (mostly compressive) of the cycles are less accurately represented by the global mean stress than was the case for the top deck node. The Walker method has therefore proven to be less adequate for including the global mean stress only. This can also be attributed to the fact that the stress range has become involved, forcing the global method to still correct local cycles for the global mean stress. It therefore makes sense that large differences occur; using the global mean diverges too much from the local mean values. The presented global Walker approach for rainflow cycles can therefore be argued to be a quite cumbersome method.

6.1.7 Concluding Remarks

From the findings of the temporal approach, the following conclusions have been drawn:

- No concrete relation was found between the rainflow cycle frequency and any of the other rainflow parameters $\{\Delta\sigma, \sigma_m\}$.
- The strongest contributor to the fatigue damage is the stress range $\Delta\sigma$. This is mainly due to the choice of the r_{lr}-coefficient parameter to be $\gamma = 0.92$ in the Walker mean stress correction as well as the chosen wave case which has a high significant wave height.
- The quasi-constant mean stress variance is significantly small in comparison to the stress range variance.
- The SWBM-induced mean stress $\sigma_{m,SWBM}$ is within 7-12% accordance with the {time domain, quasi-constant rainflow} mean.
- Adopting a global mean stress model over a local one causes small differences for the Gerber and Goodman methods (max. 2.5%). This is in line with the statements of Łagoda and Niesłony [50, 6].
- For the Walker method, a global approach was constructed and compared to the conventional local one. Differences were observed from around ∼8% at the top deck to ∼37% beneath the waterline. The (mainly compressive) cases at the bottom of the ship were less well represented by the global stress than was the case for the top deck.
- The global Walker time domain method was deemed to be cumbersome. Efforts to construct a global method in the frequency domain are therefore continued.

With the arguments formed in this section, the novel spectral approach is constructed and compared to state-of-the-art spectral methods in the following section.

6.2 Spectral Approach Implementation

From the temporal approach, it was found that the still water bending moment can be used as input for a spectral approach with global mean stress correction. Also, using the stress response spectrum, stress range information can be introduced. The mean stress and stress range data then enable the Walker mean stress correction method in the spectral approach. The approach is displayed schematically in figure 6.11.

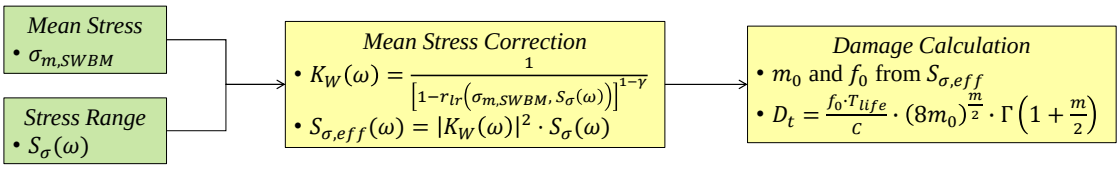

Figure 6.11: Workflow for the novel spectral approach. Colours green and yellow indicate the modules *Mechanical* and *Fatigue*, respectively.

6.2.1 Comparison

The novel spectral approach will be compared to previous methods, both operating in the time domain and frequency domain.

!! For the frequency domain data, the VA temporal spectrum has been cleared of its mean value and transformed into a stress response spectrum $S_{\sigma,VA}$. The following spectral methods and comparison study are performed according to this time trace and its spectrum. It is acknowledged that an error is present in the time domain data, as discussed in section 5.8.3. As this error has not been solved within the timeframe of this thesis, the construction of the novel spectral approach was continued by using the time domain data. The methodologies and comparisons that are performed are still considered to be legitimate because the VA spectrum is 'correct' with respect to the time trace it originates from.

Table 6.2 shows the six methods that are considered, including the novel approach as the sixth. With the point of comparison being the fatigue damage, $S1$ uses the D_t formula based on the narrow-band Rayleigh assumption (section 2.3, equation 2.14). In this equation, T_{life} is set at $T_{sim} = 3\ h = 10,800\ s$ and m_0 and f_0 are obtained based on the stress response spectrum (eq. 2.6 and 2.14). $S2$ corrects for mean stress using the Goodman method, as used by Niesłony and Böhm and $S3$ marks the novel spectral approach which includes the Walker mean stress. These are both *global* mean stress corrections. For the time domain methods, $T1$ is the rainflow damage using the stress ranges of individual cycles only. $T2$ uses the *global* mean stress correction of Goodman, which was used by Niesłony and Böhm [6]. $T3$ calculates the damage using the Walker mean stress; correcting for *local* cycles using their respective r_{lr}values.

Although it is not properly applicable to welded joints, the Goodman method has been implemented in methods $S2$ and $T2$. This is done to show what the choice of Walker does to improve upon Niesłony's proposed method. They serve as extra steps between no mean stress correction ($S1$, $T1$) and a detailed mean stress correction which includes material parameters ($S3$, $T3$).

The fatigue damage has been calculated according to the methods discussed above. For the top deck, waterline and bottom node (figure 6.6), the methods are compared with each other in figure 6.12. The methods are compared to the Rayleigh-based spectral damage method

Table 6.2: Desciption of the six MSE methods.

Method	Rainflow/Rayleigh	MSE Approach
S1	Rayleigh	None
S2	Rayleigh	Niesłony + Goodman
S3	Rayleigh	SWBM, $S_\sigma(\omega)$, Niesłony + Walker (Novel)
T1	Rainflow	None
T2	Rainflow	Global SWBM Goodman
T3	Rainflow	Local Walker

of $S1$. It can be stated that, from $S1$ to $T3$ (left to right), complexity is increased. The most 'simple' case of $S1$ therefore serves as a good point of reference; other methods improve upon it. The individual methods can also be compared to each other quite easily as each damage is divided by D_{S1}.

Top Deck Node

The results for the top deck node are displayed in figure 6.12a. For $S1$, the conservatism of the spectral approach becomes clear. It has an 11% higher damage than $T1$. When including the *global* Niesłony + Goodman mean stress ($S2$), a 24% higher damage is reached. The novel spectral approach $S3$ brings the damage down to 0.5% compared to $T1$, but still differs around 8% with the detailed time domain Walker method $T3$.

$T2$ shows that a 11% increase in damage is the result of introducing Goodman with the *global* SWBM included. Recalling the previous chapter, a global hogging SWBM is present, causing the mean stress correction to be higher than 1 in order to account for it. For $T3$, the result is 7% below $T1$. This shift in damage indicates mostly the effect of shifting from Goodman to Walker. The material's sensitivity to mean stress is accounted for ($\gamma = 0.92$), resulting in lower mean stress corrections. This is mostly due to the partially compressive course the top deck node experiences. These cycles lower the fatigue damage substantially. Recalling figure 6.5a, one can see that a substantial amount of cycles are located beneath $r_{lr} = 0$, which leads to a K_W-value smaller than 1; a decreasing effective stress. For the top deck node, it is evident that these cycles play a large role in reducing the damage.

Waterline Node

The node at the waterline is close to the neutral axis of the midship section. The global mean stress is therefore close to zero. With $S1$, a 17% increase of the damage occurs. Comparing $S1$ to $S2$, there is once again no notable influence of the mean stress because the global mean stress is zero. Using the novel spectral approach, $S3$ actually shows a good accordance with $T3$; only a 2% higher damage.

When comparing $T2/T1$, the effect of mean stress is indeed negligible. When accounting for local mean values using Walker, $T3$ shows that a reduction of 18% in damage is at hand.
It must be stated that at the waterline, damages were significantly small compared to the top deck and bottom locations. They therefore do not contribute much to the total damage done by the NSX component.

Bottom Node

Moving to the bottom, a compressive mean stress is at hand due to the hogging SWBM. The spectral approach is once again conservative ($S1/T1$: +11%), but damages also decrease when introducing the compressive mean stress. $S2$ equals $T1$ while $S3$ is even more decreased (-9%). In this case, $T3$ and $S3$ are not in line; $S3$ is 22% higher.
Given the definition of both the Goodman and Walker correction (eq. 3.11 and 3.15), damages are to be decreased. $T2$ does indeed decrease the damage compared to $T1$ by 9% and $T3$ has decreased even more: 25%.

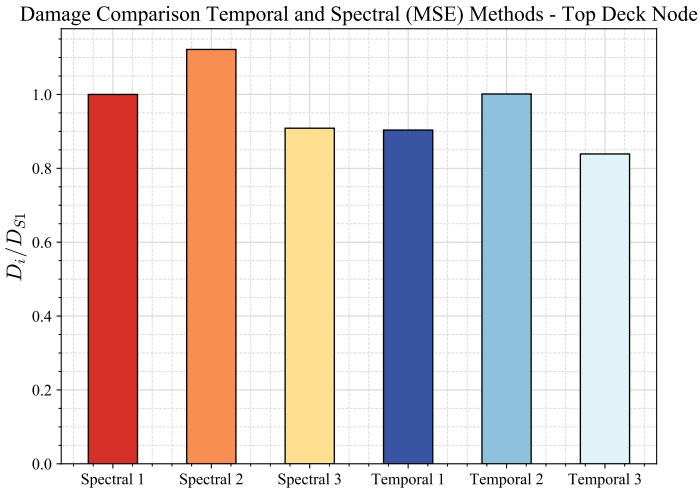

(a)

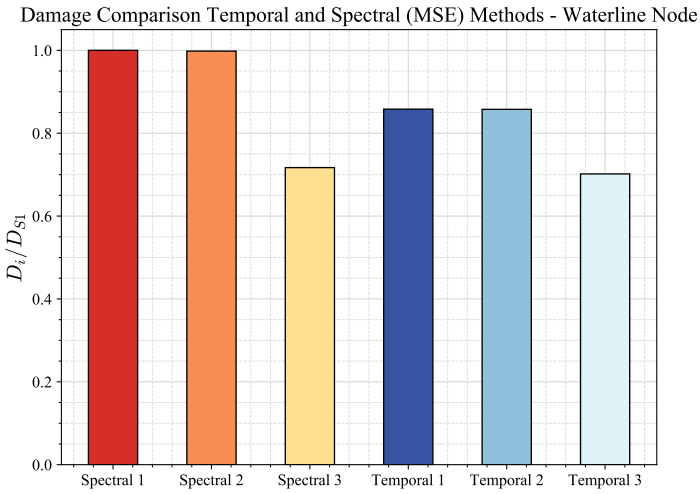

(b)

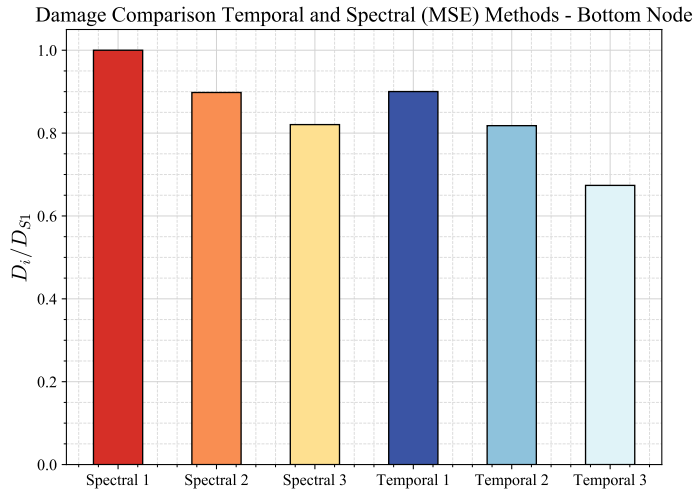

(c)

Figure 6.12: Damage comparison for the six MSE methods for the top deck (a), waterline (b) and bottom node (c).

Full Node Set

For the full node set, the damage values of the three spectral methods $\{S1, S2, S3\}$ are compared with the local Walker time domain method $T3$. Figure 6.13 shows this comparison. The D_i/D_{T3} value is plotted for every node over the nondimensional ship height z/D_{ship}. For every data set $(S1, S2, S3)$, the mean value of D_i/D_{T3} is calculated.

For each data set a large scatter showed around the waterline, even though mean stress and stress range levels have shown to be quite small here. The fact that they are small is the cause of this scatter. For some nodes, mean stress and stress range levels approach the limit of the software's precision (< 1 MPa). Resulting damages around the waterline calculated for the different methods ended up being in the order of magnitude of 1E-100. They were therefore considered to be negligible with respect to the nodes closer to the outer fibres, which showed orders of magnitude of around 1E-5 to 1E-8. Therefore, a filter was set at 1E-8. If a damage of a node for a certain method would go below this threshold, the result was filtered out. The filtered plot of figure 6.13 therefore shows no data points around the waterline. The unfiltered plot is provided in appendix C.7, figure C.13.

Looking at figure 6.13, the course of the damage over the ship height is observed. For $S1$, above the waterline the damage difference is around $1.2T3$. Moving below the waterline, this difference increased towards around $1.5T3$. This difference is due to the fact that there is no mean stress effect correction done in this method. Compressive cases therefore end up having a much higher damage. For $S2$, a linear course shows above and below the waterline. Because the Goodman method does not differentiate between tensional and compressive cases, the difference with $T3$ grows substantially beneath the waterline. As $S3$ incorporates the Walker correction, the results lie much closer to $T3$. Therefore, no big leap shows when moving below the waterline.

Regarding the mean values of each set, one can see that $S3$ lies the closest to $T3$ with a mean value of $1.16T3$. After that, $S1$ and $S2$ follow close to each other at $1.35T3$ and $1.34T3$.

For the specific wave case and side shell selection, the adoption of the novel spectral approach over the conventional spectral mean stress corrections provides a mean reduction in conservatism of **21%**. Comparing $S3$ with $T3$, a difference of 16% is still present. As $S3$ has used a spectral approach with the VA time trace of $T3$ as input, this percentage gives a clear indication of the conservatism of the pure conservatism of the proposed spectral approach. The adoption of a global mean stress value in the form of $\sigma_{m,SWBM}$ also contributes to this conservatism, as shown in section 6.1.6.

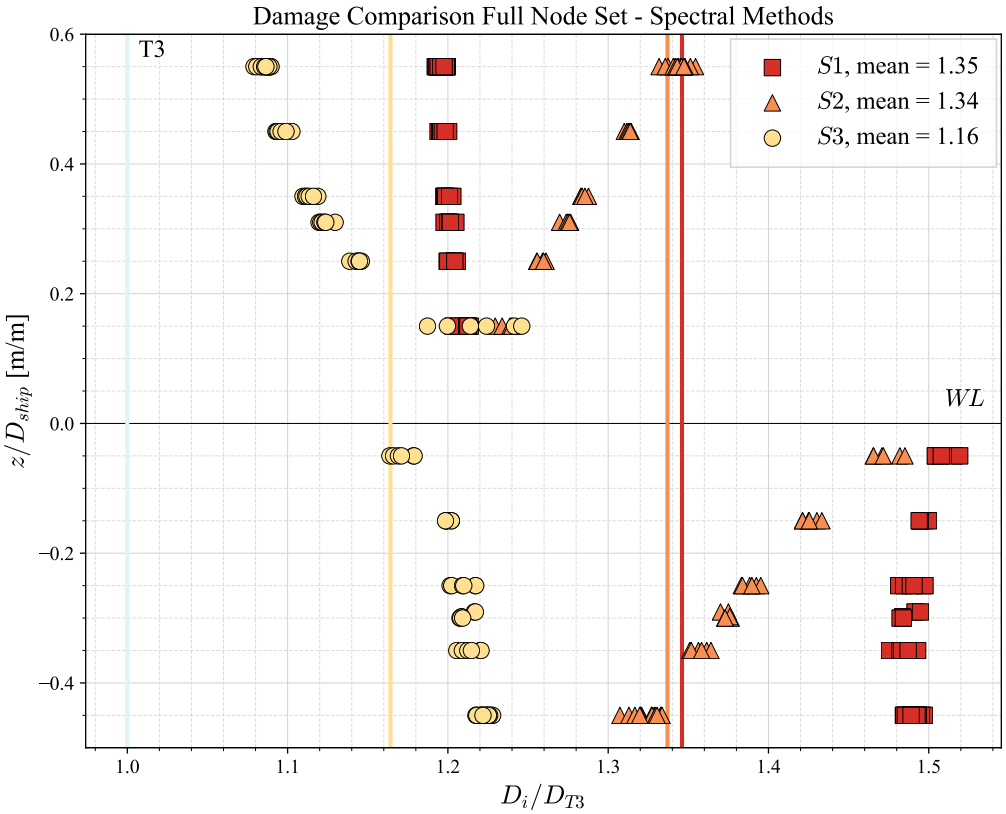

Figure 6.13: Comparison of the three spectral methods $\{S1, S2, S3\}$ against the detailed local Walker time domain method $T3$. Damages below 1E-8 are filtered out. Unfiltered plot in appendix C.7.

6.3 Concluding Remarks

In this chapter, the novel spectral approach has been constructed. The main objective of this approach is to incorporate new, detailed mean stress information into the spectral approach. A first step in this direction was to analyse the rainflow data of the 3-hour stress signal for wave case $JS(V_s = 3\ kn, H_s = 5\ m,\ T_p = 7.5\ s,\ \gamma = 3.3)$. Frequency content of each cycle was added to the analysis by using the starting and end step of each cycle. Thorough attention was paid to the underlying relations of the rainflow data $\{\Delta\sigma, \sigma_m, \omega\}$. The damage of each cycle was also evaluated with respect to the frequency and loading & response ratio r_{lr}.

For the top deck, waterline and bottom node, the analyses have been carried out. The mean stress behaved in a quasi-constant manner over increasing stress range and also frequency. Furthermore, no clear relations between the frequency and any of the other rainflow data was found. The attempt to form a general $r_{lr}(\omega)$ formulation was therefore not feasible.

The quasi-constant mean did however give an indication on the validity of adopting a single, global mean stress for the spectral model. By comparing the variance of the mean stress data with that of the stress range data, it turned out that this ratio, over the entire node set, was quite small. Also given the fact that the stress range still contributes the most to the fatigue damage, the quasi-constant assumption was adopted.

From a spectral approach perspective, local mean stress data is not available. Given the quasi-constant adoption, a simplified mean stress input was pursued. The still water bending moment-induced mean stress ($\sigma_{m,SWBM}$) turned out to be a good representation of the actual mean value of the time trace as well as the rainflow mean. The comparison showed a mean difference of 7% compared to the global mean and 12% when compared to the rainflow mean.

These differences were accepted.

The adoption of the global mean stress correction over a local one was also justified by comparing the two. Over the ship height, differences in damage by the *global* and *local* were checked using the Gerber and Goodman. Maximum difference was found for Goodman at the outer fibres; around +2.5%. This difference was also accepted and the Goodman method was selected for further comparisons.

With the justification of using $\sigma_{m,SWBM}$, along with the stress response spectrum $S_{\sigma,VA}(\omega)$ as input for the stress range, the novel spectral approach was constructed ($S3$). It has been compared against two other frequency domain methods ($S1$ and $S2$) and three time domain methods ($T1$, $T2$, $T3$). The order of the methods was with increasing detail. It was found that the novel spectral approach reaches fatigue damage estimations closer to the detailed $T3$ method than its predecessors $S1$ and $S2$. Over the ship height, the damage values at the selected nodes have been evaluated. The adoption of the novel spectral approach provided a mean reduction in conservatism of 21%; a fair amount.

6.3.1 Sub-Question 2

The analysis regarding the rainflow mean stress (section 6.1)) has enabled the second sub-question to be answered. Sub-question 2 states:

What are the consequences of nonlinear mean stress response contributions for the fatigue damage?

To answer this question, the NLFK force influence was investigated in the previous chapter. Here, the NLFK component was emulated by adopting a 2nd-order Stokes CA wave, while the linear case was characterised by a 1st-order Airy wave (section 5.5.1).

For the VA analysis, the NL and L cases were marked by the temporal and spectral approach, respectively. This was summarised in table 5.3. The CA and VA mean stress data have been evaluated in their respective sections (5.6, 6.1).

For both the CA and VA cases, it was observed that nonlinear mean stress contributions were small compared to the more damage inducing stress range. For the CA analysis, the largest NL/L differences were encountered at the outer fibres.
With the VA rainflow data, it became clear that the mean stress is quasi-constant over increasing stress range and frequency. For the spectral approach, which was the linear case, no mean stress information is available at all. A linear implementation of the SWBM-induced mean stress was justified because of the small nonlinear influences on the mean stress.

These findings have led to the answer to sub-question 2:

Nonlinear mean stress response-induced fatigue damage is small for the considered CA and VA cases. Adopting a global mean is therefore justified.

Following this conclusion, with regards to the NLFK-induced mean stress response damage, **H2** is *accepted*.

6.3.2 Sub-Question 3

The final section of this chapter has covered the performance of the novel spectral approach (*S*3). Section 6.2.1 has shown that, in comparison to the detailed time domain method with the local Walker mean stress effect included, the novel spectral approach offers a reduction in conservatism of 21%.

Sub-question 3 states:

Can state-of-the-art WB correction, spectral MSE, stress assessment concept, and (nonlinear) damage accumulation methods be combined to produce a novel spectral approach with improved accuracy?

In retrospect, the construction and verification of the time domain hydrodynamic and structural model took substantial time. The novel spectral mean stress approach was constructed afterwards and therefore the other goals, being the adoption of WB correction, stress assessment concept and nonlinear damage accumulation, have not been reached within time. Chapter 8 will elaborate further on this.

The construction and comparison of the novel spectral mean stress approach has led to the answer of sub-question 3:

> A spectral mean stress model which uses the still water bending moment and stress response spectrum to perform a Walker correction is able to reduce conservatism of previous spectral methods by 21% for the pontoon midship side shell section. With respect to the time domain benchmark case, a difference of 16% remains.

With this conclusion, **H3** is *partially accepted*. The novel spectral approach has showed an improvement. However, this only covered a better implementation of the mean stress. WB correction, stress assessment concept and nonlinear damage accumulation methods are yet to be combined and applied. Due to the extensive time the construction of the hydrodynamic and structural model took, the goal of applying these models has not been reached within time.

III

Judgement and Perspective

Chapter 7

Evaluation

This thesis has provided research findings in the field of nonlinear contributions to hydrodynamic loading & structural (mean stress) response, as well as their implementations in a novel spectral fatigue analysis. The focus on nonlinear contributions to the mean stress response originated from a comprehensive review of the literature on temporal and spectral fatigue analysis. In the constructed model, time domain simulations were carried out to provide a verification data set and to form the basis of the novel spectral approach.

Initially, the time domain data set was to be compared to spectral results provided by Damen Naval. Upon comparison, differences between the stress response spectra of the two sets were too large not to expect an error. The cause has been narrowed down to the hydrodynamic module of *Ansys AQWA*. When shifting from a CA to a VA wave analysis, a large discrepancy occurs. As of now, the error has not been fixed.
Nonetheless, the research was continued using the variable amplitude time domain data, as its spectrum served to continue the research on mean stress. These data were used to construct the novel spectral approach.

With the model constructed in chapter 5, it was performed and reviewed in chapter 6. The conclusions drawn in both chapters have enabled the answering of the three sub-questions. The main research question is then answered. This is all done in the following section; 7.1. Then, the discussion points of this thesis are evaluated in section 7.2. With the conclusion of this thesis, chapters 8 and 9 will provide recommendations and discuss the future outlook for mean stress effects in temporal and spectral fatigue analysis.

7.1 Conclusions

Sub-questions 1, 2 and 3 were answered in sections 5.9.1, 6.3.1 and 6.3.2. In addition, for each sub-question, a hypothesis was formulated. The conclusions regarding them are summarised below.

SQ1

How does the NLFK force affect the mean stress response?

The global hull girder bending component induces the largest NL/L difference for the mean stress. This occurs at the outer fibres, where for the load case of head seas, NL/L mean stress differences rised over increasing wave height. The maximum NL-induced mean stress response was however small in comparison to the global mean stress and the stress ranges.

H1

NLFK force effects will be most dominant around the waterline of the ship structure.

Rejected - For this model, NL effects around the waterline were found to be small compared to those at the outer fibres.

SQ2

What are the consequences of nonlinear mean stress response contributions for the fatigue damage?

Nonlinear mean stress response-induced fatigue damage is small for the considered CA and VA cases. Adopting a global mean is therefore justified.

H2

The NLFK force has an increasing influence on the mean stress response and therefore fatigue damage.

Accepted - For the chosen head seas load cases the NL stress response at the outer fibres was observed to be slightly larger than the L response.

SQ3

Can state-of-the-art WB correction, spectral MSE, stress assessment concept, and (nonlinear) damage accumulation methods be combined to produce a novel spectral approach with improved accuracy?

A spectral mean stress model which uses the still water bending moment and stress response spectrum to perform a Walker correction is able to reduce conservatism of previous spectral methods by 21% for the pontoon midship side shell section. With respect to the time domain benchmark case, a difference of 16% remains.

H3

As state-of-the-art NG correction, spectral MSE, stress assessment concept, and (nonlinear) damage accumulation methods individually improve fatigue damage accumulation, combining them will also yield improved results.

Partially Accepted - The novel spectral MSE model yields results closer to the detailed time domain model than conventional spectral MSE methods. The application of the novel WB, NLDAM and ENSC methods was, however, not reached.

7.1.1 Main Research Question

The main research question stated:

How can the nonlinear Froude-Krylov loading & response-affected mean stress as well as the fatigue resistance consequences be incorporated in a spectral fatigue analysis?

In this question, a loading & response, fatigue damage, and spectral approach improvement part were distinguished. The three sub-questions have reflected these parts. With SQ1 and SQ2, the NLFK-induced mean stress response and damage consequences were investigated for global hull girder bending and a critical wave case of head seas. It was found that nonlinear mean stress response effects are quite small compared to the damage-governing stress range. Largest effects were observed at the midship's outer fibres. A quasi-constant mean stress was observed over the rainflow stress ranges, justifying the use of a single-value global mean input. This input took the form of the still water bending moment-induced mean stress; a parameter easily obtainable when operating solely in the frequency domain.

The findings of the three sub-questions have led to the answer to the main research question:

For the presented model, the nonlinear Froude-Krylov-affected mean stress effect is small compared to the damage-governing stress range. This enables the input of the still water bending moment-induced mean stress in combination with the stress response spectrum to construct a novel spectral approach using Walker's correction. For a pontoon vessel, over a midship side shell selection, this approach provides a mean reduction in conservatism of 21% compared to conventional spectral methods.

7.2 Discussion

The conclusion provides a promising outlook with regards to an efficient implementation of the Walker mean stress model into the spectral approach. However, before a future outlook can be formed, a discussion which reflects on the methodology and results will be formulated. After the discussion, chapter 8 will elaborate on the recommended next steps in succession of this thesis.

Stress Response Discrepancy

Upon comparing the VA temporal stress response spectrum to the spectral stress response spectrum, large differences were observed. With the pseudo-time domain method actually being in line with the spectral results, the cause of this discrepancy has been narrowed down to the *hydrodynamic* model, when shifting from a CA to a VA analysis (section 5.8.3). The error has however not been solved.

The construction of the novel spectral approach was continued with the VA temporal spectrum. As the novel spectral approach has been verified against the actual time domain data the stress spectrum was coming from, the results have shown what the 'real' differences are between both the time domain and frequency domain method. The mean difference between $S3$ and $T3$ of 16% (figure 6.13) can be considered to be a 'minimal' difference between temporal and spectral mean stress fatigue methodology because the spectrum came directly from the actual time trace.

The method is expected to also work when applied to the (Damen Naval) spectral data set. However, this would only be possible if the temporal and spectral spectra lined up in an expected way. The time domain spectrum would then lie beneath that of the spectral approach [7]. In that case, a smaller reduction in conservatism is expected because the spectrum on which the model is applied would be conservative with respect to the 'actual' time domain spectrum.

Ship Model

The ship model considered in this thesis is that of a Damen pontoon vessel (figure 5.1) [1]. As stated by Wang [5] and covered in section 2.4.4, the more nonlinear a hull shape is (larger bow flare, smaller block coefficient), the more nonlinear hydrodynamic forces will play a role (slamming, NLFK). With a block coefficient of 0.93, the pontoon model can be considered to have a quite linear hull shape.

Nonlinear effects have proven to be quite small during different simulations along the course of this thesis. The pontoon's hull shape is expected to be a large contributor to this.

The pontoon model was selected because the FEM models of naval vessels were not made available by Damen Naval due to confidentiality reasons. Furthermore, the spectral data set which was to be compared with the novel time domain model was based on the same pontoon model [1]. This provided a convenient comparison case.

Overall, the linear hull shape of the pontoon model has made for a base case to which more nonlinear hull shapes can be tested.

NL/L FK Modelling

For the CA analysis, the influence of the nonlinear versus the linear Froude-Krylov force (NL/L FK) was investigated. Bound to the limitations of the available software, the only way to formulate the NL/L cases was by applying Stokes 2^{nd}-order (NL) and Airy 1^{st}-order (L) waves. The difference between these waves was discussed in section 5.5.1. With this methodology, the pure (NL/L) FK force was not isolated. The NL/L response effect was observed due to the different waves altering the wave potential, and subsequently the pressure distribution.

This way of modelling NL/L waves was accepted for this thesis, but isolating the NL/L FK force would give a better indication on the actual contributions. The same goes for the variable amplitude case, where only nonlinear wave modelling was available within the software.

Fourier Transform

Section 5.7.2 covered the convergence study of the stress response. For the raw VA temporal stress signal, the zero-frequency component indicated the mean value. This component did not converge over increasing simulation time; it kept rising linearly. Upon removing the mean, the statistical content of the stress response did in fact converge after roughly 2 hours of simulation time.

The lack of convergence for the mean lies within the Fourier transform code. It seems to be incapable of dealing with zero-frequency mean components. New checks are needed to uncover where this error exactly lies.

As the variance did in fact converge, and further calculations were performed with the converged removed-mean spectrum, the error was accepted.

Chapter 8

Recommendations

Following the discussion points that concluded the previous chapter, this chapter will go over the recommendations for future research. Chapter 9 will conclude this thesis by going over the opportunities of implementing the presented model.

8.1 Response Spectra Discrepancy

One of the major obstacles that was encountered in this thesis was the discrepancy between the time and frequency domain spectra 5.8.3. The cause of the error was narrowed down to the shift from CA to VA waves; a substantial increase in response was observed.

Before new time domain simulations are performed, it is of great importance to find the cause of this discrepancy. Only then, the model can be fully accepted and verification can be completed.

8.2 Ship Model

As discussed, the hull shape of the pontoon is strongly linear due to its box-like shape. It is expected that this caused the weak nonlinear contributions to the hydrodynamic response. In order to obtain and research higher nonlinear behaviour, new ship hulls need to be addressed. According to Wang, slender ships with a high bow flare will encounter more nonlinear hydrodynamic forces [5]. Naval vessels fit this profile, and therefore need to undergo the same procedure as presented in this thesis [1]. The findings regarding the pontoon will serve as a base case to which the more nonlinear hull shapes can be compared. It is expected that these vessels demonstrate significant NL loading and response due to their hull shapes [5].

8.3 Slamming

In section 2.4.4, dominant contributors to the NL hydrodynamic force were discussed. Wang identified the NL FK and slamming force as the leading contributors in NL loading [5]. Tuitman constructed a time domain model incorporating slamming to a detailed extent [27].

When the model presented in this thesis is applied to naval vessels, it is recommended to incorporate slamming for the more extreme load cases. For an accurate representation of the slamming added mass, the time step should be sufficiently small [56].

Considering the above, a naval vessel model would require mesh refinements at the critical locations, as well as shorter time steps in order to capture nonlinear effects better. This will be at the expense of additional computational time and file size. In the end, a compromise between time consumption and detail has to be made.

Regarding the available software at Damen Naval, *Ansys AQWA* makes use of a 'slamming factor', which is user defined [32]. A combination of the seakeeping software of *AQWA* and Tuitman's slamming model would make for a much more detailed model, capable of incorporating slamming nonlinearities for naval vessels.

8.4 Novel Fatigue Models

The answer to sub-question 3 (**SQ3**) stated that the goal of implementing multiple fatigue models was not fully met. The application of the wide-band (WB), the effective notch stress concept (ENSC) and nonlinear damage accumulation (NLDAM) models was not reached.

For further research and implementation, it is therefore recommended to add the above methods to the novel spectral approach. As Deul combined the ENSC with NLDAM, it was recommended to apply the Walker mean stress in addition [10]. As this has been one of the focus points of this thesis, there remains an interesting opportunity of combining both models and reduce conservatism further by increasing accuracy.

Mesh

It must be noted that the mesh of the presented model was quite coarse. For the considered side shell, mesh panels were roughly 0.5 by 0.5 metres. Accurate fatigue assessment at hot spot structural details can only be carried out when mesh refinements are performed. An accurate stress representation can then be obtained which is to be used as input to the ENSC. To prevent the structural mesh from becoming too large, submodelling can be applied [59].

8.5 Long Term Fatigue Damage

The presented time domain model performed simulations for a total of 3 hours; a short-term period regarding fatigue damage. As discussed in section 2.1.2, the long-term seakeeping of a vessel is typically emulated by the summation of multiple short-term cases.

In order to extend the presented model to the long-term, additional 3-hour runs need to be performed for multiple wave cases, depending on the ship's operational profile. This will give a better view on the critical cases of the ship and the resulting fatigue damage.

For the short-term, the Rayleigh-distributed stress range assumption is typically adopted. The long-term distribution is based on this assumption and takes on the shape of the 2-parameter Weibull distribution [8]. Literature and the time domain simulations have shown that nonlinear response translates into wide-banded, non-Gaussian spectra. For nonlinear long-term loading & response, it must be made sure that the long-term Weibull distribution still holds.

8.6 Operational Profile

As stated in section 2.1.2, the long-term is modelled as a large number of stationary short-term sea states, each with their own probability of occurrence. In the presented research, only one short-term wave case was addressed; a JONSWAP spectrum with $\{H_s,\ T_p\} = \{5\text{ m},\ 7.5\text{ s}\}$. This is quite a high sea state, and its probability of occurrence is likely to be quite low. In the long-term, milder sea states (e.g. $H_s = 1$ m) contribute much more to fatigue damage because they occur more often [8].

Therefore, more short-term sea states must be evaluated according to the presented methodology. An actual ship operational profile will provide information on which sea states are the most prevalent. Reviewing these cases will enable a wider verification of the novel spectral approach. For the $H_s = 5$ m wave case, it was found that the stress range contributed the most to fatigue damage. It is expected that the mean stress will play a larger role for the milder cases where stress ranges are smaller. Because the mean stress is expected to stay inside the vicinity of $\sigma_{m,SWBM}$, $\sigma_m/\Delta\sigma$ will increase, leading to a larger contribution of the mean stress effect to the damage.

8.7 Automation

Following the need for numerous time domain wave cases, automation becomes a pressing issue. Section 5.2.1 elaborated on the level of automation for the time domain model. Working with *ANSYS Workbench*, automation did not reach a level at which a single wave case specification could be used as input and the stress results were outputted.

As the time frame of this thesis did not allow it, additional research in the field of automation is required, specifying in the underlying code used to steer *Ansys Workbench*. For data extraction, the result file (.RST) of *Ansys Mechanical* can be exploited. When fully automated, multiple wave cases could be run and extracted. A computational cluster would be required for this, as RAM and data storage capacity quickly became an issue when working from a local PC.

Chapter 9

Implementation

The presented research has shown that a rather simple input parameter, the SWBM-induced mean stress, is able to capture mean stress effects quite well when working solely in the frequency domain. As discussed in the recommendations, more research is required to provide additional verification and therefore certainty to these findings. Only then, the novel spectral approach can be applied in combination with the other state-of-the-art fatigue models (WB correction, ENSC, NLDAM) to arrive at a highly-detailed fatigue life model. This chapter will provide a perspective on step-by-step future work required to achieve this goal.

9.1 Road map

The future perspective for the continuation of this research is depicted in the road map of figure 9.1. Within this road map, three separate models on which research is to be performed are shown: *'Slamming Model'*, *'Pontoon'* and *'Naval Vessel'*. For the *Pontoon* model, solving the discrepancy between the time and frequency domain results (section 5.8.3) has the highest priority. Simultaneously, automation efforts like addressed in the recommendations should be carried out.

When these two steps are taken, new wave cases can be added to the analysis, focusing on the milder cases in which the mean stress will become more prevalent. This will provide a better argument on the relevance of incorporating mean stress.

Within the *Slamming* model, additional research should be done on how effective the slamming factor of *Ansys AQWA* actually is. Should this be insufficient due to the operational profile (e.g. high probability of slamming occurring), then additional slamming modelling is required. A feasibility study on new software to incorporate slamming in more detail should be carried out. When its significance is demonstrated, the slamming model can be implemented in the calculation of new wave cases.

With multiple cases performed, novel fatigue models (WB, ENSC, NLDAM) should be applied in addition to the novel Walker model presented in this thesis. Then, the extension to the long-term damage can be made. The model should then be verified against conventional methodology and approval from class needs to be obtained.

Research can then be continued by using more nonlinear hull shapes; naval vessels. For these ships, it is expected that the novel spectral approach will still aid in incorporating the mean stress effect in the spectral approach. As of now, DNV regulations adopted by Damen Naval do not incorporate an increasing mean stress for welded joints when subjected to large tensional mean stresses [11]. This is an underestimation, as higher mean stresses can in fact contribute to the fatigue damage substantially. On the other hand, it has been shown that by incorporating the Walker correction, compressive (thermal residual) mean stresses and welding imperfections are accounted for more accurately in the MCF and HCF region [3, 16], leading to lower damages.

In the end, the adoption of the proposed spectral mean stress model in combination with state-of-the-art fatigue models will help to reach more accurate fatigue lifetime estimates.

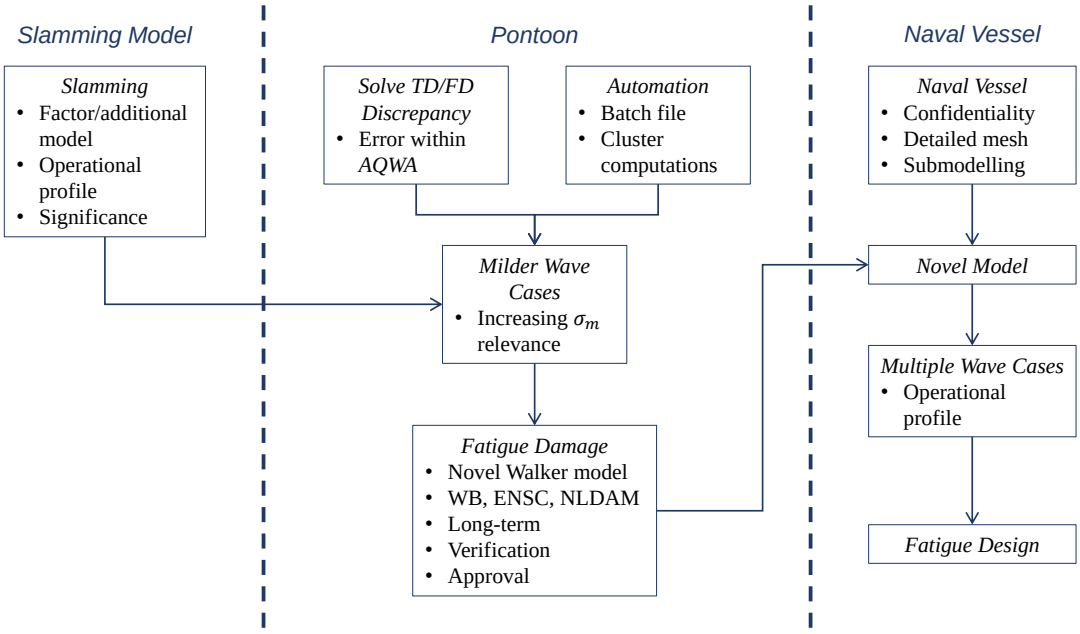

Figure 9.1: Road map of implementing recommended steps.

Bibliography

[1] A. Luna García-Valenzuela. *Automated Spectral Fatigue Analysis for Floating Structures*. Tech. rep. Hamburg: Hamburg University of Technology, Oct. 2019.

[2] A. Halfpenny. *A frequency domain approach for fatigue life estimation from Finite Element Analysis*. Tech. rep. Sheffield, 1999.

[3] Y. Qin, H. den Besten, S. Palkar, and M. L. Kaminski. "Mid- and High-Cycle Fatigue of Welded Joints in Steel Marine Structures: Effective Notch Stress and Total Stress Concept Evaluations". In: *International Journal of Fatigue* 142 (Jan. 2021). ISSN: 01421123. DOI: 10.1016/j.ijfatigue.2020.105822.

[4] F. Bigot, S. Mahérault-Mougin, and Q. Derbanne. *Comparison of different models for the fatigue analysis of details subject to side shell intermittent wetting effect*. Tech. rep. 2017. URL: https://www.researchgate.net/publication/307993317.

[5] L. Wang. *Probabilistic analysis of nonlinear wave-induced loads on ships*. Tech. rep. 2001.

[6] A. Niesłony and M. Böhm. *Mean stress value in spectral method for the determination of fatigue life*. Tech. rep. 2. 2012. URL: https://www.researchgate.net/publication/266886683.

[7] S. F. Mohammadi, N. S. Galgoul, U. Starossek, and P. M. Videiro. "An efficient time domain fatigue analysis and its comparison to spectral fatigue assessment for an offshore jacket structure". In: *Marine Structures* 49 (Sept. 2016), pp. 97–115. ISSN: 09518339. DOI: 10.1016/j.marstruc.2016.05.003.

[8] H. Den Besten. *Course on Fatigue Strength of Marine Structures*. Delft, 2020. URL: https://brightspace.tudelft.nl/d2l/home/279777.

[9] W. Fricke. "Fatigue and Fracture of Ship Structures". In: *Encyclopedia of Maritime and Offshore Engineering*. John Wiley & Sons, Ltd, Mar. 2017, pp. 1–12. DOI: 10.1002/9781118476406.emoe007.

[10] M. L. Deul. *Fatigue damage accumulation in steel welded joints, subject to (random) variable amplitude loading conditions An improved fatigue-life model for naval ship structural design*. Tech. rep. Delft: Delft University of Technology, July 2021. URL: http://repository.tudelft.nl/..

[11] DNV GL. *CLASS GUIDELINE Fatigue assessment of ship structures*. Tech. rep. 2015. URL: http://www.dnvgl.com,.

[12] *Defensievisie 2035 - Vechten voor een veilige toekomst*. Tech. rep. Ministerie van Defensie, Oct. 2020.

[13] Marineschepen.nl. *Anti-Submarine Warfare Fregatten (ASWF) | België en Nederland*. Jan. 2022. URL: https://marineschepen.nl/schepen/nieuwe-fregatten-2023.html.

[14] Marineschepen.nl. *F126 fregatten (Duitsland)*. Oct. 2021. URL: https://marineschepen.nl/schepen/mks-180.html.

[15] DNV-GL. *DIGITAL TWINS AT WORK IN MARITIME AND ENERGY*. Tech. rep. Oslo: DNV-GL, Feb. 2017. URL: https://www.dnv.com/Images/DNV%20GL%20Feature%20%2303%20ORIG2b_tcm8-85106.pdf.

[16] J. H. Den Besten. "fatigue resistance of welded joints in aluminium high-speed craft: A TOTAL STRESS CONCEPT". PhD thesis. Delft: Technische Universiteit Delft, 2015.

[17] Y. Qin, H. den Besten, S. Palkar, and M. L. Kaminski. "Fatigue design of welded double-sided T-joints and double-sided cruciform joints in steel marine structures: A total stress concept". In: *Fatigue and Fracture of Engineering Materials and Structures* 42.12 (Dec. 2019), pp. 2674–2693. ISSN: 14602695. DOI: 10.1111/ffe.13089.

[18] L. Holthuijsen. *Waves in oceanic and coastal waters*. Delft: TU Delft, Department Hydraulic Engineering, 2004.

[19] J. M. J. Journée and W. W. Massie. *OFFSHORE HYDROMECHANICS Second Edition*. Tech. rep. Delft: TU Delft, 2008.

[20] M. S. Longuet-Higgins. "On the Statistical Distribution of the Heights of Sea Waves". In: *Journal of Marine Research* XI.3 (1952), pp. 245–266.

[21] P. Naaijen and P. Wellens. *Course on Motions and Loading of Structures in Waves*. Delft, 2020. URL: https://www.studiegids.tudelft.nl/a101_displayCourse.do?course_id=60305.

[22] J. Dronkers. *Statistical description of wave parameters*. Sept. 2020. URL: http://www.coastalwiki.org/wiki/Statistical_description_of_wave_parameters.

[23] DNVGL. *Environmental Conditions and Environmental Loads*. Tech. rep. Oslo, 2017. URL: http://webshop.dnv.com/global/,.

[24] S. Gao, X. Y. Zheng, B. Wang, S. Zhao, and W. Li. "Assessment of fatigue damage induced by Non-Gaussian bimodal processes with emphasis on spectral methods". In: *Ocean Engineering* 220 (Jan. 2021). ISSN: 00298018. DOI: 10.1016/j.oceaneng.2020.108489.

[25] A. Naess and T. Moan. *Stochastic Dynamics of Marine Structures*. Cambridge: Cambridge University Press, 2012. ISBN: 9781139021364. DOI: 10.1017/CBO9781139021364.

[26] DIN and ENISO. "19902: Petroleum and Natural Gas Industries-Fixed Steel Offshore Structures". In: *DIN Deutsches Institut fur Normung eV* (2008).

[27] J. T. Tuitman. "Hydro-elastic response of ship structures to slamming induced whipping." PhD thesis. Delft: Technische Universiteit Delft, Feb. 2010. ISBN: 9789090250311.

[28] M. I. Kvittem and T. Moan. *Time domain analysis procedures for fatigue assessment of a semi-submersible wind turbine*. Tech. rep. 2014.

[29] M. Nowacka. *Non-linear hydro load correction for Spectral Fatigue Analysis*. Tech. rep. Liége: University of Liége, 2019.

[30] Z. Li, W. Mao, J. W. Ringsberg, E. Johnson, and G. Storhaug. "A comparative study of fatigue assessments of container ship structures using various direct calculation approaches". In: *Ocean Engineering* 82 (May 2014), pp. 65–74. ISSN: 00298018. DOI: 10.1016/j.oceaneng.2014.02.022.

[31] S. Gao and X. Y. Zheng. "An improved spectral discretization method for fatigue damage assessment of bimodal Gaussian processes". In: *International Journal of Fatigue* 119 (Feb. 2019), pp. 268–280. ISSN: 01421123. DOI: 10.1016/j.ijfatigue.2018.09.027.

[32] ANSYS Inc. *Aqwa Theory Manual*. Canonsburg: ANSYS Inc., Jan. 2020.

[33] J. A. Pinkster. "LOW FREQUENCY SECOND ORDER WAVE EXCITING FORCES ON FLOATING STRUCTURES". PhD thesis. Delft: Technische Hogeschool Delft, 1980.

[34] P. F. Hansen and S. R. Winterstein. *Fatigue Damage in the Side Shells of Ships*. Tech. rep. 1995.

[35] G. Giorgi and J. V. Ringwood. "Nonlinear Froude-Krylov and viscous drag representations for wave energy converters in the computation/fidelity continuum". In: *Ocean Engineering* 141 (Sept. 2017), pp. 164–175. ISSN: 00298018. DOI: 10.1016/j.oceaneng.2017.06.030.

[36] H. K. Jang and M. H. Kim. "Effects of nonlinear FK (Froude- Krylov) and hydrostatic restoring forces on arctic-spar motions in waves". In: *International Journal of Naval Architecture and Ocean Engineering* 12 (Jan. 2020), pp. 297–313. ISSN: 20926790. DOI: 10.1016/j.ijnaoe.2020.01.002.

[37] T. Dirlik. *Application of computer in fatigue analysis*. Tech. rep. Coventry, England: University of Warwick, Jan. 1985. URL: http://go.warwick.ac.uk/wrap/2949.

[38] D. Benasciutti and R. Tovo. "Cycle distribution and fatigue damage assessment in broad-band non-Gaussian random processes". In: *Probabilistic Engineering Mechanics* 20.2 (Apr. 2005), pp. 115–127. ISSN: 02668920. DOI: 10.1016/j.probengmech.2004.11.001.

[39] D. Benasciutti and R. Tovo. "Comparison of spectral methods for fatigue analysis of broad-band Gaussian random processes". In: *Probabilistic Engineering Mechanics* 21.4 (Oct. 2006), pp. 287–299. ISSN: 02668920. DOI: 10.1016/j.probengmech.2005.10.003.

[40] I. Lotsberg. *Fatigue Design of Marine Structures*. New York: Cambridge University Press, 2016. ISBN: 978-1-107-12133-1.

[41] Yapparina. *Rainflow counting vs stress-strain curve*. Nov. 2015. URL: https://upload.wikimedia.org/wikipedia/commons/3/3a/Rainflow_counting_vs_stress-strain_curve.svg.

[42] D. Gaia da Silva, J. T. Lockwood, W. Liang, and T. H. Topper. "Mean stress effect in stress-life for hard steels". In: *International Journal of Fatigue* 146 (May 2021). ISSN: 01421123. DOI: 10.1016/j.ijfatigue.2020.106101.

[43] J. Goodman. "Mechanics Applied to Engineering". PhD thesis. Leeds: University of Leeds, 1914.

[44] S. Kwofie. "An exponential stress function for predicting fatigue strength and life due to mean stresses". In: *International Journal of Fatigue* 23.9 (Oct. 2001). ISSN: 01421123. DOI: 10.1016/S0142-1123(01)00044-5.

[45] J. Papuga, I. Vízková, M. Lutovinov, and M. Nesládek. "Mean stress effect in stress-life fatigue prediction re-evaluated". In: *MATEC Web of Conferences*. Vol. 165. EDP Sciences, May 2018. DOI: 10.1051/matecconf/201816510018.

[46] J. Morrow. "Fatigue properties of metals". In: *Fatigue Design Handbook*. pub. No.AE-4. Warrendale, PA: Soc. Of Automotive Engineers, 1964. Chap. 3.2.

[47] K. Walker. "The Effect of Stress Ratio During Crack Propagation and Fatigue for 2024-T3 and 7075-T6 Aluminum". In: *Effects of Environment and Complex Load History on Fatigue Life*. 100 Barr Harbor Drive, PO Box C700, West Conshohocken, PA 19428-2959: ASTM International, 1970, pp. 1–14. DOI: 10.1520/STP32032S.

[48] N. E. Dowling. "Mean stress effects in strain-life fatigue". In: *Fatigue and Fracture of Engineering Materials and Structures* 32.12 (Dec. 2009), pp. 1004–1019. ISSN: 8756758X. DOI: 10.1111/j.1460-2695.2009.01404.x.

[49] D. P. Kihl and S. Sarkani. "Mean stress effects in fatigue of welded steel joints". In: *Probabilistic Engineering Mechanics* 14 (1999), pp. 97–104.

[50] T. Łagoda, E. Macha, and R. Pawliczek. *The influence of the mean stress on fatigue life of 10HNAP steel under random loading*. Tech. rep. 2001, pp. 283–291. URL: www.elsevier.com/locate/ijfatigue.

[51] D. Gao, W. Yao, W. Wen, and J. Huang. "A multiaxial fatigue life prediction method for metallic material under combined random vibration loading and mean stress loading in the frequency domain". In: *International Journal of Fatigue* 148 (July 2021). ISSN: 01421123. DOI: 10.1016/j.ijfatigue.2021.106235.

[52] H. Den Besten. *Fatigue damage criteria classification, modelling developments and trends for welded joints in marine structures*. Nov. 2018. DOI: 10.1080/17445302.2018.1463609.

[53] D. Leonetti, J. Maljaars, and H. H. Snijder. "Probabilistic fatigue resistance model for steel welded details under variable amplitude loading – Inference and uncertainty estimation". In: *International Journal of Fatigue* 135 (June 2020). ISSN: 01421123. DOI: 10.1016/j.ijfatigue.2020.105515.

[54] D. Leonetti, J. Maljaars, and H. H. Snijder. "Fitting fatigue test data with a novel S-N curve using frequentist and Bayesian inference". In: *International Journal of Fatigue* 105 (Dec. 2017), pp. 128–143. ISSN: 01421123. DOI: 10.1016/j.ijfatigue.2017.08.024.

[55] P. M. Kunz and G. L. Kulak. "Fatigue safety of existing steel bridges". In: *IABSE Rep* 73 (1995), pp. 1073–1078.
[56] ANSYS Inc. *Aqwa User's Manual Third-Party Software*. Tech. rep. 2020. URL: http://www.ansys.com.
[57] ANSYS Inc. *ANSYS AQWA Proven Technology for Design and Analysis of Mobile Offshore Structures*. Tech. rep. Canonsburg: ANSYS, Inc., 2010.
[58] ANSYS Inc. *Multi Object Export V1.1*. 2021. URL: https://catalog.ansys.com/product/5b3bc6857a2f9a5c90d32e7f/multi-object-expor?creator=ANSYS%20Inc.
[59] G. Bufalari. *Comparative study of multiaxial fatigue methods applied to welded joints in a container vessel*. Tech. rep. 2016.
[60] J. Christensen and C. Bastien. "Nonlinear Optimization of Vehicle Safety Structures". In: (2016), pp. 209–252. DOI: 10.1016/B978-0-12-804424-7.00005-1. URL: http://dx.doi.org/10.1016/B978-0-12-804424-7.00005-1.
[61] G. Haniotis. *Model Setup Verification*. 2022.
[62] G. B. Airy. "Tides and Waves". In: *Encyclopaedia Metropolitana* (1845), pp. 241–396.
[63] G. G. Stokes. "On the theory of oscillatory waves". In: *Transactions of the Cambridge Philosophical Society* 8 (1847), pp. 441–455.
[64] M. Dekking. *A modern introduction to probability and statistics : understanding why and how*. Springer, 2005, p. 486. ISBN: 1852338962.
[65] Scipy. *Fourier Transforms (scipy.fft)*. 2021. URL: https://docs.scipy.org/doc/scipy/reference/tutorial/fft.html.
[66] M. Ryan. *Brief Introduction of Hamming and Hanning Function as The Preprocessing of Discrete Fourier Transform*. Sept. 2019. URL: https://towardsdatascience.com/brief-introduction-of-hamming-and-hanning-function-as-the-preprocessing-of-discrete-fourier-8b87fe538bb7.
[67] R. B. Blackman and J. W. Tukey. "The measurement of power spectra from the point of view of communications engineering — Part I". In: *The Bell System Technical Journal* 37.1 (Jan. 1958), pp. 185–282. ISSN: 0005-8580. DOI: 10.1002/j.1538-7305.1958.tb03874.x.
[68] Numpy. *numpy.hamming*. 2021. URL: https://numpy.org/doc/stable/reference/generated/numpy.hamming.html.
[69] ABS. *GUIDANCE NOTES ON GLOBAL PERFORMANCE ANALYSIS FOR FLOATING OFFSHORE WIND TURBINES JULY 2020*. Tech. rep. New York: American Bureau of Shipping, July 2020. URL: www.eagle.org.
[70] ASTM. "Standard Practices for Cycle Counting in Fatigue Analysis". In: *ASTM E1049-85*. Vol. 03.01. ASTM, 2017.
[71] A. Niesłony. *Rainflow Counting Algorithm*. Feb. 2022. URL: https://nl.mathworks.com/matlabcentral/fileexchange/3026-rainflow-counting-algorithm?requestedDomain=.
[72] G. Bufalari. *Fast Fourier Transforms*. Delft, 2021.

Appendix

Appendix A

Literature - Rainflow Cycle Counting Algorithm

The algorithm for rainflow cycle counting based on a discretised peaks-valleys signal (figure A.1) is provided in the box below. This algorithm has been slightly modified to also include half cycles [8, 71]. Note that it is based on a *Matlab* language.

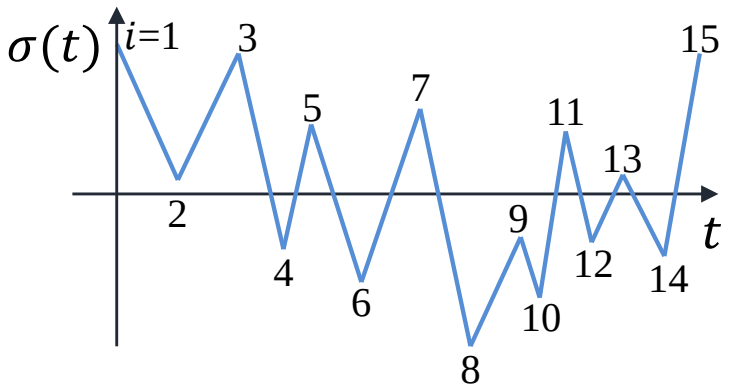

Figure A.1: Numbered peaks and valleys as input for the rainflow algorithm.

```
for i = 3:length(σ⃗)
    if |σ_i − σ_{i−1}| ≥ |σ_{i−1} − σ_{i−2}|
      Δσ_{i−1} = σ_{i−1} − σ_{i−2}
      σ_{m,i−1} = (σ_{i−1}+σ_{i−2})/2
       if σ_{i−2} = σ(1)
         N = 0.5; % remove σ_{i−2}
       else
         N = 1.0; % remove {σ_{i−1}, σ_{i−2}}
       end
    end
end
```

Appendix B

Ansys Model Details

B.1 Ship Details

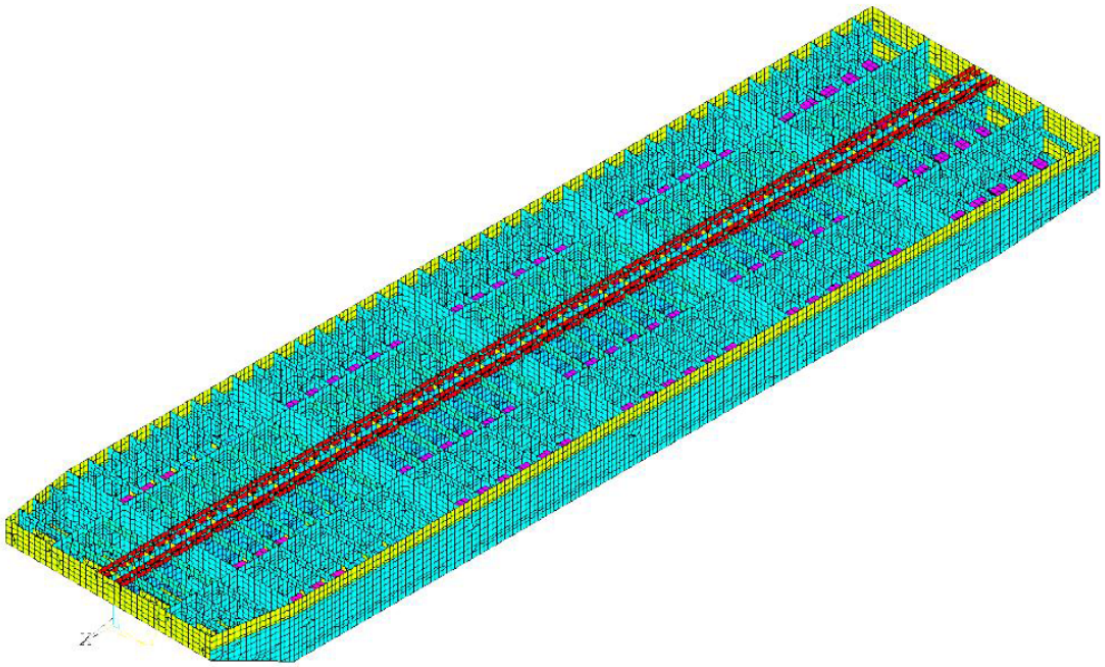

Figure B.1: The pontoon model with open deck, showing the internal structure [1].

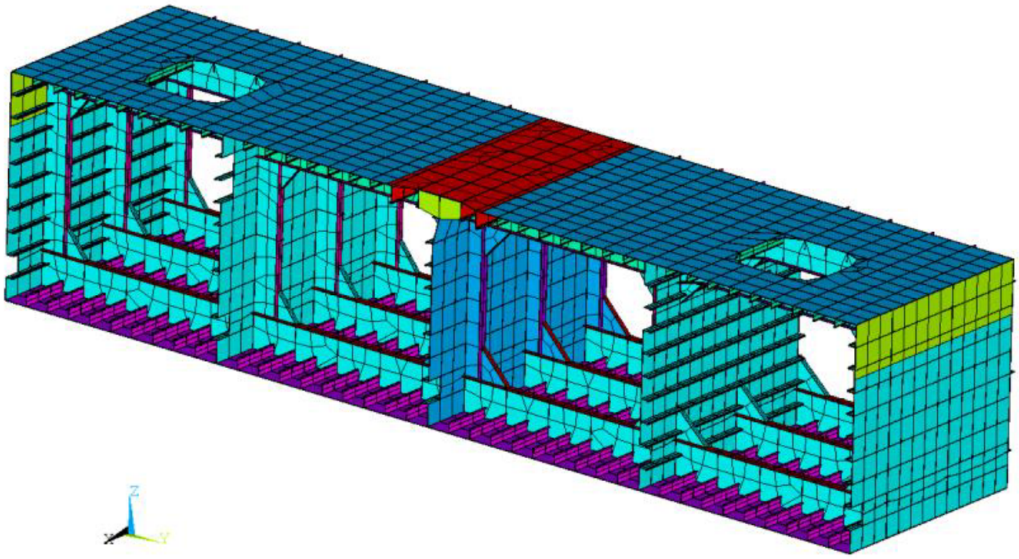

Figure B.2: The midship section of the pontoon model, showing multi-scale structural details [1].

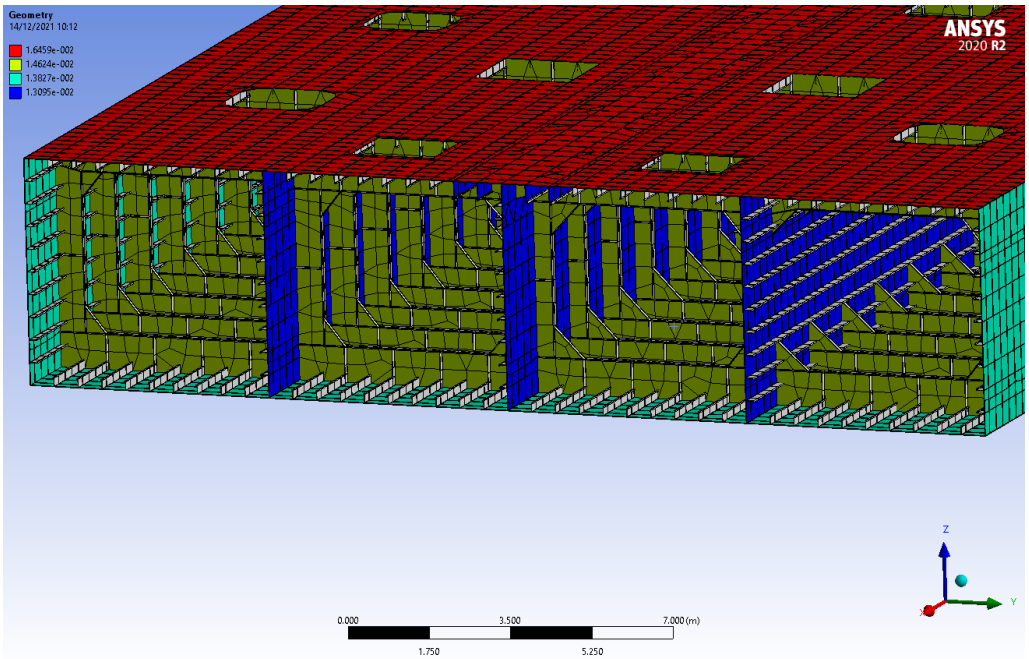

Figure B.3: Midship section plating thickness. {red, green, cyan, blue} = {16.5, 14.6, 13.8, 13.1} mm.

B.2 Project Layout

Two ANSYS models were produced for this research, considering CA and VA. For the CA model, two wave cases were applied: Airy waves (linear) and Stokes 2^{nd}-order wave (nonlinear). The Workbench layout for both projects is shown in the sections below.

B.2.1 Constant Amplitude Model

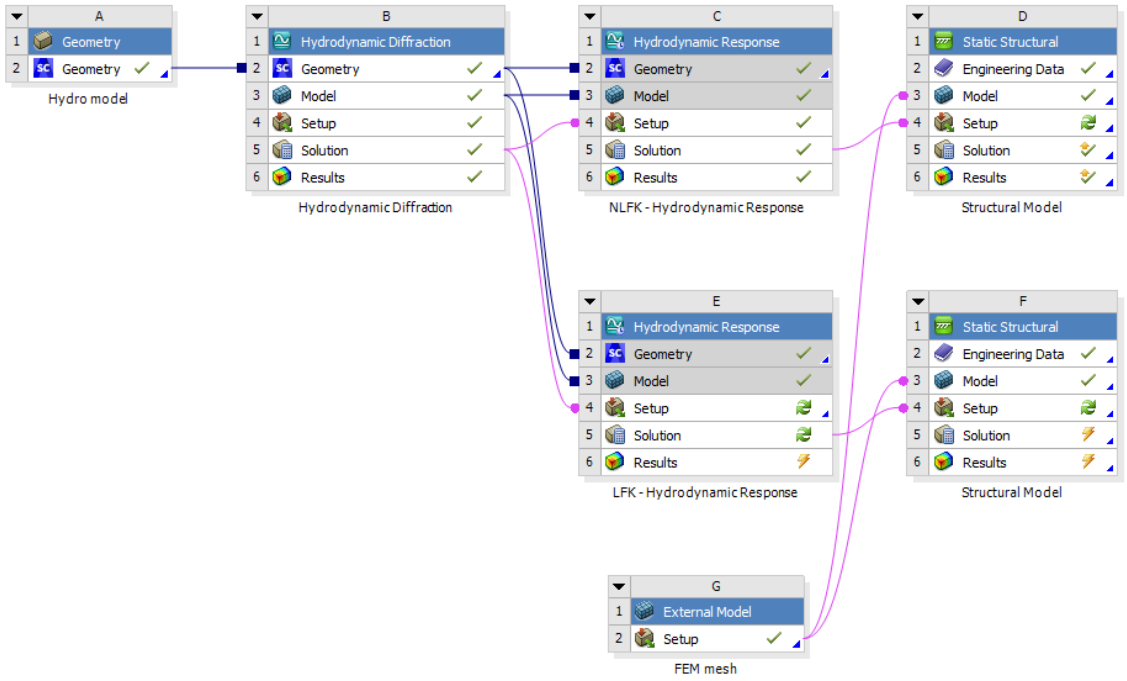

Figure B.4: *Workbench* model for the CA NL/L simulations.

B.2.2 Variable Amplitude Model

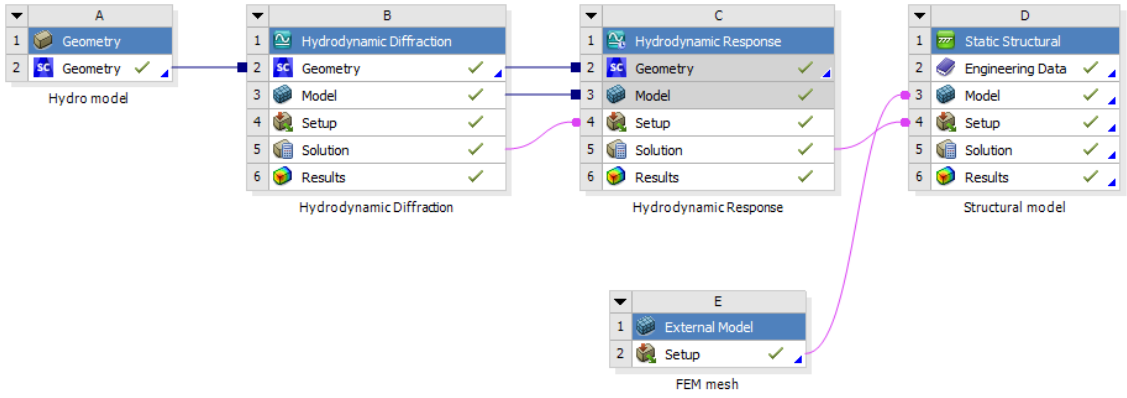

Figure B.5: *Workbench* model for the VA simulations.

B.3 Hydrodynamic Model

The settings of the VA model are used to showcase how the model has been set up.

B.3.1 Hydrodynamic Diffraction

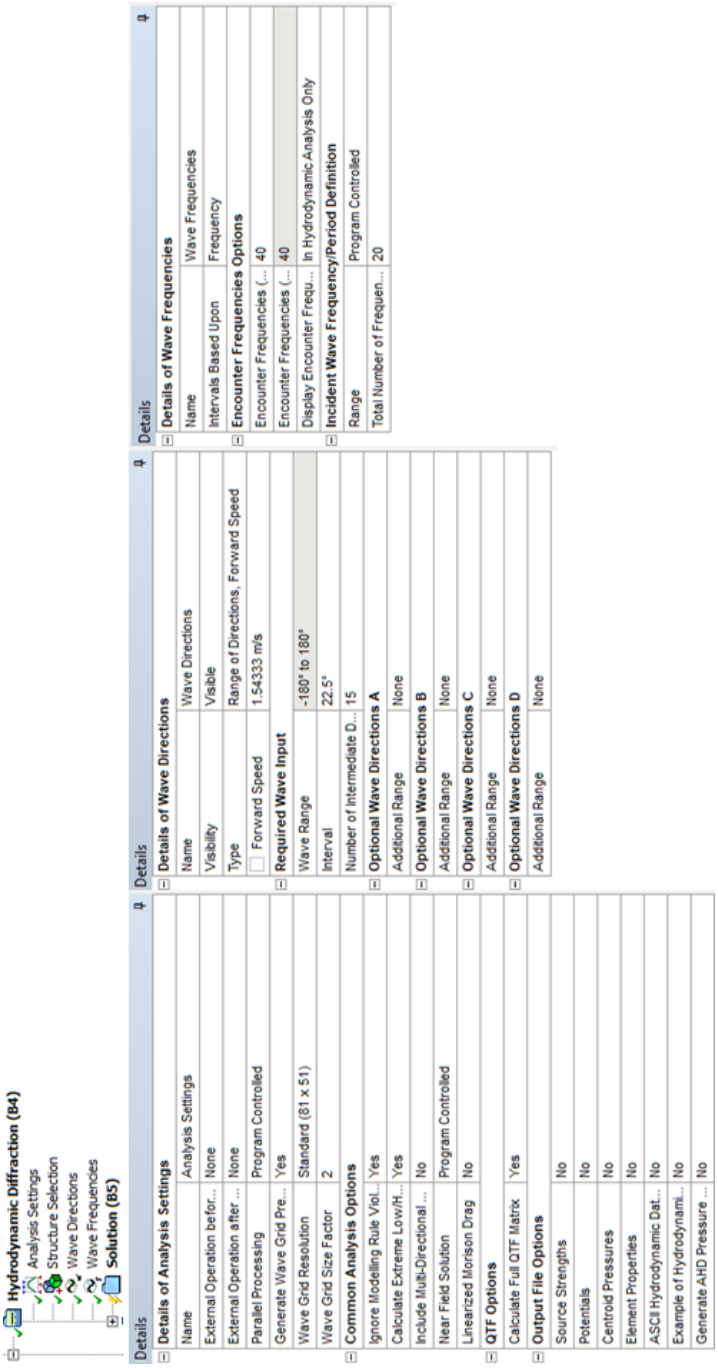

Figure B.6: The settings for the VA *Hydrodynamic Diffraction* module.

B.3.2 Hydrodynamic Response

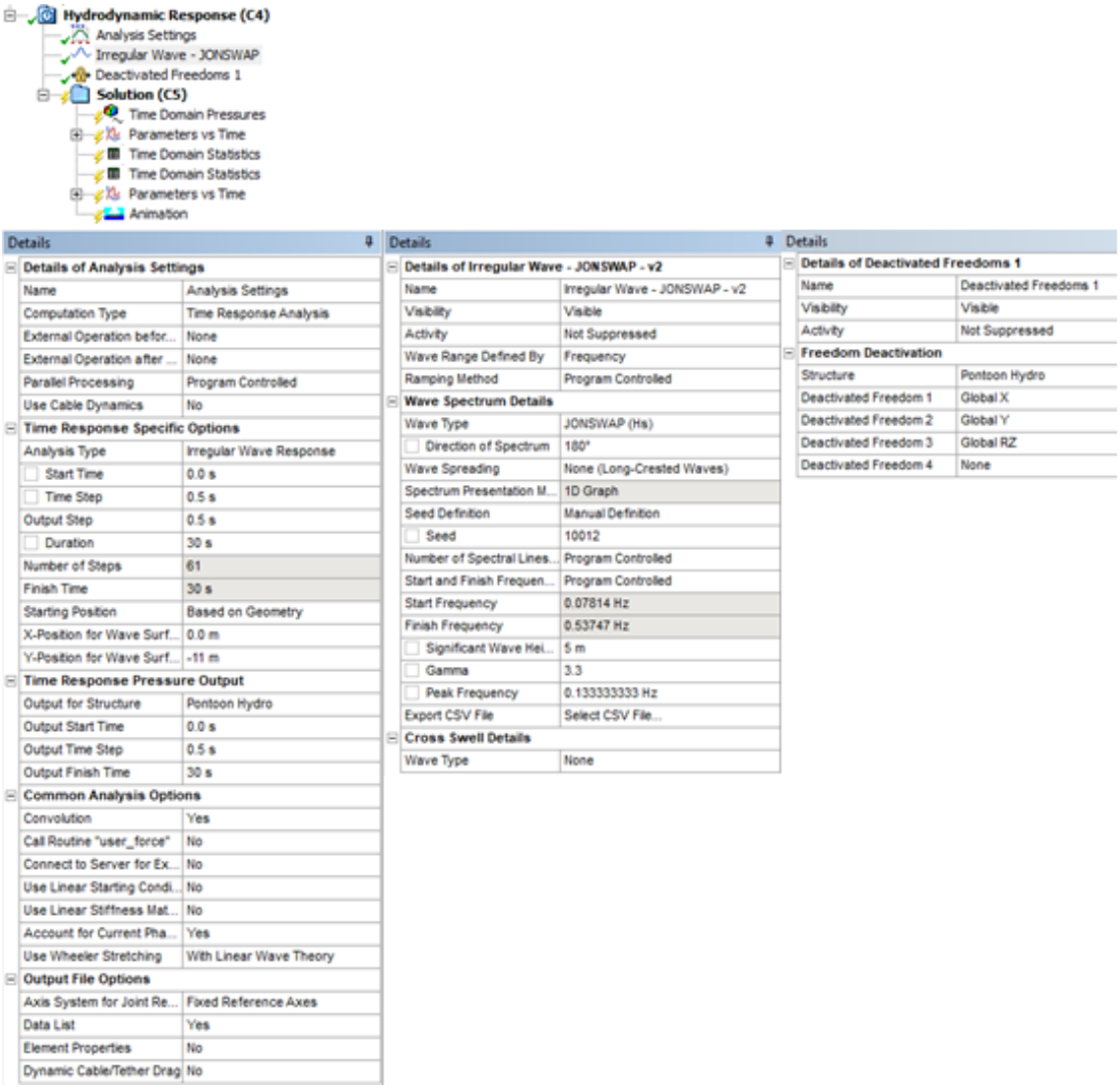

Figure B.7: The settings for the VA *Hydrodynamic Response* module.

B.4 Structural Model

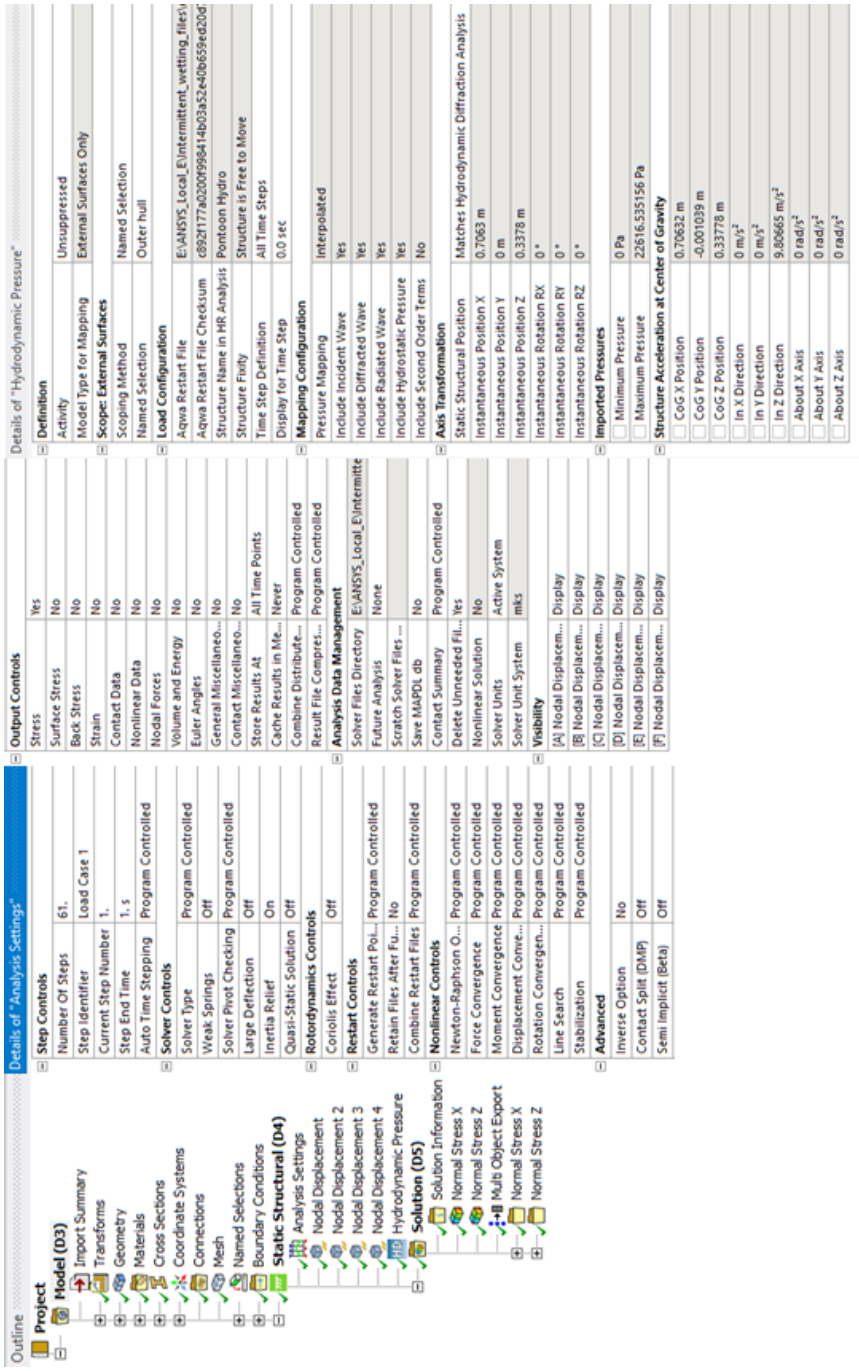

Figure B.8: The settings for the VA *Mechanical Structural* module.

B.4.1 Steel Material Properties

Table B.1: Material properties of structural steel applied in the *Structural* model. A fictitious density value was adopted to meet ship's ballast mass condition.

Structural Steel		
Property	**Value**	**Unit**
Density	25,000	kg/m^3
Coefficient of Thermal Expansion	1.2E-05	C^{-1}
Young's Modulus	2.00E5	MPa
Poisson's Ratio	0.3	-
Bulk Modulus	1.67E5	MPa
Shear Modulus	7.69E4	MPa
Tensile Yield Strength	250	MPa
Compressive Yield Strength	250	MPa
Tensile Ultimate Strength	460	MPa
Compressive Ultimate Strength	460	MPa

B.4.2 Exporting Results

Using the ACT extension *Multi Object Export* (MOE), stress time signals can be exported in .CSV format. Within *Named Selections* (figure B.8), a portion of the total nodes can be selected. This will decrease the computational burden in the post processing.

In the *Solution* module, the desired stress component can be selected for the chosen node selection (e.g. *Normal Stress X, Normal Stress Z*, etc.). After running the solution, select *'Create results at all sets'* in the right mouse button option panel of the stress component. This will generate a folder with the stress data at every time step.

The *MOE* can be added within the *Solution*. In here, one can specify the name of the result set to be exported, as well as the directory in which it should be stored (figure B.9). One should make sure that the result set name includes a space at the end. This way, only the time domain result set in the generated folder will be exported, ignoring the base case which includes the overall (mean) data. For the stress in X-direction (figure B.8), the name should therefore be:

'Normal Stress X '

Right clicking on the *MOE*-module then offers the option of exporting the data set and storing it. In the resulting .CSV-file, the rows indicate the different nodes and the columns indicate the time steps. Multiple time traces (rows) can apply to a single node. This is because multiple bodies can be attached to a node. Also, for every body, a *top* and *bottom* value is obtained, referring to the top and bottom of the plate. For the model in this thesis, the time trace with the maximum stress value was picked. Visual inspection of the results can be done within the *Structural* module by clicking on a set within the generated result folder.

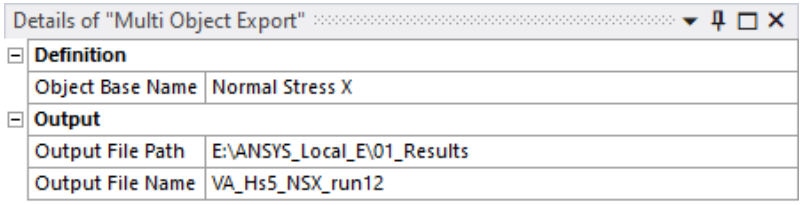

Figure B.9: Example settings of the *'Multi Object Export'* module.

Appendix C

Temporal Model Results

C.1 Ship RAO's

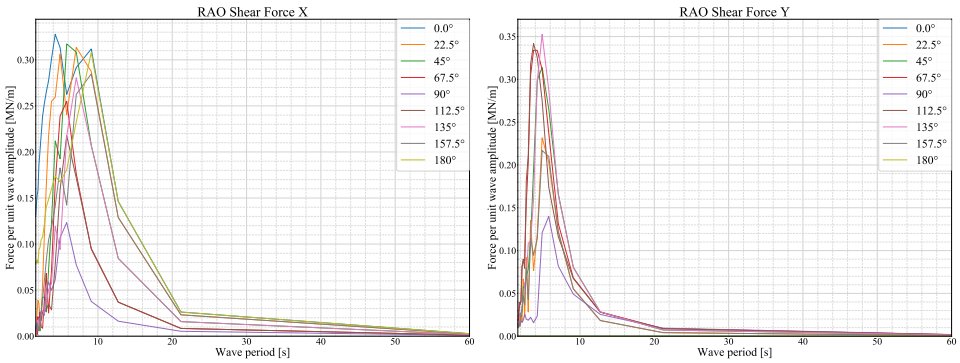

(a) RAO FX

(b) RAO FY

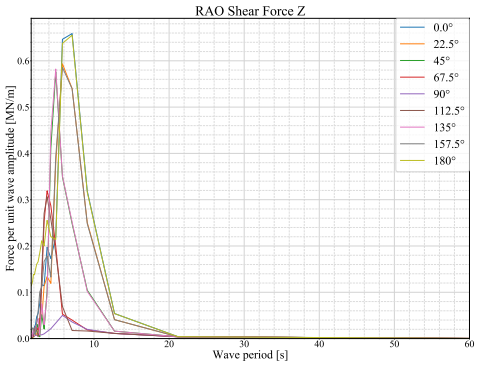

(c) RAO FZ

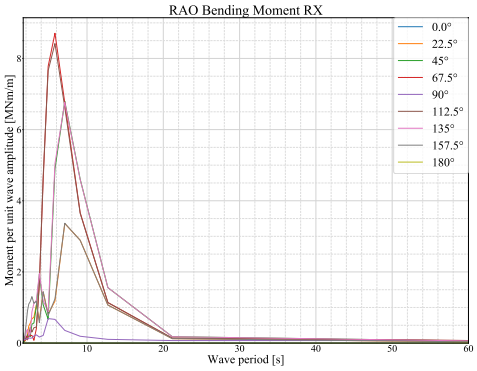

(d) RAO RX

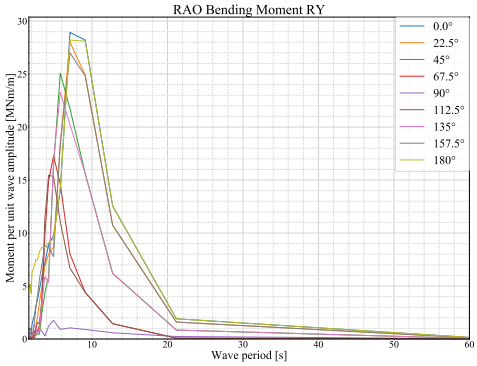

(e) RAO RY

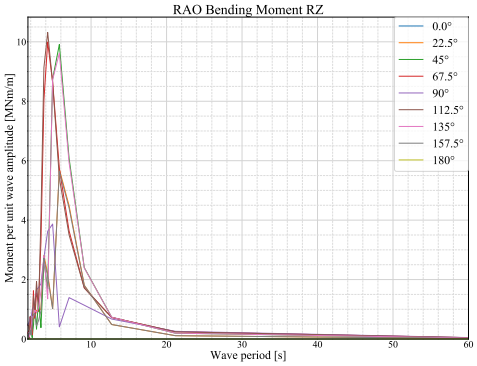

(f) RAO RZ

Figure C.1: RAO's in six DOF's for the pontoon vessel.

C.2 Constant Amplitude

C.2.1 Stress Response Midship

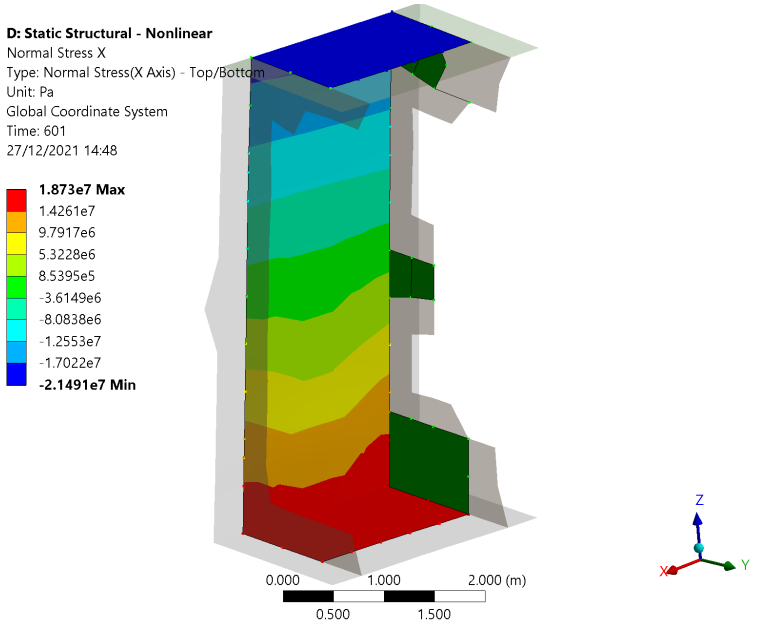

(a)

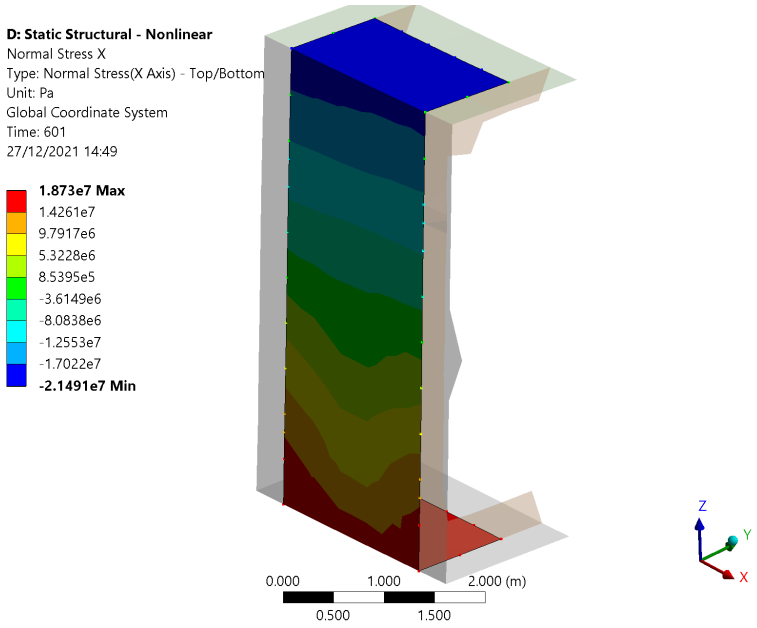

(b)

Figure C.2: Constant amplitude response - nonlinear case - ζ=5m - NSX at t=120 s.

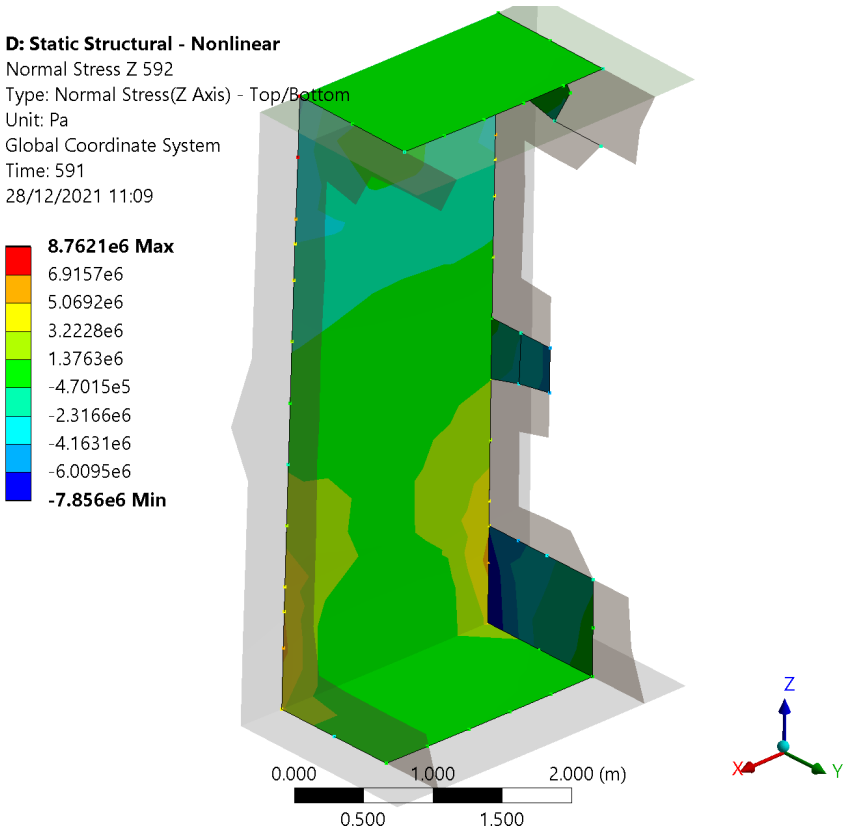

(a)

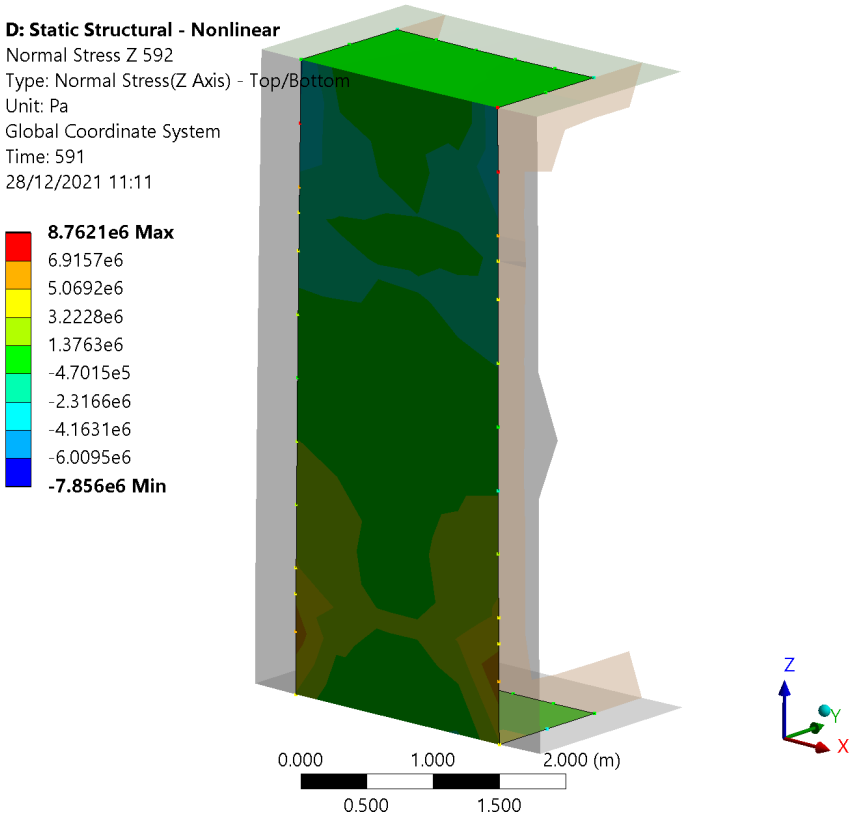

(b)

Figure C.3: Constant amplitude response - nonlinear case - ζ=5m - NSZ at t=118.4 s.

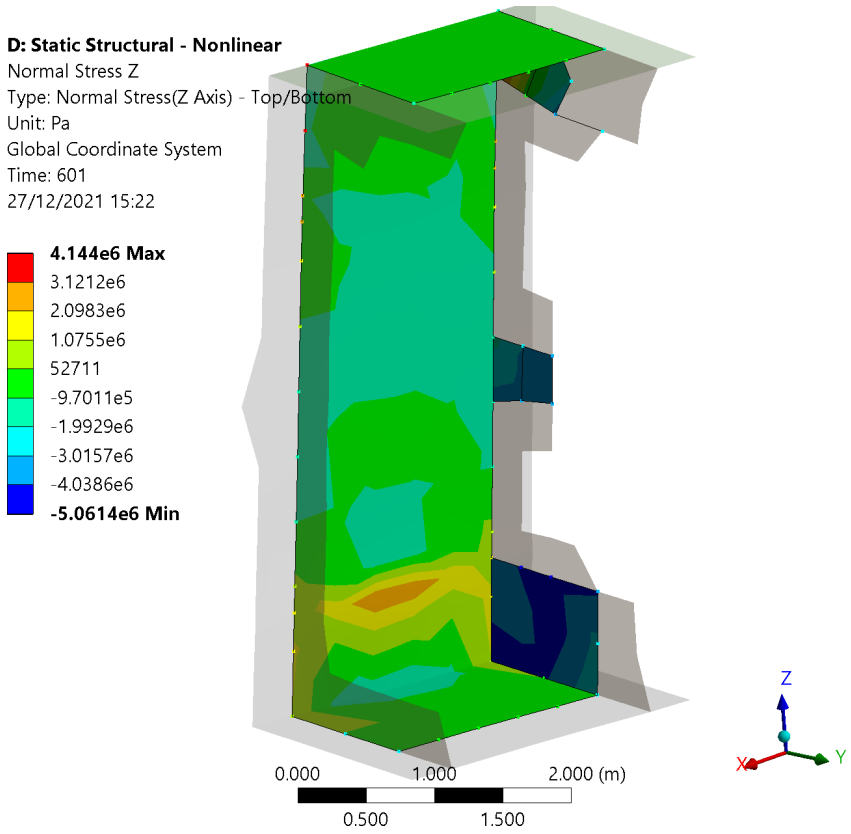

(a)

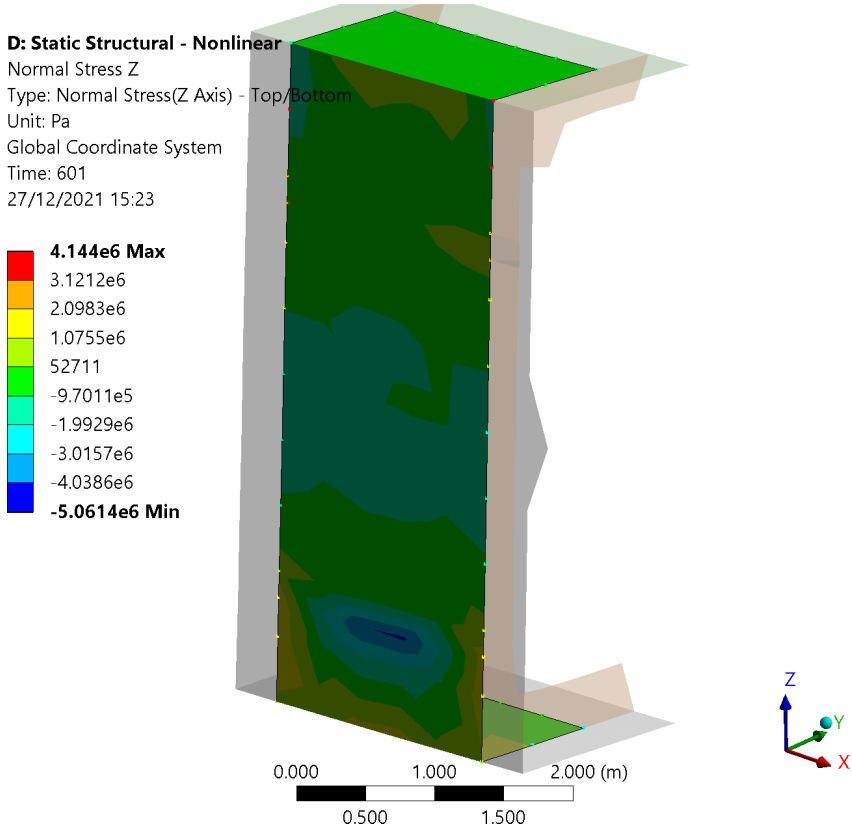

(b)

Figure C.4: Constant amplitude response - nonlinear case - ζ=5m - NSZ at t=120 s.

C.2.2 Time Trace Comparison Global Response

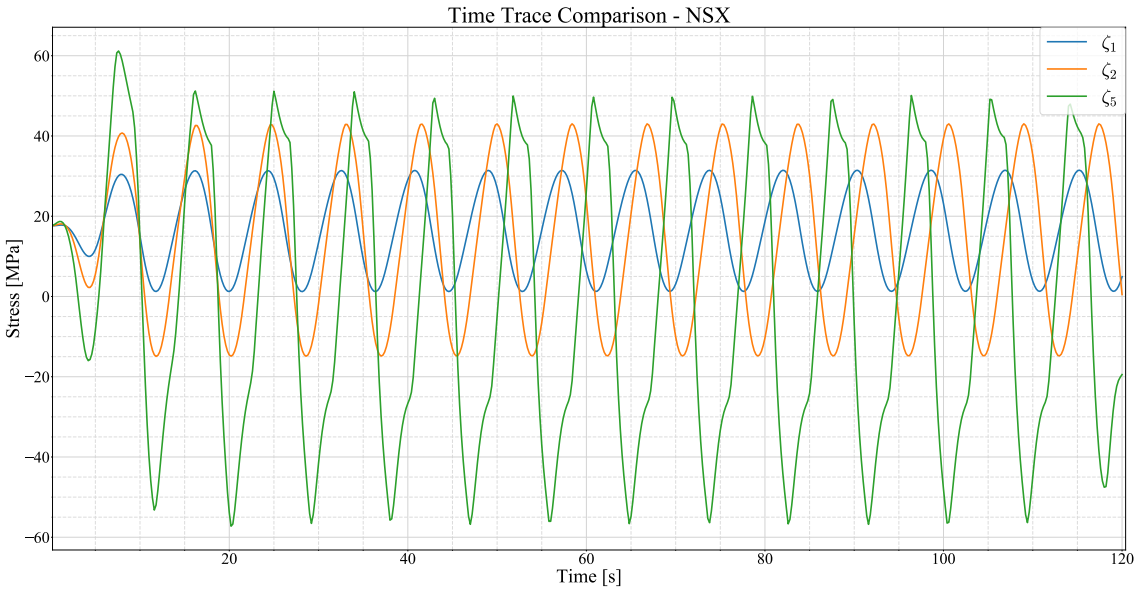

Figure C.5: Time trace for top deck node of selection 1 - NL - NSX - ζ={1,2,5} m

C.3 Variable Amplitude

C.3.1 Fourier Code (FFT, IFFT)

Matlab code provided by Bufalari (2021) [72] and converted into Python code.

FFT

```
def Timetrace_to_Spectrum(wave, dt):
    z = np.transpose(wave)
    n = len(wave)
    skl = 1 # Scaling factor
    sfr = 1/dt # Sampling frequency [Hz]

    m = 200 # Hamming, number of points in output window

    zf = fft(z) # Fourier transform of the signal
    R = zf*np.conj(zf)/n
    fr = np.arange(0, n)/n*sfr
    P = 2*R/sfr

    w = np.hamming(m) # Hamming(m) = 0.54-0.46*cos( 2*pi*n/(m-1)) 0<= n <= M-1
    w = w/np.sum(w)
    w = np.concatenate(( w[int(np.ceil(m/2)):m], np.zeros(n-m), w[0:int(np.
        ceil((m)/2))] ))
    w = fft(w)

    pavg = fft(P)
    pavg = ifft(w*pavg) # Inverse Fourier

    S = np.abs(pavg[0:int(np.ceil(n/2))])
    F = fr[0:int(np.ceil(n/2))]
    S = S/(2*np.pi)*np.sqrt(skl) # Spectral value ([main variable]^2*s)
    W = 2*np.pi*F/np.sqrt(skl) # Frequency W (rad/s)

    return W, S # Converted frequencies 'W' and spectral values 'S'
```

IFFT

```
def Spectrum_to_Timetrace(S_spectrum, w, tend, dt):
    delta_w = w[1] - w[0]  # Frequencies interval
    w = w + delta_w * np.random.uniform(size=len(w)) # Frequencies
    skl = 1 # Scale factor
    tskl = tend/skl # Time scaled (sec/min/hrs)
    sfr = 1/dt # Sampling frequency [Hz]
    t = np.arange(0, tskl, 1/sfr)*np.sqrt(skl) # Time vector
    phi = 2*np.pi*(np.random.uniform(low = 0.0, high = 1.0, size=len(w)) -
        0.5) # Random phase of ith frequency
    aj = np.sqrt(2*S_spectrum*delta_w) # Amplitude of the jth frequency from
        the JONSWAP spectrum

    wave = []
    for i, t_val in enumerate(t):
        wave.append(np.sum(aj*np.cos(w*t_val+phi)))

    # Resulting wave
    # Wave could be any oscillatory signal (stress, wave elevation, etc.)
    wave = np.array(wave)

    return t, wave
```

C.4 Rainflow Data Waterline and Bottom Nodes

C.4.1 Waterline Node

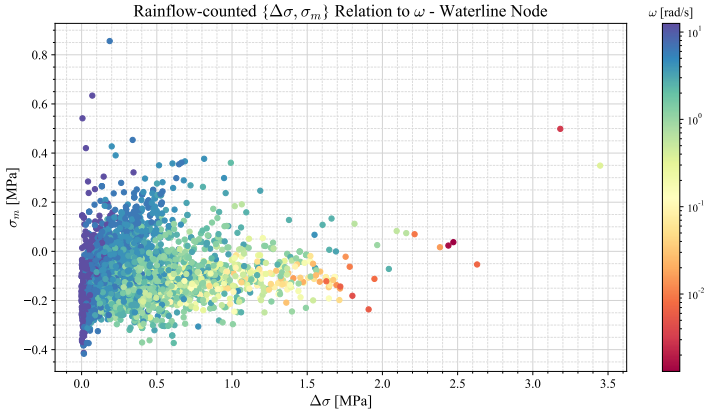

(a)

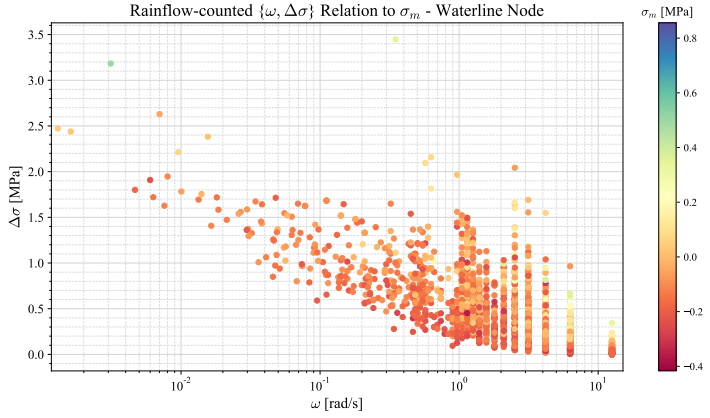

(b)

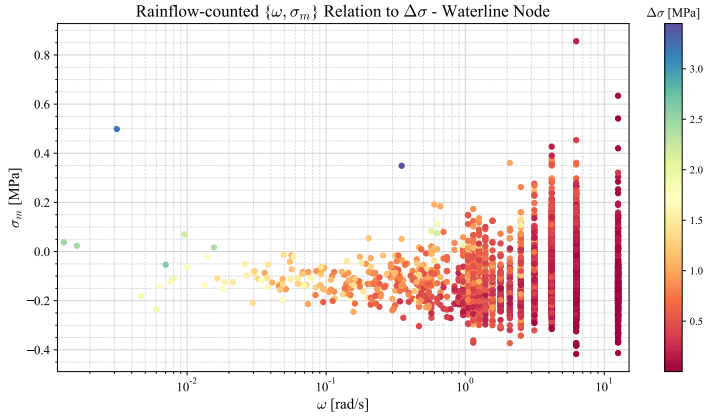

(c)

Figure C.6: Rainflow-counted $\{\omega, r_{lr}, D\}$ data with in the third axis D_i/D_{max} **(a)**, r_{lr} **(b)**, and ω **(c)** for the waterline node ($JS\{H_s = 5\text{ m}, T_p = 7.5\text{ s}, \gamma = 3.3\}, NSX$).

C.4.2 Bottom Node

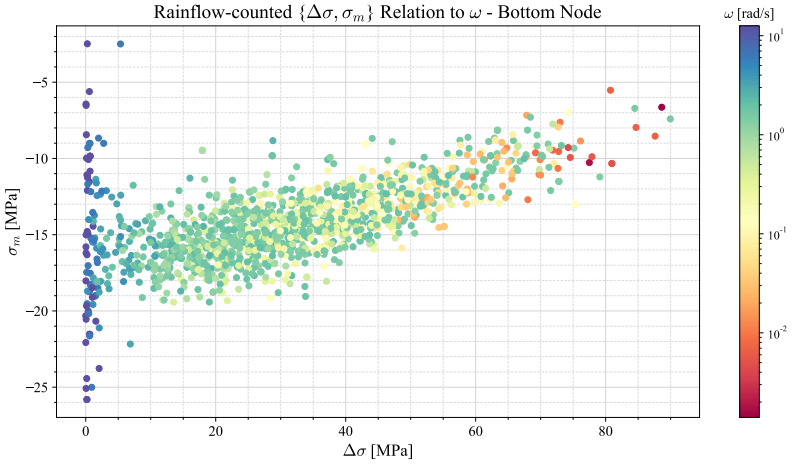

(a)

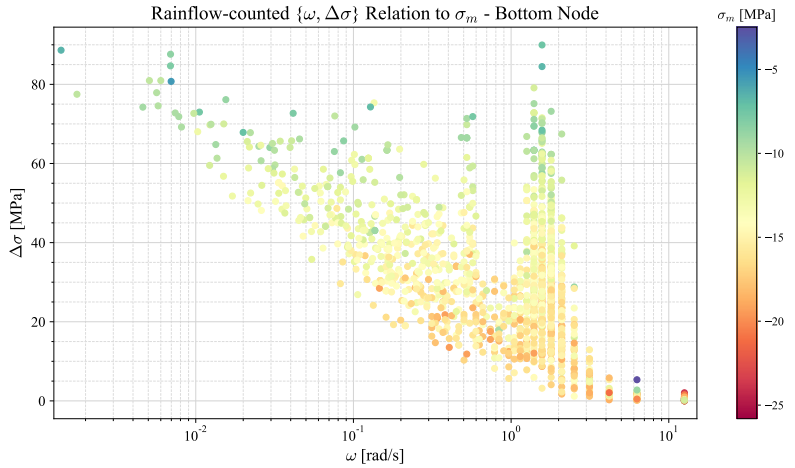

(b)

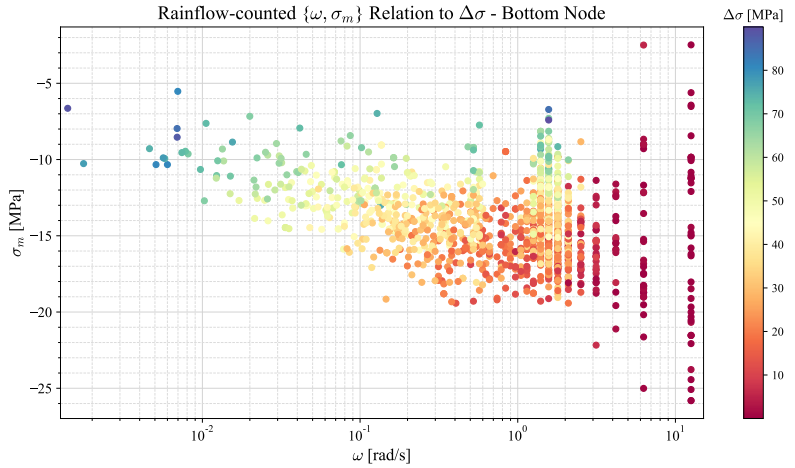

(c)

Figure C.7: Rainflow-counted $\{\omega, r_{lr}, D\}$ data with in the third axis D_i/D_{max} **(a)**, r_{lr} **(b)**, and ω **(c)** for the bottom deck node ($JS\{H_s = 5\text{ m}, T_p = 7.5\text{ s}, \gamma = 3.3\}$, NSX).

C.5 Rainflow Damage Data Waterline and Bottom Nodes

C.5.1 Waterline Node

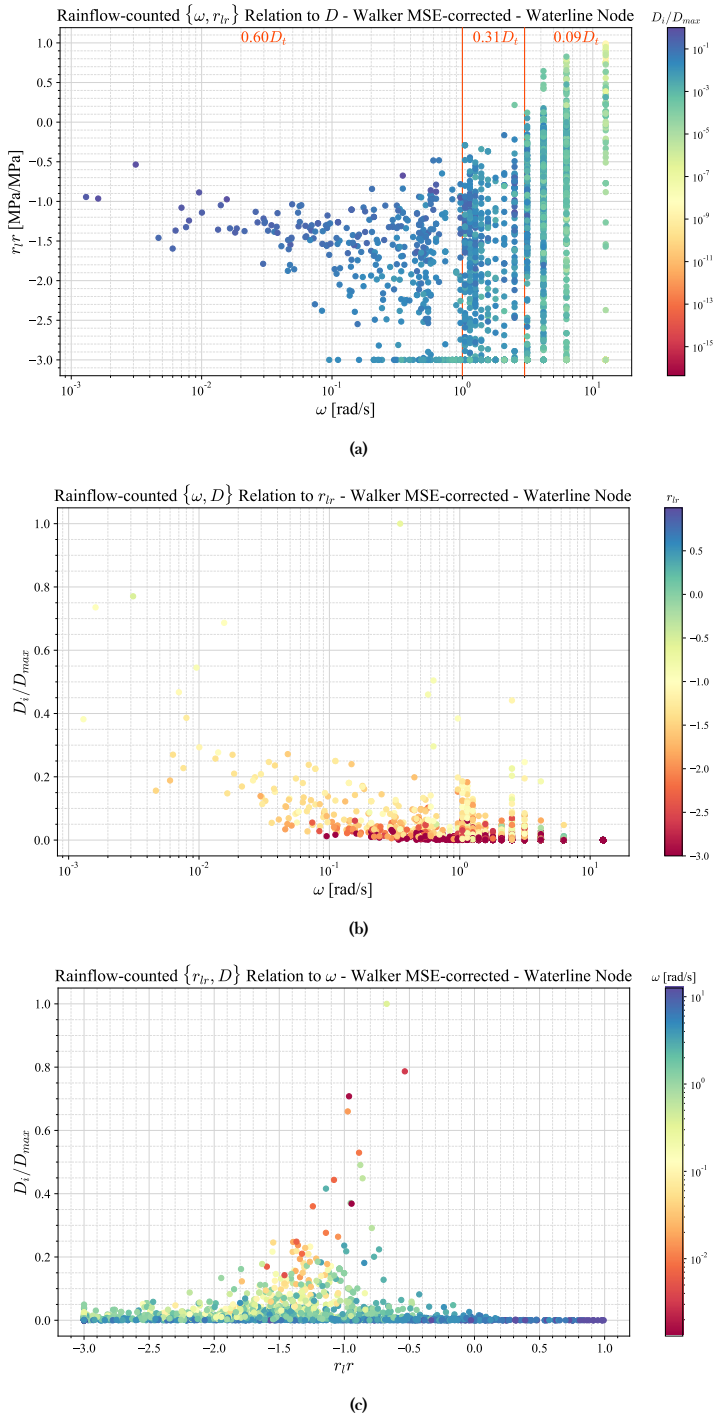

Figure C.8: Rainflow-counted $\{\omega, r_{lr}, D\}$ data with in the third axis D_i/D_{max} **(a)**, r_{lr} **(b)**, and ω **(c)** for the waterline node ($JS\{H_s = 5\text{ m}, T_p = 7.5\text{ s}, \gamma = 3.3\}$, NSX). Figure **(a)** includes the total damage distribution, focusing on the cluster at $\omega = [1, 3]$ rad/s

C.5.2 Bottom Node

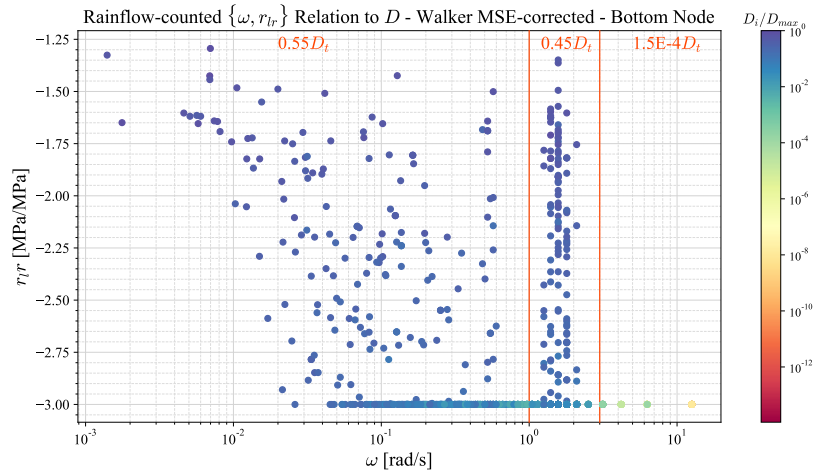

(a)

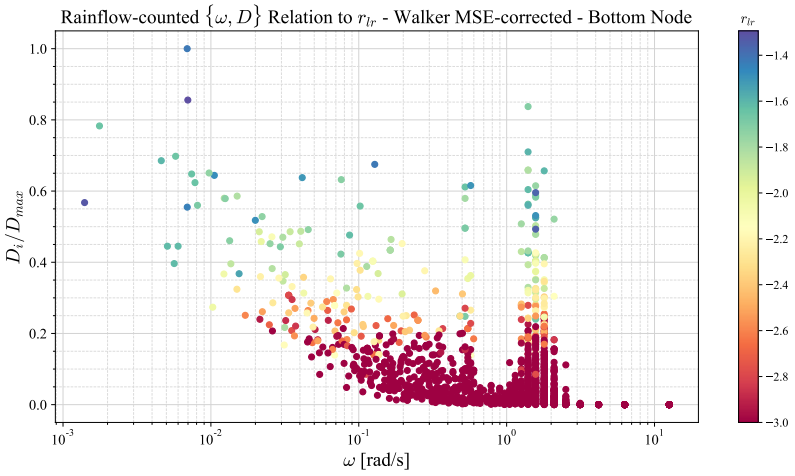

(b)

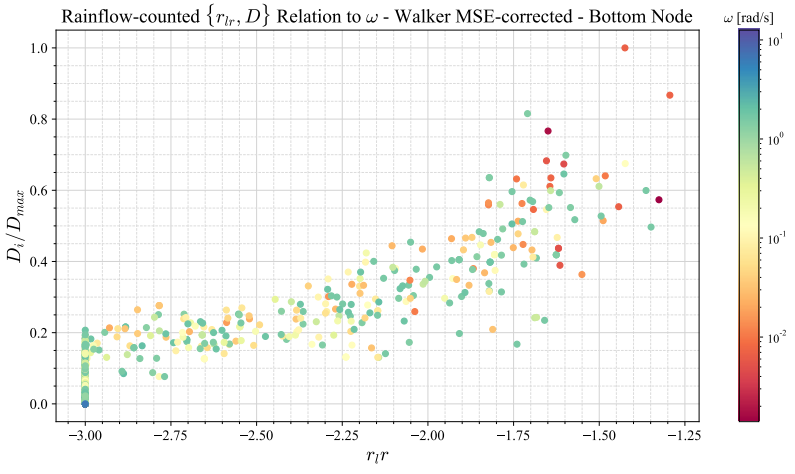

(c)

Figure C.9: Rainflow-counted $\{\omega, r_{lr}, D\}$ data with in the third axis D_i/D_{max} **(a)**, r_{lr} **(b)**, and ω **(c)** for the bottom deck node ($JS\{H_s = 5\text{ m}, T_p = 7.5\text{ s}, \gamma = 3.3\}$, NSX). Figure **(a)** includes the total damage distribution, focusing on the cluster at $\omega = [1, 3]$ rad/s

C.6 Global versus Local Walker Coefficients

C.6.1 Top Deck Node

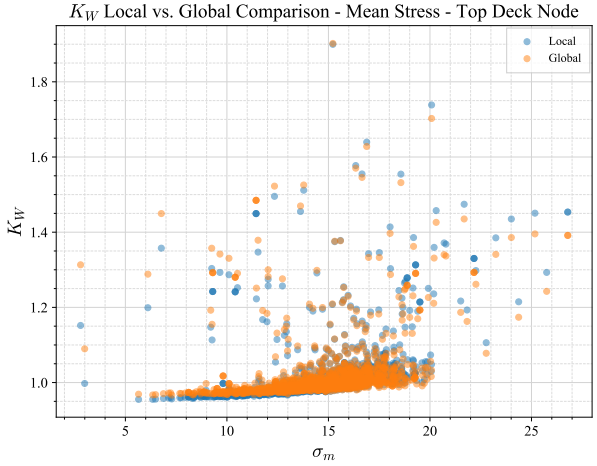

(a)

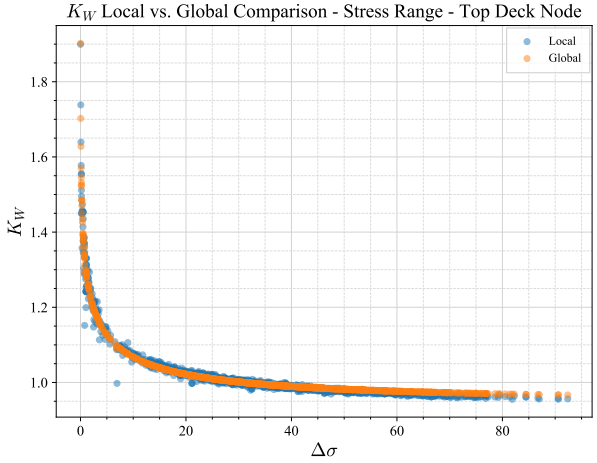

(b)

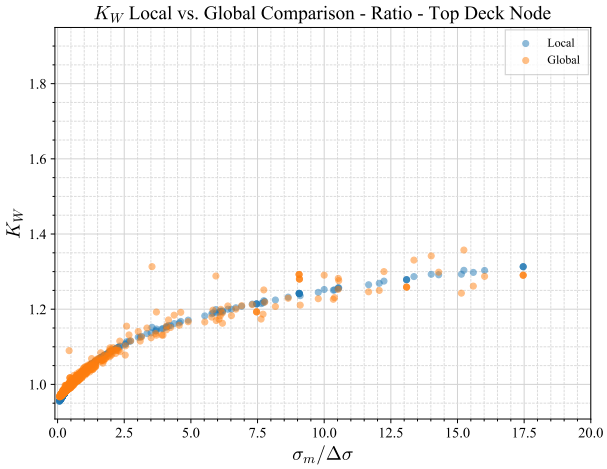

(c)

Figure C.10: Walker coefficient comparison for the global and local method, for every stress cycle, over σ_m **(a)**, $\Delta\sigma$ **(b)** and $\sigma_m/\Delta\sigma$ **(c)** for the top deck node.

C.6.2 Waterline Node

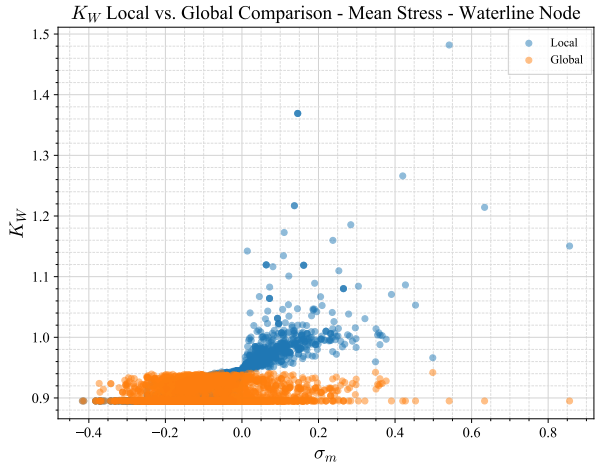

(a)

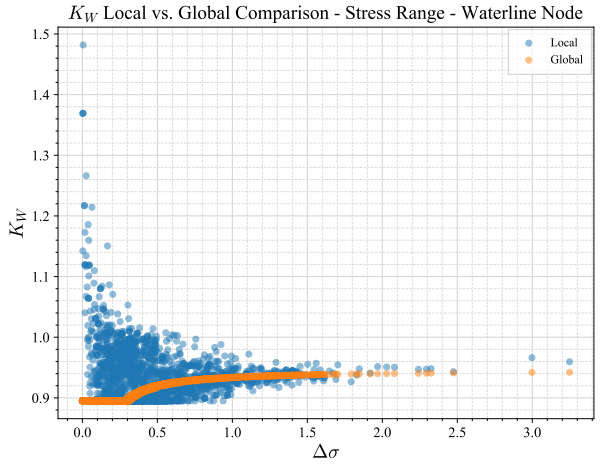

(b)

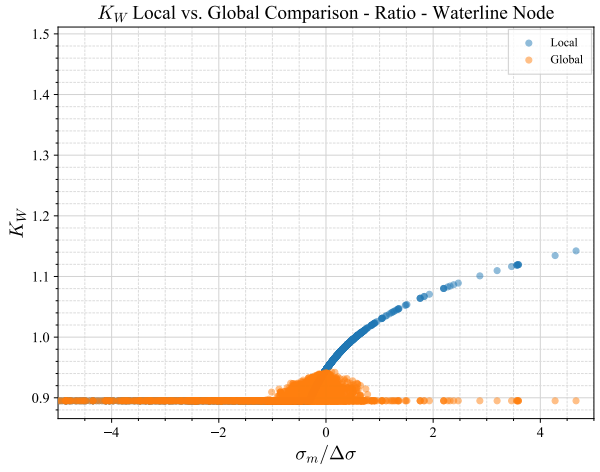

(c)

Figure C.11: Walker coefficient comparison for the global and local method, for every stress cycle, over σ_m **(a)**, $\Delta\sigma$ **(b)** and $\sigma_m/\Delta\sigma$ **(c)** for the waterline node.

C.6.3 Bottom Node

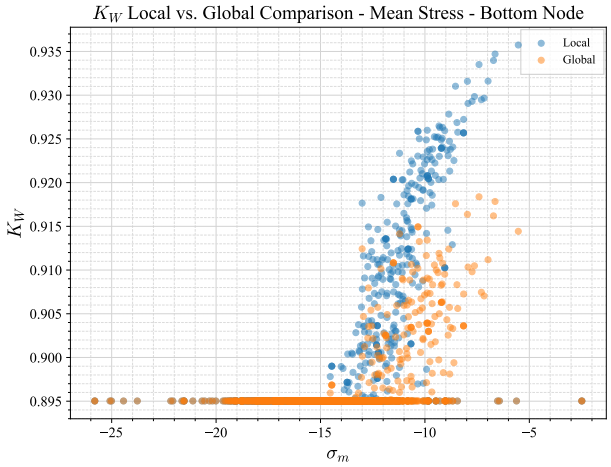

(a)

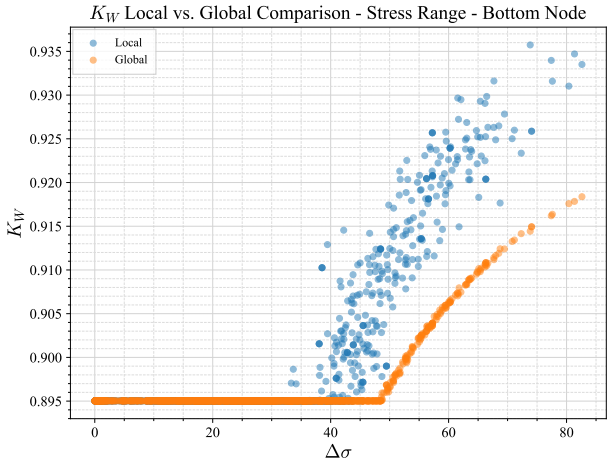

(b)

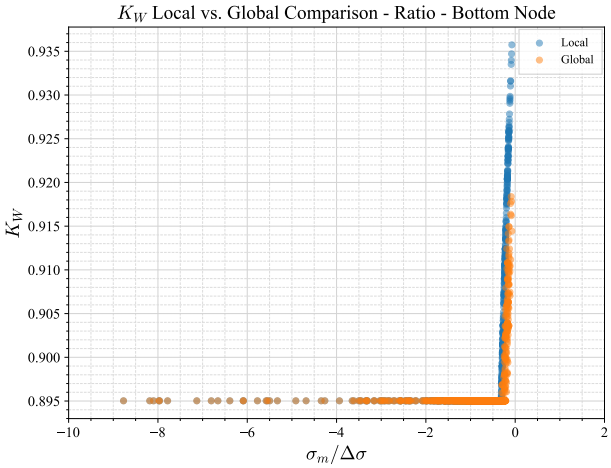

(c)

Figure C.12: Walker coefficient comparison for the global and local method, for every stress cycle, over σ_m **(a)**, $\Delta\sigma$ **(b)** and $\sigma_m/\Delta\sigma$ **(c)** for the bottom node.

C.7 Unfiltered Damage Comparison for the Full Node Set

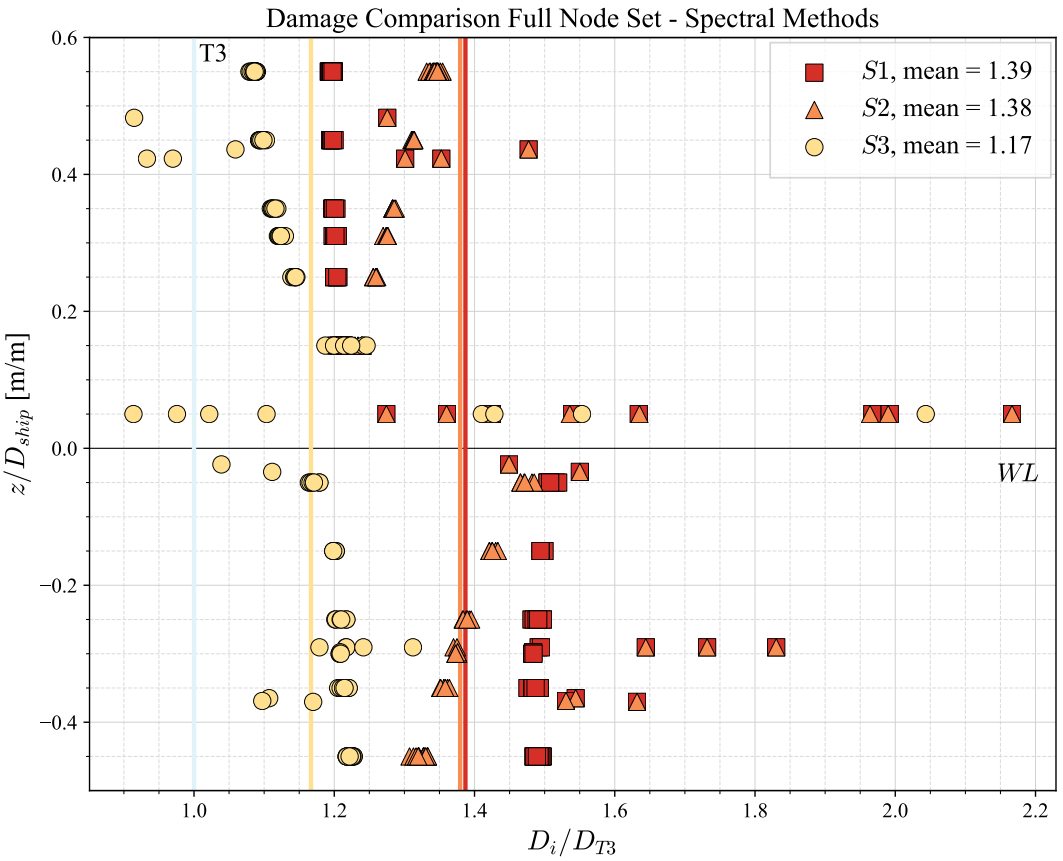

Figure C.13: Unfiltered comparison of the three spectral methods $\{S1, S2, S3\}$ against the detailed local Walker time domain method $T3$.

Delft
University of
Technology

TU Campus, Building 34
Mekelweg 2, 2628 CD Delft
T. +31 15 278 9809

www.tudelft.nl/3me